国際化推進共同研究概要

No.1

23EA-1

タ イ ト ル： The optical properties of nonspherical ice crystals and their applications to spaceborne remote sensing

研究代表者： SAITO Masanori

所内世話人： 岡本　創

研 究 概 要：

　衛星搭載ライダの解析に利用可能な、非球形の氷粒子の後方散乱特性に関して、粒子形状、表面のラフネス、粒子半径を様々に変化させた計算を波長355nm, 532nmそして1064nmに対して行った。得られた結果は、A-Train衛星やEarthCARE衛星搭載ライダの解析に適用可能であり、氷粒子特性の把握に有効なものである。

The optical properties of nonspherical ice crystals and their applications to spaceborne remote sensing

Masanori Saito (University of Wyoming)

I. Abstract

Spaceborne active sensor observations play a pivotal role in the observations of the three-dimensional distributions of ice clouds over the globe that have been performed by the NASA A-Train constellation and will be continued by the EarthCARE mission. However, spaceborne lidar observations have the critical limitation that a reliable ice crystal backscattering model is absent, resulting in using an empirical model to interpret lidar signals. We have developed both method and computational capabilities to develop a reliable ice crystal backscattering model. We computed the backscattering properties of ice crystals with various crystal shapes, which are consistent with those observed from CALIOP. The ultimate goal is to develop a physics-based radar-lidar remote sensing method to better characterize ice cloud properties for the EarthCARE mission.

II. Introduction

Ice clouds are ubiquitous across the globe and lead to a large uncertainty in the Earth's radiation budget estimations due to the complexity of their radiative and microphysical interactions in the atmosphere. Therefore, it is essential to monitor the optical and microphysical properties of ice clouds on a global scale through spaceborne observations with remote sensing techniques. Spaceborne radar and lidar observations can profile the vertical structures of ice clouds using the radar-lidar algorithm that has been developed and improved through two-decade-long efforts made by the Okamoto group (e.g., Okamoto et al., 2003). This algorithm can infer ice cloud extinction and ice water content (or effective radius) profiles. The accuracy of these retrievals hinges primarily upon the assumption of the backscattering properties of ice crystals at both radar and lidar-relevant wavelengths, where two major challenges exist: 1) the backscattering model for radar observations often relies on the Rayleigh scattering approximation, which becomes an invalid assumption for millimeter-scale ice hydrometeors. DDA is an alternative and promising approach that can account for complex particle geometries, and however this leads to an inconsistency with the optical property models at lidar wavelengths, as explained later; and 2) the reliable modeling studies of the backscattering properties of nonspherical ice crystals are still premature. In particular, some computational techniques based on geometric optics or physical optics principles are limited to simple nonspherical particle shapes, while ice crystals found in natural ice clouds show complex textures such as scall-scale surface roughness that can occur through the deposition-sublimation processes. Our light-scattering computational capabilities are applicable to such complex particle geometries.

Saito and Yang (2023) found that the coherent backscattering (CB) is essential to explain the backscattering properties of nonspherical particles in the geometric optics regime, and developed the correction method based on the geometric optics principle. Now the time has come to tackle the development of a reliable ice crystal optical property model to improve the radar-lidar remote sensing method for ice cloud property characterizations.

III. Data and Method

We use the improved geometric optics method (Yang and Liou, 1996) and the CB correction method (Saito and Yang, 2023) to compute the backscattering properties of various ice crystals at the three lidar wavelengths, including 355 nm, 532 nm, and 1064 nm. Figure 1 illustrates the shapes of ice crystals considered in this study. We consider 63 hexagonal columns with various degrees of surface roughness and aspect ratios and 20 irregular column aggregate particles. We assume a gamma particle size distribution (PSD) with an effective variance of 0.26 (Saito and Yang, 2022), which was constrained with a suite of in-situ measurements in PSDs of ice clouds.

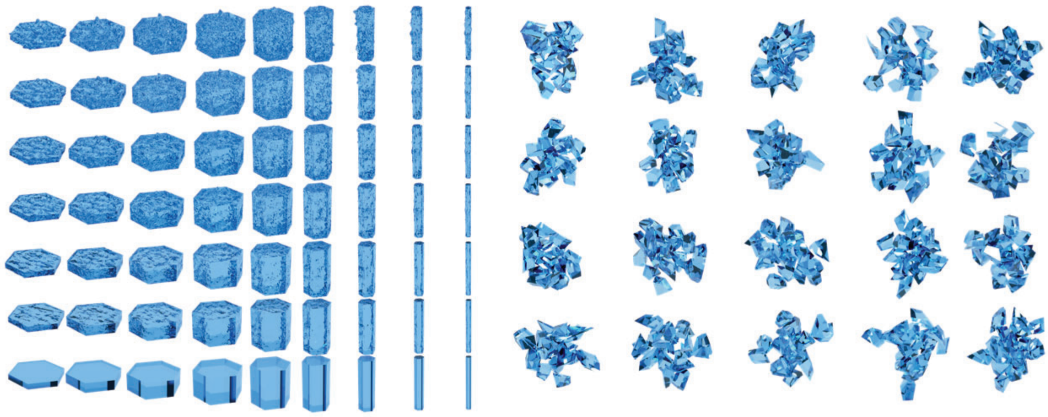

Figure 1. An illustration of ice crystal shapes considered in this study.

IV. Results

Figure 2 highlights the variations of the backscattering properties with the shape of ice crystals and effective radii for the case of aggregates. We found that the backscattering properties have a weak dependence on the effective radii and moderate dependence on the ice crystal shapes as seen in Fig 2. The lidar ratio and depolarization ratio range from 25-55 sr and 0.5-0.6, respectively, and are consistent with CALIOP lidar observations. A slight spectral dependence among lidar wavelengths is presumably associated with the spectral differences of the complex ice refractive indices at the visible to near-infrared spectra.

We tested the single hexagonal columns that show substantial variations of the backscattering properties with the aspect ratios and the degree of surface roughness. As consistent with Saito and Yang (2023), the degree of surface roughness primarily determines the depolarization ratio of ice crystals. While the lidar ratio is mainly determined by the aspect ratio. The resultant computational results will be useful to develop an optimal ice crystal backscattering property model by constraining the particle shape distributions using in-situ observations of ice crystal shapes in ice clouds.

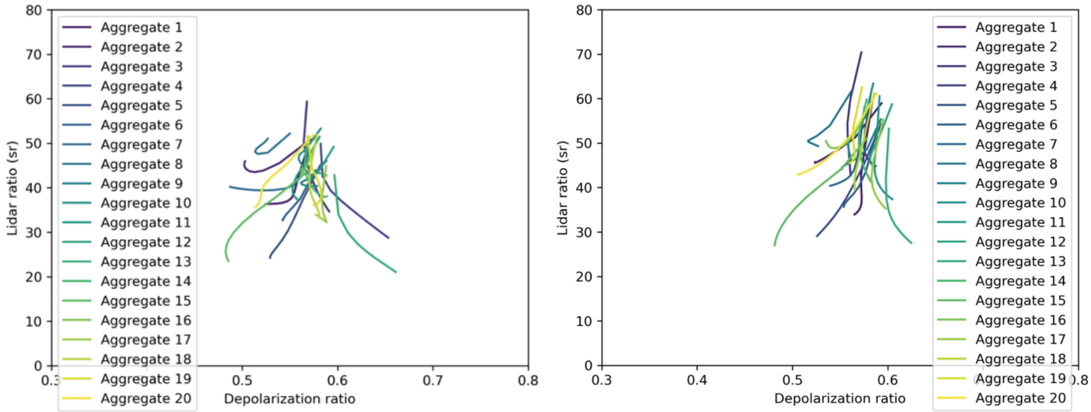

Figure 2. The backscattering properties of ice crystals with various effective radii and particle shapes at 355 nm and 532 nm.

V. Discussion/Summary

In this study, we performed sensitivity tests to investigate the importance of the ice crystal shapes and effective radii on the backscattering properties of ice crystals. The particle shape is identified to be a critical factor in the backscattering properties. Overall, the range of the backscattering properties of ice crystals assumed in this study falls within the range of those observed by spaceborne lidar instruments, implying that the ice crystal shape assumption is appropriate. This preliminary result paved the road to achieving the physics-based radar-lidar remote sensing algorithm development for a better ice cloud characterization using spaceborne active sensor observations that are relevant to the upcoming observations through the EarthCARE mission.

VI. References

Okamoto, H., Iwasaki, S., Yasui, M., Horie, H., Kuroiwa, H., and Kumagai, H.: An algorithm for retrieval of cloud microphysics using 95-GHz cloud radar and lidar, J. Geophys. Res., 108, 4226– 4247, https://doi.org/10.1029/2001JD001225, 2003.

Saito, M., and P. Yang, (2022). Generalization of Atmospheric Nonspherical Particle Size: Interconversions of Size Distributions and Optical Equivalence . Journal of the Atmospheric Sciences, 79, 3333–3349 https://doi. org/ 10.1175/JAS-D-22-0086.1.

Saito, M., and P. Yang, (2022). Generalization of Atmospheric Nonspherical Particle Size: Interconversions of Size Distributions and Optical Equivalence . Journal of the Atmospheric Sciences, 79, 3333–3349 https://doi. org/ 10.1175/JAS-D-22-0086.1.

Saito, M., & Yang, P. (2023). Quantifying the Impact of the Surface Roughness of Hexagonal Ice Crystals on Backscattering Properties for Lidar-Based Remote Sensing Applications. Geophysical Research Letters, 50(18), e2023GL104175.

Yang, P., and K. Liou (1996), Geometric-optics–integral-equation method for light scattering by nonspherical ice crystals, *Appl. Opt.*, *35*(33), 6568–6584.

VII. Research meeting and discussion

Masanori Saito visited the Research Institute for Applied Mechanics (RIAM) at Kyushu University, Japan between 18 and 22 December 2023 where he met with Dr. Hajime Okamoto and the group members for various research discussions. Saito gave a seminar at RIAM and a lecture on the usage of the database of the single-scattering properties to students, postdocs, and faculty members in RIAM, with a total of more than 10 attendees.

VIII. Other members of the joint research team

Hajime Okamoto RIAM, Kyushu University

国際化推進共同研究概要

No.2

23EA-2

タイトル： Dynamical mechanisms of stratospheric control on the tropical troposphere and ocean

研究代表者： UEYAMA Rei

所内世話人： 江口　菜穂

研究概要： 2002 年 8 月 8 日から 9 日にかけて、朝鮮半島や北日本を含む東アジアで記録的な大雨が発生しました。 この「100 年に一度の洪水現象」は、境界層汚染物質の深い対流による成層圏への輸送の影響を研究する NASA の航空機キャンペーン（ACCLIP）中に発生しました。 私たちは、上部対流圏と下部成層圏の現場観測の分析を容易にするために、昨年開発した全球の対流雲の雲頂高度と温位を分析しました。 その結果、2022 年 8 月の豪雨現象は熱帯の深い対流活動に関連していると思われ、成層圏と対流圏の相互作用に関するプロセスの理解を向上させた。

Dynamical Mechanisms of Stratospheric Control on the Tropical Troposphere and Ocean

Rei Ueyama (NASA Ames Research Center)

I. Abstract

On August 8 to 9, 2002, a record rainfall event occurred over eastern Asia including the Korean peninsula and northern Japan. This so-called "100-yr flooding event" occurred during one of NASA's airborne campaigns (ACCLIP) to study the impact of deep convective transport of boundary layer pollutants to the global stratosphere. We have analyzed the global convective cloud top altitudes and potential temperatures, developed last year, to facilitate the analysis of in situ measurements in the upper troposphere and lower stratosphere. The objective is to improve process-level understanding of stratosphere and troposphere interactions, such as the mechanism of the heavy rainfall event of August 2022 which appears to have been related to deep convective activity in the tropics.

II. Introduction

One of the important mechanisms of stratosphere and troposphere exchange (STE) is deep convection that detrains mass in the upper troposphere and lower stratosphere (UTLS). These convective storms are especially strong and frequent over the Asian and North American monsoon regions during boreal summer (ASM and NAM, respectively). Water vapor and boundary layer pollutants lofted by deep monsoon convection are typically trapped within the strong anticyclonic circulation in the UTLS and later dispersed throughout the global stratosphere, where they can have a significant impact on radiative and chemical processes, potentially including stratospheric ozone.

The Asian summer monsoon Chemical and Climate Impact Project (ACCLIP) deployed two aircraft – NSF GV and NASA WB-57 – from South Korea during Jul-Aug 2022 to obtain in situ measurements of UTLS composition in the region of ASM outflow to characterize the impact of the ASM on global chemistry and climate (https://espo.nasa.gov/acclip/content/ACCLIP). Overshooting convective storms (i.e., deep convection that penetrates the tropopause) were the target of another recent NASA airborne campaign, Dynamics and Chemistry of the Summer Stratosphere (DCOTSS), which measured the composition of these overshooting convective plumes within the North American monsoon region during summers 2021 and 2022 (https://dcotss.geos.tamu.edu/). The main objective of the DCOTSS mission was to determine the effects of these overshooting storms on the dynamics, chemistry and composition of the stratosphere. Data from both aircraft campaigns are now publicly available.

In order to place these in situ measurements from ACCLIP and DCOTSS campaigns within the context of large-scale meteorology and examine the dynamical interactions between the stratosphere and troposphere, there was a need for a global dataset of observation-based estimates of deep convection. In this study, we analyzed such a dataset to explore the mechanism of the "100-yr flooding event" that occurred in South Korea during the ACCLIP deployment.

III. Method/Data

The datasets used in this study are JRA3Q reanalysis data, NOAA outgoing longwave radiation (OLR) data, surface precipitation measurements from Global Precipitation Climatology Project (GPCP), and satellite-derived global convective cloud top altitudes (Pfister et al, 2022).

IV. Results

Figure 1 shows the anomalies of East Asian summer monsoon (EASM) convection in August 2022 scaled by the interannual variability using the standard deviation (σ). Here the distribution of the deep convection anomaly is derived from satellite infrared (IR) brightness temperature and is consistent with the satellite-derived convective cloud top altitude anomalies. The 2-3σ positive anomalies highlight the active EASM convection in late summer along the East Asia subtropical front, which migrated northward from the location of the typical Baiyu front. Also shown in the figure is the shape and location of the anticyclone in August 2022 together with the 44-year climatology. Compared to the climatology, the 2022 anticyclone was enlarged and much more elongated, with its center shifted further east, such that it encompassed more of the East Asian convergence zone than in a typical season. Furthermore, the amplification of the Tibetan anticyclone in August 2022 was associated with the strengthening of the westerlies and easterlies at the north and south of the Tibetan Plateau, respectively. The anomalies highlighted in Figure 1 are the key elements of the circulation pattern change that contributed to the findings of the ACCLIP campaign.

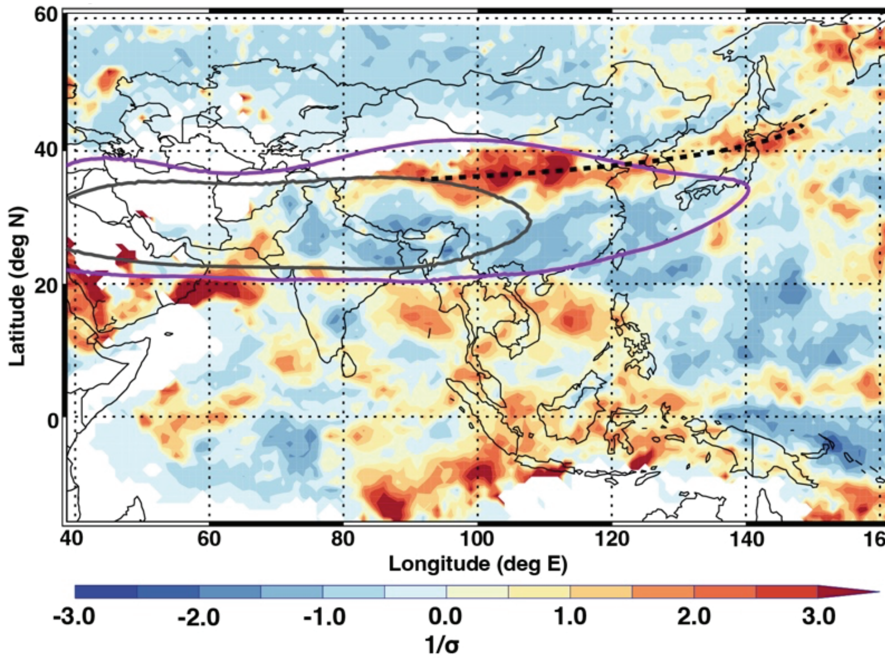

Figure 1: August 202 anomalies of the occurrence frequency of convection defined by infrared brightness temperature <235 K using GPM MERGIR satellite data. The criterion identifies convective cloud tops above ~12 km altitude. Anomalies are calculated with respect to the climatological (2006-2022) August mean occurrence frequency at each location and scaled by the standard deviation (σ). The position of the East Asian subtropical front for

August 2022 is highlighted (black dashed curve). Also shown are 150 hPa geopotential height 14350-m contours for the 44-yr (1979-2022) Aug climatology (gray) and Aug 2022 (purple).

The dominant factors that contributed to the extreme conditions in August 2022 were investigated, focusing on the dynamical mechanism behind the development of the anomalous anticyclone and the associated changes in local meridional circulation in the UTLS over Asia. Figure 2a-c shows the evolution of the circulation from May to August in 2022 as depicted by the SVD analysis. Time coefficients of the first SDV rapidly increased at the beginning of August, coincident with the surface temperature increase over the Yanez river valley (YRV) (Fig. 2d) and a strengthening of the zonal wind at 200hPa over eastern Tibetan Plateau (Fig. 2e). Strengthening of the zonal winds in July and August occurred in connection with a northward shift of tropical convection associated with boreal summer intraseasonal Oscillation (BSISO). Particularly strong convective activity was observed at the beginning of the August (Fig. 2f).

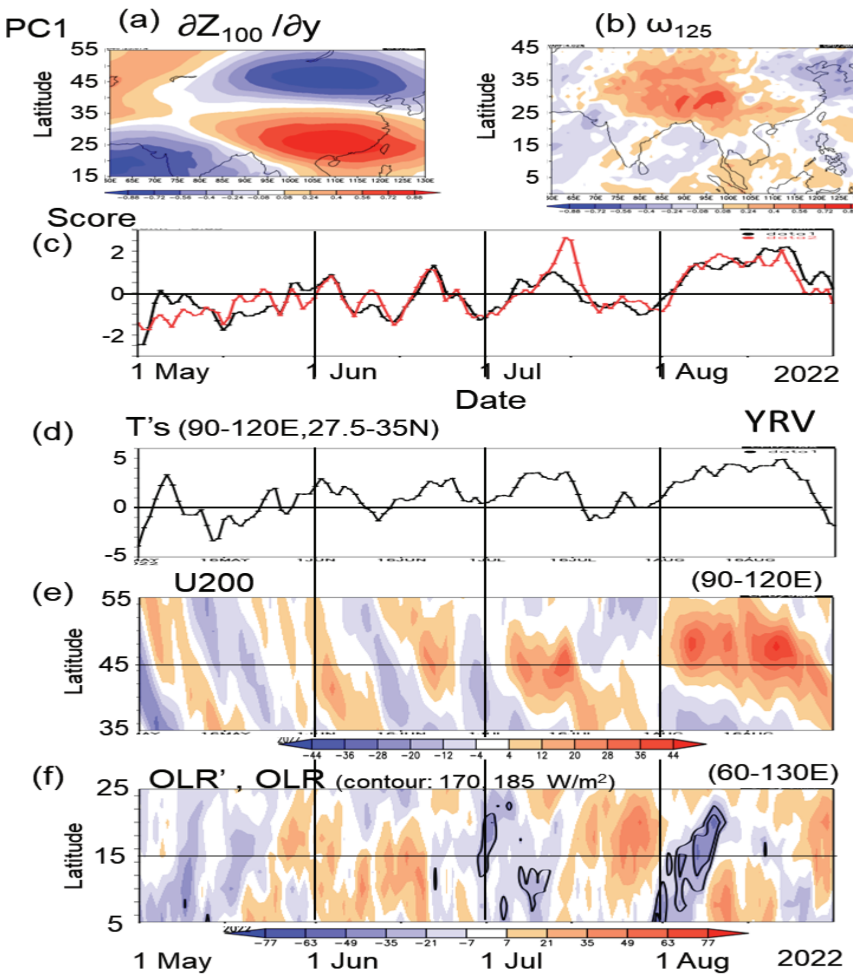

Figure 2: (a-c) SVD analysis between the meridional gradient of 100hPa geopotential height and pressure vertical velocity at 125hPa. (d) Surface temperature over YRV averaged over the area by the white box in (a) and

(b). (e and f) Latitude-time cross-sections of (e) zonal winds averaged over 90-120E at 200hPa and (f) OLR (contours:170 and 190 W/m^2) and its anomalies from climatology (color shading).

The strengthening and northward shift of very deep convection (which penetrated the UTLS) occurred in association with the northward shift of the ascending branch of the regional meridional circulation from 2 to 8 August over the Indian Ocean sector, as shown in Figure 3. Divergent meridional winds in the UTLS above the 360 K potential temperature level increased starting from 5 August across the Tibetan Plateau, which coincided with a strengthening of the westerlies north of the Plateau, and also the increased descent over China. These changes in convection and circulation led to enhanced convergence over Pakistan and descent of dry air over southwestern China. Frontal activity also increased over eastern Asia, bring about the “100-yr flooding event” over the Korean peninsula and northern Japan.

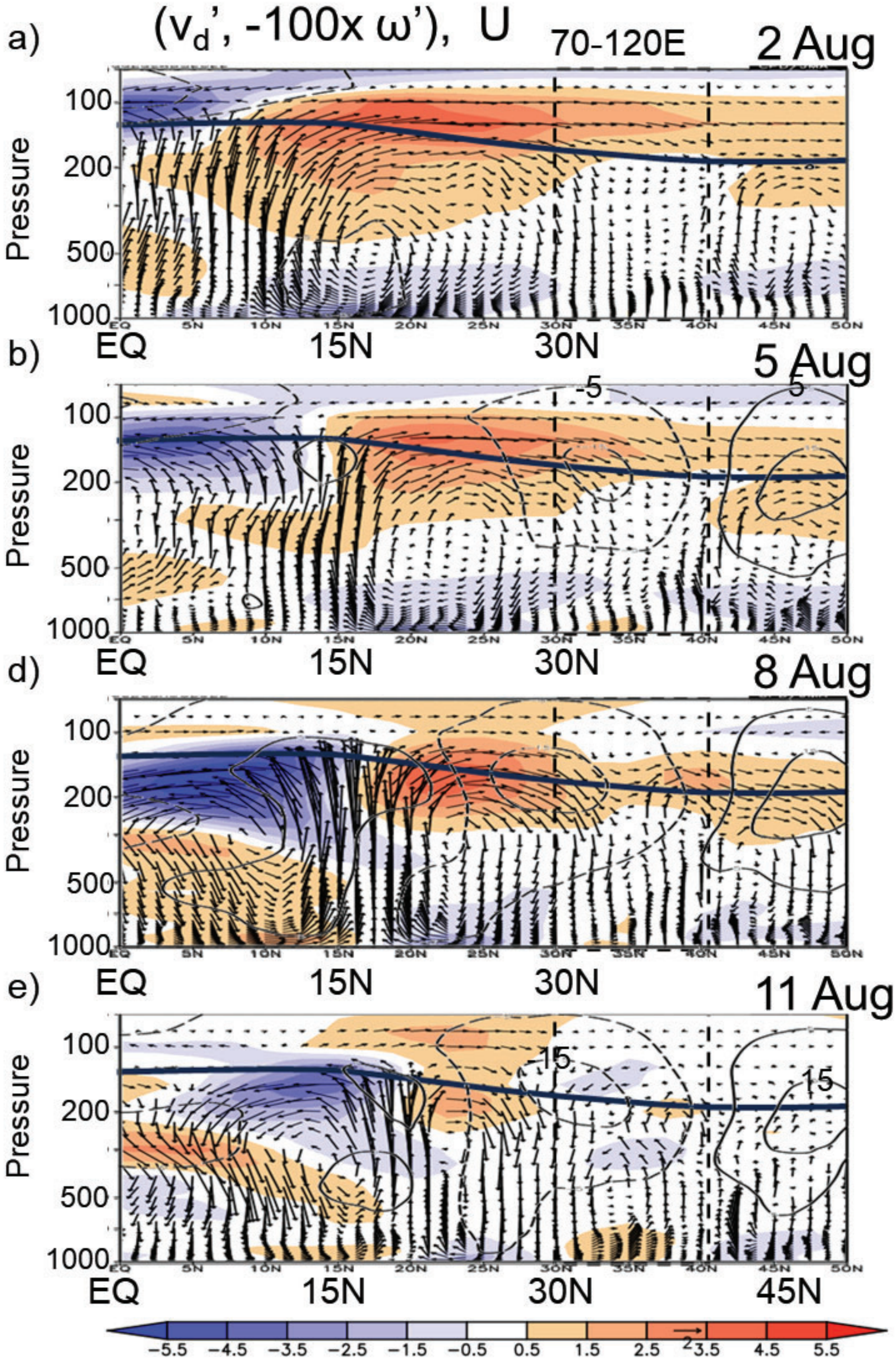

Figure 3: Time evolution of the 3-day mean regional Hadley circulation over 70-120E (arrows). Anomalous divergent meridional winds and anomalous zonal winds are shown by color shadings and contours, respectively. Thick solid lines indicate the 360 K potential temperature level.

V. Discussion/Summary

In this study, we investigated the cause of the heavy rainfall event which occurred on 8-9 August 2022 and found that a broad region of enhanced deep convective activity in the tropics with frequent cloud top penetration into the tropical UTLS likely induced an anomalously strong meridional circulation, forcing anomalous wave activity and jet structure over the East Asia subtropical front. The high temporal (3-hourly) and spatial (quarter degree) resolution data of convective cloud top altitude and potential temperature were used to estimate the strength and distribution of deep convective activity during the ACCLIP campaign in August 2022. In future work, we plan to analyze the global convective cloud top dataset to investigate the global impact of convection on UTLS cloud, composition, and dynamics.

VI. References

Pfister, L., Ueyama R., Jensen E., and Schoeberl, M., 2022: Deep convective cloud top altitudes at high temporal and spatial resolution, Earth and Space Science, 9, e2002EA002475. https://doi.org/10.1029/2022EA002475.

VIII. Research meeting and discussion

An invitation travel by Rei Ueyama to attend the JpGU Meeting 2023 in Makuhari, Japan was made possible by the International Joint Research funds from 2023. I gave an invited talk on 26 May 2023 in the SPARC session titled "Summer monsoons in the UTLS as observed by recent NASA airborne campaigns". During my visit, I met with Dr. Nawo Eguchi and Dr. Kunihiko Kodera for various research discussions.

Dr. Nawo Eguchi attended the AGU Fall Meeting 2023 in San Francisco, CA, USA in December 2023. Since Dr. Kunihiko Kodera was unable to attend the meeting in person, we presented his poster on our collaborative work on 15 December 2023 titled "Role of UTLS on the development of anomalous Tibetan High in August 2022". I also met with Dr. Nawo Eguchi to discuss future research plans.

IX. Additional information

Rei Ueyama participated in the ACCLIP campaign as a Lead Meteorologist and in the DCOTSS campaign as the Forecasting and Flight Planning Lead.

X. Other members of the joint research team

Nawo Eguchi	RIAM, Kyushu University
Kunihiko Kodera	Meteorological Research Institute

国際化推進共同研究概要

No. 3

23EA-3

タ イ ト ル： Analysis of ground-based and satellite observations of ice/liquid precipitation

研究代表者： BALDINI Luca

所内世話人： 佐藤　可織

研 究 概 要：本研究では、南極マリオ・ズッケリ基地(イタリア)で取得した地上観測データを用い、降雪を含む全球の降水観測に欠かせない衛星搭載W-バンドレーダの新たな検証手法を提案した。さらに北極域等、他の地上観測地で取得された観測データを用いて開発した手法の適用範囲の検証を実施した。本研究の成果は国際誌(Top1%)に発表し、EarthCARE衛星(JAXA/ESA)をはじめ、今後計画されている衛星レーダの検証・活用に役立つと期待される。

Analysis of ground-based and satellite observations of ice/liquid precipitation

Dr. Luca Baldini

National Research Council of Italy, Institute of Atmospheric Sciences and Climate

Rome, Italy

Summary

Research activity has been focused on the challenging environment of Antarctica and follows the research activity started in 2022, motivated both by science challenges and by the future availability of the JAXA/ESA EarthCARE satellite, whose sensors are expected to offer unprecedented opportunities to deeply investigate the structure of clouds and precipitation, including ice precipitation. Retrieval of snowfall properties using remote sensing techniques is always challenging due to the variability of microphysics of particles and uncertainties in its relationship with electromagnetic properties revealed by remote sensing devices. However, remote sensing is essential to collect information on phenomena in scarcely gauged and not easily accessible like Antarctica. There ground-based snowfall observations are rare due to the harsh environment and high logistical and operational costs. Satellite measurements are therefore crucial to provide continent-wide precipitation estimates and this highlights the importance of validating the satellite estimates with measurements collected by ground-based instrumentation.

Satellite radar sensors are particularly attractive for their unique capability of providing, with high resolution, vertical profiles of precipitating and non-precipitating clouds. The NASA CloudSat, launched in 2006, was the first satellite to be equipped with a 94 GHz Cloud Profiling Radar (CPR) and has been the major sources for Antarctica of clouds and precipitation estimates, obtained from radar reflectivity profiles. The JAXA/JAXA EarthCARE will continue these measurements with a more sensitive 94 GHz radar with Doppler capability along with a multisensory payload.

This joint research has explored how the synergy between two ground instruments available at most Antarctic stations, i.e., the Micro Rain Radar (24 GHz) and laser disdrometer, can be exploited to validate satellite-borne W-band radar measurements, including the Doppler estimates of EarthCARE. A validation methodology (K2W) was proposed in the 2022 joint research program, that combines these ground instruments for simulating 94-GHz reflectivity and Doppler measurements. Assessment of K2W methodology showed that the CloudSat Ze profiles can be simulated by the method with 0.2 dB mean difference at the lowest satellite radar range bin when time lag within ±12.5 minutes and the distance within 25 km around the CloudSat overpass were considered. With K2W, the 94 GHz Doppler velocity below 1 km altitude that would be observed by EarthCARE was obtained, and the standard deviation of the simulated Doppler velocity was found to be smaller than about 0.2 m s^{-1}. Encouraging results has suggested to adopt the methodology for EarthCARE CPR Doppler velocity measurement accuracy as well as the Level 2 standard products for precipitation in Antarctica and at other measurement sites. This methodology has been presented at several conference, has been refined and, finally, published on Remote Sensing of the Environment (Elsevier) in 2023.

To get more confident with the potential of this technique, in 2023 we have improved it and applied to other contexts and environments. Presented results referred to the Artic site of Ny Alesund where a 94 GHz radar is at ground e collocate with other instruments. The application of K2W to a snowfall dataset

collected at Ny Alesund will be reported in a manuscript submitted as summary paper at the URSI-AT-RASC Conference (May, 2024) and in a poster presentation at the EGU General Assembly 2024.

Resume of K2W

The MRR was originally designed to detect rainfall, using the relationship between velocity and diameter of falling raindrops but can be used, under some assumptions, to estimate snowfall rate. Laser disdrometers are widely used to detect the distribution of liquid hydrometeor size and more recently have been also used to determine the particle size distribution (PSD) of solid hydrometeors despite some well-known limitations.

The K2W methodology simulates W-band spectra from MRR K-band spectra using appropriate tables of backscattering cross sections at the two frequencies (K and W identified by the subscripts in the formulas) and $v_t(D)$ terminal velocity-diameter relationship for precipitation determined with the aid of Parsivel observations. It can be outlined as follows:

1. MRR spectra in terms of spectral reflectivity η are used to achieve spectral reflectivity density with respect to the velocity (v is the Doppler velocity, n the line number of Doppler spectrum, Δv the MRR velocity resolution)

$$\eta_K(v) = \frac{\eta(n)}{\Delta v}$$

2. Diameter spectral reflectivity is derived using $v_t(D)$ achieved by Parsivel observations:

$$\eta_K(D) = \eta_K(v)\frac{\partial v_t}{\partial D}$$

3. PSD is obtained by dividing η by σ(D), and it is independent of the radar wavelength:

$$N(D) = \frac{\eta_K(D)}{\sigma_K(D)} = \frac{\eta_W(D)}{\sigma_W(B)}$$

4. Combing previous equations:

$$\frac{\eta_W(D)}{\sigma_W(D)} = \frac{\eta_K(D)}{\sigma_K(D)} = \frac{\eta_K(v)}{\sigma_K(D)}\frac{\partial v}{\partial D}$$

5. Obtaining:

$$\eta_W(v) = \eta_K(v)\frac{\sigma_W(D)}{\sigma_K(D)}$$

The term on the right has measurements from MRR and the ratio of backscattering cross section for a given diameter and a given class of particle The method can be extended also to any target band, such as Ka.

Application of K2W to the Ny Alesund Dataset

The data used have been collected during the winter/spring seasons 2018 at the AWIPEV French-German Arctic research base in the Norwegian archipelago of Svalbard, specifically in the village of Ny-Ålesund (from now on NyA) (coordinates 78.9N, 11.9E, 9m a.s.l.) located along the Kongsfjord, nestled near mountains that run parallel to the fjord from the northwest to the southeast. The observations of 3 different snowfall events (7 February, 16 March, and 16 April) are available to the public through the Zenodo repository and contain measurements of the K-band MRR, the W-band radar MiRAC-A (from now on Mira) manufactured by RPG Radiometer Physics GmbH, and of the OTT-Parsivel disdrometer. The assessment of K2W is conducted against a collocated ground-based 94 radar through the following steps:

a) **Snow Particle Classification:** Snow particles were classified as aggregate or pristine by comparing MRR radar reflectivity with radar simulations derived from disdrometer data and a DDA database;
b) **Velocity-Diameter Relationship:** Disdrometer data were analyzed to establish velocity-diameter relationships for the various snowfall events and different time windows;
c) **Application:** Equations described above were applied to MRR Doppler spectra, with velocity-diameter relationships derived from disdrometer data, the DDA scattering database, and snowfall particle classification obtained in step a);
d) **Comparison of Results:** The resulting K2W reflectivity values were compared with measured W-band reflectivity at the first reliable range gate (i.e., 90m AGL for MRR and 105m AGL for Mira).

Results

Fig. 1a, 1b, and 1c depict the outcomes of this conversion methodology for the three snowfall events and for a time window of 30 minutes. It is important to note that the time window refers to the time interval considered for deriving the velocity-diameter relationships from Parsivel measurements. It is well-known that several factors, with wind being the most significant, can adversely affect the reliability of laser disdrometer performance and utilizing appropriate time windows is expected to enhance the robustness of velocity-diameter retrieval, aiming to mitigate both changes in snowflake characteristics and strong winds leading variability in snowfall estimation by disdrometers. Each comparative plot includes time series of the measured MRR K-band reflectivity at 90 m AGL, the measured W-band reflectivity by Mira at 102 m AGL, and the W2W estimated W-band reflectivity. The conversion methodology appears to perform well, often accurately mimicking the W-band observations although K2W frequently fails to replicate the W-band reflectivity, with the reflectivities almost perfectly superimposed with Ze_{MRR}, indicating imperfect operation of K2W.

Two factors could have played a critical role: strong winds affecting Parsivel observations and calibration issues with the Mira. Strong winds and the geometry of the instrument affects disdrometer measurements, leading to worsen the quality of observations. Unfortunately, wind observations were not available for the Ny Alesund cases, and this aspect could not be further mitigated. Instead, the possible calibration issue has been thoroughly investigated. A comparison between radar reflectivity measured by MIRA and that derived from disdrometer observations and DDA database for W-band revealed a constant underestimation of the Mira values for the 3 days considered. This is consistent with Chellini et al. (Earth System Science Data, 2023) which reports calibration offset values for Mira at NyA of about 3 dB for the months of February, March and April 2018, confirming our interpretation. Such value is consistent with what we have found in the Ze_{Mira} and ZeParsivel comparison.

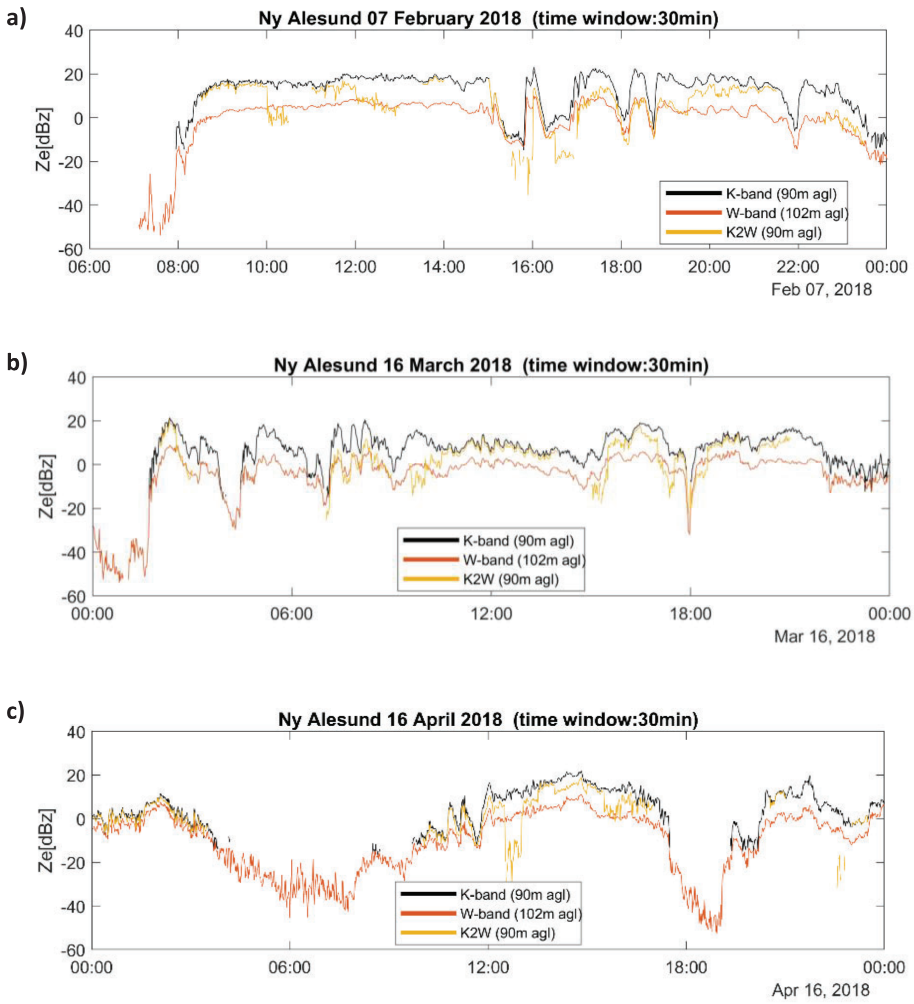

Figure 1 – Time series of radar reflectivity for the 3 case studies: the black line represents K-band reflectivity (Ze_{MRR}), the red line represents W-band reflectivity (Ze_{Mira}), and the yellow line depicts converted W-band reflectivity (Ze_{K2W}).

Hence, we have added a value of 3 dB to Mira reflectivity measurements. The final comparison between W-band Ze_{K2W} and Ze_{Mira} is reported in Fig. 2, which contains all data for the three snowfall cases using 30-minute time windows. Applying the correction significantly improved the correspondence. K2W values now correctly replicate W-band reflectivity probed by Mira, particularly for the lowest reflectivity values, but also for the higher values. However, for the most frequent values (dark red dots), K2W seems to overestimate radar observations, that could be linked to the not correction of disdrometer data.

Figure 2 – Density scatter plot between Ze_{Mira} at 102 m a.g.l. (after calibration correction) and converted Ze_{K2W} at 90 m AGL. Dots are colored according to the density of data (dark red = high density, dark blue = low density), whereas the dotted line stands for the bisecting line

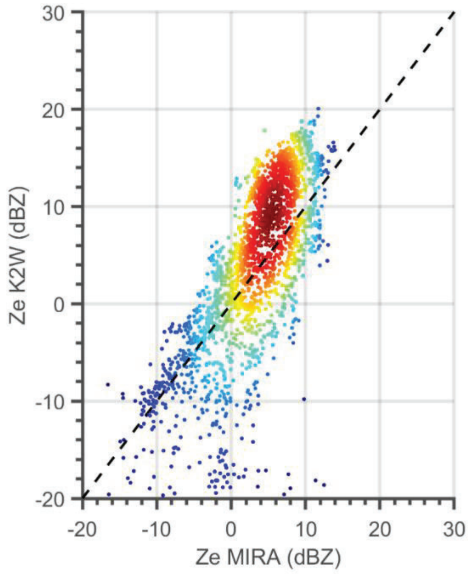

Conclusions

Satellite observations from missions like CloudSat and EarthCARE, equipped with W-band CPR, are crucial for global precipitation estimation due to their ability to cover vast areas. A key aspect of satellite missions is the validation and calibration of measurements, which relies on independent measurements typically collected by ground-based observational sites. Several stations in Antarctica are equipped with a MRR K-band profiler and a disdrometer, the K2W methodology enhance the opportunities to validate 94 GHz radar measurements. K2W simulates W-band profiles using K-band Doppler Spectra and v(D) relationships from disdrometer observations leading to direct comparison with CPR data. The effectiveness of K2W is evaluated against a ground-based W-band radar in Ny Ålesund, building upon the original comparison conducted during a CloudSat overpass over the Mario Zucchelli Station in Antarctica.

Results indicate that even if disdrometer data could not be corrected for wind artifacts (as recommended by K2W), the comparison between Ze(K2W) and Ze(Mira) at the first useful range gate shows promising results provided that the Mira calibration issue is addressed, this confirming the feasibility and the effectiveness of K2W.

List of publications

Journal paper

Bracci, K. Sato, L. Baldini,F. Porcù, H. Okamoto, 2023: Development of a methodology for evaluating spaceborne W-band Doppler radar by combined use of Micro Rain Radar and a disdrometer in Antarctica *Remote Sensing of the Environment*, 293, 113630, 2023. DOI: 10.1016/j.rse.2023.113630

Summary paper

Bracci, K. Sato, L. Baldini, H. Okamoto, 2025: Assessing 94-GHz Radar Estimates in Polar Regions through the K2W Methodology, Summary paper submitted to *4th URSI AT-RASC*, Gran Canaria, 19-24 May 2024

Congress/Workshop comunication

Bracci, K. Sato, L. Baldini,F. Porcù, H. Okamoto, 2024: K2W, una nuova metodologia per la validazione delle misure satellitari di precipitazione da radar in banda W usando dati ground-based di Micro Rain Radar e disdrometro: risultati dalla stazione Antartica “Mario Zucchelli” *AISAM (Italian Association for Atmospheric Sciences and Meteorology) Congress* 2024, 5-8 February 2024, Lecce (Italy) (Oral)

Bracci, K. Sato, L. Baldini,F. Porcù, H. Okamoto, 2023: K2W, a methodology for evaluating spaceborne W band Doppler radar using Micro Rain Radar and disdrometer: results from an Italian station in Antarctica *ESA JAXA Pre Launch EarthCARE Science and Validation Workshop* 13-17 November 2023 | ESA ESRIN, Frascati (Rome), Italy (oral)

Bracci, K. Sato, L. Baldini,F. Porcù, H. Okamoto, 2024. Enhancing Satellite Validation in Antarctica: A Novel K2W Methodology for Comparing Ground-Based Measurements with Spaceborne Radar Observations, *EGU General Assembly 2024 14-19 April, 2024,* Session: AS1.15 - The Earth Cloud, Aerosol and Radiation Explorer (EarthCARE) ready for Launch (Accepted, Poster)

国際化推進共同研究概要

No.4

23EA-4

タイトル： Detection of air pollution point sources in Mongolia by Himawari-8/9 geostationary satellite imagery

研究代表者： BATBOLD Chultem

所内世話人： 弓本　桂也

研究概要：

気候変動による降水レジームの変化により、乾燥地帯であるモンゴルの湖沼や池、泉が干上がってしまう事象が確認されている。露呈された湖底や池底からは、比較的弱い風によって砂が舞い上がってしまうため、砂塵のホットスポットとして局地的かつ地域的な大気環境に大きな影響を与えている。

本研究課題では、砂塵ホットスポットの検出と発生した砂塵の影響範囲を調べるため、最新の静止気象衛星であるひまわり８号・９号のデータを用いた。赤外波長を用いて大気中の土壌粒子を検出するDust RGBイメージを用い、2019 年から 2023 年を対象に砂塵ホットスポットの特定を行い、標高や土地利用データと照合することで地表面や周囲の環境（風の収束しやすい谷や盆地に位置していないかなど）を確認し、気象データと比較することで砂塵の発生する条件について解析を行った。

Dust Detection over Mongolian Territory using Dust RGB Imagery from Himawari-8/9 Geostationary Satellite

Contents

1. Introduction

We are concentrating on the months of March, April, and May between 2018 and 2023 for our dust survey in Mongolia. The selection of these months is based in environmental and meteorological considerations specific to the region. Here are some general reasons why these months might be suitable for a dust survey in Mongolia:

1. Springtime Conditions:

- March, April, and May are spring months in Mongolia. During this time, the weather tends to be transitional from winter to summer, with temperatures gradually rising.
- Spring is characterized by the melting of snow and ice, leading to increased soil moisture. This can impact dust emissions, making it an interesting period to assess dust levels.

2. **Wind Patterns:**

- Mongolia is known for its dry and windy climate. Spring is a season when wind patterns may play a crucial role in transporting dust particles.
- Conducting a dust survey during these months allows researchers to investigate the prevalence and transport of dust due to seasonal wind patterns.

3. **Potential for Dust Storms:**

- Dust storms are more likely to occur during the spring months in Mongolia. These storms can contribute significantly to airborne dust concentrations at both local and regional scales.
- Monitoring dust levels during March, April, and May can help capture the impact of any dust storms on air quality.

4. **Agricultural Activities:**

- Spring is a critical time for agricultural activities such as plowing and seeding. These activities can disturb the soil and contribute to dust emissions.
- A dust survey during these months can help assess the influence of agricultural practices on airborne dust concentrations

2. Materials

2.1. The region of interest

The region of interest is defined by the coordinates of the southwest (41°N, 93°E), northwest (50°N, 93°E), northeast (50°N, 112°E), and southeast (41°N, 112°E). Afterwards, we identified dust outbreaks and analyzed them by maximizing the scale.

2.2. Meteorological data

We took into account two factors: wind speed and cloud cover in the Gobi region, which is the main source of natural dust in Mongolia. For meteorological data, we utilized the website 'Visual Crossing', where weather history and forecasts are accessible (https://www.visualcrossing.com/). After identifying the locations where dust dispersion started, we searched for data using the names of the nearest places in the search box. Hourly data can be obtained from the website (in some cases, three-hourly data for wind gusts and air pressure, although this is not always available).

2.3. Satellite image processing

We used the dust RGB retrieval code for Himawari-8/9, the Japanese geostationary satellite, provided by Kyushu University. To optimize the exact locations, we modified the region of interest for each case.

2.4. Google base map

We identified the source area types by using Google Base Map as the background for the dust RGB images. Next, the National Atlas of Mongolia [1] was employed for detecting geographical objects that are potential dust hotspots.

3. Dust outbreaks

3.1 April 14, 2019

On that day, we observed natural dust dispersing from four different locations. The meteorological parameters at the onset of the dust outbreak are presented in Tables 1, 2, 3, and 4, and Figure 1.

3.1.1. S – 1: The tailings pond of the Erdenet mine, one of the world's largest copper ore mining and processing facilities, is discussed in more detail in Batbold et al. 2022 [2]. This case was not discussed in the results of our previous study [2].

Approximate coordinate: 49°5'0"N, 104°7'0"E

Meteorology: White dust from the tailings pond was driven by a wind speed of around 8-11 m/s (refer to Table 1 and Figure 1). The wind direction was from the W and WNW. Dust dispersion was observed to cease when the wind speed decreased to 4 m/s at 10 UTC (refer to Table 1 and Figure 1).

Table 1. Meteorological data nearby Erdenet city.

Date & Time (UTC)	Temp., (°C)	Precip. (mm)	Wind gust (m/s)	Wind speed (m/s)	Wind direction (angle)	Sea level pressure (hPa)	Cloud cover (%)
April 14, 2019 05:00	15.8	0		8	WNW, 292		0
April 14, 2019 06:00	17.2	0	15	11	W, 270	1005.3	30
April 14, 2019 07:00	16	0		7	WNW, 294		0
April 14, 2019 08:00	15.5	0		7	WNW, 296		0.2
April 14, 2019 09:00	17.6	0	18	7	W, 270	1002.6	50
April 14, 2019 10:00	12.2	0		4	W, 300		17.4

3.1.2. S – 2: The source was from nearby *Elsen Tasarkhai*, a part of the Mongol Els sand dunes that stretch along the Tuv, Uvurkhangai, and Bulgan aimags (The term 'aimag' is equivalent to 'province' and represents the largest sub-national administrative unit). The sand dunes stretch around 80 km.

Approximate coordinate: 47°15'0"N, 103°44'0"E

Meteorology: Dust dispersed from the sandy barren surface by the wind speed of 7-9 m/s. The wind gust wasn't too high, approximately 9-10 m/s (refer to Table 2 and Figure 1).

Table 2. Meteorological data nearby Rashaant, Bulgan.

Date & Time (UTC)	Temp., (°C)	Precip. (mm)	Wind gust (m/s)	Wind speed (m/s)	Wind direction (angle)	Sea level pressure (hPa)	Cloud cover (%)
April 14, 2019 05:00	14.4	0		7	292		0
April 14, 2019 06:00	15.7	0	10	9	270	1008.9	0
April 14, 2019 07:00	14.6	0		7	295		0
April 14, 2019 08:00	14.1	0		7	297		7.3
April 14, 2019 09:00	15.9	0	9	6	270	1006	30
April 14, 2019 10:00	10.7	0		4	298		68.1

3.1.3. S – 3: Dry lake beds: Many lakes remain dry until they receive floodwater during heavy rain, making them a potential source of dust hotspots prone to wind velocity. The Kherlen River is the second-longest river running through Mongolian territory. S–3 area is along that river and includes several detached seasonal lakes (Figure 1).

Approximate coordinate: 46°40'60"N, 107°55'0"E and 46°52'0"N, 109°18'0"E.

Meteorology: Dust was dispersed from the temporary dry lake beds with a wind speed of 9-10 m/s (Table 3).

Table 3. Meteorological data nearby Bayan, Tuv.

Date & Time (UTC)	Temp., (°C)	Precip. (mm)	Wind gust (m/s)	Wind speed (m/s)	Wind direction (angle)	Sea level pressure (hPa)	Cloud cover (%)
April 14, 2019 05:00	14.4	0		9	285		0
April 14, 2019 06:00	14.4	0	12	10	280	1008	0
April 14, 2019 07:00	14.6	0		9	289		0
April 14, 2019 08:00	14.1	0		9	292		0
April 14, 2019 09:00	15.1	0	12	10	300	1005.8	0
April 14, 2019 10:00	9.8	0		5	293		0

3.1.4. S – 4: From dry lake beds: Many lakes remain dry until they receive floodwater during heavy rain. Consequently, for the rest of the time, they tend to be sources of dust hotspots prone to wind velocity. Several lakes exist near a specially protected area called “Altan Ovoo”, primarily sustained by rainwater but also groundwater.

Approximate coordinate: 45°30'0"N, 113°11'0"E

Meteorology: Dust was dispersed from the temporary dry lake beds with a wind speed of 8-11 m/s (Table 4 and Figure 1).

Table 4. Meteorological data nearby Dariganga, Sukhbaatar.

Date & Time (UTC)	Temp., (°C)	Precip. (mm)	Wind gust (m/s)	Wind speed (m/s)	Wind direction (angle)	Sea level pressure (hPa)	Cloud cover (%)
April 14, 2019 05:00	13.6	0	N/A	11	WNW, 288	N/A	0
April 14, 2019 06:00	14	0	N/A	11	WNW, 290	N/A	0
April 14, 2019 07:00	14.1	0	N/A	10	WNW, 289	N/A	0
April 14, 2019 08:00	13.6	0	N/A	10	WNW, 288	N/A	0
April 14, 2019 09:00	12.6	0	N/A	8	WNW, 286	N/A	0
April 14, 2019 10:00	8	0	N/A	8	WNW, 284	N/A	0

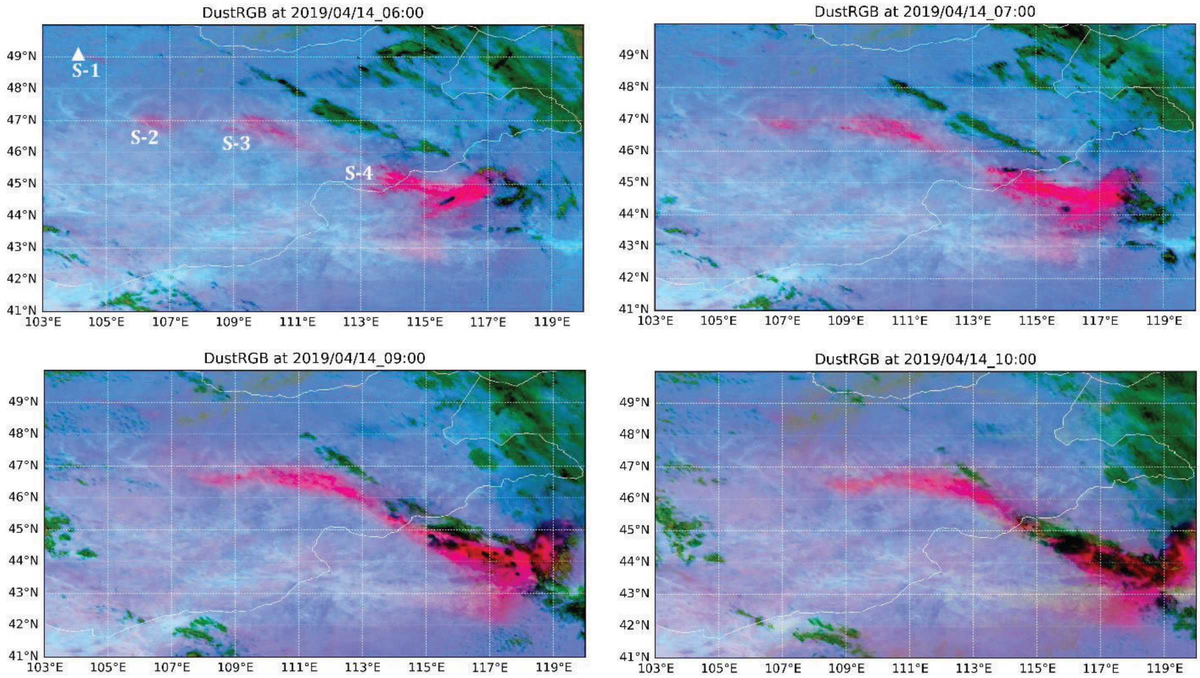

Figure 1. Dust RGB extraction using Himawari-8 geostationary satellite on April 14, 2019.

3.2. April 15, 2019

Dispersion of mining dust, commonly known as white dust, from the tailings pond.

Approximate coordinate: 47°15'0"N, 103°44'0"E

Meteorology: White dust was transported from the tailings pond by a westerly wind speed of 8-9 m/s (refer to Table 5 and Figure 2). The fluctuation of white dust outbreaks has been increasing over the years. The tailings pond is located in the north of Mongolia. Although this area is not geographically very vulnerable, the tailings pond consistently becomes a primary source near the area due to its non-soil surface.

Table 5. Meteorological data nearby Erdenet, Orkhon.

Date & Time (UTC)	Temp., (°C)	Precip. (mm)	Wind gust (m/s)	Wind speed (m/s)	Wind direction (angle)	Sea level pressure (hPa)	Cloud cover (%)
April 15, 2019 03:00	14.2	0	12	8	W, 270	1003.7	30
April 15, 2019 04:00	14.8	0		9	W, 285		0
April 15, 2019 05:00	15.6	0		9	W, 282		0.7
April 15, 2019 06:00	17.1	0	20	12	W, 270	998.7	40
April 15, 2019 07:00	16.7	0		10	W, 275		16.5

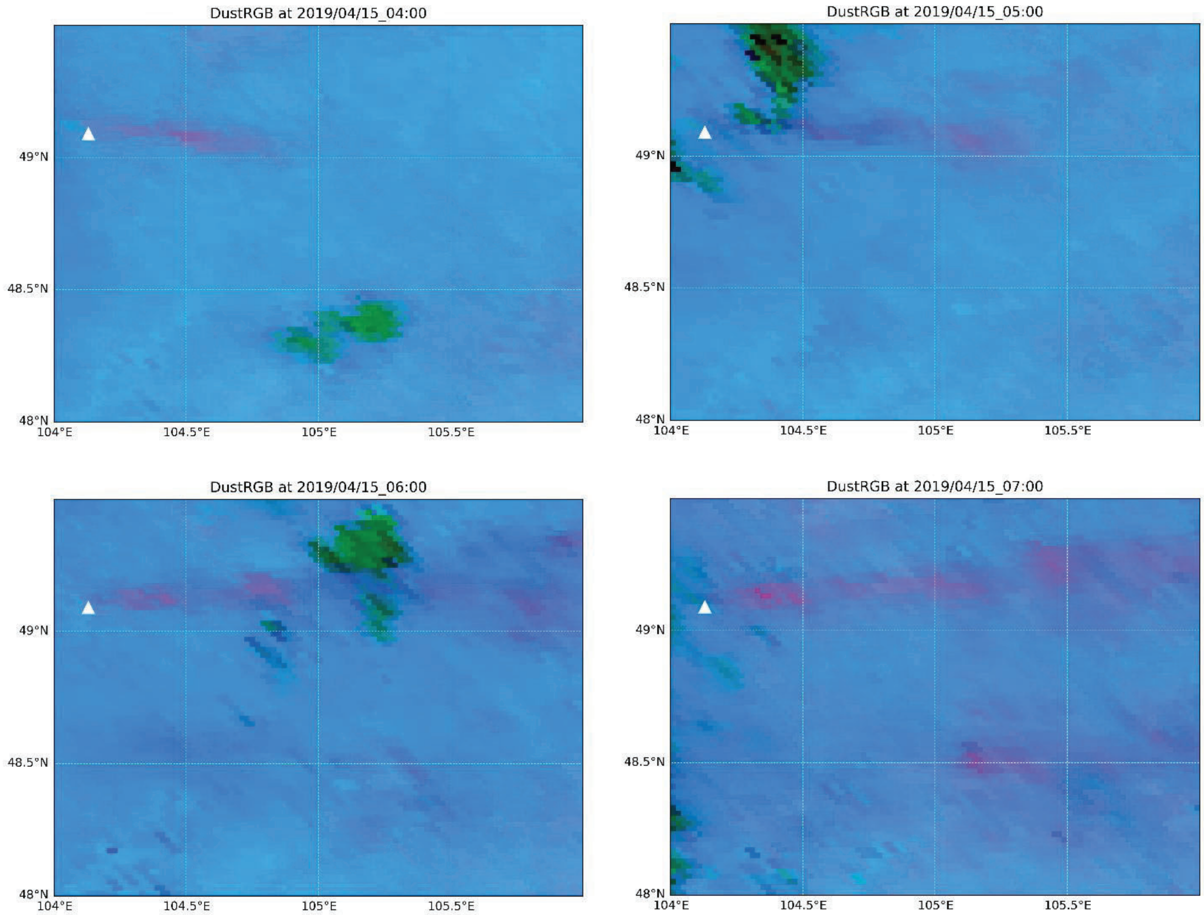

Figure 2. Dust RGB extraction using Himawari-8 geostationary satellite on April 15, 2019.

3.3. April 16, 2019

Baruun-Urt is the center of Sukhbaatar aimag, and there are some seasonal lakes in the south of Baruun-Urt. The dry beds of several small lakes and the surrounding areas near them became the initial source of dust in this dust event.

Approximate coordinate: 46°35'0"N, 113°21'0"E

Meteorology: As seen in Figure 3, Dust plume started to transport near that area with the east-southeasterly wind with 11 m/s. Around 01:00 and 02:00 UTC, wind speed was decelerated to 2-3 m/s (Table 6). During that time, dust plume moved towards the northwest (Figure 3).

Table 6. Meteorological data nearby Baruun-Urt, Sukhbaatar

Date & Time (UTC)	Temp., (°C)	Precip. (mm)	Wind gust (m/s)	Wind speed (m/s)	Wind direction (angle)	Sea level pressure (hPa)	Cloud cover (%)
April 16, 2019 00:00	3.7	0	11	11	ESE, 110	1006	80

April 16, 2019 01:00	8.5	0		2	WSW, 250		58.6
April 16, 2019 02:00	11.4	0		3	SW, 225		32.1
April 16, 2019 03:00	8.7	0	11	11	SE, 140	1002.4	80
April 16, 2019 04:00	17.1	0		6	WSW, 255		20.7

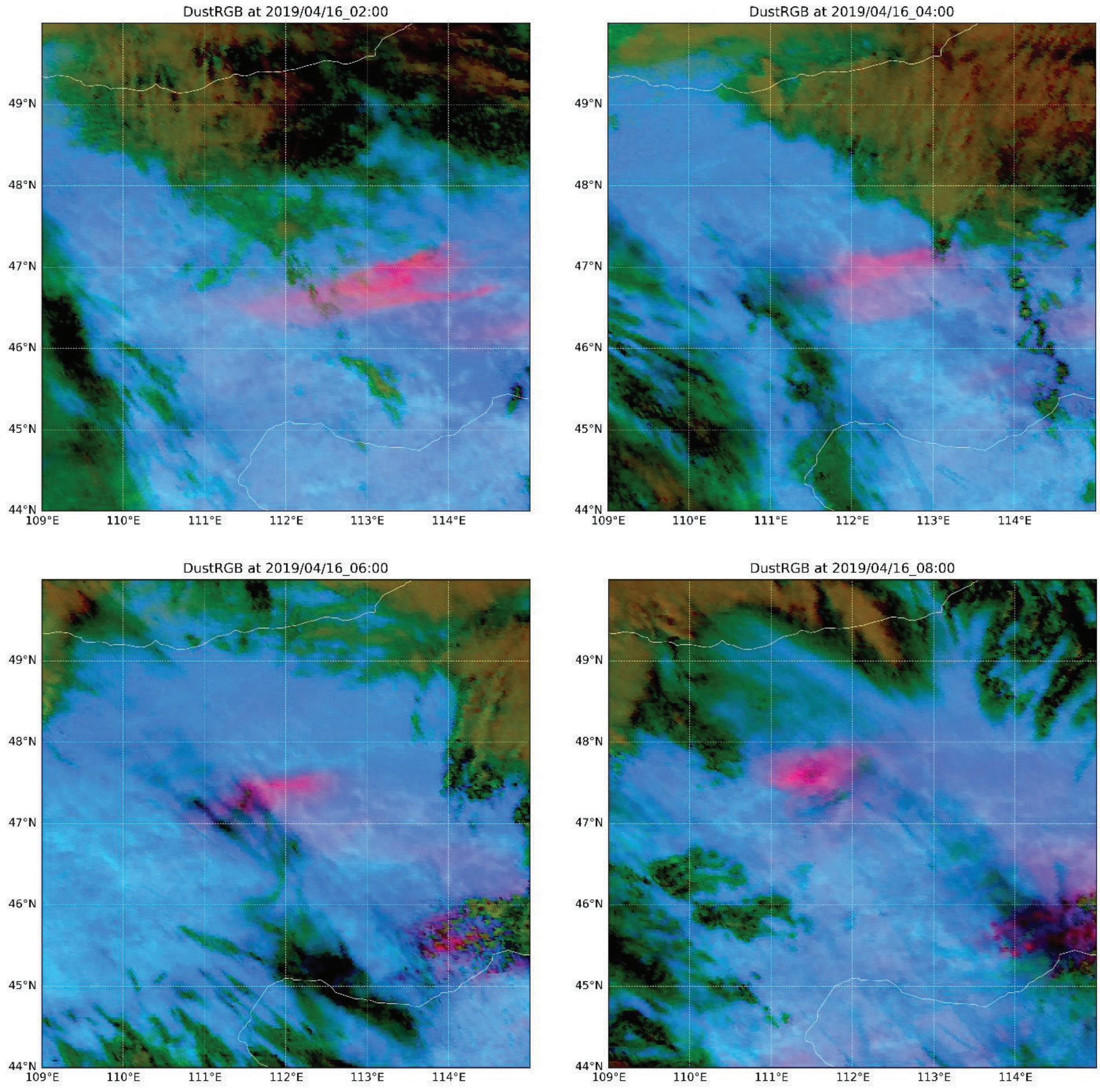

Figure 3. Dust RGB extraction using Himawari-8 geostationary satellite on April 16, 2019.

3.4. April 17, 2019

Here, we identified three distinct dust source places.

3.4.1. S–1: The first site shown on the map (Figure 4) is located at the center of the country. A weak dust plume dispersed from the dry beds of gullies and seasonal lakes in the geographical steppe zone can be seen.

Approximate coordinate: 46°57'0"N, 106°12'0"E

Meteorology: The north-northwesterly wind of 10 m/s initiated the dust outbreak at 04:00 UTC (Table 7). Although the dust plume is weak, our previous study on mine dust dispersion suggested that using dust RGB images with a 10-minute interval allows us to track the spatiotemporal dispersion effectively when we superimpose them.

Table 7. Meteorological data nearby Bayan-unjuul, Tuv.

Date & Time (UTC)	Temp., (°C)	Precip. (mm)	Wind gust (m/s)	Wind speed (m/s)	Wind direction (angle)	Sea level pressure (hPa)	Cloud cover (%)
April 17, 2019 04:00	3.2	0		10	NNW, 340		47.9
April 17, 2019 05:00	4.9	0		10	NNW, 340		20.7
April 17, 2019 06:00	6.5	0		10	NNW, 339		7.5
April 17, 2019 07:00	7.2	0		10	NNW, 339		3.9
April 17, 2019 08:00	7.1	0		10	NNW, 339		2

3.4.2. S–2: Natural dust started to disperse from the steppe zone, and there is no specific source of dust (Figure 4).

Approximate coordinate: 46°27'0"N, 110°37'0"E

Meteorology: The dust plume was transported by the north and northwesterly wind with a speed of 9-10 m/s, lasting from 00:00 to 01:00 UTC (Table 8). Therefore, a wind speed of 9-10 m/s may be inferred as the threshold velocity in this case.

Table 8. Meteorological data nearby Galshar, Khentii.

Date & Time (UTC)	Temp., (°C)	Precip. (mm)	Wind gust (m/s)	Wind speed (m/s)	Wind direction (angle)	Sea level pressure (hPa)	Cloud cover (%)
April 16, 2019 23:00	6.9	0		8	NNW, 341		0.4
April 17, 2019 00:00	9.5	0		10	N, 351		39.7
April 17, 2019 01:00	11.5	0		10	N, 351		4.7
April 17, 2019 02:00	12.9	0		9	NNW, 348		0.5
April 17, 2019 03:00	13.9	0		9	NNW, 344		10.8
April 17, 2019 04:00	14.7	0		9	NNW, 339		30.1

April 17, 2019 05:00	15.2	0		8	NNW, 334		27.1
April 17, 2019 06:00	15.3	0		8	NNW, 331		45.7

3.4.3. S–3: There are some seasonal lakes and dry gullies in the south and southwest of Baruun-Urt. The dry beds of multiple small lakes and the surrounding areas near them became the initial source in this case (Figure 4).

Approximate coordinate: 46°23'0"N, 112°41'0"E

Meteorology: With a wind speed of 8-10 m/s, the dust plume was transported by the NNW, NE, and N winds as indicated in Table 9.

Table 9. Meteorological data nearby Baruun-Urt, Sukhbaatar.

Date & Time (UTC)	Temp., (°C)	Precip. (mm)	Wind gust (m/s)	Wind speed (m/s)	Wind direction (angle)	Sea level pressure (hPa)	Cloud cover (%)
April 16, 2019 23:00	3.9	0		8	NNW, 339		10.2
April 17, 2019 00:00	3.9	0	8	8	NE, 50	997.6	80
April 17, 2019 01:00	8.8	0		10	N, 351		9.4
April 17, 2019 02:00	10.1	0		10	NNW, 348		3.1
April 17, 2019 03:00	6.1	0	18	12	NE, 50	1002.3	50
April 17, 2019 04:00	10.5	0		10	NNW, 344		24.5
April 17, 2019 05:00	10.4	0		10	NNW, 343		34.7
April 17, 2019 06:00	7.9	0	15	8	N, 360	1006.2	60

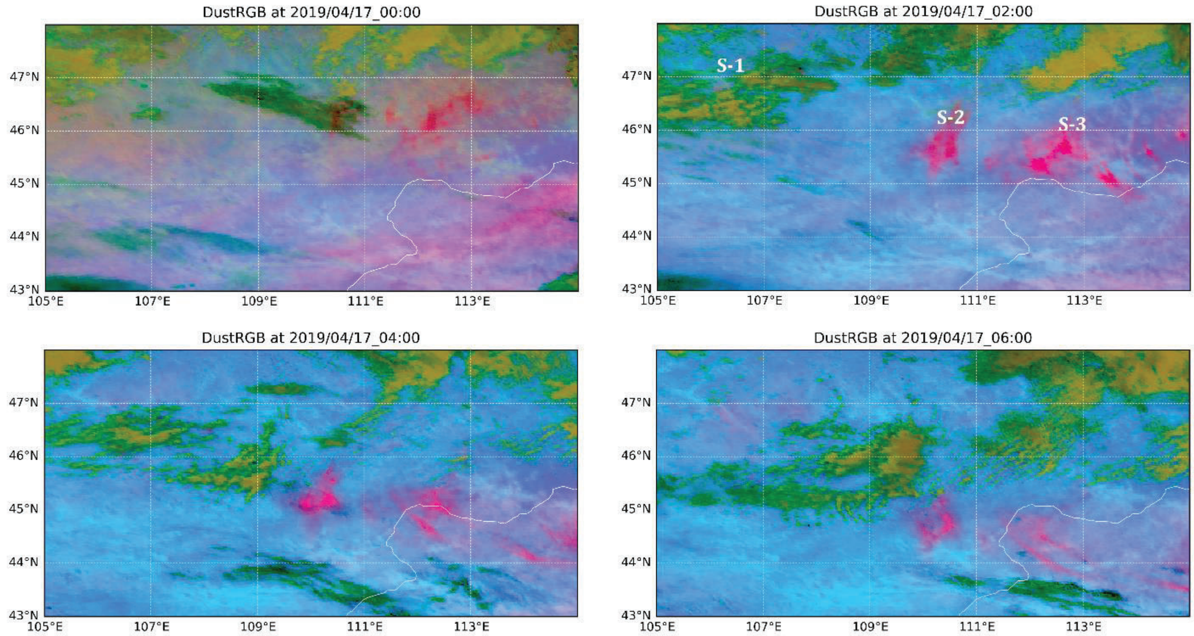

Figure 4. Dust RGB extraction using Himawari-8 geostationary satellite on April 17, 2019.

3.5. April 19, 2019

3.5.1. S–1: Dust is dispersed from the Khangai mountain range. Indeed, it is very rare to see such a dust storm over this area. The source area can be defined as forest-steppe. We presume that natural dust dispersed from the pasture because there are no mines, barren surfaces, or beds of lakes and rivers in the area (Figure 6).

Approximate coordinate: 49°21'0"N, 101°48'0"E

Meteorology: The wind gust reached 16-18 m/s, and the wind speed ranged between 9-14 m/s during this event (Table 10). The dust momentum is caused by the west-northwesterly (WNW) wind.

Table 10. Meteorological data nearby Tosontsengel, Khuvsgul.

Date & Time (UTC)	Temp., (°C)	Precip. (mm)	Wind gust (m/s)	Wind speed (m/s)	Wind direction (angle)	Sea level pressure (hPa)	Cloud cover (%)
April 19, 2019 00:00	4.5	0	17	9	WNW, 304	1010.8	47
April 19, 2019 01:00	1.5	0		12	WNW, 304		0.3
April 19, 2019 02:00	2.4	0		13	WNW,304		0
April 19, 2019 03:00	4	0	16	10	WNW, 304	1014.5	20.9
April 19, 2019 04:00	3.1	0		14	WNW, 305		0
April 19, 2019 05:00	3.4	0		13	WNW, 306		0

April 19, 2019 06:00	3.3	0	18	12	NW, 310	1018.9	5.2

3.5.2. S–2: A severe white dust outbreak occurred, although it's a bit difficult to distinguish it on the large-scale map (Figure 6). This case was emphasized as a special case in Batbold's PhD thesis in 2022.

As shown in Figure 5a, white dust is dispersing from the tailings pond, while natural dust is coming from the northeast at 05:50 UTC. They subsequently mixed at 07:40 UTC (Figure 5b). Although the dust RGB imagery illustrates both natural dust and white dust as magenta, the white dust plume appears as a brighter red compared to the natural dust. We extracted the red color component from the dust RGB algorithm by adjusting the BTD(12.4–10.4 µm) range from –4 K to +2 K with a 0–1 value in each dispersion map. Setting the minimum value of red color intensity as 0.85 at 07:40 UTC made the white dust plume distinguishable from the natural dust, with the white dust exhibiting a higher red color contribution corresponding to dense dust clouds (Figure 5c).

Approximate coordinate: 47°15'0"N, 103°44'0"E

Meteorology: The wind gust reached 16-18 m/s, and the wind speed ranged between 9-14 m/s during this event (Table 10) and the dust momentum is driven by the west-northwesterly (WNW) wind.

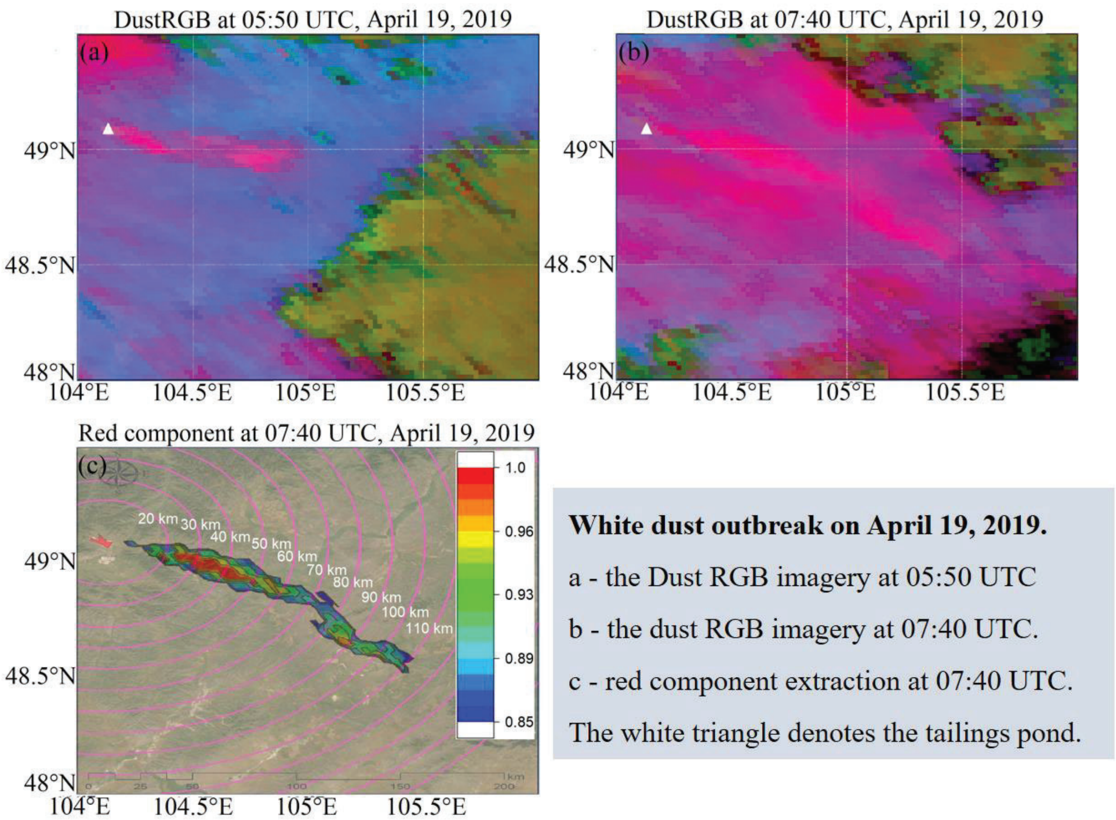

Figure 5. White dust outbreak on April 19, 2019. The Dust RGB imagery at 05:50 UTC (a), the dust RGB imagery at 07:40 UTC, and red component extraction at 07:40 UTC. The white triangle denotes the tailings pond.

Table 11. Meteorological data nearby Erdenet, Orkhon.

Date & Time (UTC)	Temp., (°C)	Precip. (mm)	Wind gust (m/s)	Wind speed (m/s)	Wind direction (angle)	Sea level pressure (hPa)	Cloud cover (%)
April 19, 2019 00:00	14.9	0	11	7	SSW, 210	996.4	14.9
April 19, 2019 01:00	7.6	0		13	NW, 311		7.6
April 19, 2019 02:00	7.2	0		13	NW, 311		7.2
April 19, 2019 03:00	10.7	0	25	13	NW, 320	1004.2	10.7
April 19, 2019 04:00	8.2	0		13	NW, 310		8.2
April 19, 2019 05:00	8.1	0		14	NW, 311		8.1
April 19, 2019 06:00	8.6	0	21	11	WNW, 300	1010.1	8.6
April 19, 2019 07:00	6.7	0		14	NW, 316		6.7
April 19, 2019 08:00	5.8	0		13	NW, 320		5.8
April 19, 2019 09:00	5.9	0	15	10	WNW, 300	1014.3	5.9
April 19, 2019 10:00	3.2	0		11	NNW, 330		3.2

3.5.3. S–3: Natural dust started to disperse from a grazing area and nearby some seasonal lakes at 02:00 UTC (Figure 6). From 02:00 to 07:00 UTC, the wind direction was from SSW and WSW. It then changed to W and N at 08:00 UTC (Table 12 and Figure 6).

Approximate coordinate: 46°50'0"N, 109°30'0"E

Meteorology: No dust outbreak is observed when wind speed reached 10 m/s. Then, at 02:00 UTC, a wind speed of 11 m/s put the dust in motion. During the dust outbreak, wind speed fluctuated between 11 and 13 m/s (Table 12 and Figure 6).

Table 12. Meteorological data nearby Bayanmunkh, Khentii.

Date & Time (UTC)	Temp., (°C)	Precip. (mm)	Wind gust (m/s)	Wind speed (m/s)	Wind direction (angle)	Sea level pressure (hPa)	Cloud cover (%)
April 19, 2019 01:00	9.2	0		10	S, 195		52.7
April 19, 2019 02:00	12.6	0		11	SSW, 203		17.4
April 19, 2019 03:00	15.5	0		12	SSW, 209		10.1
April 19, 2019 04:00	18.2	0		12	SSW, 218		9
April 19, 2019 05:00	20.7	0		12	SW, 229		7
April 19, 2019 06:00	22.4	0		11	SW, 238		7.7

April 19, 2019 07:00	23.2	0		11	WSW, 252		11.2
April 19, 2019 08:00	22.8	0		11	W, 282		27.3
April 19, 2019 09:00	19.7	0		13	NW, 311		27.9
April 19, 2019 10:00	15.2	0		13	NW, 323		65.7

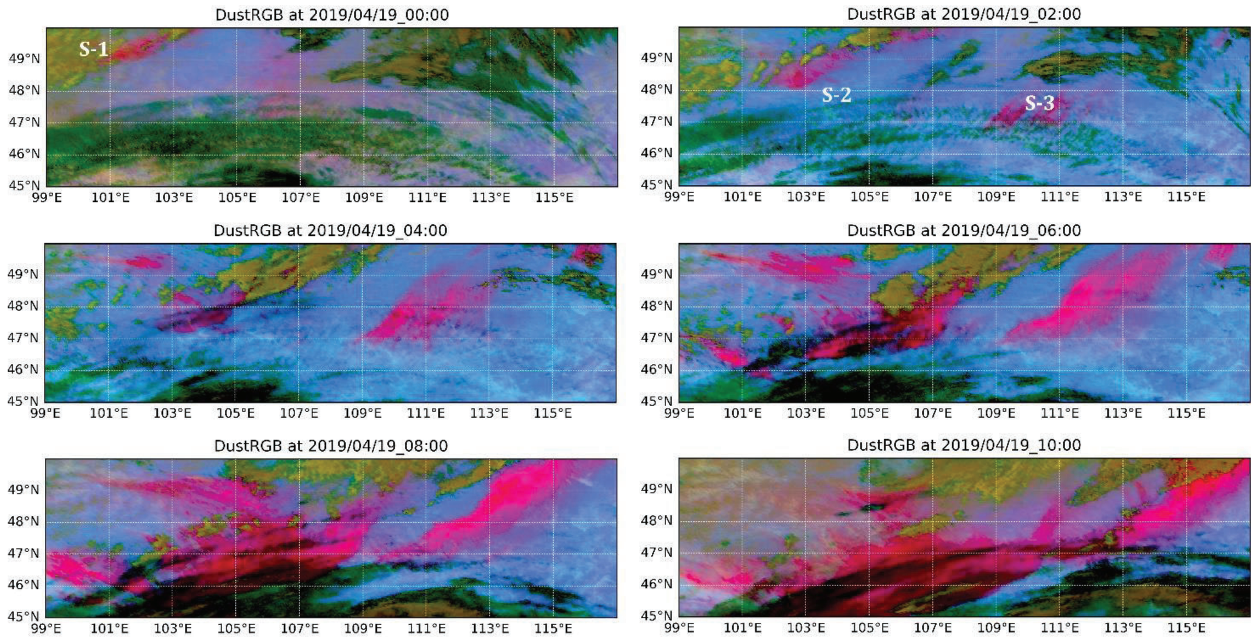

Figure 6. Dust RGB extraction using Himawari-8 geostationary satellite on April 19, 2019.

3.6. April 22, 2019

3.6.1. S–1: Dust hotspot originated from the dry seasonal lake bed in the grazing area.

Approximate coordinate: 46°59'0"N, 106°11'0"E

Meteorology: Natural dust is propelled by a wind speed of 11 m/s at 05:00 UTC by the NNW wind. Subsequently, a wind gust of 16 m/s increasingly magnified the dust plume at 06:00 (Table 13 and Figure 7).

Table 13. Meteorological data nearby Bayantsagaan, Tuv.

Date & Time (UTC)	Temp., (°C)	Precip. (mm)	Wind gust (m/s)	Wind speed (m/s)	Wind direction (angle)	Sea level pressure (hPa)	Cloud cover (%)
April 22, 2019 04:00	13.5	0		12	NNW, 333		0
April 22, 2019 05:00	13.7	0		11	NNW, 333		0.4

April 22, 2019 06:00	12.6	0	16	16	NNW, 330	1004	80
April 22, 2019 07:00	13.3	0		10	NNW, 333		10.6
April 22, 2019 08:00	12.6	0		9	NNW, 334		0.1

3.6.2. S–2: A gully created by floodwater cross through the center of Bayan soum (Aimags are divided into soums). For S–2, the gully served as the dust hotspot.

Approximate coordinate: 47°16'0"N, 107°31'0"E

Meteorology: A wind gust of 16 m/s from the NNW direction propelled the dust plume to the leeward area (Table 14 and Figure 7).

Table 14. Meteorological data nearby Bayan, Tuv.

Date & Time (UTC)	Temp., (°C)	Precip. (mm)	Wind gust (m/s)	Wind speed (m/s)	Wind direction (angle)	Sea level pressure (hPa)	Cloud cover (%)
April 22, 2019 04:00	13	0		11	NW, 325		0.2
April 22, 2019 05:00	12.6	0	16	16	NNW, 330	1004	80
April 22, 2019 06:00	12.4	0		10	NW, 325		0.1
April 22, 2019 07:00	11.5	0		10	NW, 326		0.3
April 22, 2019 08:00	10.9	0	18	14	N, 350	1005.5	30

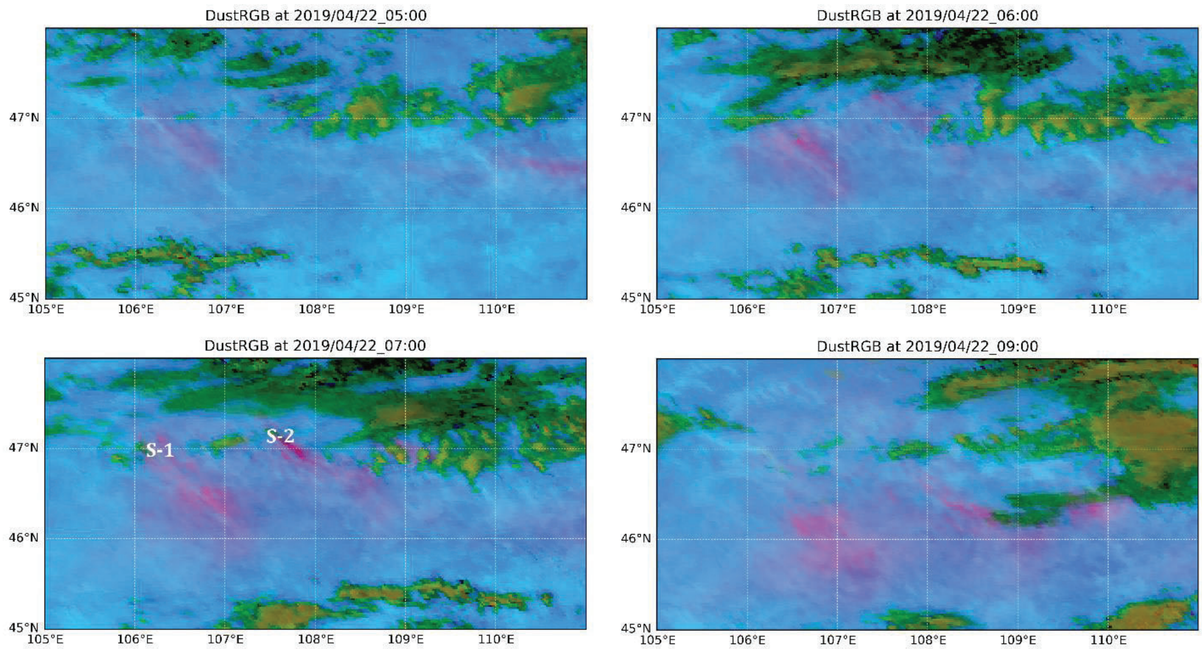

Figure 7. Dust RGB extraction using Himawari-8 geostationary satellite on April 22, 2019.

3.7. April 28, 2019

3.7.1. S – 1: Uvs is the largest lake in Mongolia in terms of coverage. The lake swash located at the southwest of Uvs Lake has been identified as a hotspot.

Approximate coordinate: 50°14'0"N, 91°59'0"E

Meteorology: Dust plume is driven by a 10 m/s wind from WNW at 04:00 UTC. With decreasing wind speed, the dust plume shifted towards the southeast (Table 15 and Figure 8).

Table 15. Meteorological data nearby Ulaangom, Uvs.

Date & Time (UTC)	Temp., (°C)	Precip. (mm)	Wind gust (m/s)	Wind speed (m/s)	Wind direction (angle)	Sea level pressure (hPa)	Cloud cover (%)
April 28, 2019 03:00	4	0		10	WNW, 300		30.6
April 28, 2019 04:00	4.6	0		10	WNW, 302		17.9
April 28, 2019 05:00	13.6	0	19	7	NW, 310	1015.4	30
April 28, 2019 06:00	6.2	0		8	NW, 310		6.3
April 28, 2019 07:00	6.5	0		8	NW, 314		1.6
April 28, 2019 08:00	13.9	0	17	4	SSE, 160	1016.6	80

3.7.2. S – 2: We identified the second source area from the so-called Great Lakes Valley, where there are several permanent lakes and some sand dunes. The dry bed of Holboo Lake was the most intense hotspot of the dust outbreak (Figure 8).

Approximate coordinate: 47°13'55.55"N, 92°42'0"E

Meteorology: During the dust outbreaks shown in Figure 8, natural dust dispersion at 03:00 UTC was driven by a 15 m/s wind from the west. Several dust sources then created a bigger dust storm. Wind gusts were recorded at 19 m/s (05:00 UTC) and 17 m/s (08:00 UTC) (Table 16).

Table 16. Meteorological data nearby Mankhan, Khovd.

Date & Time (UTC)	Temp., (°C)	Precip. (mm)	Wind gust (m/s)	Wind speed (m/s)	Wind direction (angle)	Sea level pressure (hPa)	Cloud cover (%)
April 28, 2019 03:00	0.5	0		15	W, 268		21.4
April 28, 2019 04:00	1.3	0		14	W, 271		8.3
April 28, 2019 05:00	12.2	0	19	8	W, 270	1016.9	30
April 28, 2019 06:00	2.4	0		11	W, 275		1.9
April 28, 2019 07:00	2.2	0		10	W, 276		3.7

April 28, 2019 08:00	13.2	0	17	9	WNW, 290	1016.6	30

3.7.3. S – 3: We identified the third source area near the so-called Lakes Valley (Figure 8). Through the valleys between mountainous areas, soil degradation due to water erosion, for example seasonal dry lakes and dry gullies, is common.

Approximate coordinate: 44°56'0"N, 100°7'0"E

Meteorology: The wind speed during the event fluctuated between 9 and 13 m/s from the west (W) and west-northwest (WNW) directions (Table 17).

Table 17. Meteorological data nearby Bayan-Ovoo, Bayankhongor.

Date & Time (UTC)	Temp., (°C)	Precip. (mm)	Wind gust (m/s)	Wind speed (m/s)	Wind direction (angle)	Sea level pressure (hPa)	Cloud cover (%)
April 28, 2019 03:00	13.6	0		9	W, 282		0
April 28, 2019 04:00	14.6	0		11	W, 285		0.2
April 28, 2019 05:00	15.1	0		12	W, 288		3
April 28, 2019 06:00	15.3	0		12	WNW, 291		7.8
April 28, 2019 07:00	15.5	0		13	WNW, 293		6.3
April 28, 2019 08:00	15.4	0		13	WNW, 292		4.4

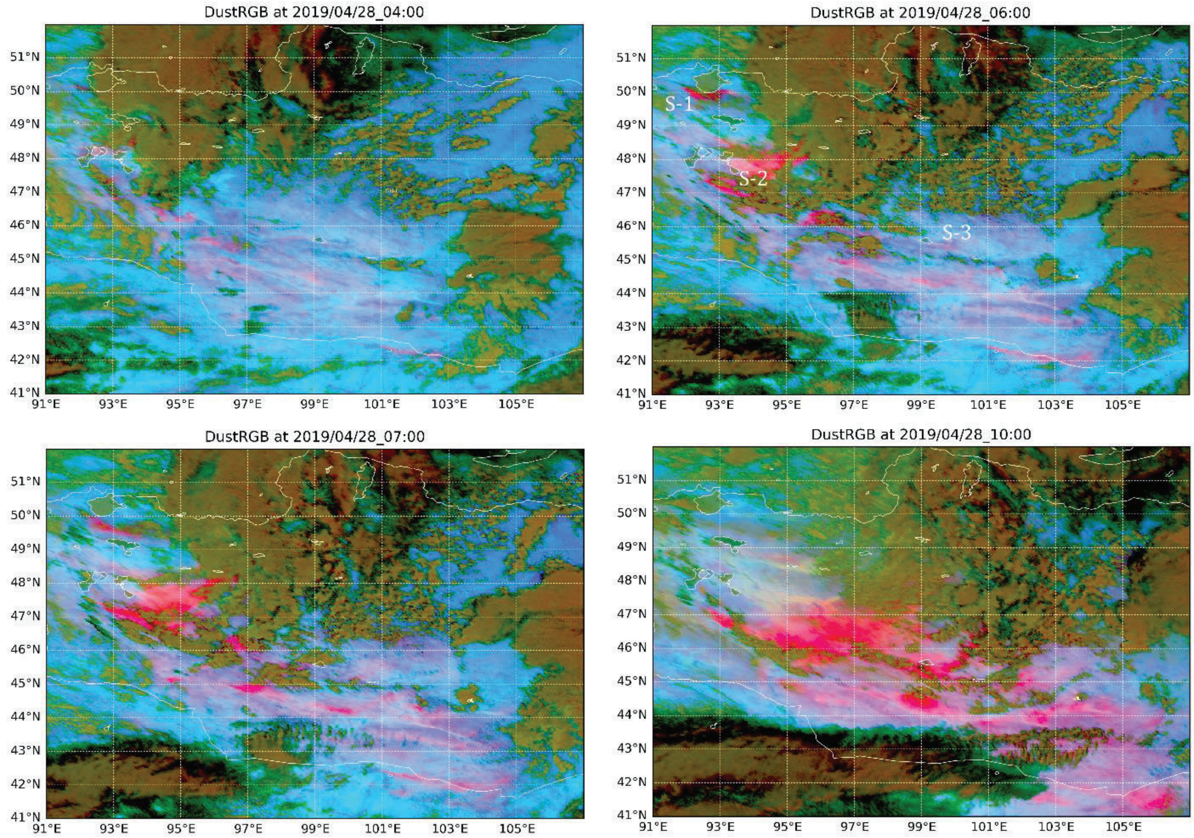

Figure 8. Dust RGB extraction using Himawari-8 geostationary satellite on April 28, 2019.

3.8. April 6, 2020

Two distinct and intense dust outbreaks were observed on the 6th of April 2020.

3.8.1. S – 1: Dust outbreak is initiated near the Khangai mountain range, which is a geographically forest-steppe. Annually, dust storm is a very rare event in this region.

Approximate coordinate: 47°13'0"N, 101°46'0"E

Meteorology: It's noteworthy that the wind speed was between 1 and 5 m/s at the beginning of the dust dispersion from 01:00 to 03:00 UTC. Additionally, the wind gust reached only 4 m/s (Table 18). However, the plume direction conforms with the meteorological data given in Table 18 and Figure 9.

Table 18. Meteorological data nearby Tsenher, Arkhangai.

Date & Time (UTC)	Temp., (°C)	Precip. (mm)	Wind gust (m/s)	Wind speed (m/s)	Wind direction (angle)	Sea level pressure (hPa)	Cloud cover (%)
April 05, 2019 23:00	-4.1	0		3	S, 174		0

April 06, 2020 00:00	-5.6	0	4	1	S, 170	1032.7	60
April 06, 2020 01:00	5.3	0		4	S, 195		0
April 06, 2020 02:00	8.8	0		5	SSW, 209		0
April 06, 2020 03:00	0.4	0	4	4	ESE, 120	1025.9	0
April 06, 2020 04:00	11.5	0		7	SSW, 216		0
April 06, 2020 05:00	12.1	0		8	SSW, 219		0
April 06, 2020 06:00	5.2	0	5	5	ESE, 110	1019.8	0
April 06, 2020 07:00	11.9	0		9	SW, 223		0
April 06, 2020 08:00	11.4	0		9	SW, 226		0
April 06, 2020 09:00	6.1	0	6	4	E, 80	1018.1	50

3.8.2. S – 2: An intense dust storm initiated from the steppe zone, moving towards the west (W) and west-northwest (WNW). By 09:00 UTC, the dust cloud merged with the S–1 dust plume (Figure 9).

Approximate coordinate: 47°3'0"N, 106°59'0"E

Meteorology: It can be seen that dust storm started at 23:00 UTC on the 5th of April 2020, with 8 m/s wind from Easterly. As shown on the table, wind gusts ranged rfrom 11 to 20 m/s. From 00:00 to 03:00 UTC wind force reached 10-17 m/s (Table 19).

Table 19. Meteorological data nearby Bayantsagaan, Tuv.

Date & Time (UTC)	Temp., (°C)	Precip. (mm)	Wind gust (m/s)	Wind speed (m/s)	Wind direction (angle)	Sea level pressure (hPa)	Cloud cover (%)
April 05, 2019 23:00	-2.6	0		8	E, 87		75.9
April 06, 2020 00:00	-1.4	0	17	17	E, 100	1030.4	77.2
April 06, 2020 01:00	3.5	0		10	E, 104		88.4
April 06, 2020 02:00	6.1	0		10	ESE, 110		85.6
April 06, 2020 03:00	1.4	0	20	15	E, 100	1029.6	65.5
April 06, 2020 04:00	10	0		9	ESE, 125		47.8
April 06, 2020 05:00	11.3	0		9	SE, 132		40
April 06, 2020 06:00	5.9	0	20	10	ESE, 120	1025.8	40
April 06, 2020 07:00	12.3	0		8	SE, 140		17.7
April 06, 2020 08:00	11.9	0		8	SE, 139		3.1
April 06, 2020 09:00	6.2	0	11	11	ESE, 110	1024.2	0

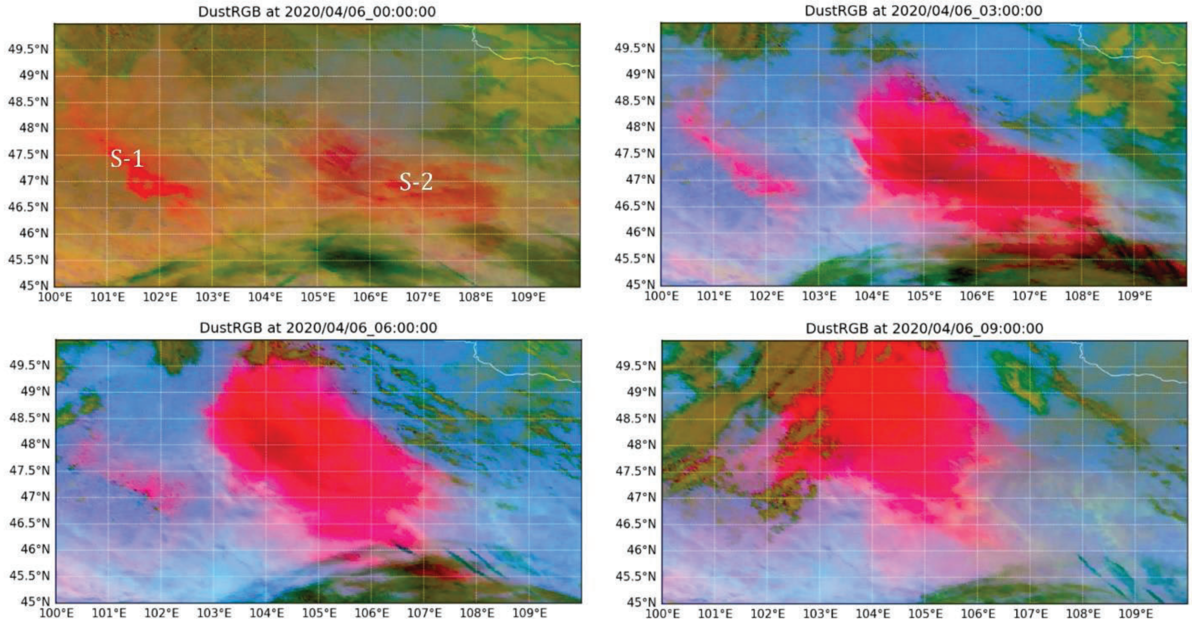

Figure 9. Dust RGB extraction using Himawari-8 geostationary satellite on April 28, 2019.

3.9. April 7, 2020

An intense and rare dust storm occurred in the northern part of Mongolia on the 7th of April 2020 (Figure 10). To provide more elaborate details on the meteorological conditions, we have included data from the two stations.

Approximate coordinate: 49°5'0"N, 104°7'0"E, and 49°28'0"N, 105°56'0"E

Meteorology: Similar to S–1 in April 6, 2020, the wind speed was not particularly high (Table 20 and 21). Therefore, these cases could be considered special events warranting detailed investigation in meteorology.

Table 20. Meteorological data nearby Erdenet, Orkhon.

Date & Time (UTC)	Temp., (°C)	Precip. (mm)	Wind gust (m/s)	Wind speed (m/s)	Wind direction (angle)	Sea level pressure (hPa)	Cloud cover (%)
April 06, 2019 23:00	-2.9	0		4	WNW, 300		4.4
April 07, 2020 00:00	0.7	0	4	1	NNW, 330	1023.8	40
April 07, 2020 01:00	3.2	0		3	NW, 319		0.8
April 07, 2020 02:00	5.1	0		3	NW, 322		1.9
April 07, 2020 03:00	6.7	0	3	2	SE, 130	1021.3	1.8
April 07, 2020 04:00	7.6	0		3	NW, 310		2.9
April 07, 2020 05:00	8.5	0		3	WNW, 308		5.3

April 07, 2020 06:00	9.4	0	5	4	WNW, 300	1018.6	40
April 07, 2020 07:00	9.1	0		3	NW, 318		11.8
April 07, 2020 08:00	8.8	0		3	NW, 325		35.7
April 07, 2020 09:00	8.6	0	5	2	NW, 320	1018.7	80
April 07, 2020 10:00	6.8	0		3	N, 354		33.1
April 07, 2020 11:00	2.9	0		3	N, 12		31.1

Table 21. Meteorological data nearby Darkhan, Darkhan-Uul.

Date & Time (UTC)	Temp., (°C)	Precip. (mm)	Wind gust (m/s)	Wind speed (m/s)	Wind direction (angle)	Sea level pressure (hPa)	Cloud cover (%)
April 06, 2020 23:00	-0.2	0		4	S, 170		86.9
April 07, 2020 00:00	6.4	0	8	5	SE, 140	1022.8	90
April 07, 2020 01:00	3.7	0		7	S, 180		87.3
April 07, 2020 02:00	5.3	0		8	S, 184		87.5
April 07, 2020 03:00	8.2	0	6	4	S, 170	1023.1	90
April 07, 2020 04:00	7.1	0		8	S, 182		80.1
April 07, 2020 05:00	8	0		7	S, 178		72.8
April 07, 2020 06:00	12.7	0	10	5	SSW, 210	1019.9	80
April 07, 2020 07:00	10	0		6	SSE, 168		16.2
April 07, 2020 08:00	10.3	0		6	SSE, 165		1.5
April 07, 2020 09:00	14.4	0	7	4	S, 170	1017.6	60
April 07, 2020 10:00	7.2	0		3	SSE, 156		0.1
April 07, 2020 11:00	3.6	0		3	SE, 132		0.2

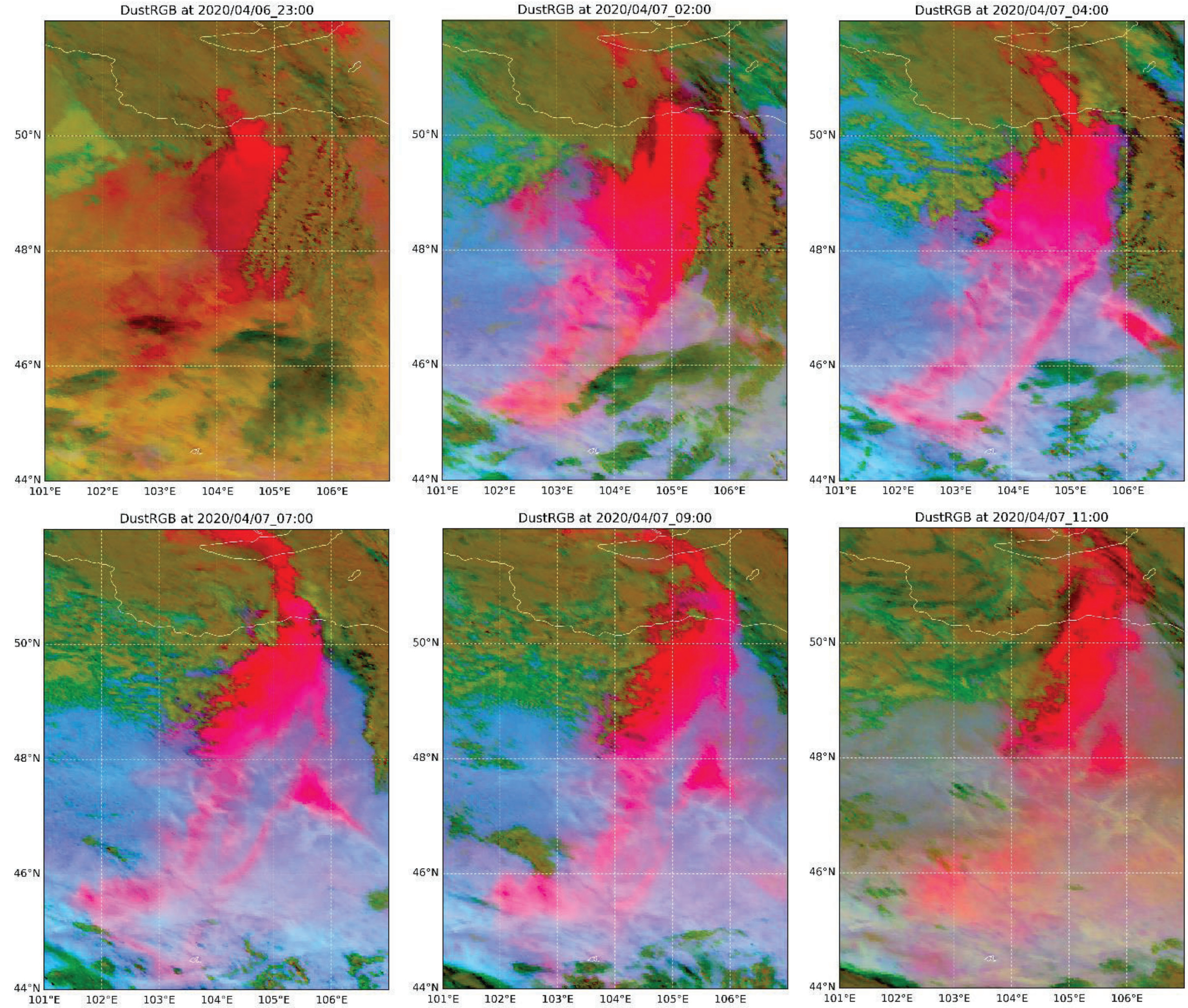

Figure 10. Dust RGB extraction using Himawari-8 geostationary satellite on April 7, 2020.

3.10. May 15, 2020

A regional-scale dust storm occurred on the 15th of May 2020. We aimed to illustrate the initial stage of the dust storm and identified two distinct locations (Figure 11).

3.10.1. S – 1: The dry gullies in the valley of the Khangai mountain range (southwestward) were identified as the initial source region.

Approximate coordinate: 46°55'0"N, 98°42'0"E

Meteorology: Throughout the dust storm, wind speeds ranged from 10 to 21 m/s, with gusts reaching 19-23 m/s between 00:00 and 10:00 UTC. The wind direction was primarily from WNW and NW (Table 22 and Figure 11).

Table 22. Meteorological data nearby Bayanbulag, Bayankhongor.

Date & Time (UTC)	Temp., (°C)	Precip. (mm)	Wind gust (m/s)	Wind speed (m/s)	Wind direction (angle)	Sea level pressure (hPa)	Cloud cover (%)
May 15, 2020 23:00	8.2	0		9	WNW, 301		0
May 15, 2020 00:00	4.6	0	19	14	NW, 320	1009	0
May 15, 2020 01:00	12.4	0		15	NW, 313		0
May 15, 2020 02:00	13.6	0		16	NW, 314		0.1
May 15, 2020 03:00	7.9	0	23	21	WNW, 300	1007.6	0
May 15, 2020 04:00	14.9	0		17	NW, 317		0
May 15, 2020 05:00	15.5	0		17	NW, 319		22.2
May 15, 2020 06:00	10.4	0	21	19	WNW, 300	1006.3	56.1
May 15, 2020 07:00	16.2	0		16	NW, 322		84.6
May 15, 2020 08:00	16.2	0		15	NW, 323		22.5
May 15, 2020 09:00	11.4	0	19	10	NW, 320	1005.4	60
May 15, 2020 10:00	15.5	0		13	NW, 323		29.9

3.10.2. S – 2: Like defined in S–1 of April 14, 2019, the dust outbreak is observed dispersing near Elsen Tasarkhai (Figure 11).

Approximate coordinate: 47°15'0"N, 103°44'0"E

Meteorology: Wind speeds ranged from 9 to 16 m/s (wind gusts reached 12-18 m/s), causing such an intense dust storm. The wind direction was from the NW and NNW.

Table 23. Meteorological data nearby Rashaant, Bulgan.

Date & Time (UTC)	Temp., (°C)	Precip. (mm)	Wind gust (m/s)	Wind speed (m/s)	Wind direction (angle)	Sea level pressure (hPa)	Cloud cover (%)
May 15, 2020 23:00	6.9	0		13	NW, 323		0.5
May 15, 2020 00:00	10.2	0	18	16	W, 270	999.1	80
May 15, 2020 01:00	6.2	0		12	NNW, 336		43.4
May 15, 2020 02:00	5.8	0		12	NNW, 344		57.3
May 15, 2020 03:00	3.9	0	18	12	N, 360	1006.6	100
May 15, 2020 04:00	5.6	0		12	NNW, 348		49.6
May 15, 2020 05:00	5.5	0		11	NNW, 347		56.4

May 15, 2020 06:00	2.1	0	12	9	N, 360	1011.9	100
May 15, 2020 07:00	4.7	0		11	NNW,347		55.2
May 15, 2020 08:00	4.2	0		10	NNW, 348		54.4
May 15, 2020 09:00	1.2	0	12	9	N, 360	1014.8	100
May 15, 2020 10:00	2.9	0		10	N, 353		45.9

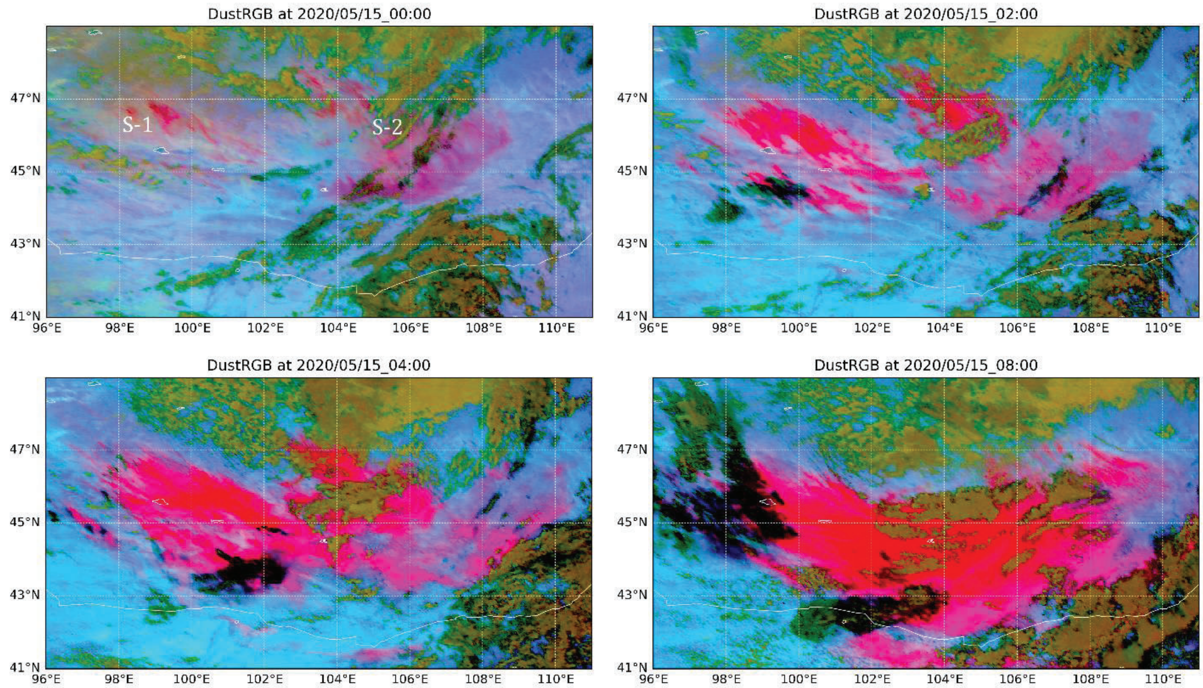

Figure 11. Dust RGB extraction using Himawari-8 geostationary satellite on May 15, 2020.

Conclusion

To be continued…

Reference

[1] Mongolian Academy of Science (2009) Mongolian National Atlas, vol II. MAS, Ulaanbaatar.

[2] Chultem Batbold, Keiya Yumimoto, Sonomdagva Chonokhuu, Batdelger Byambaa, Batdavaa Avirmed, Shuukhaaz Ganbat, Naoki Kaneyasu, Yutaka Matsumi, Teppei J. Yasunari, Kenji Taniguchi, Noriko Hasebe, Keisuke Fukushi, Atsushi Matsuki (2022). Spatiotemporal Dispersion of Local-Scale Dust from the Erdenet Mine in Mongolia Detected by Himawari-8 Geostationary Satellite. https://doi.org/10.2151/sola.2022-036

国際化推進共同研究概要

No. 5

23NU-1

タ イ ト ル： Advanced tokamak physics and integrated transport modelling

研究代表者： NA Yong-Su

所内世話人： 文　贊鎬

研 究 概 要：

本研究は、ソウル大学とRIAMの国際共同研究プログラムを通じて、先進トカマク物理の徹底的な理解と統合輸送モデリングを目指し、非線形乱流特性の理論的研究、PANTA実験測定と解析を行いました。PANTAプラズマの揺動解析の結果、コアと周辺部の間の領域において、予想外の高度に放射状に局在した乱流揺らぎと非線形相互作用が示されました。この興味深い特徴は、プラズマのコアと周辺部の相互作用の振る舞いを示しており、統合的モデリングの必要性を示しています。今後の共同研究プログラムでは、先進トカマク運転の観点から、より深く理解するために、磁気プローブを用いてより広範な研究が行われる予定です。

Advanced tokamak physics and integrated transport modelling

Yong-Su NA, Gyungjin CHOI, Chweeho HEO, Huiwon CHUNG

Department of Nuclear Engineering, Seoul National University, Seoul, Republic of Korea

It is crucial to develop novel advanced operation scenarios to achieve commercial tokamak fusion reactor. In the advanced tokamak operation scenarios, along with avoidance or mitigation of abrupt MHD activities, reduction, control, and optimization of transport level has long been an essential issue. It is well-known that turbulence is the main origin of transport of confined plasma in toroidal fusion machines. A thorough understanding of the turbulence physics is thus needed to achieve high-performance advanced tokamak operation. However, even after half-century research of turbulence in tokamak plasmas, still there are physics issues remaining. One of those is the self-organized criticality induced by nonlinear self-organization of mesoscale structures from the turbulence.

Recently, there has been experimental findings of direct fast ion effect on core confinement enhancement from ASDEX-U and KSTAR. It is worth noting that the main auxiliary heating methods of the two cases are largely different that it is ICRH for ASDEX-U while NBI for KSTAR. This implies the presence of a universal mechanism working for the confinement enhancement. Indeed, previous extensive experimental studies of various transport barrier formations have demonstrated that ExB flow shearing is the main mechanism of suppression of drift wave turbulence and enhancement of tokamak plasma confinement. While the role of profile-induced equilibrium ExB shear flow has first been highlighted due to its easier experimental measurements and estimations, theoretical and simulation studies have revealed that mesoscale zonal ExB flow, nonlinearly self-generated from the drift wave turbulence, is the major physical object triggering the transition to an enhanced confinement state. The equilibrium ExB flow plays a role in the later part of the transition, altering the zonal flow. One of interesting features of the turbulence-zonal flow interaction is the Dimits shift, a nonlinear upshift of the turbulence onset threshold from linear marginal stability to self-organized criticality (SOC) because of the quenching of turbulence after its initial burst by flow self-generation. We would like to remark that the transient turbulence bunch near SOC could be considered as a seed of the intermittent transport event visible near marginality. Therefore, understanding the flow self-organization from turbulence is essential to understand all the nontrivial transport properties near marginality, more precisely near SOC, in high-performance advanced tokamak operations.

Accordingly, we have addressed theoretical and simulation studies of turbulence-zonal flow interaction in high-performance advanced tokamak plasmas. Linear and nonlinear gyrokinetic simulations have shown importance of thermal ion dilution effect by the presence of fast ions. It significantly reduces linear growth rate of turbulence, and in nonlinear stage leads to a dramatic reduction in the transport flux. It is noticeable that zonal flow growth rate is even stronger in the presence of fast ions, even in the presence of much weaker turbulence prey. This result indicates much efficient zonal flow growth from turbulence. This could be relevant to our analytic theoretical extension of the Hasegawa-Mima equation to the case with fast ions. It is worth noting that the Hasegawa-Mima equation is an adiabatic limit of the Hasegawa-Wakatani equation which is relevant to the PANTA plasma in RIAM. It has also been widely accepted as a paradigm equation for the drift wave turbulence-zonal flow nonlinear interaction in magnetized plasmas. By the 4-wave-coupling calculation we have shown that while the Reynolds stress drive for the modulational growth of zonal flow is weakened by the dilution effect, the finite threshold of the zonal flow growth by frequency mismatch among the pump drift wave and sidebands is much more strongly reduced. As a result, we have an easier zonal flow growth near its threshold, that is, near SOC.

As a next step, we initiated PANTA experimental analyses for comparative study of flow self-organization from turbulence. It is important that the Hasegawa-Wakatani equation is based on the straight magnetic field, similar to PANTA plasma, which is still relevant to study nonlinear physics of tokamak plasmas. Moreover, its relevance to the tokamak SOL is striking. Note that it is easier to find nonlinear self-generated streamers rather than zonal flows in the PANTA plasmas. Recall that radial anomalous diffusion of transient heat flux in tokamak SOL is crucial to reduce divertor heat load. Another remarkable point is that many fusion researchers have addressed electromagnetic fluctuations and perturbed structures in tokamak SOL, while it has been known to be electrostatic in core confined region. Interestingly, it is also well-known that electromagnetic effect on the core turbulence and Alfvenic modes are influential in the core confinement in advanced tokamak operations. The two limits of hot and cold plasmas in the same device point to one signature of the electromagnetic perturbation. Therefore, through this international collaboration, we have trained to use diagnostics in PANTA device, in particular the Langmuir probe and the ball-pen probe. Our final goal is a thorough understanding of nonlinear turbulence physics relevant to the advanced tokamak plasmas by comparative analysis of the electric potential fluctuations obtained by the two probes, and the magnetic field fluctuations obtained by the magnetic probe which will be installed in 2024.

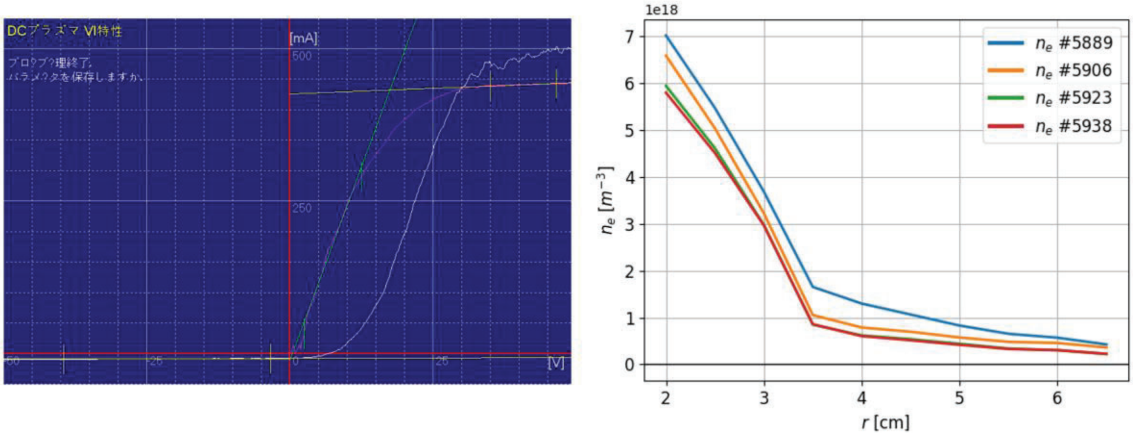

Fig. 1. I-V curve obtained from Langmuir probe by voltage sweeping (left), and electron density profile obtained from the 10-channels radial array of the Langmuir probes (right).

With the guidance of Prof. Chanho Moon and DiMatteo Donato, we have first trained to understand the Langmuir probe system of PANTA. Fig. 1 shows a successful measurement of electron density profile using the Langmuir probe array consisting of 10 radial channels. Clear distinction of the core and edge regions are visible.

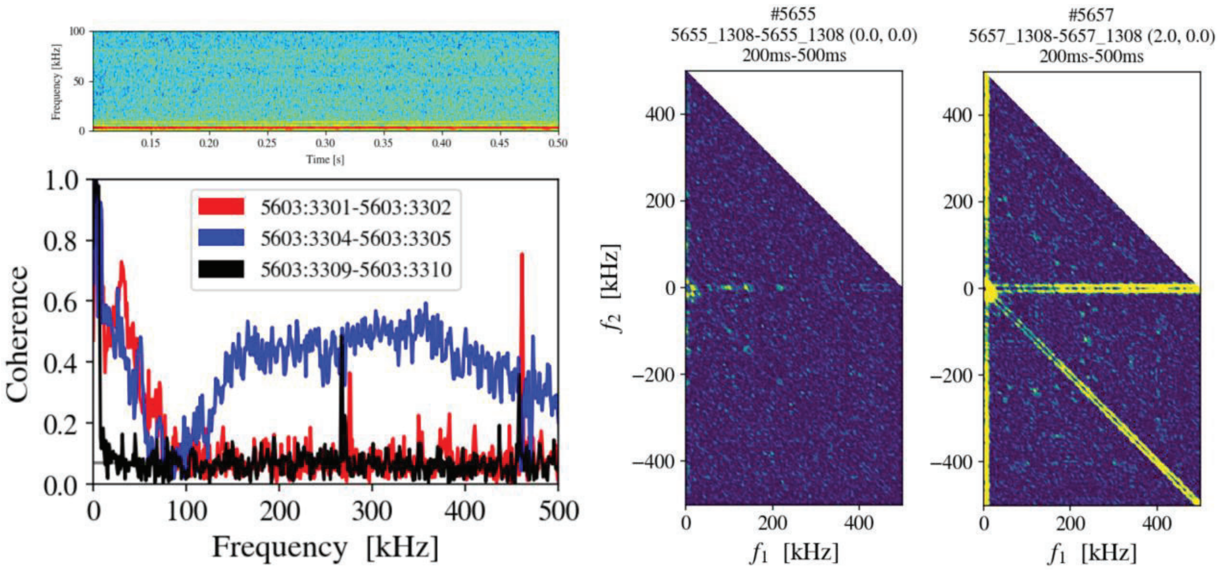

FIG. 2. Fourier analysis (left) and bicoherence analysis (right) of potential perturbation in different radial locations. Radially localized turbulence and nonlinear coupling have been observed.

Next, we have trained to obtain potential perturbation data using the Langmuir probes from PANTA experiments and performed Fourier spectrum analysis and the bicoherence analysis. Fig. 2 shows the results of the fluctuation analyses. The left figure shows that broadband turbulent fluctuation is robust only in the region connecting core and edge, indicating importance of core-edge coupling which was unexpected before and cannot be fully described by a core or edge-specialized modeling. That is, the result reveals the need of an integrated modeling for a proper understanding of the turbulent transport in PANTA plasmas. The right figure is the result of bicoherence analysis in different radial locations, also showing radial localization of nonlinear interactions. These interesting features showing the symptom of core-edge coupling will be further investigated by extensive experimental measurements and analyses coupled with an integrated modeling.

In summary, through an international collaboration with PANTA, we have performed analytic theoretical studies and experimental measurements and analyses of nonlinear turbulence properties toward thorough understanding of advanced tokamak physics and integrated transport modeling. Fluctuation analyses of PATNA plasma have shown unexpected highly radially localized turbulent fluctuations and nonlinear interactions, which is the opposite nontrivial limit of turbulence physics in contrast to non-local transport events. This unexpected, interesting feature found during the collaboration will be more extensively investigated using the magnetic probe and an integrated modeling for its deeper understanding from the perspective of the advanced tokamak plasmas in the upcoming international collaboration program.

国際化推進共同研究概要

No. 6

23NU-2

タ イ ト ル： Analysis of specific plasma characters using the 3-D tomographic system for advanced plasma-enhanced atomic layer deposition

研究代表者： CHUNG SEUNG-MIN

所内世話人： 文　贊鎬

研 究 概 要:

プラズマ励起 ALD(Atomic Layer Deposition; 原子層堆積)は、エネルギー強化手法の一環として使用され、オングストローム単位の分解能で超薄膜を生成する手法です。この手法では、プラズマを反応物として使用することで、従来の熱駆動 ALD 法よりも加工条件においてより柔軟性があり、材料特性の包括的な調整が可能です。ただし、プラズマ中のイオンとラジカルのフラックスおよび表面での反応は正確には推定されていません。たとえば、プラズマ中で 2 つの反応ガスを混合すると、ガス相または表面再結合反応を介して新しい分子が形成される可能性があります。本研究では、3 次元トモグラフィーシステムを適用してプラズマ励起 ALD の全反応場を大域的に測定しようとしています。ただし、現在の段階ではプラズマ励起 ALD プロセスが時間を要するため、このトモグラフィーシステムはまだ利用されていません。一方で、将来的には 3 次元トモグラフィーシステムを用いてプラズマ励起 ALD のプラズマ挙動を検証する予定です。

Analysis of specific plasma characters using the 3-D tomographic system for advanced plasma-enhanced atomic layer deposition

Yonsei University

Seung-min Chung

In order to successfully develop a dynamic random access memory (DRAM) of less than 20 nm, a high dielectric constant (k) of the film with a good step coverage and low leakage current density must be required. For this characteristic, atomic layer deposition (ALD) should be a promising technique for the fabrication of nanomaterials, as it enables the deposition of a thin film with good uniformity over a large area. Advantages of the ALD technique include thickness control at the atomic scale, production of highly conformal films, and low-temperature growth. Otherwise, plasma-enhanced atomic layer deposition (PE-ALD) is an energy-enhanced method for synthesizing ultra-thin films with angstrom-level resolution in which plasma is employed during one step of the cyclic deposition process. Using plasma species as reactants allows for more freedom in processing conditions and a more comprehensive range of material properties than the conventional thermally-driven ALD method. However, the fluxes of ions and radicals from plasma and their reaction on the surface do not estimate precisely. For example, when admixing two reactant gases in the plasma, new molecules could be formed through gas-phase or surface recombination reactions.

ZrO_2-based metal-insulator-metal (MIM) capacitors are being actively studied among high-k materials that replace silicon oxide and silicon oxynitride. In particular, ZrO_2 has received considerable attention due to its good thermal stability, high dielectric constant, and wide bandgap (5.16-7.8 eV) [1],[2]. As the electrode of the capacitor, TiN is widely used as the electrode of the capacitor in terms of mass production. However, when ZrO_2 is deposited on TiN, the electrical properties of ZrO_2 thin film are deteriorated. For example, the leakage current density can be increased due to the formation of interlayer between dielectric film and TiN. This interlayer occurs due to the oxidation of the electrode during the film deposition process, which is affected by the potential barrier height of the oxidation reaction [5]. Since the potential barrier height depends on the work function of the metal electrode, proper selection of the electrode is required. Herein, we studied the factors of the interlayer formation on ZrO_2 thin films deposited by atomic layer deposition (ALD), especially focused on the effect of interlayer formation using thermal or plasma reactive process on the electrical properties of ZrO_2 thin films. For comparative study, two different bottom electrodes such as TiN and Ru were used. ZrO_2 films are deposited on these bottom electrodes by using $CpCH(Me)CH_2NMeZr(NMe_2)_2$ (CMENZ) as a precursor and two different oxidants, respectively. Further, to comparatively investigate the oxidation of the electrodes, two different types of oxidants such as oxygen plasma and hydroperoxide were employed on ALD ZrO_2 process.

Experient Method

The PE-ALD chamber for depositing the thin film consists of a showerhead-type injector and a capacitively coupled plasma (CCP) reactor. The sample stage in the chamber's center is heated up to 400 °C. Each ALD cycle consists of four sequential steps: exposure of $CpCH(Me)CH_2NMeZr(NMe_2)_2$ to the hydroxylated TiN and Ru substrate, purging of residual precursor molecules by inert Ar gas, exposure to O_2 plasma gas or N_2 gas exposure, and purging of byproducts and residual reactant gas using inert Ar gas. The CMENZ precursor from Sigma-Aldrich was vaporized at 60 °C, and the supply line must be continuously heated at a relatively high temperature of ~70 °C to maintain good flux stability and avoid the precursor condensation. The reactants were H_2O_2 for thermal ALD, and O_2+N_2 plasma was used as PE-ALD on the substrate.

Results & Discussion

Figure 1 shows the electrical properties of the C-V characteristic of MIN capacitors made using ALD ZrO_2 films on the bottom electrodes of TiN and Ru. The dielectric constant measured on the Ru substrate was 27.1 (using O_2 plasma reactant) and 13.4 (using H_2O_2 reactant), whereas, on TiN, it was lower at 17.6 (using O_2 plasma reactant) and 12.9 (using H_2O_2 reactant). As shown in Figure 1, the I-V (current-voltatge) characteristics are displayed. A significant leakage current was observed at a measured electric field of -1MV/cm due to the different electrodes using H_2O_2 reactant; the leakage current was measured at 4.53 x 10-5 A/cm^2.

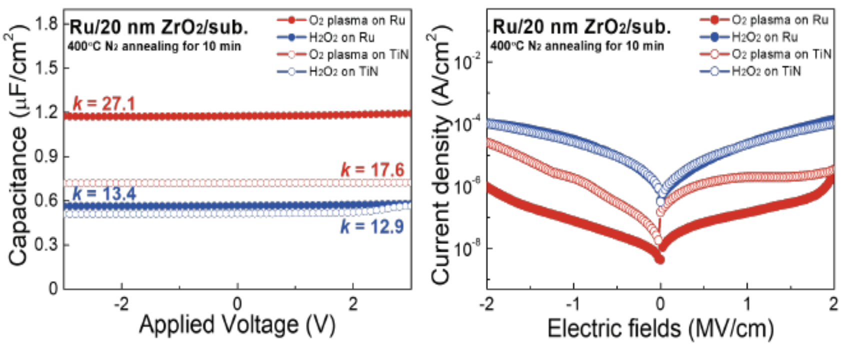

Fig 1. Electrical Property (C-V,I-V)

The deposited electrode films determine this difference in leakage current, and the electrode quality is made by the reaction energy-specific character when the chemisorbing atoms exchange the oxygen or ligands on the surface. Plasma energy affects the debonding of the ligand sufficiently compared with thermal energy. Therefore, activated oxygen radicals or ions could be chemisorbed and linked to the Zr atoms. Furthermore, the crystal structure significantly influences the dielectric constant and leakage current. Ideally, amorphous cases or perfect single-crystalline structures are preferred to maintain physical and electrical properties uniformly. The amorphous structure is particularly advantageous in minimizing various defects, such as anisotropy, grain boundaries, and electrically active sites. However, proper crystallization may sometimes be required to enhance the dielectric constant. In the context of these criteria, Zirconium Dioxide (ZrO_2) emerges as an up-and-coming candidate among the high-k materials, considering its high thermal stability, excellent dielectric properties, a high dielectric constant (k ~ 20), and a broad bandgap (5.16-7.8 eV). There are several crystal structures of ZrO_2, each with different dielectric constants. Theoretically, the cubic and tetragonal phases of ZrO_2 are known to have higher k values, over 30, compared to the monoclinic (k = 16-20) and amorphous (k ~ 16-20) phases. As the temperature increases, ZrO_2 transitions from the monoclinic phase (≤1400 K) to tetragonal (1400-2570 K) and then to cubic (2570-2980 K). However, the cubic and tetragonal phases of ZrO_2 could be made using the plasma characteristics under specific conditions. In conclusion, the plasma reactant has the potential to depend on how it is used in the semiconductor manufacture.

国際化推進共同研究概要

No.7

23NU-3

タ イ ト ル： Plasma start-up and sustainment in spherical tokamak configuration by RF

研究代表者： TAKASE Yuichi

所内世話人： 出射　浩

研究概要：
令和6年2月1、2日の2日間で国際 WS をハイブリッド形式で開催した。英国から 3 名、米国から 5 名、国内から多数の参加があった。QUEST 実験の最近の進展・検討に加え、国内外実験の進展・検討、新たなシミュレーション解析などが議論された。英国から 3 件、米国から5件、国内で 9 件の研究成果発表があり、主に球状トカマクでの非誘導プラズマ電流立ち上げに関し、活発な議論があった。

Plasma start-up and sustainment in spherical tokamak configuration by RF

TAKASE Yuichi
(Tokamak Energy Ltd., United Kingdom)

An on-site/on-line hybrid workshop on "Plasma start-up and sustainment in spherical tokamak configuration by RF" was held on 1st and 2nd February at Advance Fusion Research Center in Research Institute for Applied Mechanics, Kyushu University. Lively discussions were held following each presentation.

Agenda

1st February

9:20 -9:30

Yuichi Takase / Kazuaki Hanada

WS purpose and agenda

9:30 - 10:00

Yuichi Takase

Fusion Development at Tokamak Energy

10:00 - 10:40

Akira Ejiri

Study of current drive in the TST-2 spherical tokamak (Remote)

10:40 - 11:20

Hitoshi Tanaka

Recent Result of EC Start-up Experiment on LATE (Remote)

11:20 - 11:50

Yusuke Kosuga

Bootstrap current and flow in spherical tokamaks

11:50 - 12:50 **Lunch**

12:50- 13:30

Hiroshi Idei

Recent Progress and ECH Plans in QUEST

13:30 - 14:10

Takumi Onchi

Electron cyclotron current start-up using a retarding electric field in the QUEST spherical tokamak

14:10 - 14:50

Masayuki Ono

Efficient ECCD non-inductive start-up and ramp-up and transition to a sustainment phase for an ST fusion reactor

14:50 – 15:30

Ryuya Ikezoe

Studies of fast electrons and corresponding kinetic modes on QUEST

15:30 – 15:40 **Coffee Break**

15:40 - 16:10

Makoto Hasegawa

Plasma control system of QUEST and fast plasma shape recognition with Machine Learning

16:10 - 16:50

Luis Delgado-Aparicio

Non-Maxwellian LHCD anisotropic features in the edge and core measured with a multi-energy HXR detector at WEST

16:50 - 17:30

Vladimir Shevchenko

ECRH Progress and Plans for ST40 (Remote)

17:30 - 18:10

Bodhi Biswas

Fully-relativistic EBW current drive simulations in STEP (Remote)

18:10 – **Group Photo**

2nd February

9:00 - 9:40

Roger Raman

Closed flux plasma startup using Transient CHI on QUEST

9:40 - 10:10

Shin Kubo

Toward the numerical estimation of the power flow of the electron Bernstein wave (Remote)

10:10 - 10:50

Atsushi Fukuyama

Kinetic full wave modeling of O-X-B mode conversion

10:50 - 11:30

Nicola Bertelli

Initial study of the impact of the edge density fluctuations on the HHFW propagation in NSTX/NSTX-U plasmas

11:30-12:10

Syunichi Shiraiwa

Implicit method for plasma conductivity and its application to electron Bernstein wave mode conversion

12:10 - 13:10 **Lunch**

2nd February PM

Discussion of proposals for experiments, diagnosis, and analysis

Summary of Presentations

Yuichi Takase

Tokamak Energy is aiming for early commercialization of fusion energy by combining the advantages of the low aspect ratio tokamak and high temperature superconducting (HTS) coils. In addition to achieving ion temperatures exceeding 100 million degrees K needed for fusion burn, we are developing technologies needed for fusion reactors. In HTS coil development, we have achieved a world record magnetic field of 24T at 20 K, greatly improved quench resilience, and beginning tests of an HTS coil system in the spherical tokamak configuration (Demo4). We have established the Magnet Business Unit to commercialize these technologies.

Akira Ejiri

Preliminary experiments with the new antenna suggested the expected core power deposition. Orbit expansion of fast electrons (hitting the limiters) can be a significant loss channel, and experiments using a movable target is underway. Sheath effect is the present dominant source of copper and molybdenum impurities, but fast electron heating effect on the limiter can be important for a longer discharge duration. Ion heating occurs at the near edge region, and the estimated heating power is much smaller than the LHW power. Ion heating through parametric decay instabilities (ion-cyclotron quasi-mode and ion-sound quasi-mode) is suggested as the mechanism, and it is consistent with theoretical and experimental results.

Hitoshi Tanaka

Firstly, effects of the background magnetic field in the experiment room on the formation of closed flux surface (CFS) by ECH under steady B_v was investigated. A toroidal plasma current flows when a weak vertical field is applied to the ECR plasma, so as to cancel the applied vertical filed. The plasma current does not flow when the applied vertical field cancels the vertical component of the background magnetic field ($B_{z\text{-background}}$ = 0.27 mT). After the formation of CFS, there are no significant effect on I_p ramp-up at least up to 5 kA. Secondly, effects of the vertical vacuum vessel space was investigated. A movable limiter was installed from the top port in the vacuum vessel to change the vertical elongation of the plasma generating region (the vertical elongation ratio κ_{vv} = 1.7 ~ 2.3). In the case of κ_{vv} =1.7, n-index or P_{inj} should be high enough to form CFS (n-index > 0.25 @ P_{inj} = 10 kW, n-index > 0.15 @ P_{inj} = 20 kW). In the case of κ_{vv} =2.3, formation of CFS is achieved in the wide range of n-index and P_{inj} (n-index ≧ 0.07 @ P_{inj} = 10 kW). For the same P_{inj}, the larger κ_{vv} allows lower n-index and brings larger current-flowing area and larger I_p. In addition, formation of CFS is achieved at higher B_v. Large κ_{vv} allows flexibility of current-flowing area and tokamak equilibrium.

Yusuke Kosuga

It is shown that appreciable amount of current can be carried by the precession motion of trapped energetic electrons in QUEST. Relative importance of this current to bootstrap current scales as $\varepsilon^{1/2}/(1-\varepsilon^2)^{1/2}$, where ε is the inverse aspect ratio. Thus precession driven current can be more important for spherical tokamaks with ε < 1. For typical plasma parameters in QUEST, the precession driven current can reach up to O(10) kA. Inductive field may decrease this current due to conservation of toroidal canonical momentum.

Hiroshi Idei

Recent progresses in QUEST were briefly explained as introduction of several talks to follow. In addition, ECH plans are shown. The toroidal magnetic field will be doubled to 0.5 T. The second harmonic and fundamental resonance layers will be at center of the device and inboard side, respectively. Heating scenarios at 0.5 T are considered through one pass absorption analysis using the TASK/WR code. The 60-keV energetic electrons of several percentage populations are considered as well as the bulk electrons of 500 eV. The incident 28-GHz waves are strongly damped at the fundamental and second harmonic resonances in low- and high-density plasmas, respectively. The strong damping at the second harmonic layer is considered through a resonant ellipse analysis in the momentum space. EBWHCD scenarios based on the multiple ray-tracing analysis by using the Gaussian optics are explained.

Takumi Onchi

The latest plasma current start-up experiment conducted through electron cyclotron heating in the QUEST spherical tokamak is introduced. By applying toroidal electric field in the anti-direction to plasma current, the growth of energetic electrons is suppressed. Efficient bulk electron heating has been observed with such retarding electric field.

Masayuki Ono

The elimination of the need for an Ohmic heating solenoid may be the most impactful design driver for the realization of economical compact fusion tokamak reactor systems. However, this would require fully non-inductive start-up and current ramp-up from zero plasma current and low electron temperature of sub-keV to the full plasma current of ~ 10 - 15 MA at 20 - 30 keV electron temperature. To address this challenge, an efficient solenoid-free start-up and ramp-up scenario utilizing a low-field-side-launched extraordinary mode at the fundamental electron cyclotron harmonic frequency (X-I) is proposed, which has more than two orders of magnitude higher electron cyclotron current drive (ECCD) efficiency than the conventional ECCD for the sub-keV start-up regime. A time dependent model was developed to simulate the start-up scenarios. For the Spherical Tokamak Advanced Reactor (STAR), it was found that to fully non-inductively ramp-up to 15 MA, it would take about 25 MW of EC power at 170 GHz. Because of the relatively large plasma volume of STAR, radiation losses must be considered. It is important to make sure that high Z impurities are kept sufficiently low during the early current start-up phase where the temperature is sub-keV range. Since the initial current ramp up takes place at a factor of ten lower density compared to the sustained regimes, it is important to transition into a higher bootstrap fraction discharge at lower density to minimize the ECCD power requirement during the densification. For the sustainment phase an array of eight gyrotron launchers with a total of about 60 MW of fundamental O-mode was found to be sufficient to provide the required axis-peaked external current drive. High efficiencies between 19 – 57 kA/MW were found with optimal aiming, and these were resilient to small changes in aiming angles and density and temperature profiles.

Ryuya Ikezoe

Energetic particle probe (EPP) developed on QUEST for the studies of fast electrons gave (1) radial profile of fast electron flux, showing the wide existing range exceeding the local limiter, (2) its pitch-angle profile, and (3) its fluctuation with excited kinetic modes. A rotation drive system has been attached to the EPP, enabling fine pitch-angle distribution measurement. As a result, strong correlation between the pitch-angle and the energy spectrum of fast electrons of > keV was found to emerge at far SOL on QUEST, suggesting a narrow velocity distribution in this region.

Makoto Hasegawa

Using Deep Neural Network (DNN), plasma shapes can be predicted quickly and with high accuracy. It is necessary to consider new methods that handle not only plasma shape but also plasma pressure, beta value, etc. For practical applications, it is necessary to incorporate the effect of local toroidal current distributed in the z direction.

Luis Delgado-Aparicio

Multi-energy soft and hard x-ray (SXR & HXR) pinhole cameras have been designed, built and deployed at Alcator C-Mod, MST and WEST to aid the study of particle and thermal transport, heating and RF current drive as well as MHD stability physics. This novel imaging diagnostic technique employs a pixelated xray detector in which the lower energy threshold for photon detection can be adjusted independently on each pixel. The 2D detector of choice is a PILATUS3 100K configuration fielded with a 0.45 mm thick silicon and 1.0 mm thick CdTe sensors and ~100 kpixels sensitive to photon energies between 1.6 to 30 keV and 20-200 keV, respectively. Careful trimming of the lower energy threshold for photon detection allowed our team to circumvent the contribution from radiative recombination steps and line-emission from medium to high-Z impurities like Al, Mo and W. Central values of T_e can be obtained by modeling the slope of the continuum radiation from ratios of the inverted radial emissivity profiles over multiple energy ranges with no a-priori assumptions of plasma profiles, magnetic field reconstruction constraints, high-density limitations, or need of shot-to-shot reproducibility. The latest of our results include measuring the temporal evolution of central electron temperature at 100 Hz in 70 s steady-state L-mode at WEST at CEA. A novel application has recently been tested tokamak plasmas for early detection, 1D imaging and study of the birth, exponential growth and saturation of runaway electrons at energies comparable to 100 × $T_{e,0}$. We have also used the high-efficiency of the CdTe sensor at high energies to probe non-Maxwellian tails and the resultant emission-anisotropies at the edge and core of WEST's LHCD plasmas.

Vladimir Shevchenko

A multi-frequency electron cyclotron resonance heating (ECRH) and current drive (CD) system is currently under construction on the ST40 spherical tokamak at Tokamak Energy Ltd. The system employs 1 Kyoto Fusioneering gyrotron with a maximum output power of 1 MW and a pulse length of 2s. The gyrotron can be tuned to operate either at 104 GHz or 137 GHz. The system is designed to study non-inductive plasma start-up, current ramp-up and sustainment. At present ST40 has the highest for STs toroidal magnetic field up to 3T which allows testing of reactor relevant radio frequency (RF) based methods of plasma start-up, current ramp-up and sustainment with commercially available MW range RF power sources. Well-established conventional ECRH and CD schemes are planned to be tested in ST40 plasma using a poloidally and toroidally steerable launcher installed at low field side (LFS) of the tokamak. In addition to conventional ECRH, plasma start-up and CD scenarios using electron Bernstein waves (EBW) are planned to be tested on ST40. Efficient EBW excitation in the plasma requires RF power to be launched as a slow extra-ordinary (X) mode from the high field side (HFS) of the machine. To achieve that, the O-mode polarized RF beam is launched from LFS towards mirror-polariser (MP) installed on the central post of ST40. At MP the RF power is mode-converted into the X mode and reflected towards the fundamental EC resonance layer. The slow X mode experiences a subsequent mode conversion into the EBW mode at the upper hybrid resonance (UHR) and then EBW propagates back to the EC resonance. This scheme allows experimental studies of non-inductive plasma start-up, current ramp-up and sustainment. The present status of the ECRH system development and plans for the first experimental campaign will be presented and discussed.

Bodhi Biswas

Electron Bernstein waves (EBWs) are theorised to efficiently drive current in reactor-grade spherical tokamaks, e.g. STEP. At high temperatures (T_e > 5 keV), relativistic effects can significantly impact wave propagation (and surely impacts wave damping). This work presents relativistic calculations of EBW wave propagation, damping, and current drive (CD) in a conceptual STEP plasma. Kramers-Kronig relations are exploited to efficiently evaluate the fully-relativistic dispersion relation for arbitrary wave-vectors, leading to a ~ 50x speed-up compared to previous efforts. A recently verified linear adjoint model is used to estimate CD efficiency. Thus, for the first time, large parametric scans of fully-relativistic EBW CD simulations are performed through ray-tracing. In STEP, three main classes of rays are identified. The first class propogate deep into the core (rho < 0.5), but only exist if relativistic effects are accounted for. They damp strongly at the 1st harmonic on nearly-thermal electrons and thus drive little current. A second class of rays propagate to intermediate depths (rho = 0.3 - 0.7) before damping at the 2nd harmonic. Their CD efficiencies are significantly altered due to relativistic changes to trajectory and polarisation. The third class of rays damp strongly far off-axis (rho > 0.7), predominantly at the first harmonic. These ray trajectories are sufficiently short and "cold" such that relativistic effects are unimportant. Presently, the EBW antennas for STEP are being optimised around this third class of rays due to their large CD efficiencies. This suggests that non-relativistic simulations are adequate for this particular operating point.

Roger Raman

Results from QUEST show that Transient CHI start-up is compatible with a floating biased electrode (FSB) configuration. The FSB configuration is much more suitable for a fusion reactor as large vacuum insulators are not needed. Transient CHI discharges have been generated over a very wide parameter range, and the discharges can be easily started. About 100 kA closed flux current has been generated. This is consistent with earlier current startup projections for QUEST. Near term plans are to reduce the electron density so that the discharges coupled to induction can be heated, initially using ECH & later using EBW.

Shin Kubo

Project of direct detection of EBW in QUEST using HCN laser scattering is briefly introduced. The estimation of the power flux of EBW is essential for the heating/current drive and scattering consideration. It is indicated that optical vortex might excite EBW directly from low field side by mode conversion. For the precise estimation and power flux and EBW excitation by optical vortex, a new Quasi-optical beam tracing code that takes diffraction into account (EQUASI) is under development.

Atsushi Fukuyama

Kinetic full wave analysis using the integral form of dielectric tensor has been formulated and applied to the analysis of the O-X-B mode conversion of electron cyclotron waves in QUEST. Two-dimensional analysis on midplane in tokamak configuration (slab model) has shown the spatial structure of O-mode, X-mode, and electron Bernstein wave (EBW). It was confirmed that O-mode is efficiently converted to EBW near the optimum injection angle and a small amount of collision near the upper hybrid layer causes strong damping of the wave. Analysis on a poloidal cross section requires the formulation including inhomogeneity of magnetic field strength along the field line, and the implementation in 2D FEM analysis is under way.

Nicola Bertelli

An analytical edge density fluctuation model was implemented in Petra-M to investigate its impact on the HHFW propagation. 2D Petra-M simulations with a cold plasma model clearly show a significant perturbation of the HHFW propagation to the core plasma when density fluctuations with large amplitudes ($A > 30\%$) exist. Similar results in terms of HHFW propagation are found when a local hot plasma approximation is employed. With the local hot plasma model, we can also make some observations on the effects on the edge perturbations on the ion and electron absorption. For amplitude of the edge density perturbations larger than 10% and for the plasma/wave parameters used in these simulations, the density fluctuations seem to have a strong impact on both the electron and ion absorption. The deuterium/hydrogen power deposition area tends to spread vertically and scatter into multiple sub-regions. 3D Petra-M simulations were performed assuming a 3D axisymmetric edge density perturbation for a cold plasma model for three antenna phasing values: 30, 90, and 150 degrees. Overall reduction of the electric field amplitude in the core plasma for large A was found. A strong modification of the vertical wave field mainly on the poloidal cross-section as similarly found in the 2D runs for a cold plasma. Finally, initial attempts to implement an edge 3D filament geometry along the magnetic field line in the NSTX-U geometry used in Petra-M was also shown and discussed. This subject though is still in progress.

Syun'ichi Shiraiwa

It is well known that the dielectric response to the RF fields in hot plasma is non-local, and the Maxwell wave problem is an integro-differential equation. A differential form of dielectric operator, based on the small $k_\perp\rho$ expansion, typically includes up-to the second order terms, and thus the use of such an operator is limited to the waves that satisfy $k_\perp\rho < 1$. We propose an alternative approach to construct a dielectric operator, which includes all-order finite Larmor radius effects without explicitly containing higher order derivatives. We use a rational approximation of the plasma dielectric tensor in the wave number space, in order to yield a differential operator acting on the dielectric current (J). Then, we solve the resultant partial differential equation for J simultaneously with the Maxwell equation. To demonstrate this approach, we use the Petra-M framework and solve the 1D O-X-B mode-conversion of the electron Bernstein wave in the non-relativistic Maxwellian plasma. An agreement with analytic calculation and the conservation of wave energy carried by the Poynting flux and electron thermal motion ("sloshing") is found. An approach to extend the operator in a 2D poloidal cross-section setting was also discussed.

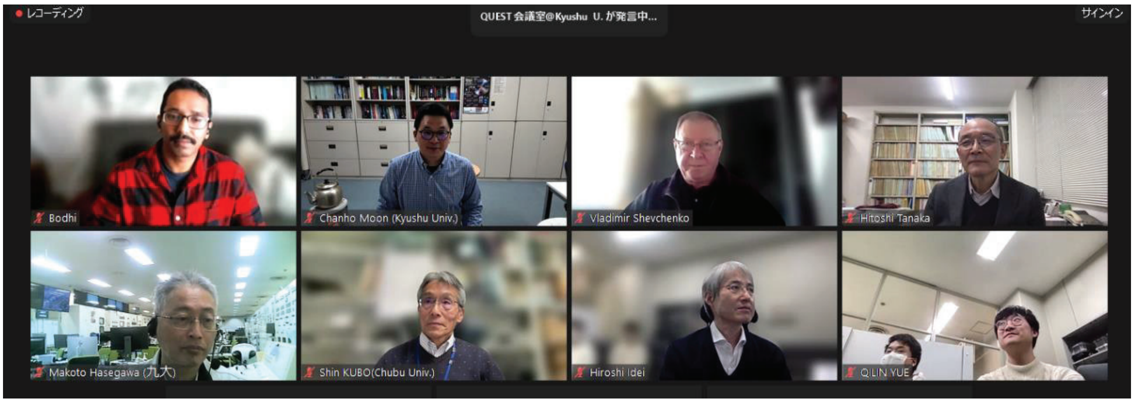

国際化推進共同研究概要

No.8

23NU-4

タイトル： Develop and improve EFIT code of the plasma equilibrium reconstruction for SSO operation and advanced physical study on QUEST

研究代表者： QIAN Jinping

所内世話人： 花田　和明

研究概要： 研究代表者は中国のフラグシップ装置である EAST の平衡制御を担当しており、EAST から離れることができないため遠隔で議論を実施した。通常燃料粒子として用いる水素同位体（重水素や軽水素）ではないガスを導入した際にプラズマ中心のイオン温度が上昇する現象が良く観測されており、その現象について解析を行った。イオン温度の上昇は Ar ガスで最大となった。トロイダル回転が Ar ガスの入射によって増加しており、輸送を生む揺動が抑制されていることが観測された。QuaLiKiz コードを用いたジャイロ運動論的な解析（TEM と ITG についての解析）を行い、アルゴンガス注入によるＴＥＭに対する抑制が示された。この結果から、イオン温度の上昇はアルゴンガスによる揺動の抑制で定性的に説明できることが分かった。

国際会議発表

[1] K. Hanada, ……, X.　Gao, H.Q.　Liu, J. Qian,　Jie,…… “Recovery from wall saturation using temperature control of plasma facing wall on QUEST” Fusion Energy Conference, 2023.10 London, UK

Research subject: Develop and improve EFIT code of the plasma equilibrium reconstruction for SSO operation and advanced physical study on QUEST

In EAST radiative divertor feedback control experiments, it is commonly observed that seeding impurity can raise the central Ti . One EAST typical discharge is shown in figure 1. It is noticeable that central Ti increases while Ti remains unchanged at ρ = 0.45.

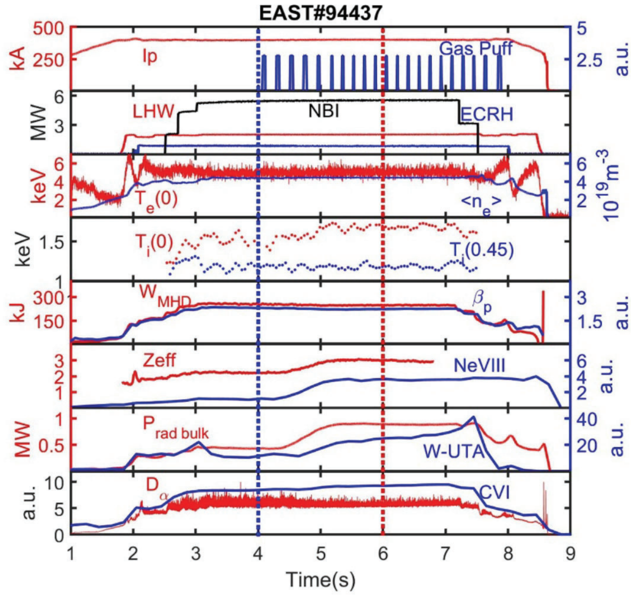

Figure 1 Time traces of the plasma current and gas puff, heating power, and central Te and volume averaged ne, Ti at ρ = 0 and 0.45, plasma's stored energy and poloidal beta etc.

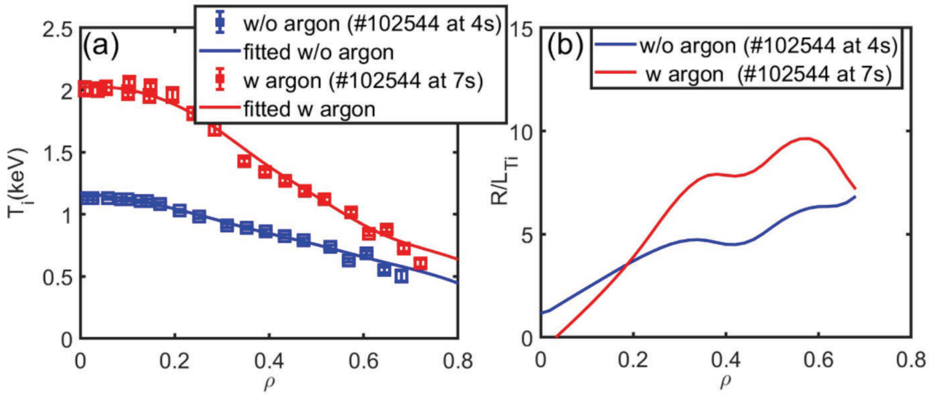

Figure 2 Comparison of Ti and R/LTi at two time slices

Comparisons of Ti profiles for argon seeding, as well as their corresponding R/LTi, are illustrated in figure 2. These Ti profiles, as well as the following Ti profiles are measured by tangential x-ray crystal spectrometer (TXCS) [39]. It can be seen that a more peaked Ti profile by argon seeding leads to higher central Ti.

To research the underlying mechanism for the enhanced Ti, the latest updated QuaLiKiz is applied to perform instability analysis and ONETWO is applied to perform the power balance analysis, taking into account power depos- ition by auxiliary heating, collisional equipartition and radi- ated power. In QuaLiKiz, TEM and ITG are included.

It is found that high Z with argon injection is beneficial to stabilize TEM (figure 3) due to its higher charge and heavier mass.

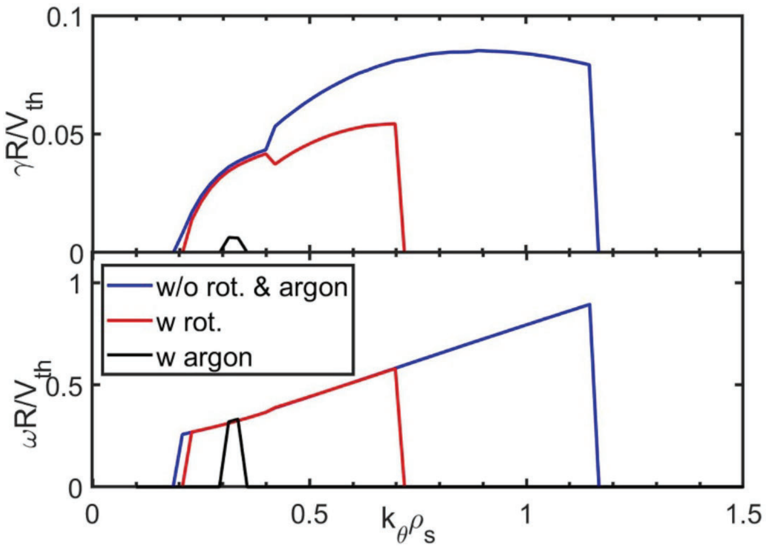

Figure 3 Normalized growth rate and frequency spectra of TEM versus $k_\theta \rho_s$

These findings and analysis may help those discharges with RF dominant heating discharges to improve the core ion temperature in EAST. More experiments with different impurities and modeling will be carried out in the near future.

国際化推進共同研究概要

No.9

23NU-5

タイトル： Joint study of long pulse high beta discharges and related edge turbulence transport in steady state operation (SSO) plasmas on QUEST and EAST

研究代表者： GAO Xiang

所内世話人： 花田　和明

研究概要：２３年度のトピックスとして本共同研究を含めた多くの共同研究を通じて世界最長のＨモード（403秒、Tungsten　Divertor、LHCD at 1.6MW and ECRH at 1.7MW. H98（y2）>1.3, fGr ~0.7, 入射トルク０、βP～2.5,　βN～1.5,fBS>50%,　Small　ELM　(fELM >2.5kHz)）が達成された。この際に fishborn タイプの不安定性がプラズマ中心部の q 分布の平坦化に寄与して、結果的に ITB の維持につながっている。一方、タングステンのプラズマ中心への蓄積が観測され、トロイダル回転と密度ピーキングによる新古典インワード対流とピンチ効果が主なタングステン蓄積の原因であることが確認された。この結果は all タングステン壁での実験を目指す QUEST での実験の際にも重要な知見となると考えられる。

国際共著論文発表

[1] Yunfei Wang, <u>Kazuaki Hanada</u>, Haiqing Liu, <u>Xiang Gao</u> et al., ″ Hot spots induced by RF-accelerated electrons in the scrape-off layer on Experimental Advanced Superconducting Tokamak ″, Nuclear Fusion　(2023). DOI 10.1088/1741-4326/acb726

本研究とは直接関係しない国際共著論文発表

[2] Yunfei Wang, <u>Kazuaki Hanada</u>, ……, <u>Xiang Gao</u>, et al., “Phase jump detection and

correction based on the support vector machine", Plasma phys. Control fusion, 2023, https://doi.org/10.1088/1361-6587/accaa2.

国際会議発表

[1] X. Gao*, ……, H.Q. Liu,……, K. Hanada and the EAST team., ″ Tungsten transport and its Effect on the Pedestal in EAST Hybrid Plasmas ″, 41st ITPA meeting of PEP Group, April 24-28, 2023

[2] X. Gao*, ……, H.Q. Liu, K. Hanada, ……, and the EAST team., ″ Tungsten transport in hybrid discharges on EAST tokamak ″, 10th Asia Pacific-Transport Working Group Meeting, June 13-16, 2023 Hanyang University, Seoul, Korea.

[3] K. Hanada, ……, X. Gao, H.Q. Liu, J. Qian, Jie,…… "Recovery from wall saturation using temperature control of plasma facing wall on QUEST" IAEA Fusion Energy Conference, 2023.10 London, UK

（様式 11・拠点）

RESEARCH REPORT

Date: March 7　2023

Visiting scientists: (name) Xiang Gao

(position) Professor

(university / institute) Institute of Plasma Physics,

Chinese Academy of Sciences

Host scientist: (name) Kazuaki Hanada

(position) Professor

(university / institute) Kyushu University

Research period: (from) March 12 2023 (to) March 16 2024

Research subject: **Joint study of long pulse high beta discharges and related edge turbulence transport in steady state operation (SSO) plasmas on QUEST and EAST**

Introduction

Steady state operation (SSO) of tokamak plasma is one of the basic requirements for future fusion reactors. Long pulse high beta operation is one of important missions for ITER. Joint study long pulse high beta discharges in SSO plasma research field on QUEST and EAST is strongly supporting ITER experiment from both experience and theory. In 2023, the collaboration research continue focused on the power balance in SSO high performance discharge and coupling of injected energy and plasma during discharge, which is benefit for the SSO high beta discharges of EAST and QUEST. A steady-state plasma with a world-record pulse length of 403 s H mode plasma was obtained, where the density and the divertor peak heat flux were well controlled, with no core impurity accumulation.

With this visit, I will also give an annual summary presentation of “Hybrid plasma and tungsten transport on EAST tokamak”, which introduced the recent results hybrid plasma physics study on EAST and to discuss with our QUEST collaborators.

New results in 2023-2024

EAST-Highlights: 403-second Reproducible H-mode

Record Duration of 403-second Reproducible H-mode Plasma Achieved with Tungsten Divertor on EAST, as shown in figure 1. To access this steady state long-duration H-mode plasmas, experiments have been performed in using LHCD at 1.6MW and ECRH at 1.7MW. $H_{98}y2$ >1.3, f_{Gr}~0.7, zero injected torque β_P~2.5, β_N ~1.5, f_{BS}>50%, Small ELM (fELM >2.5kHz) with negligible transient heat load. Robust iso-flux control with SP to W-divertor. It is a new milestone in Fusion community.

The operation regime was extended in last year. Enable investigation on key physics (core turbulence, MHD, stability…) in ITER-like condition, as shown in figure 2.

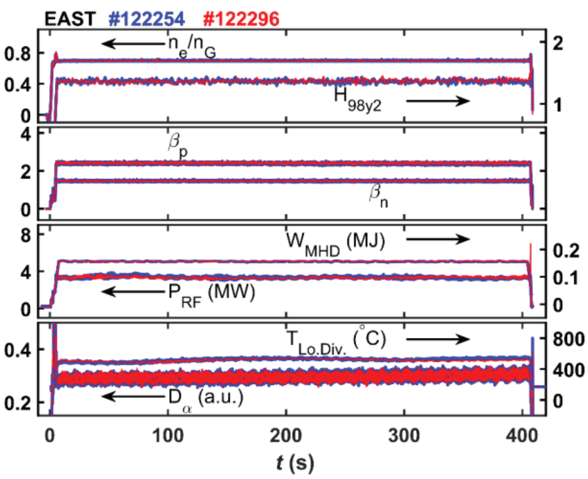

Fig. 1. Waveform of the 403s reproducible H-mode discharge #122254 and #122296

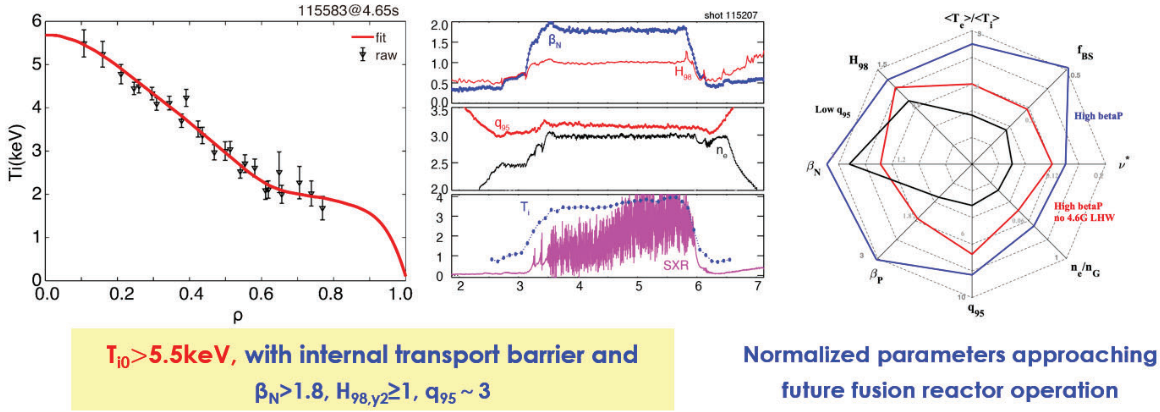

Fig. 2. The operation regime was extended

Fig. 3 represents Tungsten transport and its Effect on the Pedestal in EAST Hybrid Plasmas. The poloidal asymmetry of tungsten impurity due to larger toroidal rotation velocity can enhance the neoclassical pinch of heavy impurities, then leading the central heavy impurities accumulation between 2.6 s and 3.4 s.　The W emission decreases gradually when counter-NBI injected at 3.5s and the toroidal rotation velocity decrease gradually.

Fig. 4 represents From 4.3 s to 4.7 s, the core density increase with almost the same edge electron density, where the toroidal rotation velocity is only 50 km/s.　The W content starts to increase slowly from 4.35 s. The increase of the Mo31+ and Fe22+ emission lines diagnosed by EUV can be observed during the period of increased central electron density (4.3–4.7 s), which does not appear before 4.3 s. The light impurity C (carbon) also starts to accumulate even earlier than the Fe22+. These results show that the peaking of electron density and improved particles confinement maybe play an important role in both the heavy and light impurities accumulation. The simulation reproduces the experimental observations of W accumulation and identifies that neoclassical inward pinch by the toroidal rotation and turbulence suppression by the large density peaking of the bulk plasma are the main reasons for the W accumulation respectively. Pedestal density increased during tungsten accumulation from 3.2s to 3.4s
No change at ELM frequency during tungsten accumulation.

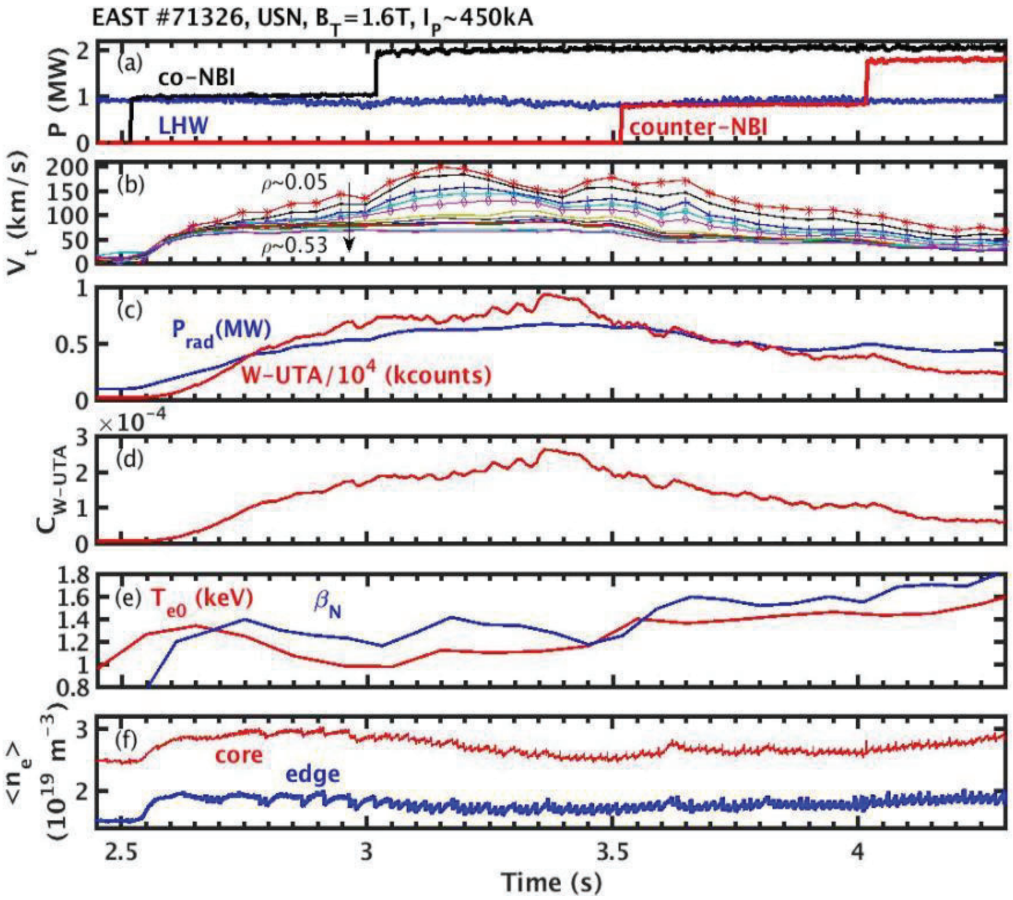

Fig. 3. The poloidal asymmetry of tungsten impurity due to larger toroidal rotation velocity can enhance the neoclassical pinch of heavy impurities

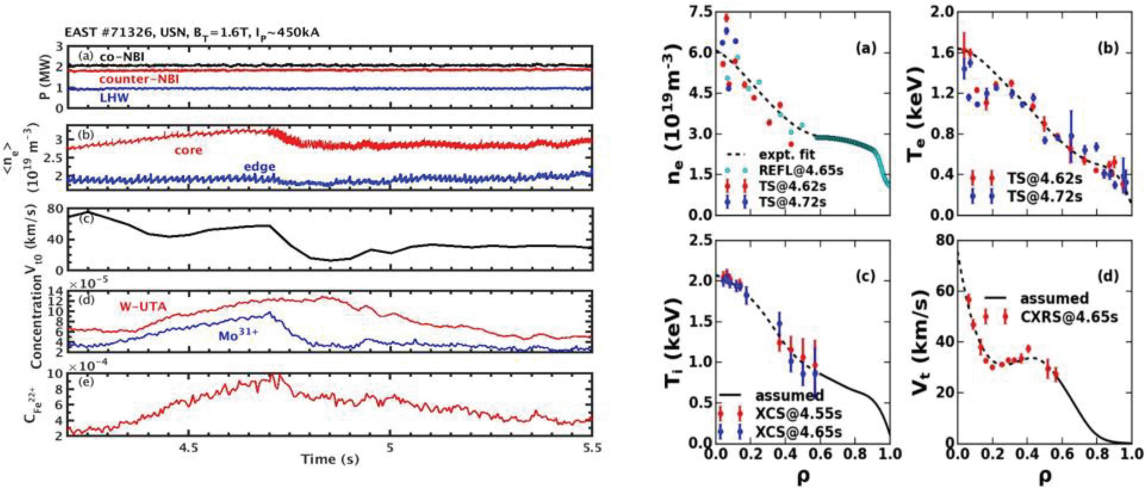

Fig. 4. Tungsten transport in EAST hybrid discharge

Summary

Partly support with this joint research, record Duration of 403-second Reproducible H-mode Plasma Achieved with Tungsten Divertor on EAST, the operation regime was extended on EAST in last year and tungsten transport in EAST hybrid discharge was studied in detail. Experiments of hybrid operational scenario have been carried out on EAST tokamak with ITER-like tungsten (W) divertors recently. In the hybrid H-mode plasma, the internal transport barrier (ITB) has been obtained with central flat q prfile and it is found that the fishbone mode(m/n=1/1) can be beneficial to sustain the central flat q(0）=1 profile with a stable ITB. The behavior of W in the core of hybrid plasma scenario on EAST with ITER-like divertor is studied. W accumulation is often observed and seriously degrades the plasma performance. It is found that the toroidal rotation and density peaking of the bulk plasma are usually large in the central region, which is particularly prone to the W accumulation. The simulation reproduces the experimental observations of W accumulation and identifies the neoclassical inward convection/pinch velocity of W due to the large density peaking of the bulk plasma and toroidal rotation in the central region as one of the main reasons for the W accumulation. These results will be compared with QUEST results and made further analysis during my stay.

Acknowledgement and comments:

Work supported by the international joint research at the Joint Usage of Research Centers for Applied Mechanics for 2023. I would like to thank our host, Professor K. Hanada. We hope that the international joint research at the Joint Usage of Research Centers for Applied Mechanics could continue to enhance China-Japan cooperation on fusion plasma research in the future.

My Co-Publications in 2023-2024:

[1] Yunfei Wang, Kazuaki Hanada, Haiqing Liu, Xiang Gao et al., " Hot spots induced by RF-accelerated electrons in the scrape-off layer on Experimental Advanced Superconducting Tokamak ", Nuclear Fusion (2023). DOI 10.1088/1741-4326/acb726

[2] Yunfei Wang, Kazuaki Hanada, ……, Xiang Gao, et al., “Phase jump detection and correction based on the support vector machine”, Plasma phys. Control fusion, 2023, https://doi.org/10.1088/1361-6587/accaa2.

[3] X. Gao*, ……, H.Q. Liu,……, K. Hanada and the EAST team., " Tungsten transport and its Effect on the Pedestal in EAST Hybrid Plasmas ", 41st ITPA meeting of PEP Group, April 24-28, 2023

[2] X. Gao*, ……, H.Q. Liu, K. Hanada, ……, and the EAST team., " Tungsten transport in hybrid discharges on EAST tokamak ", 10th Asia Pacific-Transport Working Group Meeting, June 13-16, 2023 Hanyang University, Seoul, Korea.

(Signature)______________________________

(Name in print) Xiang Gao

国際化推進共同研究概要

No.10

23NU-6

タイトル： The research on the confinement and loss mechanism of alpha particle through the research of energetic electron on QUEST

研究代表者： JIE Yinxian

所内世話人： 花田　和明

研究概要： α粒子の損失は将来の核融合炉である CFETR（中国）や Japan DEMO（日本）の性能に大きくかかわる課題である。現在は高速イオンの閉じ込めを実際に得られた QUEST 配位で軌道計算している段階である。p—B 核融合にも活用可能な 400keV の高速イオンの軌道を実際の QUEST で得られたプラズマ配位からトロイダル磁場やプラズマ電流を変えて種々計算している最中である。軌道計算は順調に進んでおり、この結果を受けて次はα粒子の軌道計算を行っていく予定である。

ホットスポットの形成理由については EAST では入射した LHW が SOL で衝突吸収されることで起こることが分かっており、2.45GHz のシステムよりは 4.6GHz の方が優れている。ホットスポットを回避しながらコアへの有効な加熱を増やすためには 4.6GHz でのパワー入射が推奨され、EAST では 4.6GHz でのパワー入射を増やす方向で実験が進んでいる。

国際会議発表

[1] K. Hanada, ……, X.　Gao, H.Q.　Liu, J. Qian, Y.　Jie,…… "Recovery from wall saturation using temperature control of plasma facing wall on QUEST" IAEA Fusion Energy Conference, 2023.10 London, UK

RIAM JOINT RESEARCH REPORT SUMMARY (English Form)

1. Research ID: No.10 _23NU-6
2. Research Title: The research on the confinement and loss mechanism of alpha particle through the research of energetic electron on QUEST
3. Category: International
4. Applicant

Affiliation: Institute of Plasma Physics, Chinese Academy of Sciences

Name: Yinxian Jie

5. RIAM Attendant: K. Hanada
6. Summary (150~200 words in Japanese or 100~150 words in English):

After COVID-19 pandemic，this year we worked on QUEST in site from March 1 2023 to March 8 2023. Though the Research Title was “the research on the confinement and loss mechanism of alpha particle through the research of energetic electron on QUEST” , but the real work was : discussing the paper “Hot spots induced by RF-accelerated electrons in the scrape-off layer on Experimental Advanced Superconducting Tokamak” by Mr. Yunfei Wang.

Preventing impurity emission from hot spots on plasma-facing materials is a critical issue in the maintenance of high-performance plasma on the Experimental Advanced Superconducting Tokamak (EAST). In this study, experimental and theoretical analyses were performed to investigate the mechanism of hot spot formation.

*) Submit either one of Japanese or English forms.

Research subject: The research on the confinement and loss mechanism of alpha particle through the research of energetic electron on QUEST

I discussed the paper in details with Mr.Yunfei Wang. And the paper “Hot spots induced by RF-accelerated electrons in the scrape-off layer on Experimental Advanced Superconducting Tokamak” by Mr. Yunfei Wang has published in Nucl.Fusion.

Preventing impurity emission from hot spots on plasma-facing materials is a critical issue in the maintenance of high-performance plasma on the Experimental Advanced Superconducting Tokamak (EAST). In this study, experimental and theoretical analyses were performed to investigate the mechanism of hot spot formation. Experiments on plasma configuration control indicated that the reduction in the gap between the lower (secondary) separatrix and lower hybrid antenna is effective in preventing hot spot formation on the lower divertor, which frequently emits impurities in long-duration discharges.

This effectiveness was quantitatively confirmed by magnetic field lines tracking simulation and calorimetric measurement of divertors in the experiment. Two-frequency power modulation of the lower hybrid wave (LHW) was conducted to evaluate power deposition on the scrape-off layer (SOL) during propagation from the LHW antenna to the main plasma. This experiment clarified that LHW-accelerated electrons in the SOL via collision damping deliver their energies to hot spots along the magnetic field line. These findings help alleviate or even liminate the formation of hot spots and maintain the performance of plasma.

Hot spots are caused by the excessive localized heat load on the PFCs. Although hot spot formation must be avoided, hot spots often appear on the divertors, main limiter, and LHW guarding limiter during discharges in the EAST. In this study, we investigated the mechanisms underlying the hot spot formation on the lower divertor during the EAST 2017 campaign and found that two factors, namely the magnetic configuration in the SOL and the energy deposition of the LHW in the SOL, played an important role in hot spot formation. By slightly changing the SOL plasma configuration, the hot spot on the lower divertor was effectively alleviated. This helped achieve a record of steady-state H-mode plasma in the EAST for 101.2 s. Experiment analyses and GENRAY/CQL3D simulations showed that the two LHWs had different plasma heating and current driving efficiencies in the main plasma owing to their different frequencies; the LHW at 2.45 GHz likely deposits more energy than the LHW at 4.6 GHz in the SOL through collision damping, which leads to hot spot formation in the LHW modulation experiment.

The findings of this study provide two primary insights. First, reduce the auxiliary heating power (such as LHW) deposition in the SOL. This part of the energy directly contrib utes to the heat load of related PFCs that are magnetically connected from the SOL. Therefore, efforts to increase the auxiliary heating power deposition in the core plasma for heating and current driving are needed. This will improve the confinement performance of the plasma and reduce the cost-of-energy of the fusion device. Second, the heat load between different PFCs can be redistributed by slightly adjusting the magnetic configuration in SOL. This can be used to alleviate excessive heat load on a particular PFC, thus avoiding problems, such as impurity emission and subsequent plasma degradation. In the near future, the EAST aims to realize a higher performance plasma operation with higher power injection; there fore, it is important to achieve full FoV detection for PFCs on the EAST to monitor the condition of PFCs, including hot spots. Besides, the mechanism of association between the LHW and plasma should be further investigated to improve the efficiency of plasma heating and current driving through the LHW to achieve lengthier H-mode operations and noninductive current driving. These results have potential applications in exploring advanced operating modes on CFETR in China and ITER.

(Signature) Y. Jie

(Name in print) Yinxian Jie

国際化推進共同研究概要

No. 11

23NU-7

タイトル： Joint study of calorimetric measurement of heat load and power balance estimation and measurement and simulation of energetic electrons loss in steady state operation (SSO) plasmas on QUEST and EAST

研究代表者： LIU Haiqing

所内世話人： 花田　和明

研究概要： これまでの共同研究で、中国の超伝導トカマク EAST に SSO 時のパワーバランス計測用の流量計と水温測定器を設置している。下側ダイバータがタングステンに交換される前当時の世界最長のＨモードショットを得るために行われた一連の調整放電での熱負荷を解析し、下側ダイバータに形成される Hot spot が SOL 領域でのＬＨ波の衝突吸収が原因であることを見出した。2023 年度には適切な量のネオンを注入した際に負磁気シア配位が形成され、その結果として電子スケールの揺動の抑制が観測され、電子温度の上昇に伴う高パフォーマンスプラズマが生成していることを POINT システムと CO2 レーザーによる協同トムソン散乱計測から明らかにした。QuaLiKiz による計算で、ネオン注入と負磁気シアの効果が重畳されていることがわかった。

国際共著論文

[1] Yunfei Wang, Kazuaki Hanada, Haiqing Liu, Xiang Gao et al., ″ Hot spots induced by RF-accelerated electrons in the scrape-off layer on Experimental Advanced Superconducting Tokamak ″, Nuclear Fusion (2023) Accepted manuscript online. DOI 10.1088/1741-4326/acb726

[2] Yunfei Wang, Kazuaki Hanada, ……, Haiqing Liu, et al., “Phase jump detection and correction based on the support vector machine”, Plasma phys. Control fusion,

2023, https://doi.org/10.1088/1361-6587/accaa2.

[3] Chu Y Q, Zhang S, Li P, ……, H.Q. Liu, ……, K. Hanada and the EAST team. Observation of electron-scale turbulence suppression under weak magnetic shear with neon seeding in EAST plasma[J]. Nuclear Fusion, 2023, 63: 086021.

国際会議発表

[1] K. Hanada, ……, X. Gao, H.Q. Liu, J. Qian, Jie,…… “Recovery from wall saturation using temperature control of plasma facing wall on QUEST” IAEA Fusion Energy Conference, 2023.10 London, UK

（様式 11・拠点）

RESEARCH REPORT

Date: March 7 2024

Visiting scientists: (name) **Haiqing LIU**

(position) **Professor**

(university / institute) **Institute of Plasma Physics,**

Chinese Academy of Sciences

Host scientist: (name) **Kazuaki Hanada**

(position) **Professor**

(university / institute) **Kyushu University**

Research period: (from) March 12 2024 (to) March 16 2024

Research subject: Joint study of calorimetric measurement of heat load and power balance estimation and measurement and simulation of energetic electrons loss in steady state operation (SSO) plasmas on QUEST and EAST

Introduction

Maintaining long-pulse steady-state operation of plasma is one of the crucial prerequisites for achieving commercial fusion energy in the near future. Both the QUEST and EAST tokamaks possess the capability to sustain plasma long-pulse steady-state operation, serving as excellent experimental platforms for relevant research. One of the main focuses of collaborative research this year is to explore the causes of hot spot formation. Through experimental data and simulation analysis, two results have been obtained: firstly, changes of the magnetic configuration in the scrape-off layer (SOL) have a significant impact on the hot spot formation, and the appearance of hot spots is accompanied by a great change of heat load distribution between different plasma-facing components (PFCs). Secondly, the LHW can deposit energy to electron in the SOL through the collision damping, these electrons move along the magnetic field lines then attack the PFCs, cause the hot spot formation.

The enhancement of plasma confinement is highly important for sustaining long-pulse steady-state plasma operation and improving the economic viability of fusion power generation. A new study of ‘Ne injection with improved confinement’ has been performed on EAST. Ne injection with a finite rate can change the equilibrium with reversed magnetic shear of the plasma and promote improvement of the confinement.

With the continuous development of artificial intelligence algorithms and the rapid advancement of computing power, the field of AI has experienced rapid growth in recent years, as exemplified by ChatGPT, and is increasingly being applied in scientific research. Magnetic confinement fusion research inherently possesses massive datasets, making it highly suitable for integration with machine learning (ML). Another collaborative research endeavor this year is ‘phase jump detection and correction based on the support vector machine’, representing an attempt to integrate machine learning with fusion research. The POINT system on EAST has measured a large amount of chord-integrated electron density data, which can be categorized into two types: normal data and anomalous data caused by fringe jumps. By identifying classification features, ML algorithms automatically determine feature boundaries, thereby detecting the fringe jump data from the database. This approach has yielded promising results.

During this visit, I will also give an annual summary presentation which introduced the recent results and progress of the steady state operation and physics research on EAST and to discuss with our QUEST collaborators.

.

Recent results in 2023-2024

Preventing the emission of impurities from hot spots on PFCs represents a crucial challenge in maintaining high-performance plasma on the EAST. This study conducted experimental and theoretical analyses to investigate the mechanism underlying hot spot formation. Experimental investigations into plasma configuration control revealed that reducing the gap between the secondary separatrix and the LHW antenna effectively mitigates hot spot formation on the divertor. This effectiveness was quantitatively confirmed through magnetic field lines tracking simulations and calorimetric measurements of divertors in the experiment. Figure 1 shows the hot spot gradually formed on the lower divertor, on the 101.2 s long-pulse H-mode discharge, #73 999, in the 2017 campaign. The zero drift of the magnetic measurement system resulted in small, persistent changes of the plasma configuration during discharges, which cause the hot spot formation.

Additionally, two-frequency power modulation of the LHW was implemented to assess power deposition on the SOL during propagation from the LHW antenna to the main plasma. This experimentation elucidated that LHW-accelerated electrons in the SOL, via collision damping, transfer their energies to hot spots along the magnetic field line. These findings contribute to the mitigation or potential elimination of hot spot formation, thereby supporting the maintenance of plasma performance.

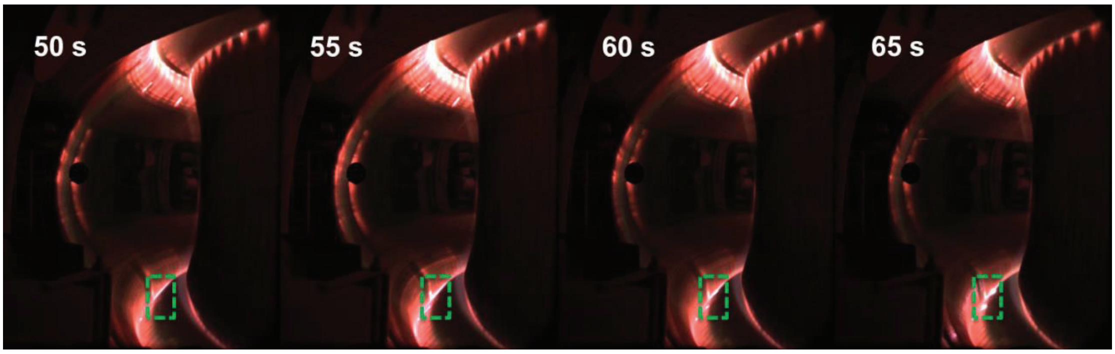

Figure 1. Photographs of the EAST discharge #73 999 at 50 s, 55 s, 60 s, and 65 s obtained using a visible-light camera. The hot spot gradually formed.

The effect of Ne injection on improved plasma confinement is investigated in the EAST. A series of Ne injection experiments were conducted, wherein the safety factor q profile and electron-scale turbulence were examined using the POINT system and a CO_2 laser collective scattering system. It was found that Ne injection at an appropriate rate can induce negative magnetic shear in the plasma core, thereby suppressing electron-scale turbulence. Moreover, continuous Ne injection under reversed shear conditions further decreases the intensity of electron-scale turbulence, leading to an increase in core electron temperature and improvement in confinement. The QuaLiKiz model is employed to simulate the impact of impurity and reversed q on turbulence. The combined effects of negative magnetic shear and Ne injection on turbulence suppression surpass the inherent effect of the impurity alone, which potentially elucidates the observed increase in electron temperature and turbulence suppression. Furthermore, the relationship between pedestal structure induced by Ne injection and LHW-driven current deposition is discussed. These findings offer a novel perspective for enhancing confinement through Ne injection, suggesting the adjustment of Ne injection to modify the ideal plasma equilibrium.

Figure 3 shows the evolution of turbulence with Ne injection in step 2. In step 2, all electron-scale turbulence in the interval is further suppressed, the maximum reduction of integrated turbulence power is half. And the average reduction ratio is about 30%, which is higher than that outside the interval. Turbulence suppression in step 1 and step 2 may be the reason of Te increase in step 2.

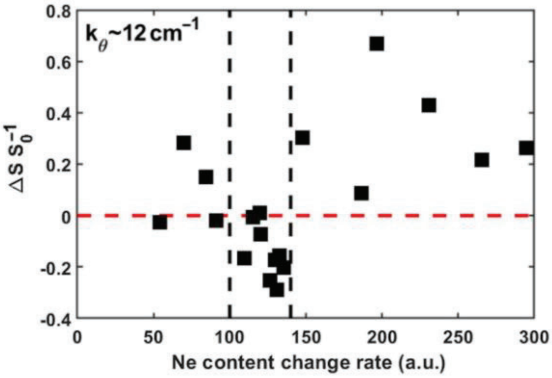

Figure 2. Relation of Ne content change rate to relative variation of turbulence amplitude with $k_\theta = 12$ cm^{-1} at step 1. Here, $\Delta S = S_1 - S_0$, where S_1 and S_0 are the amplitude of turbulence measured by CO_2 system at the end and beginning of step 1.

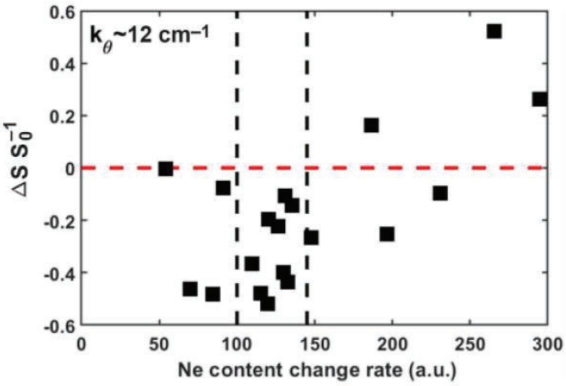

Figure 3. Relation of Ne content change rate to relative variation of turbulence amplitude with $k_\theta = 12$ cm^{-1} at step 2. Here, $\Delta S = S_1 - S_0$, where S_1 and S_0 are the amplitude of turbulence measured by CO_2 system at the end and beginning of step 2.

Interferometers are commonly utilized for electron density measurements in magnetically confined plasma. These measurements entail comparisons of phase shift variations between the probe and reference laser beams. The plasma electron density ideally exhibits continuous variation during discharge, the fringe jump is a step-like change of the apparent electron density caused by a sudden jump of the measured phase shift. Such fringe jumps can significantly compromise the accuracy of interferometric measurements. This study addresses the fringe jump issue in the POINT system of the EAST by introducing a support vector machine model for electron density fringe jump correction. The proposed model effectively distinguishes fringe jump data from raw measurement data, demonstrating robustness against noise and interference, and subsequently rectifies the jump. This model markedly enhances the efficiency and precision of electron density data correction derived from the POINT system in EAST. Integration of this model into the plasma control system is anticipated to enable more accurate real-time electron density feedback control. One example to demonstrate the performance of fringe jump detection and correction by the support vector machine model is shown in figure 4. In this figure, all 23 fringe jumps in chord 8 were detected and corrected. With the advantage of multi-chord measurement of the POINT system, the accuracy of the corrected line-integrated electron density can be confirmed by using the measurement data of two adjacent chords in space. Further, the electron density profile can be calculated by using the corrected electron density data.

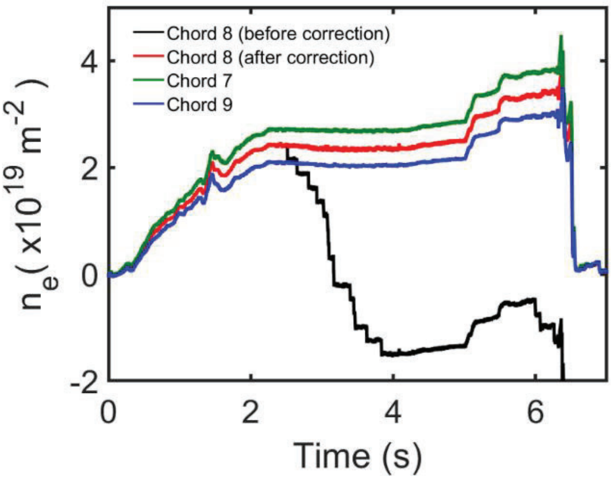

Figure 4. Apparent line-integrated electron density measured by the chord 7 (green), 8 (black), and 9 (blue) of the POINT system for discharge 80142, and the corrected electron density for the chord 8 (red).

Discussions

The collaborative research this year continues to focus on the plasma long-pulse steady-state operation and achieve good results, which include two parts, avoiding excessive local heat loads on the PFCs and improving plasma confinement through neon seeding. Both two topics conducive to achieving plasma long-pulse steady-state operation. The study of avoiding excessive local heat loads on the PFCs is conducted by Dr. Wang Yunfei, Prof. Hanada's doctor student, with whom I have engaged in many fruitful discussions. The findings of this study yield two principal insights. Firstly, mitigating the auxiliary heating power deposition in the SOL is crucial. A substantial portion of this energy directly contributes to the heat load on the PFCs. Hence, endeavors to enhance the deposition of auxiliary heating power within the core plasma for both heating and current drive purposes are warranted. This approach will enhance plasma confinement performance and reduce the cost-of-energy associated with fusion devices. Secondly, redistribution of heat load among different PFCs can be achieved by making slight adjustments to the magnetic configuration within the SOL. This strategy can effectively alleviate excessive heat loads on specific PFCs, thereby forestalling issues such as impurity emission and subsequent plasma degradation.

The research on 'electron-scale turbulence suppression under weak magnetic shear with neon seeding' is performed by Dr. Chu Yuqi, my doctor student. In this study, a new perspective on impurity injection-induced confinement improvement is presented. For the ITER-like RF heating tokamak, equilibrium reestablishment by impurity injection should be considered. Maximizing the beneficial effect of impurity injection and allowing it to be dominant in front of the deleterious effects of impurity injection could help us to promote better plasma confinement. To promote rather a positive impact of impurities on fusion power, it is necessary to further study the influence of impurity injection on the pedestal and the influence of impurity injection on turbulence suppression. Exploring suitable impurity injection methods is important for future fusion devices.

Building upon this foundation, we have also explored the integration of machine learning into the field of fusion, yielding promising results. This part of research is completed by Dr. Wang Yunfei, utilizing measurement data from POINT provided by EAST. This study introduces a novel ML-based method for electron density fringe jump correction for the POINT system of the EAST tokamak. This method automatically identifies and rectifies fringe jump data from the digital phase demodulator output, offering high accuracy and robust noise tolerance, thereby notably enhancing the efficiency of post-processing data from the POINT system. Furthermore, this method extends beyond specific discharge devices and interferometer diagnostics, rendering it applicable to interferometer systems in diverse fusion devices. Consequently, this algorithm holds considerable promise for fusion data processing applications. This model can be further enhanced and incorporated into the real-time electron density feedback control algorithm of the Plasma Control System.

During this stay, I was also discussed with Prof. Hanada and Prof. Ido under this international joint research frame. And we will make new co-proposals in the next EAST experimental campaign. We will continue to study the power balance (particle balance) estimation in steady state operation (SSO) plasmas on QUEST and EAST.

Acknowledgement and comments:

Work supported by the international joint research at the Joint Usage of Research Centers for Applied Mechanics for 2023. I would like to thank our host, Professor K. Hanada. We hope that the international joint research at the Joint Usage of Research Centers for Applied Mechanics could continue to enhance China-Japan cooperation on fusion plasma research in the future.

Co-publication list of the joint usage / research in 2023-2024:

[1] Wang Y, Hanada K, Liu H, et al. Hot spots induced by RF-accelerated electrons in the scrape-off layer on Experimental Advanced Superconducting Tokamak[J]. Nuclear Fusion, 2023, 63: 056001.

[2] Chu Y Q, Zhang S, Li P, et al. Observation of electron-scale turbulence suppression under weak magnetic shear with neon seeding in EAST plasma[J]. Nuclear Fusion, 2023, 63: 086021.

[3] Wang Y, Hanada K, Sakurai D, et al. Phase jump detection and correction based on the support vector machine[J]. Plasma Physics and Controlled Fusion, 2023, 65: 065001.

[4] X. Gao*, ……, H.Q. Liu,……, K. Hanada and the EAST team., " Tungsten transport and its Effect on the Pedestal in EAST Hybrid Plasmas ", 41st ITPA meeting of PEP Group, April 24-28, 2023

[5] X. Gao*, ……, H.Q. Liu, K. Hanada, ……, and the EAST team., " Tungsten transport in hybrid discharges on EAST tokamak ", 10th Asia Pacific-Transport Working Group Meeting, June 13-16, 2023 Hanyang University, Seoul, Korea.

(Signature)______________________________

(Name in print) Haiqing Liu

国際化推進共同研究概要

No. 12

23NU-8

タ イ ト ル : Identifying flow patterns in a linear magnetized plasma experiment

研究代表者 : KNAUER Stefan

所内世話人 : 文　贊鎬

研 究 概 要 :

　この研究では、線形磁化プラズマ内部のフラックスの二次元スキャンを測定し、その中でリターンフローと高圧力の相関を調査しました。特に、磁場を変化させることでリターンフローの挙動と高圧力の変化を詳細に検討しました。これにより、ソース半径を超えた領域における未知の流れの存在を予測しました。従来までは、高圧力や高磁場の領域についてのデータが不足しており、さらにソース半径を超える領域についての情報が欠如していました。したがって、本研究では、線形プラズマ内の粒子フラックスに関する洞察を得ることを目指しました。

Identifying flow patterns in a linear magnetized plasma experiment

KNAUER, stefan; University of Greifswald, Physics department; Researcher
Grant number 12_23NU-8

Abstract

Two-dimensional scans of the flux inside a linear magnetized plasma will be measured. To investigate the return-flow higher pressures at varying magnetic fields will be investigated. Unrecorded flows are expected beyond the source radius. Preliminary studies do not cover high pressures and/or high magnetic fields, additionally no data is present beyond the sources radius. Thus a wider radial area will be investigated. Ideally this data will give further insight into the particle flux of linear plasmas, although the return-flow might mainly consist of neutral particles. For this a related study with the tomography system will gain information even about neutral particles. The comparison of both approaches can be used to gain 2D information of the flux inside the entire chamber, although the tomography system only covers a region close to the source.

Purpose

Flows in a linear plasma device are driven by density gradients. They are expected to be results of different kind of turbulence, like drift-wave turbulence or Kelvin-Helmholtz instabilities. The measurement of the flux can be utilized to gain information about the underlying phenomena and develop theories about their formation. This was already used in PANTA at RIAM to develop the concept of cross-ferroic turbulence [1]. Further investigations of the flux were done by [2] suggesting behaviour with changing plasma parameters. We aim to deepen the understanding of the flow inside a linear magnetized plasma such as PANTA. The unique tomography system at PANTA [3] offers the chance to compare 3D flux data with conventional probe techniques. The proponents from the University of Greifswald are already familiar with the set up and desire to continue the cooperation with RIAM.

Experimental method

The PANTA experiment consists of a NAGOYA-III antenna, an approximately 4m long and 45cm in diameter vacuum vessel, 17 coils to create the magnetic field and a Langmuir probe array with 64 radially aligned probes see fig. 1. All experiments were supervised by Prof. Dr. Chanho Moon and performed by the team from University of Greifswald and RIAM together. The current generating the magnetic field is adjustable. Magnetic field strengths B=30-150 mT were utilized. Experiments were carried out with an argon pressure in the range of p_{Ar}=0.26–0.66 Pa and a power range P = 0.2–5kW and heating frequency of 5–10 MHz. As the mach-probes dedicated to measure the flux were unavailable during our stay we instead improved the ground work for this research. We deepened the understanding of phase transitions [4] and the development of turbulence [5]. To this end the magnetic field was varied, to generate different drives for turbulence. We enhanced the evaluation of the plasma profiles by the usage of a 5Ch-probe, which was moved for each measurement to yield high-resolution profile data. In addition a 64-channel Langmuir probe array [6] was utilized to measure current and potential in radial direction.

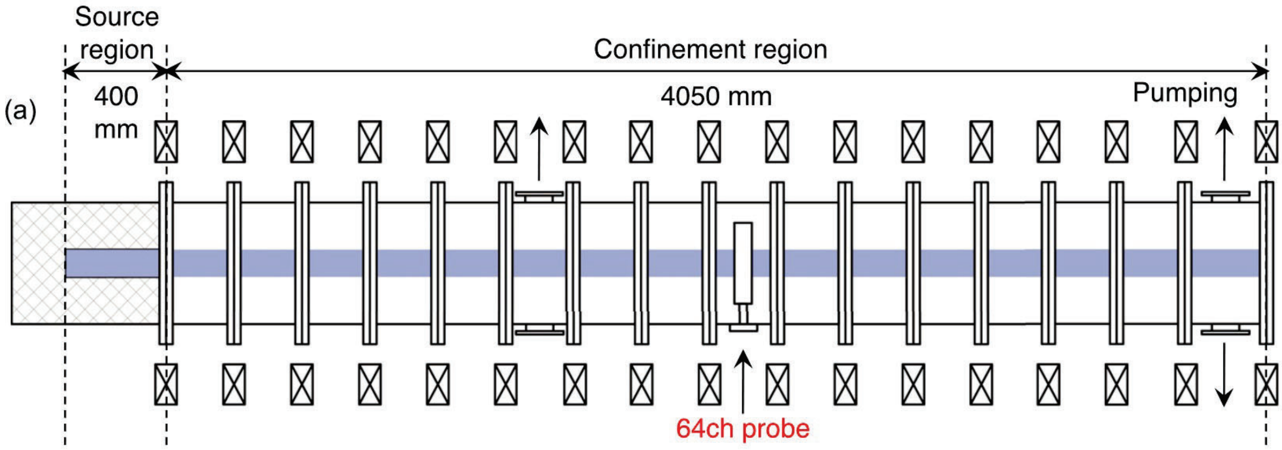

Figure 1: Scheme of the PANTA experiment. Source at the left, termination plate at the right. Crossed boxes indicate field coils. The utilized probe array is placed approximately in the center.

Experimental results

Density and temperature

At first we measured the profile of the plasma column. It was meant to yield the density of the discharge and to find a critical magnetic field [7], which depends on the discharge parameters. Example densities for varying parameters at different radial positions are shown in fig. 2. We are excited to share the findings from our series of measurements, they are in good agreement with both: formerly reported values at PANTA and threshold values known as helicon discharges. All profiles resemble an expected Gaussian distribution around the center, with the steepest region at a radial position of around 2 cm, which is a valuable insight. For varying pressures and magnetic fields different shapes and maxima of the profile were observed, which is also in agreement with preliminary expectations.

Furthermore investigating the profile distributions high at the center and depicting it against the magnetic field is shown if fig. 3. There a critical magnetic field can be observed at 60 and 70 mT respectively, which are novel results for PANTA.

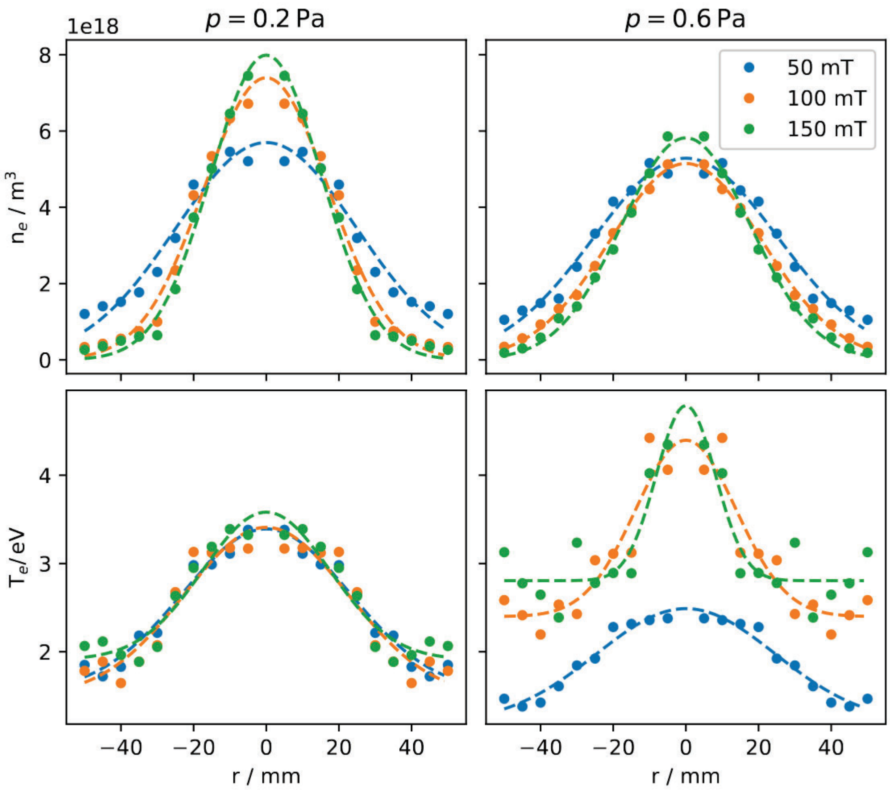

Figure 2: Example radial profiles of n_e (upper row) and T_e (lower row) measured by a sweeping Langmuir probe. The columns represent two pressures: 0.2 Pa and 0.6 Pa, as given in their title. The magnetic field is displayed as different colors, which is the same for each subplot. A Gaussian distribution is assumed for each graph and the respective fit is displayed as a dashed line with the same color. The rows and columns share their abscissa and ordinate, respectively

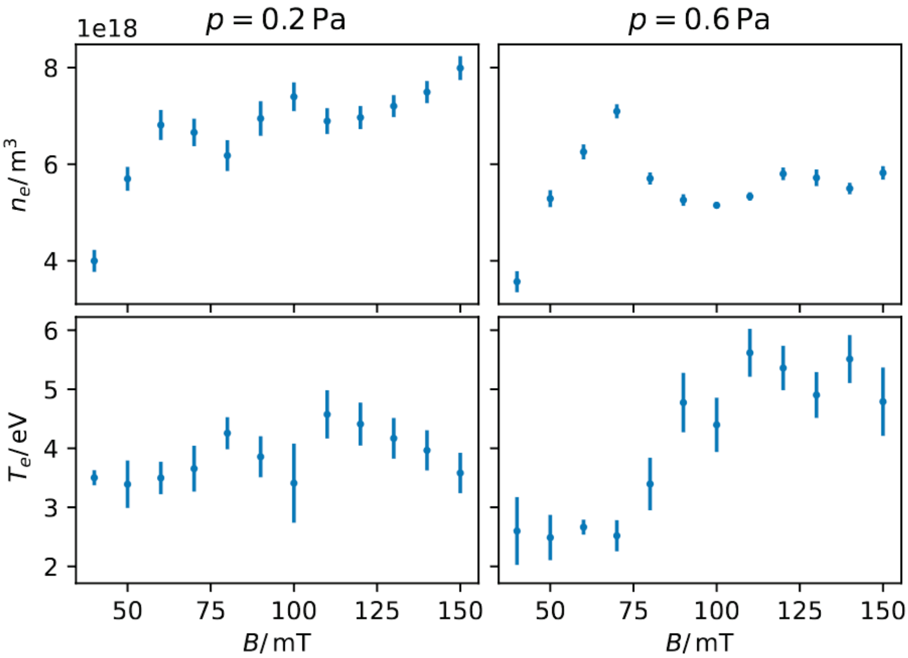

Figure 3: Plasma parameters determined by taking the maximum in fig. 1 plotted against the magnetic field. The columns represent two pressures: 0.2 Pa and 0.6 Pa, as given in their title. Rows show the electron density n_e and electron temperature T_e. The rows and columns share their y-axis and x-axis respectively.

Frequency and wavenumber spectra

To measure turbulence frequency and wavenumber spectra can be utilized. In double logarithmic presentation, regions that drive the turbulence appear as a kink. It is a measure of where the turbulence gets its energy from. While some of the behavior is similar to fluid turbulence, the low frequencies can also stimulate density fluctuations in a plasma. Thus the drive regions are not as localized. Fig 4 shows the respective spectra for I_s and V_{fl}. Our research and evaluation of the graphs is still on-going. However the data is most promising, as each graph shows the expected kink and expected behavior. The scaling of I_s and V_{fl} is also very promising and shows expected behaviour.

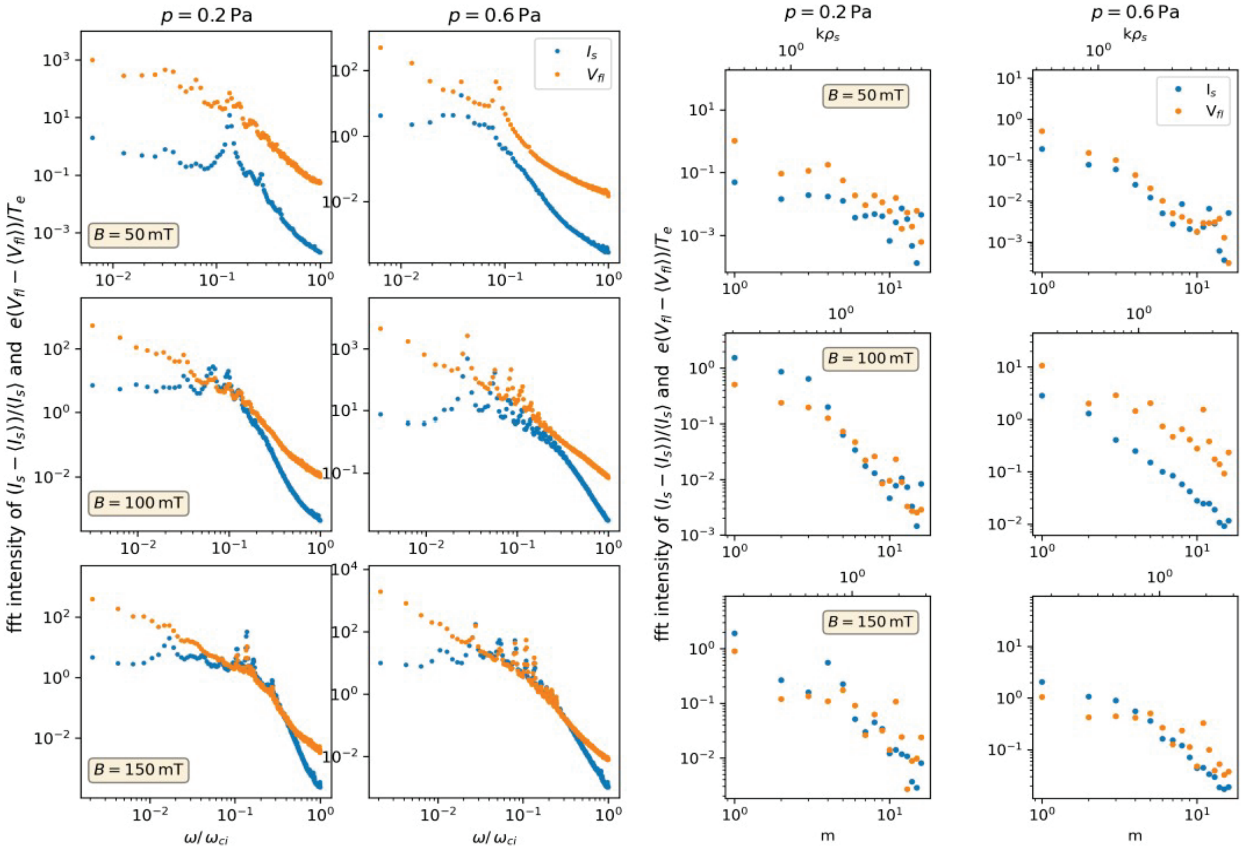

Figure 4: Normalized frequency and wavenumber spectra, for B=[50,100,150] mT. Magnetic fields are the same for each row and pressure for each column.

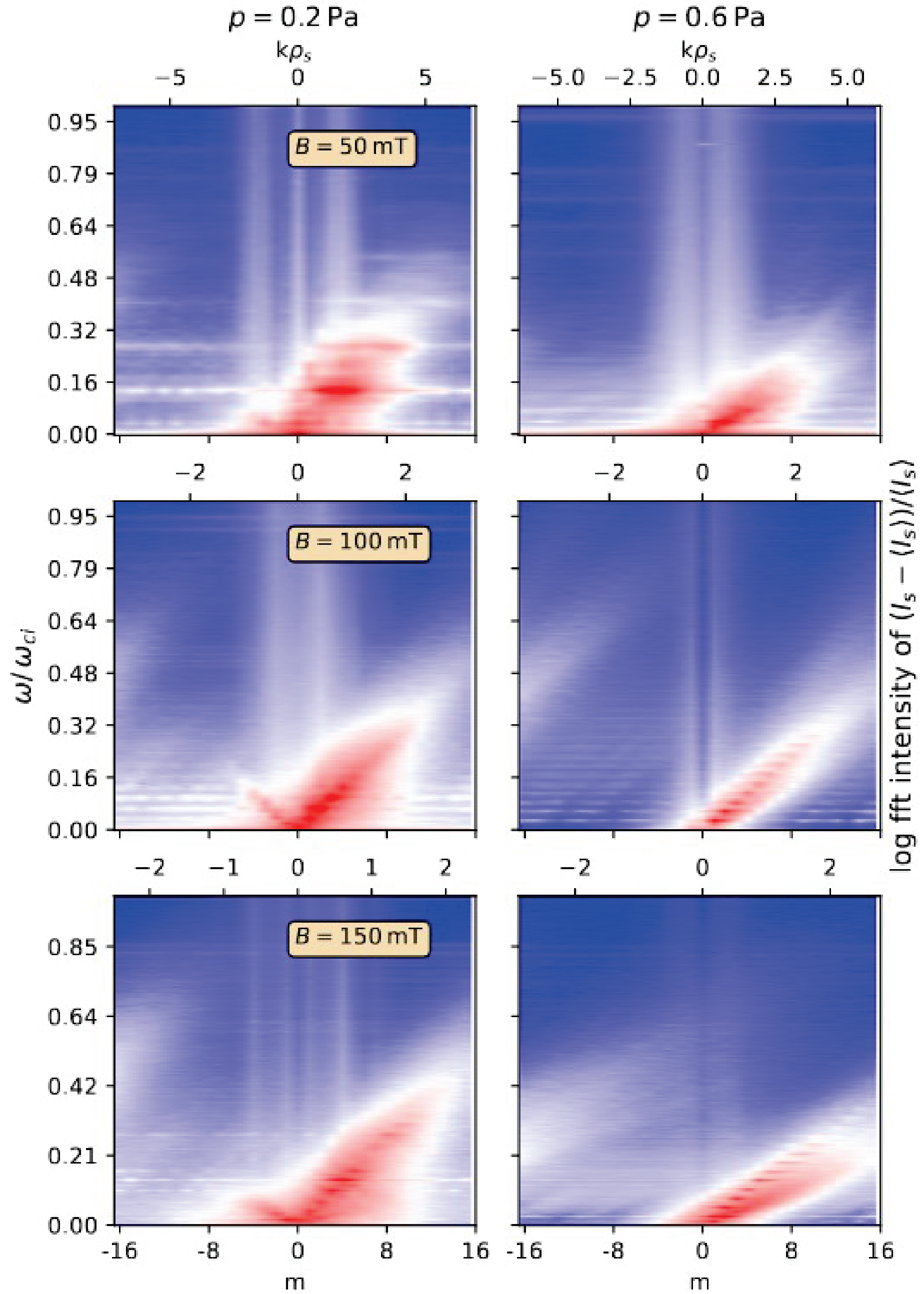

Figure 5: m and ω spectra for p = 0.2 and 0.6Pa and B=[50,100,150]mT of I_s.

Both graphs can be combined into a 2D color plot, shown in fig. 5. From this graph one can deduce relation ships between *m* and *ω.* E.g. the *m*=0 is associated with the zonal flow, and it is apparent that it is not prominent in the density. However the zonal flow is more pronounced at low magnetic fields, which can be attributed to resonance shrinking. This is only a part of the interpretation, there is an on-going discussion about the line (or better lines) formed by the modes in the spectrum and also about the coupling of *m* and *ω.*

Phase defects on the route to turbulence

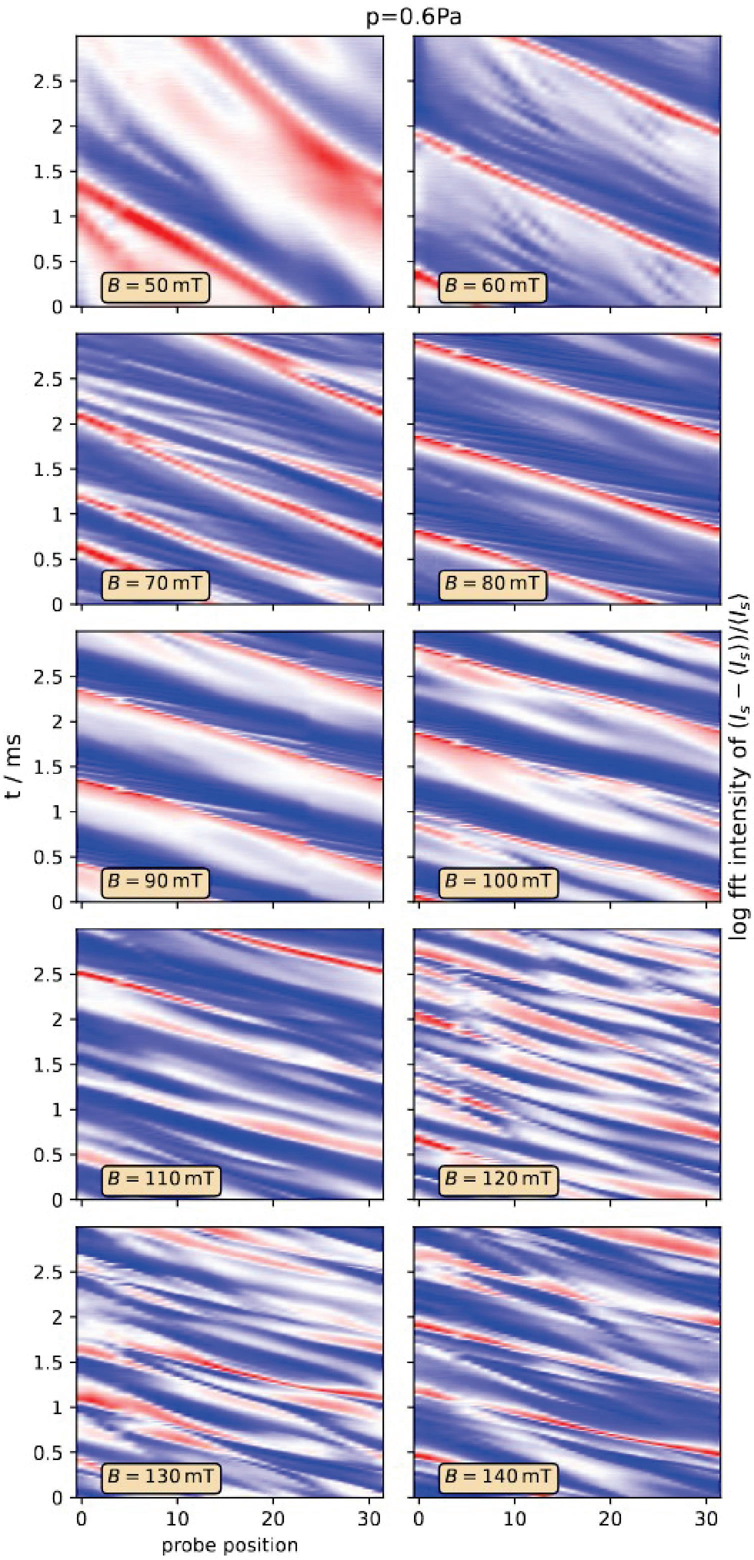

With increasing magnetic field the dynamic first enters a coherent state. This is known at PANTA as the quasi-coherent mode regime / solitary wave. This quasi-coherent mode is particularly stable and long-living. The structures indicated by a red color are then destabilized by so-called phase defects. The occurrence of phase defects increases with increasing magnetic field strengths beyond the quasi-coherent mode regime. Our assumption is, that these phase defects break the symmetry of the mode and thus are a phenomenon of increased turbulence. The transition of one state into another is fluent, thus the transition to turbulence should be fluent too. We aim to investigate parameters regarding these phase defects to describe the route to turbulence.

Figure 6: 2D color plot of Is for varying B. The y-axis on each plot is the time and the x-axis the probe number. Red indicates a high value and blue a low value

Lifetimes and split times

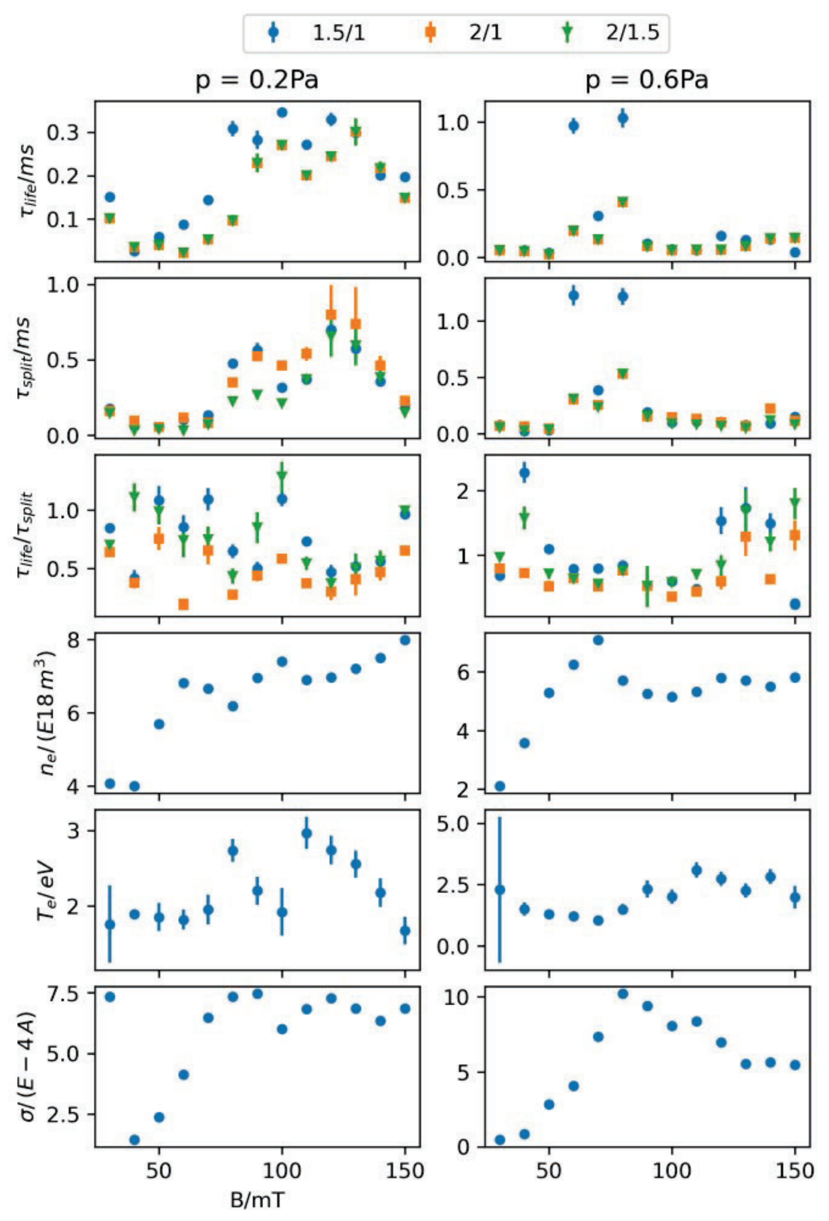

Figure 7: Lifetimes and split times as deduced by means of a flood fill algorithm from fig.6. The rows represent the lifetime, split time and the ration of the two. Density and temperature are already known from fig. 4. The last value σ is the standard deviation of the current. Everything is plotted against the magnetic field and different colors represent different threshold values to calculate the life- and split times.

From fig.6 one can see that the structures have an associated lifetime, that is dependent on the occurrence of the phase defects. Calculated values are displayed in fig.7. Although the solitary wave is particularly stable, the overall lifetime for a magnetic field is calculated via an exponential fit and thus the lifetime may increase beyond the quasi-coherent mode regime. A high lifetime and a short split time is associated with high turbulence. The behavior of the calculated values is complex and subject to on-going discussion. We assume that a full-scale turbulence should approach a ration of both values of 1, which is the case for both displayed pressures. However each graphs needs a detailed investigation, which will be subject to a publication.

Discussion

Our research team has explored new and innovative methods to evaluate the turbulence in a linear plasma. The results are most promising and are valuable information for future analysis. We achieved to outstanding results: first we measured a critical magnetic field for which the density does no further increase. Additionally we developed a novel approach to measure turbulence in a turbulent plasma, which was inspired by fluid physics. This novel approach yields life- and split times for a discharge and their rations are a measure for the turbulent state of this discharge. The application of a flood fill algorithm allows to calculate these values even in a full developed turbulent state, while formerly a controlled transition, not realizable in a plasma experiment, was required. We are very thankful for the opportunity to do this research and the phenomenal support we received from RIAM and the PANTA team.

List of publications

[1] S.Inagaki Sci.Rep. 6, 22189 (2016)
[2] R.Hong Phys. Plasmas 25, 055710 (2018)
[3] C. Moon Sci.Rep. 11, 3720 (2021)
[4] Tianliang ZHANG *et al* 2020 *Plasma Sci. Technol.* **22** 085405
[5] Avila, Kerstin, et al. *Science* 333.6039 (2011): 192-196.
[6] T. Yamada et al., Review of Scientific Instruments 78, 123501 (2007)
[7] J.G. Kwak et al Physics Letters A, Volume 267, Issues 5–6, 2000, Pages 384-388, ISSN 0375-9601

List of participants (specify the affiliation, division, and job title)

KNAUER, stefan; University of Greifswald, Physics department; Researcher
MOON, chanho, RIAM, Assistant professor

国際化推進共同研究概要

No. 13

23NU-9

タイトル： Investigation of flow patterns in a linear magnetized plasma experiment

研究代表者： FAHRENKAMP Nils

所内世話人： 文　贇鎬

研究概要：

本研究では、直線装置 PANTA を用いて異なる放電パラメータにおける測定を行い、特に異なる放電モードとそれに対応する臨界密度に焦点を当てました。得られた結果は極めて有望であり、ヘリコン放電における磁場の存在との比較から、本研究の重要性が明らかになりました。しかしながら、観察された挙動は単純ではなく、機能的な依存関係を理解するにはより多くのデータが必要です。今後は、この課題に対処するための測定実験を展開していきます。

Investigation of flow patterns in a linear magnetized plasma experiment (13_23NU-9)

N. Fahrenkamp
Institute of Physics, University of Greifswald,
Felix-Hausdorff-Str.6, 17489 Greifswald, Germany

I. AIM

Turbulence in a linear plasma device are driven by gradients. resulting from different kinds instabilities, like drift-waves or Kelvin-Helmholtz instabilities. Both can appear together as discussed in detail within the concept of cross-ferroic turbulence [1] impacting the overall flow pattern. Inside the source region, an axial flow from the source to the target is observed. Outside the source, we expect a return-flow from the target towards the source occurred. Further investigations of the flow pattern were done by [2] suggesting behavior with changing plasma parameters. We aim to deepen the understanding of the flow pattern inside a linear magnetized plasma such as in PANTA. The unique tomography system at PANTA [3] offers the chance to compare 3D flow data with conventional probe techniques. Three-dimensional tomographic scans of the flow paatern inside a linear magnetized plasma at different axial positions can be measured. To investigate the return-flow in plasmas in a linear devices higher pressures at varying magnetic fields can be investigated due to expected unrecorded flows beyond the source radius. Preliminary studies do not cover high pressures and/or high magnetic fields, additionally no data is present beyond the source radius. Thus a wider radial area can be investigated. Ideally this tomographic data will give further insight into the particle flux of linear plasmas, because the return-flow might mainly consist of neutral particles. A related study was aimed by Dr. Stefan Knauer with the electrical 2D-probe system and Mach-probes will gain information also about charged particles along the whole vacuum chamber. The comparison of both approaches can be used to gain detailed information of the flux inside the entire chamber, although the tomography system only covers a region close to the source. This was the plan we had in mind. Since it was not possible at sight to measure with the electrical 2D-probe system and Mach-probes due to unforeseen difficulties on the first day of our stay, we were forced to change our measurement plan and aim of our research. First of all measurements from the year before were repeated to increase the quality of these measurements for the use of publication. Furthermore the high ionization rates of helicon discharges and their heating mechanism are not understood to this day. A key piece to this understanding is the dispersion relation of the propagating wave. Effects of the dispersion relation also relate to a rarely studied parameter of the wave, its frequency. The influence of the heating frequency on the phase transitions of the discharge modes was investigated in this research. The existence of a critical magnetic field B_c as postulated by Kwak et al. [4] was the research topic of Stefan Knauer. Going beyond the work of Kwak we furthermore look for a dependency of B_c on the heating frequency f_{rf}. PANTA allows us to study the influence of the f_{rf} on a helicon discharge, which is and will not be possible for us in our helicon plasma device VINETA in Greifswald. In addition to the dependence of B_c on f_{rf}, another topic of open research is the question in which way phase transitions of the discharge modes (E-H-W modes, explained in the next section in more detial) dependent on f_{rf}, too. To increase the insight of the scientific community into these topics we measured plasma discharges at PANTA with varying magnetic fields, pressures, heating powers and heating frequencies to derive a dependency for the mode transitions.

II. SCIENTIFIC CREDENTIALS, THE E-H-W MODE TRANSITIONS

It is now well known that helicon discharges exhibit three modes of operation: a capacitive mode (known as the E mode), which is a low-density mode an inductive mode (known as the H mode) with higher densities and a helicon-wave sustained mode (known as the W mode) with very high densities. In [5] critical densities are proposed, observed with a double loop antenna ($m = 0$). The transition between E and H-modes should occur when the skin depth δ is equal to the half radius of the Pyrex tube [6]. Similarly a minimum density depending on the magnetic field strength is necessary to observe the first longitudinal helicon-wave mode. At higher magnetic field strength the critical density for the H-W transition is higher and at higher f_{rf} the critical density for the H-W transition is lower [7]. This relation is linear in theory, but somewhat less pronounced in experiments. In [6, 8], both with $m = 1$

antennas, a direct transition from E-mode to W-mode is observed. This is in contrast to a minimum density responsible for the transition. The density in E-mode is simply to low to reach the critical density.

III. EXPERIMENTAL SETUP

Experiments have been carried out in the linear magnetized plasma experiment PANTA [9] at RIAM (Kyushu University). The experiments were led by Prof. Dr. Chanho Moon, he was also our first contact. We would like to thank him again for the experiments. PANTA exhibits a length of 4.05 m and a diameter of 45 cm. A homogeneous axial magnetic field up to 150 mT is generated by a set of Helmholtz coils. The plasma is heated by a double loop helicon source ($m = 0$) with a diameter of 10 cm at one end of the device. The typical cylindrical plasma radius is 5 cm. At the other end the plasma terminates at a stainless steel iris diaphragm. The density has been measured as a function of power $n_e(P)$ with Langmuir probes. Each pin of the existing 5-pin probe was used as an independent Langmuir probe. A combination of Langmuir measurements at different radial positions of the 5 pin probe was used to get a radial density profile. This profile was subsequently fitted with a Gaussian to get the center plasma density n_e. In a $\log(n_e)$ vs. $\log(P)$ diagram, the behavior at lower (E-mode) $n_e \sim P^{\alpha_E}$ and higher densities (W-mode) $n_e \sim P^{\alpha_W}$ and the H-W mode intersection $n_{e,trans}(P_{trans})$ can now be fitted.

IV. RESULTS

These power scans have been conducted for different heating frequencies f_{rf}, magnetic fields B_0 and neutral pressures p_0. The results are shown in figure 1 and figure 2. The central plasma density over absorbed RF power at labeled p_0 and B_0 at different heating frequencies are shown in logarithmic scaled graphs. The three different discharge modes are clearly distinguishable and color coded. The modes E (grey), H (red) and W (blue) are fitted as described above and the intersection of the H-W modes is calculated. The results of the fits P^{α_E} and P^{α_W}, and the calculated H-W mode intersection $n_{e,trans}(P_{trans})$ from the fits are shown in table I.

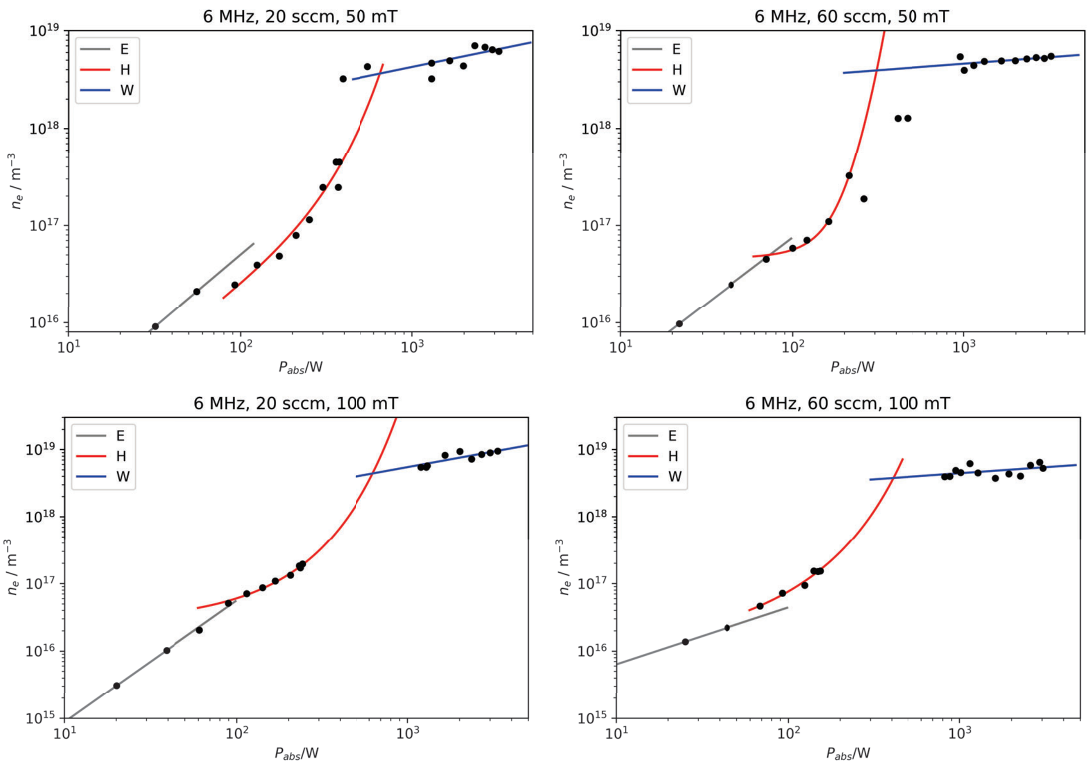

FIG. 1: Plasma density over absorbed RF power at labeled p_0 and B_0 at $f_{rf} = 6$ MHz. The three different discharge modes are clearly visible. The modes E (grey), H (red) and W (blue) are fitted and the intersection of H-W is calculated.

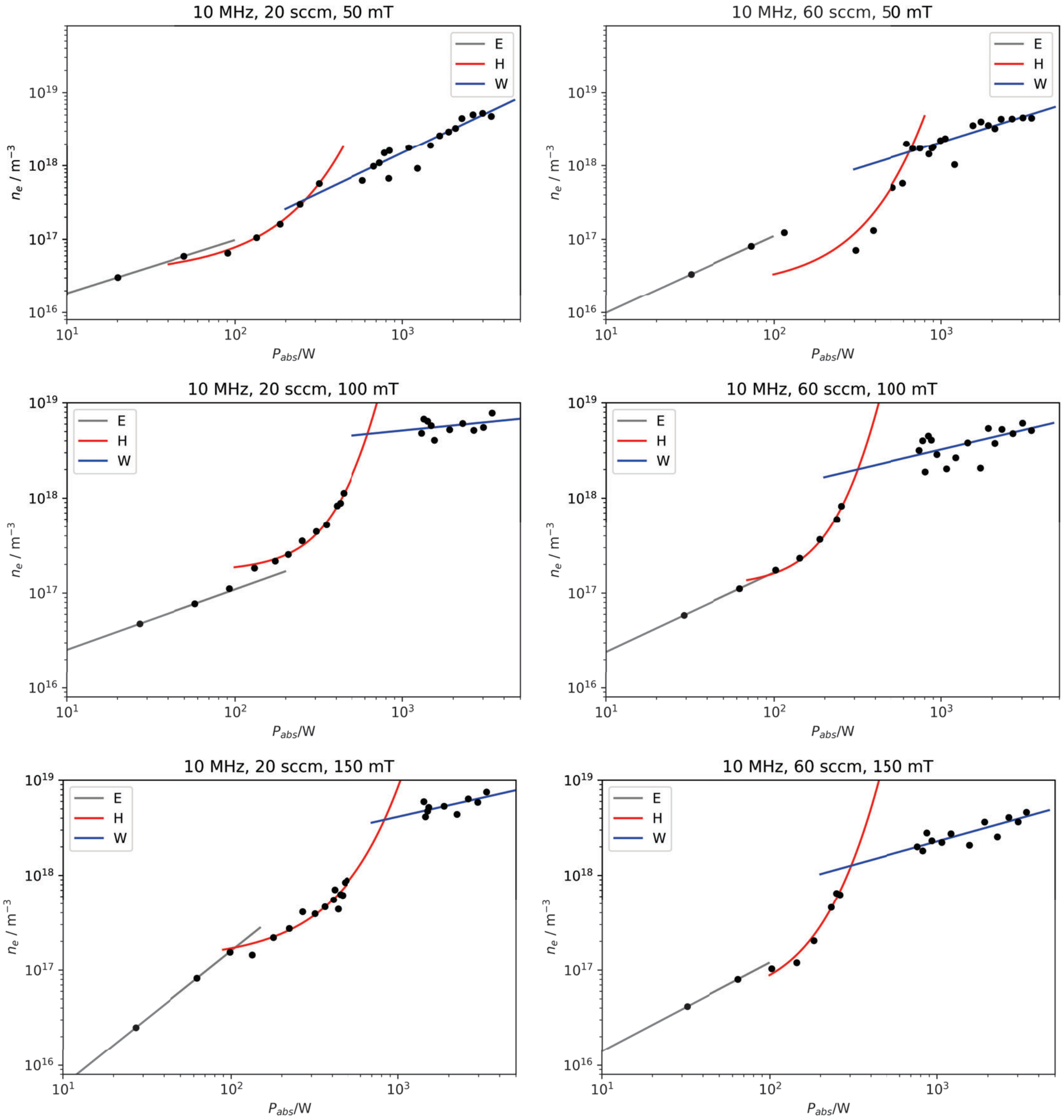

FIG. 2: Plasma density over absorbed RF power at labeled p_0 and B_0 at $f_{rf} = 10$ MHz. The three different discharge modes are clearly visible. The modes E (grey), H (red) and W (blue) are fitted and the intersection of H-W is calculated.

TABLE I: Parameters of discharges, fitted and calculated results for the graphs in figures 1 and 2.

f_{rf}/MHz	p_0/sccm	B_0/mT	α_E	α_W	$n_{e,trans}/10^{18}\,\mathrm{m}^{-3}$
6	20	50	1.49	0.36	3.65
6	20	100	1.80	0.46	4.40
6	60	50	1.35	0.13	3.95
6	60	100	0.84	0.18	3.77
10	20	50	0.75	1.09	0.35
10	20	100	0.63	0.18	4.71
10	20	150	1.41	0.40	3.84
10	60	50	1.05	0.72	1.54
10	60	100	0.83	0.42	2.01
10	60	150	0.93	0.49	1.27

Examine the values of $n_{e,trans}$ for the same heating frequency and neutral gas pressure, four pairs with magnetic fields of 50 mT and 100 mT are found. Comparing the densities of the H-W transition for these pairs, it is shown that at higher magnetic field strength B the critical density for the H-W transition is rising. However, at higher magnetic field strength of 150 mT at a heating frequency of $f_{rf} = 10$ MHz this directly proportional dependency is not valid anymore. It seems that the magnetic field strength dependency of the critical density for the W-mode is not linear and shows a non-monotonic behaviour. Taking a closer look at discharges with the same neutral gas pressure and magnetic field strength but varying f_{rf}, it is in accordance with [7] that at higher f_{rf} the critical density for the H-W transitions is lower. Finally, with higher neutral gas pressure at constant f_{rf} and B_0 the critical density of the H-W transition is lower. Regarding the exponents α_E and α_W from the fits $n_e \sim P^{\alpha_E}$ (E-mode) and $n_e \sim P^{\alpha_W}$ (W-mode), an inverted correlation to the critical plasma density behavior in dependence of the discharge parameters f_{rf}, p_0 and B_0 is observable. Meaning, the higher the critical density is, the less dependent the plasma density is from higher P_{abs}, reducing the slope of the regression line, indicating a plasma density limit for the W-mode. In E-mode the absorbed power should decrease with increasing heating frequency at low collisionality, and this observed here at low pressure. At high collisionality the effect is weaker and this is the case for higher pressure.

V. CONCLUSION

Measurements in PANTA at different discharge parameters have been performed to investigate the different discharge modes and their corresponding critical densities. The results are very promising. In comparison with the data regarding the existence of a critical magnetic field in helicon discharges underscore the findings discussed here. Currently both results together are prepared to be published. However, the behavior shown here is not monotonic and we need a larger database to regress the functional dependencies. We will tackle this in future measurement campaigns. The next steps to increase the insight of the scientific community into these topics are: a) turbulence characteristics at the position of the 5-channel probe used to gain the profiles of the discharge. We assume that the upper limit of the density originates from turbulence. And b) more data points with varying magnetic fields, pressures, heating powers and heating frequencies to derive a clear functional dependency for the mode transitions. For (a) we would need to include 64Ch array measurements to the magnetic field scans or other means to measure the turbulence and for (b) we need more detailed multi dimensional scans of the pressure, magnetic field and power. Elaborating on these would underscore the importance of smaller laboratory experiments as PANTA.

[1] S. Inagaki, T. Kobayashi, Y. Kosuga, S.-I. Itoh, T. Mitsuzono, Y. Nagashima, H. Arakawa, T. Yamada, Y. Miwa, N. Kasuya, et al., Scientific Reports **6** (2016).

[2] R. Hong, J. C. Li, R. Hajjar, S. Chakraborty Thakur, P. H. Diamond, and G. R. Tynan, Physics of Plasmas **25** (2018), ISSN 1089-7674, URL `http://dx.doi.org/10.1063/1.5017884`.

[3] C. Moon, K. Yamasaki, Y. Nagashima, S. Inagaki, T. Ido, T. Yamada, Y. Kasuya, N. Kosuga, M. Sasaki, Y. Kawachi, D. Nishimura, et al., Scientific Reports **11**, 3720 (2021).

[4] J. G. Kwak, H. D. Choi, H. I. Bak, S. Cho, J. G. Bak, and S. K. Kim, Physics of Plasmas **4**, 1463 (1997).

[5] V. Kaeppelin, M. Carrère, and J. B. Faure, Review of Scientific Instruments **72**, 4377 (2001), ISSN 0034-6748, https://pubs.aip.org/aip/rsi/article-pdf/72/12/4377/19295379/4377_1_online.pdf, URL `https://doi.org/10.1063/1.1419228`.

[6] C. M. Franck, O. Grulke, and T. Klinger, Physics of Plasmas **10**, 323 (2003).

[7] K. P. Shamrai, Plasma Sources Science and Technology **7**, 499 (1998), URL `https://dx.doi.org/10.1088/0963-0252/7/4/008`.

[8] S. C. Thakur, C. Brandt, L. Cui, J. J. Gosselin, A. D. Light, and G. R. Tynan, Plasma Sources Science and Technology **23**, 044006 (2014).

[9] T. Yamada, S.-I. Itoh, T. Maruta, N. Kasuya, S. Shinohara, Y. Nagashima, M. Yagi, K. Terasawa, S. Inagaki, Y. Kawai, et al., Plasma and Fusion Research **3**, 044 (2008).

国際化推進共同研究概要

No.14

23NU-10

タ イ ト ル： Development of Core-SOL-Divertor model for simulating tokamak with impurities

研究代表者： WISITSORASAK Apiwat

所内世話人： 糟谷　直宏

研 究 概 要：

トカマクプラズマにおける不純物輸送について統合的な解析を可能とするために、TASK コードへ SOL・ダイバータ領域の効果を組み合わせるのが本研究の課題である。SOL・ダイバータ領域の密度・温度の動的な変化を解く計算コードを開発した。今後このモデルを TASK コードに組み込む予定である。また、本年度は研究代表者が九大応力研を訪問し、セミナーや個別の研究打合せを通じて、九大の多くの核融合研究者との研究交流を行うことができた。

Development of Core-SOL-Divertor Model for Simulating Tokamak with Impurities

Apiwat Wisitsorasak

Department of Physics, Faculty of Science,
King Mongkut's University of Technology Thonburi,
Bangkok, Thailand

1 Introduction

Impurities in tokamak plasma introduce several deleterious effects on the overall performance of the devices. A large amount of impurities can dilute the fuel and reduce the rate of fusion reactions. Furthermore, one of the most immediate effects is the loss of radiated power, which leads to lower plasma temperatures. For example, impurity ions such as oxygen and carbon, originating from the tokamak vessel, strongly cool the plasma near the edge. However, excessive edge cooling destabilizes the plasma and leads to plasma disruption, which can severely damage the wall and other structures [1]. On the other hand, metal ions from the plasma-facing components, such as tungsten, can travel farther from the edge and cause significant radiation in the core. This prevents the plasma from reaching a high enough temperature for ignition. Hence, the concentration of impurities should be minimized. For a tokamak with a divertor configuration, the impurities should be pumped away near the divertor; otherwise, they will accumulate in the vessel. Despite the downside effects of impurities, the radiation of plasma impurities nevertheless has some helpful consequences. Injection of noble gases such as argon or neon is intentionally used to increase radiation in the edge region of the plasma. A well-controlled amount of these seeded impurities helps to disperse the plasma power exhaust over wider surface areas and reduce the temperature in front of the plasma-facing components.

In order to dynamically model the SOL and divertor plasma, one may reduce the complexity of the problem by only considering the transport along a magnetic field line. The five-point dynamics model further simplifies the transport and is developed to investigate the response of the plasma in the SOL and divertor regions at five points [2]: the stagnation point (0), upstream throats of divertors (u_A, u_B), and divertor plates (s_A, s_B), as shown in figure 1.

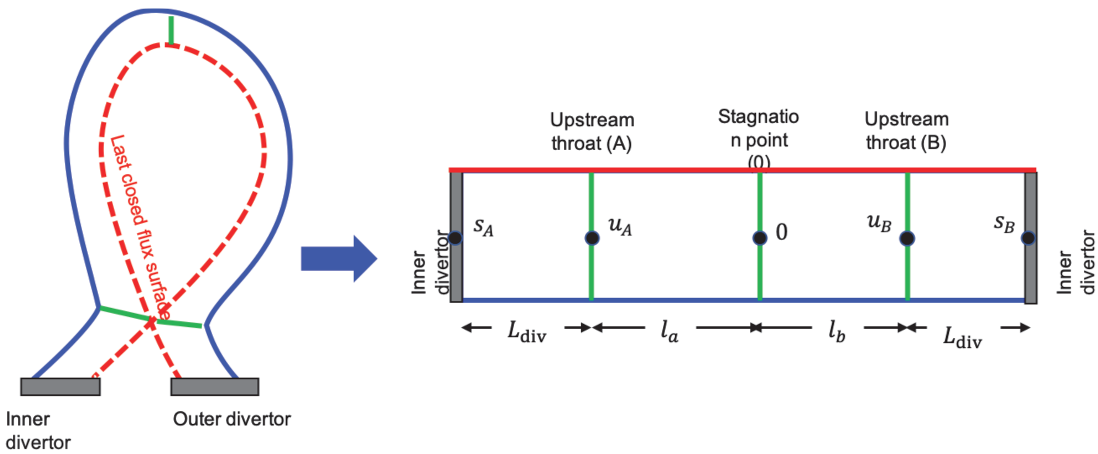

Figure 1: Schematic diagram showing the geometry of the five-point model which considers the transport along the magnetic field.

Model Equations

Through integrating the fluid equations along the magnetic flux tube in each region, one obtains the dynamical equations of the density (n), ion particle flux (Γ), electron (T_e), and ion (T_i) temperatures at each point along the open field lines as follows [2]:

$$
\begin{aligned}
L_{\mathrm{SOL}} \frac{dn_0}{dt} &= -\Gamma_{\mathrm{uB}} - \Gamma_{\mathrm{uA}} + S_0 L_{\mathrm{SOL}}, &(1)\\
L_{\mathrm{div}} \frac{dn_{\mathrm{sA,B}}}{dt} &= -\Gamma_{\mathrm{uA,B}} - \Gamma_{\mathrm{sA,B}} + S_{\mathrm{A,B}} L_{\mathrm{SOL}}, &(2)\\
\frac{m_i}{2}\left(l_{a,b} + \left(R_{\mathrm{A,B}}+1\right) L_{\mathrm{div}}\right) \frac{d\Gamma_{\mathrm{uA,B}}}{dt} &= n_0 \left(T_{e0} + T_{i0}\right) \\
&\quad -n_{\mathrm{sA,B}} \left(2T_{\mathrm{esA,B}} + (1+g) T_{\mathrm{isA,B}}\right) &(3)\\
1.5 L_{\mathrm{SOL}} \frac{d\left(n_0 T_{j0}\right)}{dt} &= -Q_{j\mathrm{uB}} - Q_{j\mathrm{uA}} - \delta_j J \left(\phi_{\mathrm{uB}} - \phi_{\mathrm{uA}}\right) \\
&\quad + \left(W_{j0} + W_{j\mathrm{eq}0} + W_{\mathrm{rad}}\right) L_{\mathrm{SOL}}, &(4)\\
1.5 L_{\mathrm{div}} \frac{d\left(n_{\mathrm{sA,B}} T_{j\mathrm{sA,B}}\right)}{dt} &= -Q_{j\mathrm{uA,B}} - Q_{j\mathrm{sA,B}} - \delta_j \sigma_{\mathrm{A,B}} J \left(\phi_{\mathrm{uA,B}} - \phi_{\mathrm{sA,B}}\right) \\
&\quad + \left(W_{j\mathrm{A,B}} + W_{j\mathrm{eqA,B}} + W_{\mathrm{rad}}\right) L_{\mathrm{div}}, &(5)
\end{aligned}
$$

where the subscript j refers to particle species (i for ions and e for electron) with $\delta_e = 1$, $\delta_i = 0$, $\sigma_A = -1$ and $\sigma_B = 1$. S_0 and W_0 are the particle and energy source in the radial direction. The neutral particle source and the ionization energy due to these neutrals are given by $S_{\mathrm{A,B}}$ and $W_{j\mathrm{A,B}}$, respectively. W_{rad} is the radiated energy due to impurity. Γ and Q are the particle and heat flux from the core. Detailed calculation of each term is provided in reference [3, 2].

Modelling of Impurity Production and Transport

The dynamic five-point model can be extended to explicitly describe impurity production and transport in the tokamak edge region. This task can be achieved by considering the multi-fluid equations of impurity species. Upon considering an impurity species with atomic number $Z_{\max}$, the continuity equation of the jth charge state, $j = 1, ..., Z_{\max}$, can be written as [4, 1]:

$$\frac{dn_j}{dt} = -\frac{dn_j v_j}{dz} - \frac{d\Gamma_j^{\perp}}{dx} + n_{j-1}\alpha_{j-1} - n_j(\alpha_j + \beta_j) + n_{j+1}\beta_{j+1}, \tag{6}$$

and the momentum equation:

$$\begin{aligned} \frac{d(m_Z n_j v_j)}{dt} &= -\frac{d(m_Z n_j v_j^2)}{dz} - \frac{d(m_Z n_j v_j u_j)}{dx} - \frac{dp_j}{dz} - m_Z n_j \left(\frac{v_H - v_j}{\tau_j}\right) \\ &= +m_Z \left[n_{j_1} v_{j-1}\alpha_{j-1} - n_j v_j(\alpha_j + \beta_j) - n_{j+1} v_{j+1}\beta_{j+1}\right], \end{aligned} \tag{7}$$

where m_Z is the impurity mass, n_j is the impurity density of the jth charge state, v_j is the parallel component of velocity, u_j is the perpendicular component, α_j and β_j are the ionization and recombination rate coefficients, respectively, v_H is the velocity of hydrogen species, and τ_j is the impurity-hydrogen collision time. Note that z is the direction along the field line, and x is the perpendicular (radial) direction. $\Gamma_j^{\perp}$ is the impurity flux from the core. For simplicity, we may take the impurity temperature to be equal to the hydrogen temperature, i.e. $T_Z = T_i = T_H$, and the pressure $p_j = n_j T_H$.

For the typical plasma edge, the temperature is less than 100 eV, and the density is between 10^{18} and 10^{21} m^{-3}. The recombination of the impurity ions can be ignored. Neglecting the perpendicular fluxes and integrating equation 6 in the SOL region ($z = -l_a$

to $z = l_b$) yields:

$$L_{\rm SOL}\frac{dn_{j,0}}{dt} = -\Gamma_{j,\rm uB} - \Gamma_{j,\rm uA} + L_{\rm SOL}\left(n_{j-1,0}\alpha_{j-1,0} - n_{j,0}\alpha_{j,0} + S_{j,0}\right), \tag{8}$$

where $S_{j,0}$ is the impurity source rate from the core. One can also integrate equation 6 in the divertor regions ($z = u_{\rm A,B}$ to $z = s_{\rm A,B}$):

$$\begin{aligned} L_{\rm div}\frac{dn_{j,\rm sA}}{dt} &= \Gamma_{j,\rm uA} - \Gamma_{j,\rm sA} + L_{\rm div}\left(n_{j-1,\rm sA}\alpha_{j-1,\rm sA} - n_{j,\rm sA}\alpha_{j,\rm sA} + S_{j,\rm sA}\right), & (9)\\ L_{\rm div}\frac{dn_{j,\rm sB}}{dt} &= \Gamma_{j,\rm uB} - \Gamma_{j,\rm sB} + L_{\rm div}\left(n_{j-1,\rm sB}\alpha_{j-1,\rm sB} - n_{j,\rm sB}\alpha_{j,\rm sB} + S_{j,\rm sB}\right). & (10)\end{aligned}$$

Integrate equation 7 from $z = 0$ to the divertor plate of each side, one obtains:

$$\begin{aligned} \frac{m_Z}{2}\left(l_{\rm b} + (R_j+1)L_{\rm div}\right)\frac{d\Gamma_{j,\rm uB}}{dt} &= n_{j,0}T_{\rm H,0} - 2n_{j,\rm SB}T_{\rm H,SB}\\ &\quad + \frac{m_Z}{\tau_j}\left[\frac{1}{2}n_{j,0}v_{\rm H,0} + \frac{1}{2}n_{j,\rm sB}v_{\rm H,sB} + \frac{m_Z}{2}\left(l_{\rm b} + (R_j+1)L_{\rm div}\right)\Gamma_{j,\rm uB}\right]\\ &\quad + m_z\left(l_{\rm b} + (R_j+1)L_{\rm div}\right)\left(\alpha_{j-1,\rm uB}\Gamma_{j-1,\rm uB} - \alpha_{j,\rm uB}\Gamma_{j,\rm uB}\right), \qquad (11)\end{aligned}$$

where $m_Z n_j v_j^2$ is approximately less than $n_j T_H$. The impurity-flux amplification factor is defined as $R_j \equiv \Gamma_{j,\rm sB}/\Gamma_{j,\rm uB}$. The other equation on the other side can be obtained by changing subscript uB to uA. In this analysis, the parallel velocity of the main ion v_H is unknowns, but it can be obtained by an appropriate model for the main-ion dynamics [1]. In principle, the impurity density (n_j) and particle flux (Γ_j) of each charge state at each location along the SOL and divertor (equations 8 - 11) can be numerically determined by using standard numerical techniques such as the Runge-Kutta method.

In the present work, we have developed a computer code based on Python programming for solving the dynamical equations for the densities and temperatures in the core, the scrape-off layer, and the divertor regions, which we described previously. The code is also

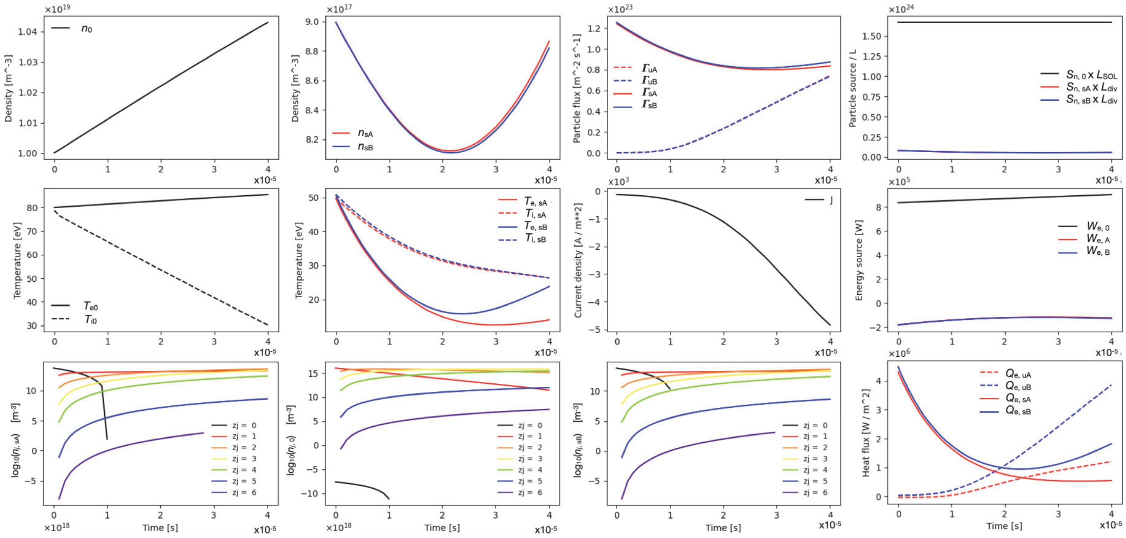

Figure 2: The figures show the time evolution of the plasma densities (n_0, n_{sA}, n_{sB}), temperatures (T_{e0}, T_{i0}, $T_{e,sA}$, $T_{e,sB}$, $T_{i,sA}$, $T_{i,sB}$), particle and heat fluxes (Γ_{uA}, Γ_{uB}, Γ_{sA}, Γ_{sB}), current density (J), particle and energy sources (S, W), and impurity densities of different charge states (n_j) at different locations.

able to solve for the impurity densities of each charge state. Figure 2 illustrates an example of the time evolution of the plasma densities (n_0, n_{sA}, n_{sB}), temperatures (T_{e0}, T_{i0}, $T_{e,sA}$, $T_{e,sB}$, $T_{i,sA}$, $T_{i,sB}$), particle and heat fluxes (Γ_{uA}, Γ_{uB}, Γ_{sA}, Γ_{sB}), current density (J), particle and energy sources (S, W), and impurity densities of different charge states (n_j) at different locations. Note that the locations of 0, u_A, u_B, s_A, and s_B are referred to in Figure 1. In future work, we will implement the code in Fortran and incorporate it into the TASK code for simulating tokamak plasmas with more accurate models.

References

[1] P. C. Stangeby *et al.*, *The plasma boundary of magnetic fusion devices*, vol. 224. Institute of Physics Publishing Bristol, 2000.

[2] N. Hayashi, T. Takizuka, and M. Hosokawa, "Modeling of dynamic response of sol-divertor plasmas to an elm crash," *Journal of nuclear materials*, vol. 363, pp. 1044–1049, 2007.

[3] N. Hayashi, T. Takizuka, A. Hatayama, and M. Ogasawara, "Onset condition of thermoelectric instability in divertor tokamaks," *Nuclear fusion*, vol. 38, no. 11, p. 1695, 1998.

[4] R. Zagorski and F. Romanelli, "Modelling of impurity production and transport in the scrape-off layer of a high density limiter tokamak," *Nuclear fusion*, vol. 36, no. 7, p. 853, 1996.

国際化推進共同研究概要

No.15

23NU-11

タ イ ト ル： Tokamak startup experiments using flux ropes for PLATO

研究代表者： PARK JongYoon

所内世話人： 文　贊鎬

研 究 概 要：

本研究は、韓国ソウル大学で開発されたプラズマガンに焦点を当て、その応用可能性について概説しています。プラズマガンは、VESTおよびPLATOプロジェクトにおいて重要な役割を果たすことが期待されており、オーミック運転やシードプラズマ生成などの研究に利活用される見込みです。本報告書では、プラズマガンの開発状況やPLATOプロジェクトにおける課題について解説し、また、VESTとPLATOの装置サイズの違いがプラズマガンの配置に与える影響についても議論しています。さらに、プラズマガンの設置場所と真空磁場のシナリオに関する詳細な検討が、次のフェーズにおける重要な課題であることが示唆されています。

Plasma startup experiments using flux ropes for PLATO

JongYoon Park
(Seoul National University, Seoul, South Korea)

The magnetized plasma column is called a flux rope in plasma physics. This simple structured plasma can be easily observed on the Sun[1]. Furthermore, it can be widely used for plasma physics research, ranging from basic ideal instability[2] to fusion research[3]. This study aims to utilize flux ropes to initiate and drive plasma current for the PLATO tokamak. To achieve this, a device capable of discharging flux ropes with various plasma parameters (such as current, voltage, density, temperature, etc.) in diverse external environments (vacuum or plasma) within PLATO stably is necessary. This year's task prioritizes the design and development of such a device and establishing the foundation for the application of PLATO, including the installation locations for power supplies and devices.

To discharge flux ropes in a vacuum chamber, simple methods such as filament[4] (heat electron emission) can be employed. However, these simple methods are known to result in limited current levels of A and can easily contaminate the chamber with foreign substances[4]. Additionally, it is not easy to control the plasma material characteristics (such as density, temperature, etc.) within the flux rope, leading to decreased utility. In order to overcome the limitations of flux rope discharge systems with restricted current generated through thermionic emission or electron emission from electrodes, a new method of flux rope discharge has been proposed, which involves emitting electrons from arc plasma to achieve higher current, density, temperature, and reduced contamination[5]. Based on washer-stacked chamber in the device, the method prioritizes generating arc discharge within the device and then applying voltage to this arc plasma to emit electrons and initiate discharge in the form of a flux rope with neutral gas at the outside of device. While this method may be somewhat more complex than the filament method utilizing thermionic emission, it offers superior controllability and discharge capabilities, making it adaptable to various future requirements.

The terms "Arc plasma gun" or "Washer gun" are widely used to describe a device that discharges flux rope using electrons from arc plasma. As the terms suggest, the most crucial component is the washer-stacked arc chamber in the gun, as the arc plasma determines the density of the flux rope (and consequently the current within it)[5]. Additionally, the temperature rise during arc plasma discharge in the gun is significant, necessitating the selection of materials that can tolerate high temperatures[6]. Another crucial aspect is achieving stable discharge with the high impedance of the flux rope during high-current operations. High impedance implies high-voltage operation, which sustains the discharge of the flux rope. Some applications, such as magnetic reconnection and helicity injection[6], require high-voltage operation to drive specific physical phenomena. When the flux rope is discharged by an arc plasma gun, the outer region of the gun typically remains at zero potential[6]. However, if there is high-density plasma around the gun, short circuits or discharge failures can easily occur through the plasma, potentially causing damage or limiting the gun's operation. Therefore, if high-voltage, high-current operation can be achieved through the design of the gun, it can be more suitable for various operations and applications within PLATO.

Designed and developed arc plasma gun for PLATO

Based on the aforementioned description, the plasma gun design is illustrated in Figure 1. This form of plasma gun resembles the initial version but differs in the presence of multiple external floating potential rings and a larger area arc plasma chamber capable of withstanding high-density arc plasma discharges. This design is based on the results of previous research conducted by the PEGASUS group at the University of Wisconsin, USA[6]. The overall length is 245 mm, with a diameter of 22.6 mm at the one-end of flux rope discharge, and a cross-sectional area of 4 cm^2. Vacuum testing has been completed up to the 10^-7 Torr range. As depicted in Figure 1, the plasma gun can be divided into the Arc-chamber section and the Feed section for power and vacuum seal. Additionally, the installation of pneumatic lines for cooling has been implemented to effectively control heat, ensuring stable operation even during repeated discharges. The materials used are as indicated in Figure 1, with the internal arc chamber specifically constructed using Molybdenum and Ceramic to withstand high temperatures. Figure 2 show the developed plasma gun for PLATO.

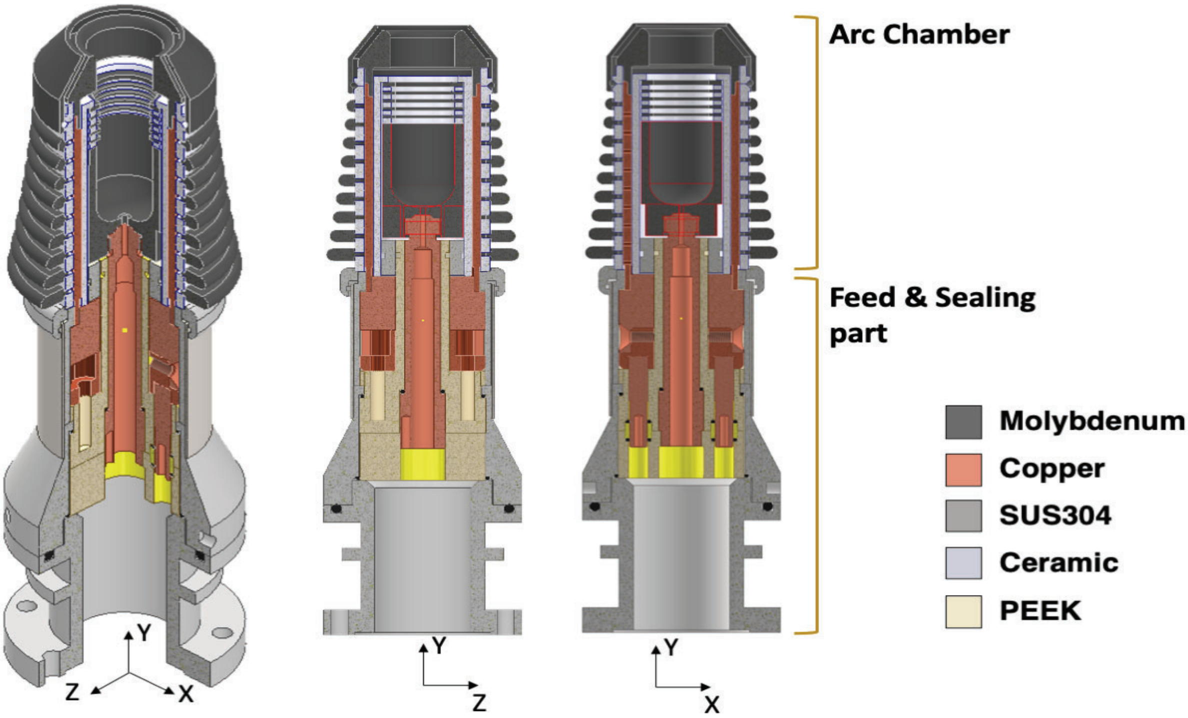

Figure 1. Designed plasma gun for PLATO. AutoCAD Inventor used for drawing.

Figure 2. Developed plasma gun for PLATO.

Discussion

The plasma gun has been successfully developed in Seoul, South Korea, and it will also be utilized in VEST for ongoing research, such as seed plasma generation for Ohmic operation, helicity injection, and combined operation with Ohmic discharge. For PLATO, both seed plasma generation and startup for Ohmic operation will be possible. Therefore, it is expected that sharing experiences between the VEST and PLATO teams or collaborating with each other would be beneficial.

Even though the plasma gun has been developed, other components such as the holder for the gun in PLATO and the gas injection system remain to be developed. This task will be undertaken by the PLATO team with my guidance. The positioning of the plasma gun is not simply a matter of parts; it will have implications for future applications. For example, in the case of seed plasma generation, utilizing arc plasma discharged along vacuum magnetic field lines, it is crucial to consider the location where these magnetic field lines intersect with strong Ohmic electric fields. Similarly, for helicity injection, efficiency decreases as the distance from the center increases.

One major difference between VEST and PLATO is the device size; VEST has a shorter major radius (Spherical Torus). Since the operation of the plasma gun highly depends on its location, unlike in VEST, the gun's placement will be in the vicinity of the outer wall of PLATO. Therefore, the detailed selection of the gun's location and the scenario of vacuum magnetic fields are important tasks for the next phase.

Reference

[1] Kronberg P P 2002 Intergalactic magnetic fields Phys. Today 55 40–1

[2] Furno, I., et al. "Current-driven rotating-kink mode in a plasma column with a non-line-tied free end." Physical review letters97.1 (2006): 015002.

[3] Park, Jong Yoon, et al. "Identification of kink instability in 3D helical flux ropes at VEST." Physics of Plasmas 29.5 (2022).

[4] Hwang, Yong-Seok. Studies of non-inductive current drive in the CDX-U tokamak. Princeton University, 1993.

[5] Fiksel, G., et al. "High current plasma electron emitter." Plasma sources science and technology 5.1 (1996): 78.

[6] Hinson, Edward Thomas, et al. "Impedance of an intense plasma-cathode electron source for tokamak startup." Physics of Plasmas 23.5 (2016).

国際化推進共同研究概要

No. 16

23NU-12

タ イ ト ル： Three-dimensional electromagnetic particle-in-cell simulation for the instabilities in the magnetized plasmas

研究代表者： LEE Hae June

所内世話人： 文　贊鎬

研 究 概 要：

本研究では、PANTA装置を用いてヘリコンプラズマの非線形乱流特性や加熱メカニズムに関するシミュレーションを行っています。主な目的は、強磁場ヘリコンプラズマの物性や生成プロセスを詳細に理解することです。具体的には、静電プローブで測定されたプラズマの浮遊電位データを活用し、強磁化ヘリコンプラズマ内部の支配波の周波数をシミュレーション結果と比較します。これらの波の周波数は、電子やイオンのエネルギー吸収や加熱に密接に関連しています。今後の研究では、プラズマ生成周辺、中間部、終端部など、異なる領域でのシミュレーションを行う予定です。最後に、実験結果に基づいたシミュレーションを通じて、プラズマの半径方向における電子温度の変化やプラズマ中のエネルギー輸送について詳細に調査します。

Three-dimensional electromagnetic particle-in-cell simulation for the instabilities in the magnetized plasmas

Haejune Lee, Hanshin Cheong

Department of Electrical Engineering, Pusan National University, Busan 609-735, Korea

Understanding plasma instability and turbulence is essential for the advancement of nuclear fusion technology. Therefore, direct measurements using probes have been used to study physical characteristics and energy transport in various linear magnetized plasma devices. However, as fusion devices have become larger and more complex in recent years, direct measurements have been challenged by plasma instabilities. To overcome these difficulties, there is a growing need for research through simulation. This research presents to the complexity of magnetized-plasma behavior and energy transport through electrons. Focusing on phenomena that are difficult in experimental measurement such as real-time changes in electron temperature, azimuthal changes in the electric field within the plasma. So, comparison three-dimensional particle-in-cell (PIC) simulations using a code called plexSIM with real experimental draw comprehensive conclusions. In addition, this research will be carried out using a magnetized linear plasma device known as Plasma Assembled Nonlinear Turbulence Analysis (PANTA). It is an ideal device for investigating the tokamak plasmas physics, as it is particularly effective for studying nonlinear plasma turbulence. Under different power, pressure and magnetic field conditions, comparing simulation with experimental data improves our understanding of plasma dynamics. It is expected to contribute to the study of plasma stability and turbulence, paving the way for more sustainable and effective fusion technologies.

Accordingly, we have conducted several experiments and studies in laboratory. One of collaborative research is a PIC-simulation for plasma nonlinear instability. We are also trying to conduct plasma PIC simulations with the results of the PANTA experiment conducted by the RIAM, Kyushu university. We want to simulate changes in electric and magnetic fields and wave propagation under the same conditions as PANTA. Through PIC simulation, we will calculate the variation of electron temperature and potential energy and study energy transfer and plasma instability.

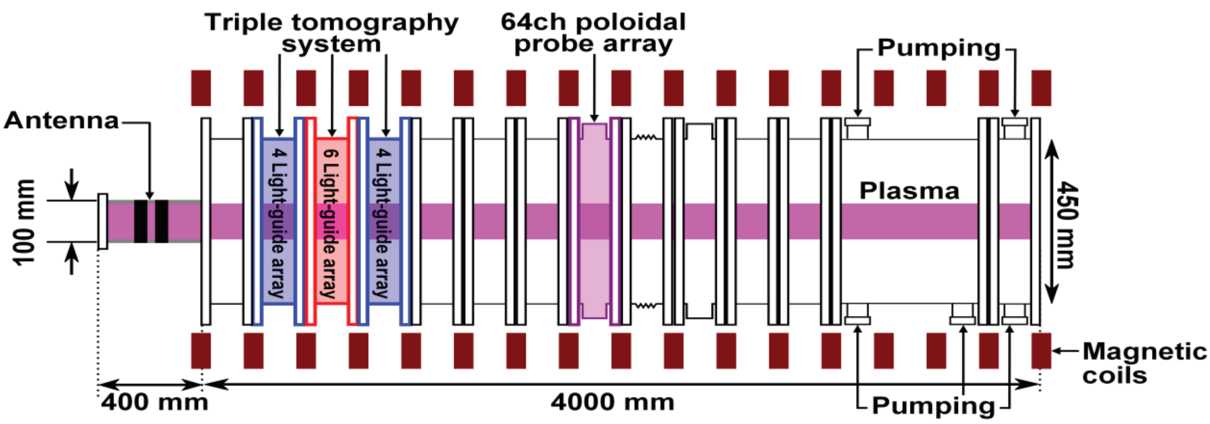

Fig.1 Schematic of PANTA (Plasma Assembly for Nonlinear Turbulence Analysis) device.

We needed real plasma data from the PANTA device to make the PIC simulation converge faster and give accurate results. So, with Prof. Chanho Moon, we have first trained to understand the probe analysis system of PANTA and Ball-pen probe. Fig. 1 shows Schematic of PANTA device.

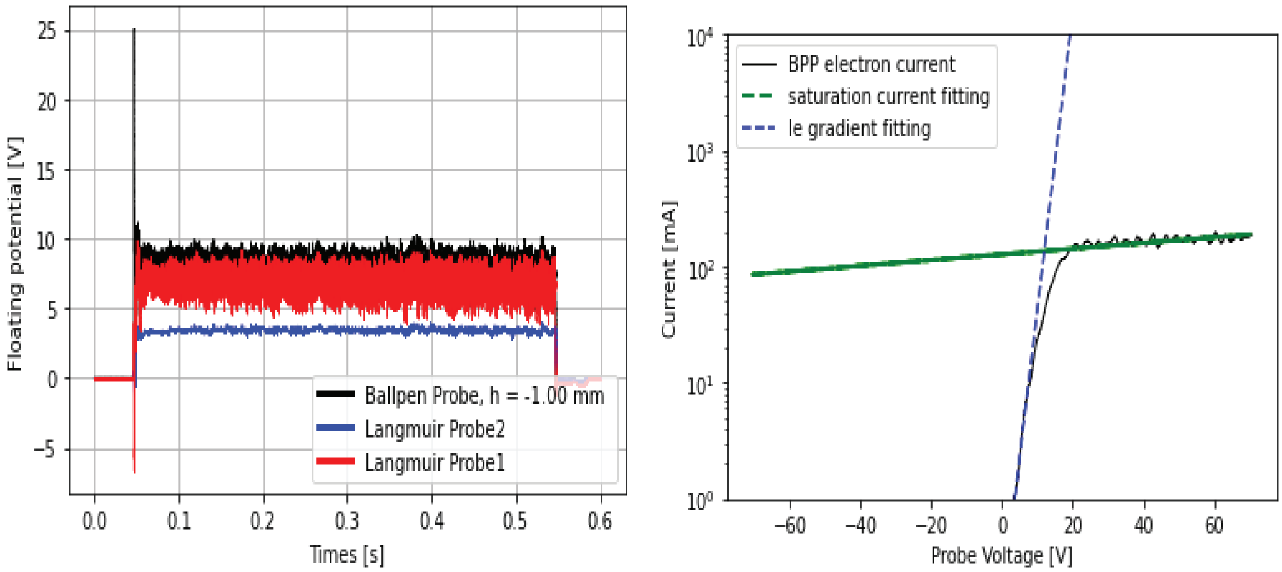

Fig.2 Result of plasma floating potential by Ball-pen probe(left) and curve fitting by Langmuir probe(right).

We tried to find a usable point (a point that works well) for the ballpoint probe in the PANTA device, which is a plasma-assembled nonlinear turbulence analysis device. Finally, We found a point where the ballpoint probe activates well under certain conditions. Figure. 2 is the result of the PANTA experiment, which shows that under certain conditions, the floating potential of the ballpoint probe closely matches the floating potential of the plasma. Also, being able to measure the potential of the plasma without applying voltage to the probe, i.e. without interference with the plasma, is a powerful measure for studying the stability of the plasma.

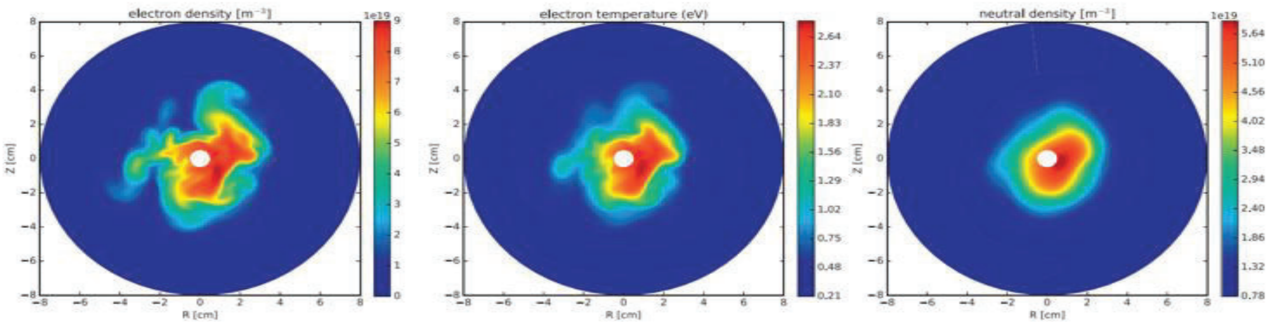

Fig.3 The electron density (left), temperature (middle), and neutral density (right) contours in the drift plane at a snapshot in time.

Figure. 3 shows the neutral and plasma density in the drift plane at a single point in time through simulation [1]. We will check the spatial distribution of variables such as density, electron temperature and ion temperature over time and their shift in the theta direction. In addition, as Figure. 4, PIC simulations can be used to calculate real-time changes of the induced magnetic fields and induced electric fields inside the plasma that are difficult to verify experimentally.

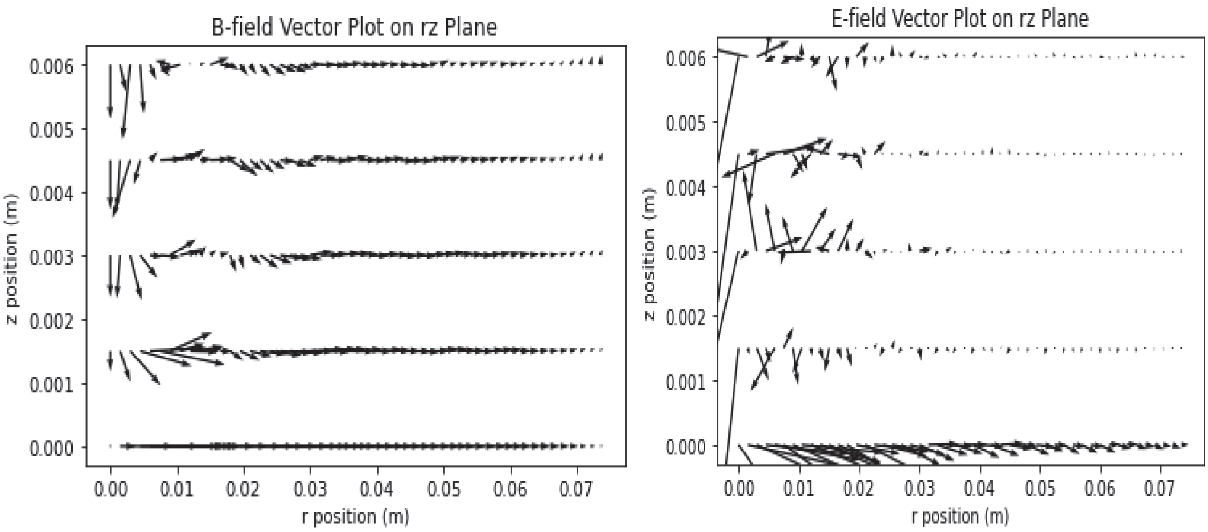

Fig.4 The induced magnetic field and induced electric field snapshot at r-z plane inside the PANTA plasma.

In conclusion, in an international collaboration with RIAM, Kyushu University, using the PANTA device, we are attempting to simulate the nonlinear turbulence characteristics of helicon plasma and the heating mechanism of helicon plasma. Therefore, the final goal of this research is to understand the physical properties and generation process of strongly magnetized helicon plasma. In addition, in future research, we will compare the frequency of the dominant wave inside the strongly magnetized helicon plasma with the simulation results using plasma floating potential data values measured by the Langmuir probe. The wave frequency of the plasma is related to the energy absorption or heating of electrons or ions. In future work, we will perform simulations in different regions, such as near the source, in the middle, and at the end of a linear device. Finally, we will study the temperature evolution of electrons in the radial direction of the plasma and the energy transport in the plasma through simulations using experimental values.

References.

[1] J. Leddy, B. Dudson, H. Willett, Simulation of the interaction between plasma turbulence and neutrals in linear devices, Nucl. Mater. Energy 12 (2017) 994–998

国際化推進共同研究概要

No.17

23NU-13

タイトル： Development of a Fourier cutoff probe to fast measure the plasma density profiles in PANTA

研究代表者： NA Byungkeun

所内世話人： 文　贊鎬

研究概要：

本研究では、PANTAプラズマに適用する先進的な診断技術の開発を目指している。フーリエカットオフプローブ（Fourier cutoff probe）は、高時間分解能測定のために開発されたものであり、繰り返しプラズマにおいてさらに威力を発揮します。PANTAプラズマの高周波スペクトルにアプローチするためには、100ps未満の短インパルス発生器と50GHz以上の帯域幅を持つオシロスコープが必要であり、利便性が悪いです。したがって、手作りの短いインパルス発生器とその信号を検出する方法が必要です。

23NU-13

Development of a Fourier cutoff probe to fast measure the plasma density profiles in PANTA

NA, Byungkeun
(Korea Institute of Fusion Energy, Daejeon, Korea)

Turbulence is one of the most important transport phenomena in magnetically confined plasmas, and PANTA provides an optimized experimental environment with linear cylindrical geometry of magnetized plasma and multiple diagnostics to study the structure of the plasma turbulence. For example, plasma structures such as ITG and ETG are generated in PANTA, and the plasma diagnostics such as Langmuir probe array and the set of tomography is already developed. [1, 2] These experimental studies provide a unique and important data set of spatiotemporal profile of the plasma density and temperature where the plasma turbulence occurs. Further challenging to this study would be independent measurements of electron density and temperature because the previous diagnostics utilized the method where both parameters simultaneously affect the measurement results. For example, constant electron temperature is assumed in the previous studies but it could be differ by location and time because it is measured at the border of two different plasma characteristics. Even though the assumption is reasonable in the previous studies, the more direct diagnostics with less assumption is required to study in more various experimental conditions, such as ETG environment.

The diagnostics which provide an independent measurement of plasma density and temperature is needed to provide more degree of freedom in experimental conditions. The ball-pen probe and the cutoff probe are suggested to independently measure the electron temperature and density respectively. Such diagnostics provide solid analysis even under steep gradient of electron density and temperature without ambiguity. In this study, only the cutoff probe is focused because the ball-pen probe is already developed in PANTA.

The cutoff probe is a diagnostics to find a plasma frequency which is converted to electron density. From the transmission spectrum, the resonance peak is found and its frequency is a function of only electron density as $n_e[10^{16}\ m^{-3}] = 1.24 \times f_{cutoff}^2\ [GHz]$. The Q-factor of the resonance is related to the electron temperature, but the peak frequency is dependent only on the electron density, not the electron temperature. One another advantage of this method is that the measurement is independent of the probe geometry. The conventional apparatus of the cutoff probe is two coaxial cables whose end tips are exposed to plasma and a network analyzer. Moreover, boxcar technique is used to provide a high time resolution for repetitive plasmas. [3] The boxcar method provides a high time resolution but it requires at least several thousands times of repetitions for frequency sweeping, therefore it is quite challenging to apply this method to PANTA since it is operated with near 1 Hz repetition rate. Moreover, the electron density in PANTA is in the range of $10^{17} - 10^{18}\ m^{-3}$, it is not easy to approach this frequency of several tens of GHz with a commercial equipment.

In this study, an advanced technique to approach PANTA plasma is introduced. Fourier cutoff probe is developed for high time resolution measurements, [4] and it is even more powerful in repetitive plasma: it requires only about ten times of repetition to enhance the quality of the signal. Fourier cutoff probe requires three apparatus: a probe, a short impulse generator (usually SRS DG645 is used) and a high bandwidth oscilloscope. Regarding PANTA plasma parameters, a short impulse generator of <

100 ps and an oscilloscope with bandwidth of > 50 GHz are required to approach high frequency spectrum, which are not convenient as well. Therefore, a handmade short impulse generator and the method to detect the signal are needed.

Several methods for short pulse generation are well known. For example, RC pulse generator with passive components such as capacitors and resistors are used so that a charged capacitor releases the energy in a short time. A more sophisticated method utilizes the fast reaction of a transistor. Since faster reaction chips are being developed as the technology is improved, it is quite convenient utilizing these chips. A method of glitch is one of those techniques. [5] In this method, two separate pulses with a small delays are merged through a logic gate, such as XOR gate. Finally, an impulse of the width compared to the delay time is generated. Since arbitrary short delay time can be generated easily, for example transmission line length difference or repeated inversion provide delayed pulse, the pulse width can be created as short. The quality of the pulse, such as rising time, depends only on the reaction time of the logic gate. One example scheme is shown in Figure 1. A single pulse is merged with a delayed pulse signal by a logic gate to create a short glitch signal. In this method, very short impulse < 100 ps can be generated.

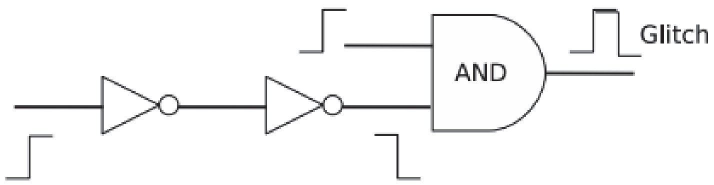

Figure 1. Schematic of Glitch generation [5]

The detection of such a short pulse is not convenient because detection of 100 ps of pulse signal requires an oscilloscope with bandwidth of much higher than 10 GHz. However, RF mixer convert the high frequency signal to low frequency signal. The scheme is shown in Figure 2. The original impulse signal and the transmitted impulse signal are down converted by mixers to be detected by a low bandwidth oscilloscope. Most of the frequency dependent characteristics of a individual mixer could be neglected during the analysis because the final transmission spectrum is acquired by comparison of the input signal and the transmitted signal. The spectrum in the region of interest is converted to a low frequency spectrum by the LO signal of the RF mixer.

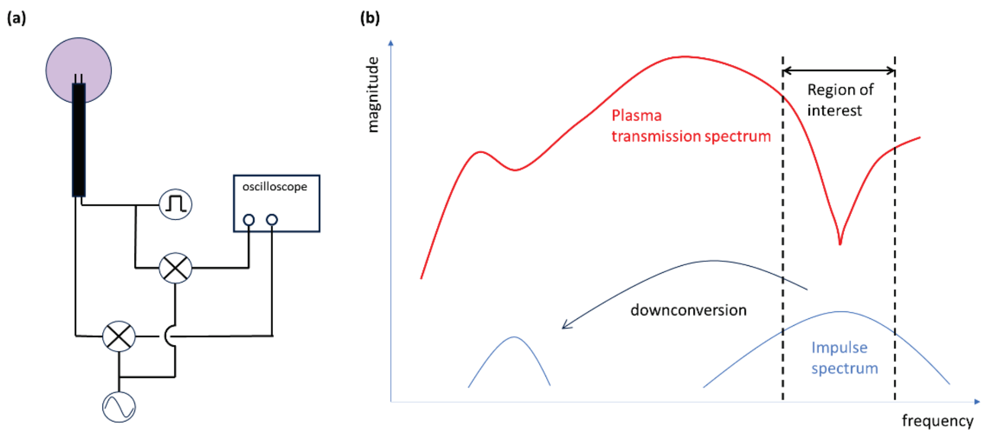

Figure 2. (a) schematic of cutoff probe and mixer configuration, (b) plasma transmission spectrum (top) and spectra of a short impulse and its down conversion.

The above methods will be expand the utilization of Fourier cutoff probe to a high frequency spectrum with low cost. More detailed engineering circuit design for both the impulse generator and low frequency conversion will be performed in the next joint research program.

References.

[1] Y. Nagashima et al., J. Phys. Soc. Jpn, 89, 093501 (2020).

[2] C. Moon et al., Sci. Reports, 11, 3720 (2021).

[3] J.-H. Kum et al., J. Kor. Phys. Soc. 51, 963 (2007).

[4] B.-K Na et al., J. Instrum. 7, C04022 (2012).

[5] M. Slimani and P. Matherat, Faible Tension Faible Consommation (2011).

国際化推進共同研究概要

No.18

23NU-14

タイトル： ECRH/ECCD modeling for QUEST by use of ray-tracing and Fokker-Planck code

研究代表者： BERTELLI Nicola

所内世話人： 出射　浩

研究概要： QUEST 装置では現状、0.25 T磁場で実験を行なっているが、0.5 T磁場増強への準備を進めている。0.5 Tでは、用いている 28 GHz 波が装置中心で第２高調波共鳴となる。これまでに比較的密度の高い場合、第２高調波共鳴層近くで 90 % を超える強い吸収が評価されている。この強い吸収を、フォッカープランク解析を用いて評価することに先立ち、相対論的ドップラーシフト共鳴条件を速度空間上で考察し、バルク電子から高速電子までの幅広いエネルギー範囲で共鳴吸収することを示した。

ECRH/ECCD modeling for QUEST by use of ray-tracing and Fokker-Planck codes

BERTELLI Nicola
(Princeton University, U.S.A)

Extra-ordinary mode second (2^{nd}) harmonic heating scenario has been considered for the 0.5 T ECHCD experiment, based on the ray tracing analysis. Figure 1 shows ray trajectories at top view and transmitted power evolution along ray propagation with parallel refractive indexes at the antenna, $N_{//a}$ = 0.15, 0.25 and 0.35, in the relatively high-density plasma. Bulk (of 0.5 keV at the center) and highly energetic (of 60 keV at the center) electron components of few percentages for the bulk density are assumed. These analyses were done in the 2021 collaboration. The rays cannot penetrate to the high-field side due to the cutoff, then they start to bend near the 2^{nd} harmonic resonance layer. The strong dumping would be expected in the case of $N_{//a}$ = 0.25 because the ray trajectory is along the resonance layer. In addition, the dumping in the case of $N_{//a}$ = 0.15 is rather stronger than that in the case of $N_{//a}$ = 0.25 even when the ray is not along the resonance layer. To begin the Fokker-Planck analysis, the resonant condition in the momentum space is considered.

The relativistic Doppler-shifted n-th harmonic resonance condition is expressed as an ellipse equation in the momentum space ($\overline{P}_{\parallel}$, $\overline{P}_{\perp}$) as follows,

(a) (b)

Fig.1 (a) Ray trajectories at top view and (b) transmitted power evolution along ray propagation with parallel refractive indexes $N_{//a}$ = 0.15, 0.25 and 0.35 in high density plasma. At the top view of (a), fundamental (1^{st}), second (2^{nd}) and third (3^{rd}) resonance field radii are shown. The central bulk and energetic electron density, and , are 3.94 10^{18} m^{-3} and 6 10^{17} m^{-3} for the parabolic profiles.

$$\left(1 - N_{\parallel}^{2}\right)\overline{P}_{\parallel}^{2} - 2N_{\parallel}\frac{nf_{ce}}{f}\overline{P}_{\parallel} + 1 + \overline{P}_{\perp}^{2} - \left(\frac{nf_{ce}}{f}\right)^{2} = 0.$$

Here, $\overline{P}_{\|}$ and $\overline{P}_{\perp}$ are the relativistic normalized momentums in parallel and perpendicular to the magnetic field. $N_{\|}$ and f_{ce} are the refractive index in parallel to the field and electron cyclotron frequency, respectively, which are functions of the major radius R. The resonant ellipses are formed in the momentum space, depending on R. Figure 2 shows the resonant ellipses for various Rs around the 2nd harmonic resonance layer of R = 0.64 m. The semi-circles with the radii $\overline{P}_{\|}^2 + \overline{P}_{\perp}^2$ of $\gamma^2 - 1$ are also shown for various energies (0.5, 10, 20 keV and so on) in the figure. The $(\overline{P}_{\|}, \overline{P}_{\perp})$ of the intersections of the resonant ellipses and the semi-circles satisfy the resonant condition for their energies. The resonant ellipse for the major radius around R = 0.64 m has many intersections for various semi-circles (wide range of the energies) in the up-shifted resonance condition of $\overline{P}_{\|} > 0$, expecting significant absorption by bulk and energetic electrons, and efficient current drive. The effects of electron cyclotron resonance heating (ECRH) and current drive (ECCD) are expressed with a diffusion term of quasi-liner operator in the momentum space on Fokker-Planck analysis. To understand strong dumping around the 2nd harmonic resonance layer of R = 0.64 m will be analyzed with the ray tracing and Fokker-Plank codes under this momentum space consideration.

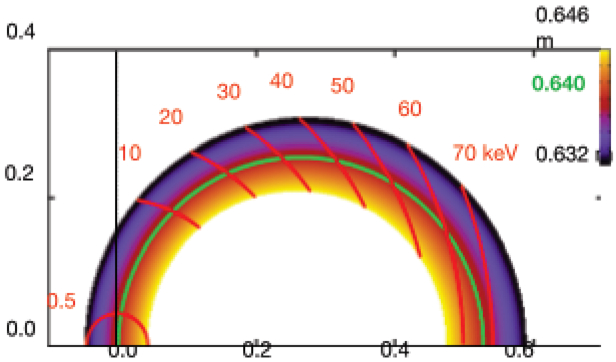

Fig.2 Resonant ellipses for major radii R around the 2nd harmonic resonance layer (R = 0.64 m) with semi-circles on various energies.

An analytical edge density fluctuation model was implemented in Petra-M [1, 2, 3] to investigate its impact on the hhfw propagation propagation [4]. 2D Petra-M simulations with a cold plasma model clearly show a significant perturbation of the HHFW propagation to the core plasma when large density fluctuations amplitudes (A > 30%). Similar results in terms of HHFW propagation are found when a local hot plasma approximation is employed. With the local hot plasma model, we can also make some observations on the effects on the edge perturbations on the ion and electron absorption. For amplitude of the edge density perturbations larger than 10% and for the plasma/wave parameters used in these simulations, the density fluctuations seem to have a strong impact on both the electron and ion absorption. The deuterium/hydrogen power deposition area tends to spread vertically and scatter into multiple sub-regions.
3D Petra-M simulations were performed assuming a 3D axisymmetric edge density perturbation for a cold plasma model for three antenna phasing values: 30, 90, and 150 degrees. Overall reduction of the electric field amplitude in the core plasma for large A was found. A strong modification of the vertical wave field mainly on the poloidal

cross-section as similarly found in the 2D runs for a cold plasma.
Finally, initial attempts to implement an edge 3D filament geometry along the magnetic field line in the NSTX-U geometry used in Petra-M was also shown and discussed. This subject though is still in progress.

This subject was presented at a workshop entitled “Plasma start-up and sustainment in spherical tokamak configuration by RF” which was held under a different international RIAM collaboration framework.

[1] S. Shiraiwa and et al, EPJ Web of Conference **157**, 03048 (2017).
[2] S. Shiraiwa and et al, 28th IAEA Int. Conf. on Fusion Energy (Virtual Event) (2021). [3] N. Bertelli and S. Shiraiwa, 29th IAEA Int. Conf. on Fusion Energy (2023).
[4] N. Bertelli, S. Shiraiwa, and M. Ono, Nucl. Fusion **62**, 126046 (2022).

国際化推進共同研究概要

No.19

23NU-15

タ イ ト ル： High power mm wave transmission line technology for advanced fusion devices

研究代表者： LECHTE Carsten

所内世話人： 出射　浩

研 究 概 要： 大電力ミリ波によるプラズマの不安定性抑制に向けた高速スイッチシステムの開発を進めている。これまで起きていた大電力試験時のアーキングを抑制するため、新たな共振器ミラー６枚、ミリ波吸収フレームを整備し、今回、量子科学技術研究開発機構（QST）那珂研究所にて高速スイッチシステムにインストールした。共振器動作を確認するため、低電力試験を行い、40 dB にも及ぶ共振器特性を得た。共振長を変えることで共振周波数も変化し、良好な共振器動作を確認した。

Report of international collaboration 2023NU-15 between RIAM and IGVP in FY2023: High power mm wave transmission line technology for advanced fusion devices

Mr. Dr. Carsten Lechte

Introduction: The MQIV diplexer developed at IGVP is a fast switch, power combiner, and mode filter for megawatt power 170 GHz millimeter waves using a Fabry-Perot resonator in a compact box design that is vacuum capable and can be directly interfaced with the 63.5 mm ITER ECRH waveguides which are available at QST. The device has 2 input and 2 output ports, which are connected as shown in Fig. 1. Our technical partners at TNO in the Netherlands have designed and built a fast mechanical tuning control unit for the device that is also vacuum-compatible.

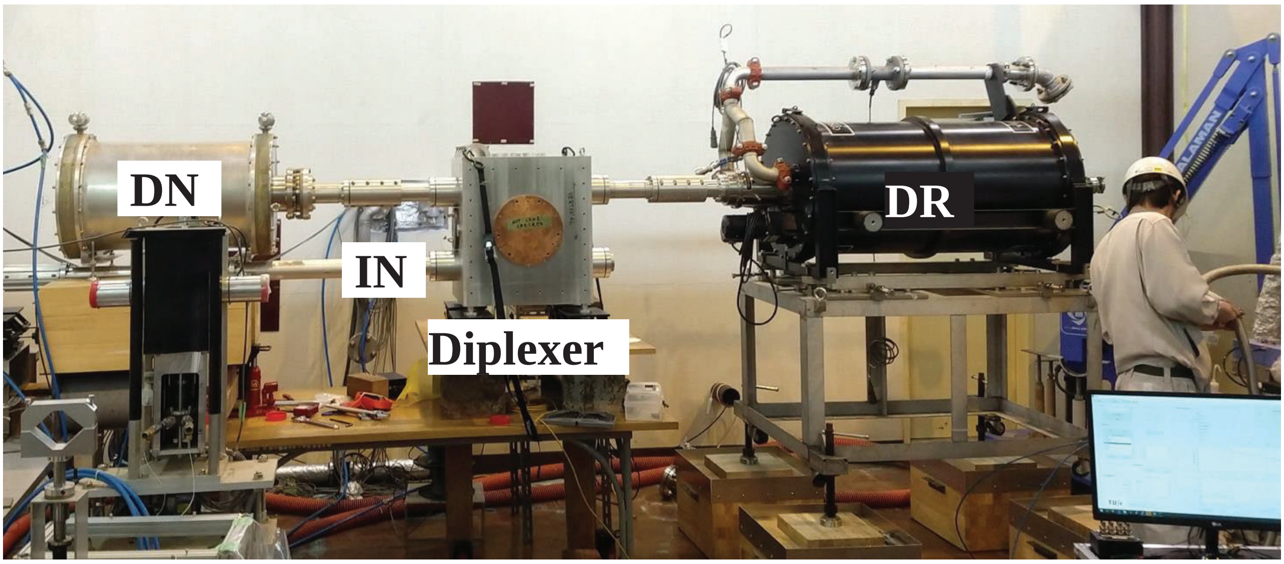

Fig 1: Diplexer integration into the gyrotron test stand at QST. DN and DR are the dummy loads at the non-resonant and the resonant channel, respectively, and IN is the input waveguide.

The highpower tests have demonstrated the switching capability of the device, but also highlighted problems with arcing and stray radiation. Both are believed to have been fully addressed in 2023.

Since no high power tests at QST were possible in 2023, the work was assembly of the new components and characterisation at low power.

Arc mitigation: The mirror surfaces were put into a “known-good” state with a galvanically deposited copper layer on the 4 surfaces of the main resonator, which were then re-machined back to the design shape.
Furthermore, 4 new observation ports are now available for 3 new cameras to watch most mirror surfaces for arcing.

Stray radiation mitigation: Six absorber plates covering the six internal surfaces of the device were designed and are being fabricated at the IGVP workshop and at our collaborating partner IFKB at Stuttgart University. The absorber consists of 8 mm aluminium plates with coutouts for all the mirrors, waveguide ports, and observation ports that will be press-fit into the diplexer box (see Fig. 2). The absorbing coating of aluminium and titanium oxide is applied by an atmorpheric plasma spraying process to a thickness of approximately 100 µm. It has a high (>70%) single pass absorption at 170

GHz from all but the shallowest angles. Cooling is achieved by radiation and contact with the box structure. Since only a fraction of the input power should end up as stray radiation, the absorbers should be able to cool down between shots if a duty cycle of 1:20 of power on to power off is adhered to. This duty cycle is also the maximum for the main mirrors.

Low power characterisation: Measurements were undertaken to certify the frequency dependent switching behaviour of the device. Low power was injected into the input port, and the power usually is measured at the output ports.
At high power use, the input and output powers are monitored via grating couplers on the matching mirrors, which divert -40dB toward small diagnostic horn antennas. The polarisation of these antennas was optimised. Because of the low coupling, the signal is very weak at low power.
It is expected that the introduction of the absorber decreases the stray radiation in the resonator volume, so that mostly the desired monitor signal hits the antennas. At nominal high power of 1 MW, the monitor signal would be 100 W. Qualitatively, the monitor signal has now a better signal to noise ratio, but the ultimate test will be operation at high power in FY2024.

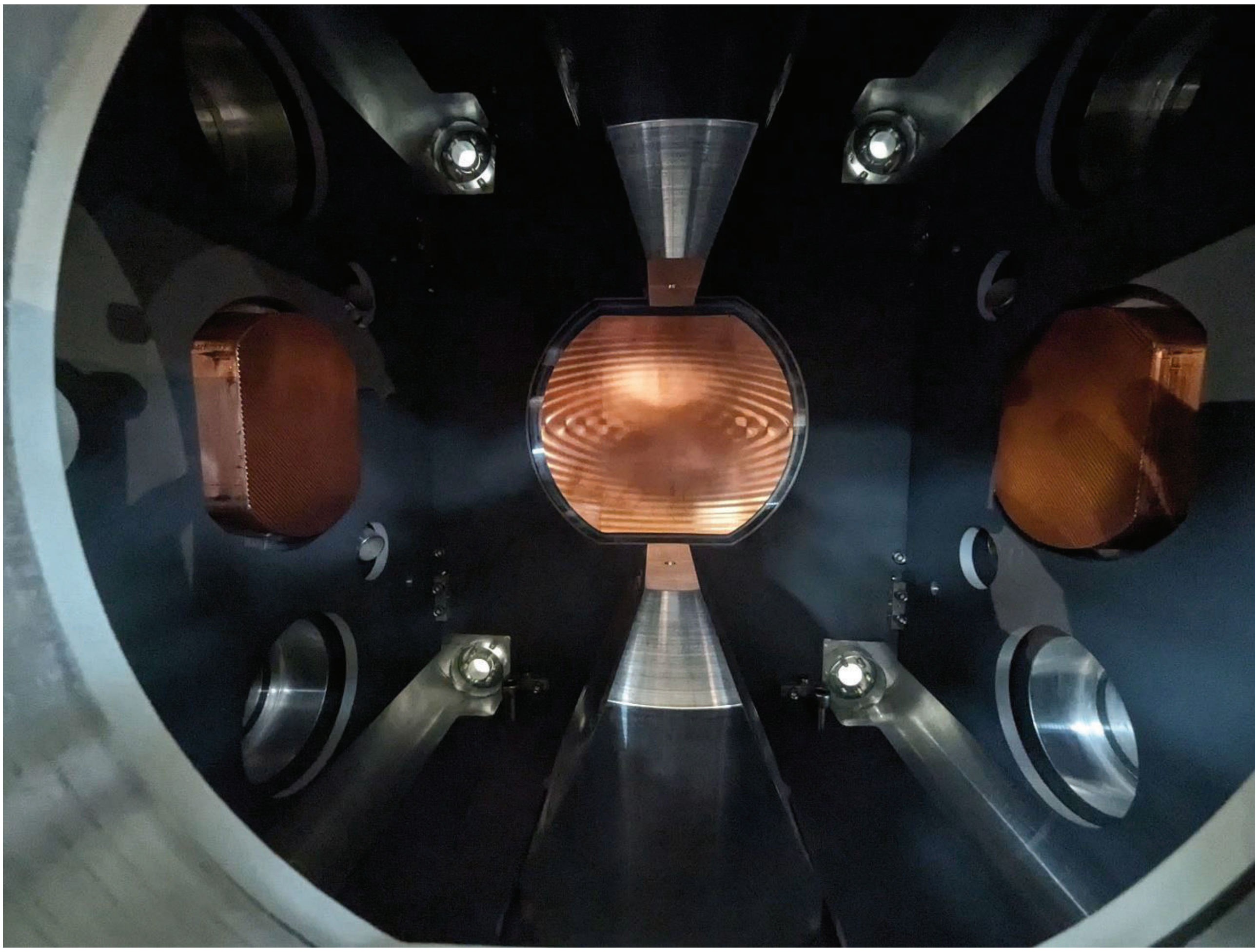

Fig. 2: Assembled absorber plates (dark) inserted into diplexer housing. Also visible are the 4 new windows in the back.

The final low power characterisation was performed with two mirror positions, at the equilibrium of the mounting hardware, and at the innermost position. The cleanest signal was obtained by measuring the monitor antenna signal, not the direct output signal. The plots are shown in Fig. 3.

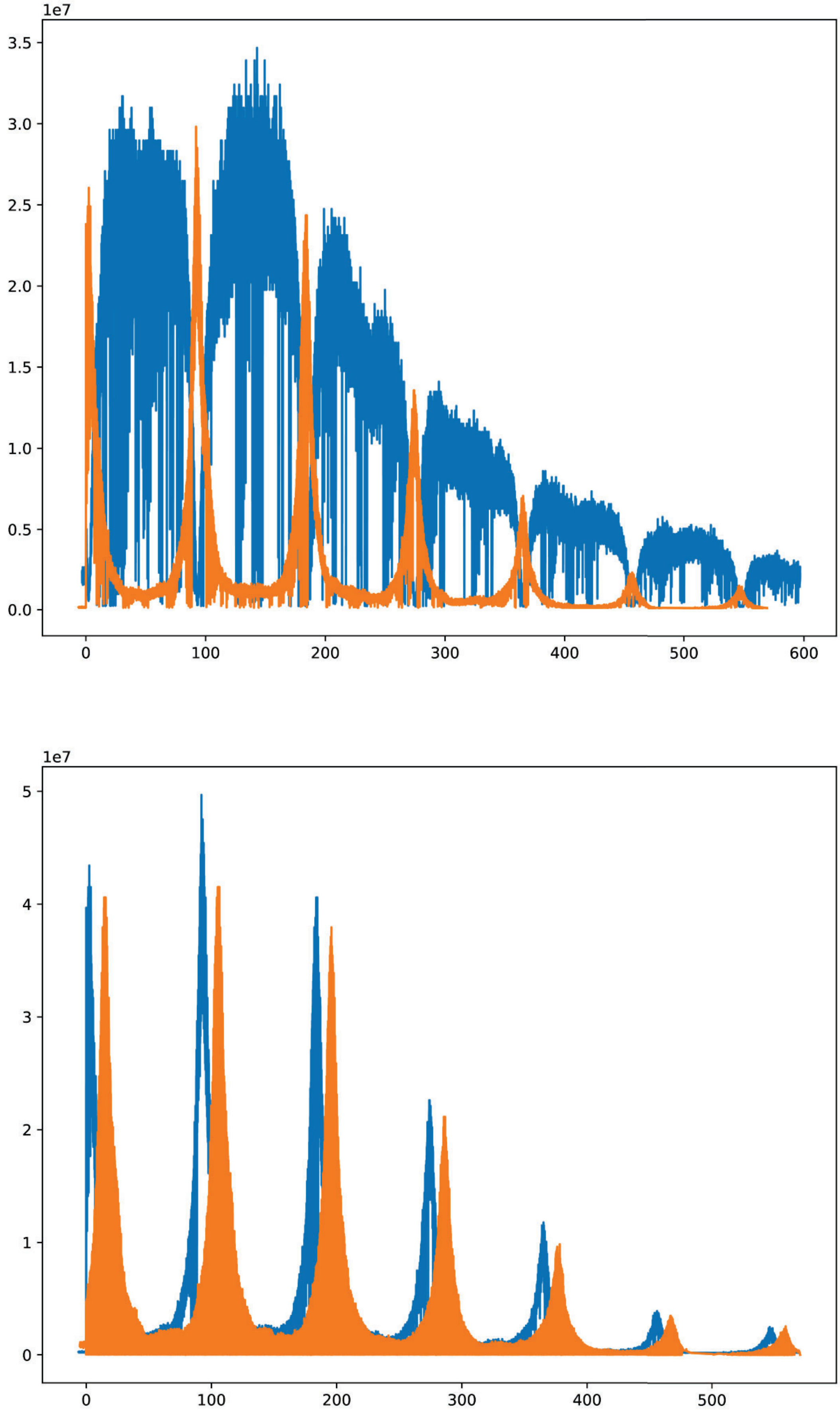

Fig. 3: Top resonant (orange) and non-resonant (blue) power over frequency (a.u.). Bottom both

resonant outputs at both mirror positions.

The figure shows the expected resonance curve with at free spectral range of 278 MHz with good switching contrast. The bottom figure shows the resonant output at two mirror positions, with a slight shift of the peaks due to the changed length of the resonator. The power changes with frequency because of the way the monitor signal is extracted. The monitor antennas look at the diffreacted beam from a grating on the coupling mirrors (aluminium in Fig. 2), and the grating is optimized for a single frequency.
In summary, the device was re-assembled and its operation was confirmed.

国際化推進共同研究概要

No.20

2023CR-FP-16

タイトル： Exploration of conditions for synthesizing heat-resistant materials using supercritical technology

研究代表者： SEONG Gimyeong

所内世話人： 文　贊鎬

研究概要：

本研究では、超臨界流体を用いた高性能ナノ材料の合成に焦点を当て、CeO2 を対象とした分子動力学シミュレーションを通じて、酸素欠陥が安定性と融点に及ぼす影響を明らかにしました。これにより、高温での酸化還元反応に関する重要な洞察を得ました。我々の理解は、耐熱性材料の開発において極めて重要であり、参考データとの整合性から理論的アプローチの有効性を確認するものです。さらに、本研究の結果は、多様な金属種の取り込みを含むより広範な材料研究への道を開くものであり、特に核融合プラズマや航空宇宙分野での応用に不可欠な耐熱合金材料の開発において重要な意味を持ちます。

Exploration of conditions for synthesizing heat-resistant materials using supercritical technology

Department of Environmental and Energy, The University of Suwon
Assistant Prof. SEONG Gimyeong

1. Background and Purpose

Supercritical fluids, known for their innovative reaction environments, have attracted significant interest and research due to their ability to promote unique chemical reactions. Combining them with a flow-type reactor in a non-equilibrium reaction environment, characterized by high-density and highly diffusive supercritical fluids, enables the development of high-performance nanomaterials. Particularly, composite materials like tungsten alloys capable of withstanding extreme temperatures are gaining attention, especially in nuclear fusion and aerospace applications.

This collaborative research, supported by the advanced plasma physics capabilities of the Research Institute for Applied Mechanics at Kyushu University, aims to advance the development of new high-performance nanomaterials. In this study, CeO_2 was chosen as a model substance to understand the easily occurring redox reactions at high temperatures. The impact of oxygen defects within the crystal structure on the melting point variation was investigated using molecular dynamics simulations.

2. Methods

Molecular dynamics simulations were conducted using Fujitsu's SCIGRESS (v3.4) MD-ME. Initially, a pristine CeO_2 structure without oxygen defects in the 4+ oxidation state was generated. The system was then subjected to high temperatures to induce amorphization, followed by a gradual cooling process to crystallize the structure. Subsequently, a CeO_{2-x} structure with oxygen defects in the 3+ oxidation state was created by generating 3+ ceria structures at concentrations of 23%, 50%, 75%, and fully reduced Ce_2O_3. The oxygen was removed proportionally to the cationic charge during the crystallization process using the same method.

3. Results and Discussion

Molecular dynamics simulations (MD) provide insights into the crystallization process of CeO_2, revealing the correlation between the degree of oxygen defects (Ce^{3+}) and the stability of CeO_2 nanoparticles. As depicted in Figure 1, initially, for CeO_2 without oxygen defects, the energy gradually decreases in the amorphous state at 6000 K, sharply dropping around 3800 K, interpreted as the onset of crystallization. While this temperature is approximately 40% higher than the actual melting point (2673 K), it is sufficient to understand the overall trend.

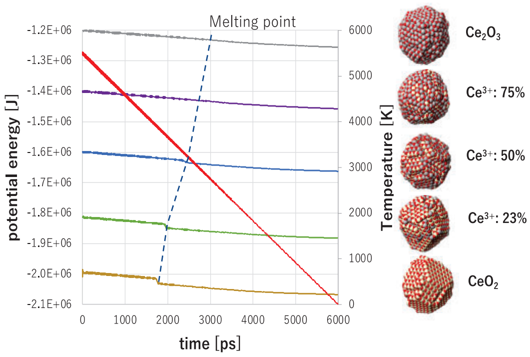

Figure 1 The crystallization process of CeO_2 with varying degrees of oxidation and the morphologies at 298K after crystallization: (yellow) Ce^{4+}; (gray) Ce^{3+}; (red) O^{2-}.

As oxygen defects increase, particles expand, with Ce^{3+} at 75% exhibiting a highly swollen morphology. Additionally, an observed decrease in the melting point and a reduction in potential energy near the melting point with increasing Ce^{3+} levels suggest a trend where phase transitions become easier. This implies that as the ceria undergoes a 3+ oxidation state, the transition to a different state becomes more facile.

4. Summary and Conclusion

This study employed molecular dynamics (MD) to investigate the structural properties of nanoparticles. The stability assessment based on oxygen vacancies not only provided crucial insights into the cerium oxidation states but also offered a comprehensive understanding of nano-materials prone to oxygen defects. The crystallization and calculated properties aligned well with reference data, confirming the effectiveness of the theoretical approach. The results of this study open the path for further investigations into materials, including the introduction of various metal species, particularly in the development of heat-resistant alloy materials.

国際化推進共同研究概要

No. 21

23RE-1

タ イ ト ル： Investigation of III-nitride semiconductor surface properties using coupled ab initio simulations and machine learning algorithms.

研究代表者： KEMPISTY Pawel

所内世話人： 草場　彰

研 究 概 要： 半導体表面の被覆構造の詳細な理解は、結晶成長過程の制御に不可欠です。本研究では、GaN 表面の Ga および H 混合被覆構造について、ベイズ最適化を活用して第一原理計算データを効率的に収集し、Ising 模型の学習を行いました。その結果、460 万以上の候補構造の中から最安定構造の特定に成功しました。これは、従来の網羅的計算によるアプローチでは達成できなかった成果です。

Investigation of III-nitride semiconductor surface properties using coupled ab initio simulations and machine learning algorithms

Pawel KEMPISTY,
Institute of High Pressure Physics PAS, Sokolowska 29/37, 01-142 Warsaw, Poland

Introduction

The project primarily aimed to enhance the theoretical model for characterizing the surfaces of nitride semiconductors. Understanding the surface phenomena is crucial for gaining better control over the crystallization process, which, in turn, could address technological challenges in growing nitride crystals, layers, structures, and devices. Dr. Kempisty's recent work at IWC PAN focused on dynamic surface properties, incorporating first-principles phonon calculations into the thermodynamic description of nitride semiconductor surface stability. Concurrently, Dr. Kusaba at RIAM has been actively developing models using machine learning, particularly exploring large-scale periodic structures through surface reconstruction informatics. By combining their computational expertise, both researchers synergized their efforts. The incorporation of machine learning models enabled them to surpass typical approximations employed in ab initio calculations.

Method

Much of the research involved a thermodynamic analysis based on data derived from first-principles calculations. The RSDFT and SIESTA codes, utilizing Density Functional Theory (DFT) within the General Gradient Approximation, was employed to calculate the energies of the systems and phonon band structures. We incorporated contributions from the vibrational motion of the crystal and its surface, obtained through phonon calculations. Subsequently, using thermodynamic relations derived from phonon spectra, various thermal properties such as constant volume heat capacity, vibrational entropy, and Helmholtz free energy were determined.

Results

The study employs DFT calculations to systematically investigate the adsorption of gallium atoms on GaN polar surfaces. The analysis begins with the clean surface and progresses to the metallic multilayer. Changes in the chemical potential of gallium adatoms were determined as a function of temperature and surface coverage, as illustrated in Fig. 1. These findings contribute to a more accurate thermodynamic description of the surface state under conditions typical for Molecular Beam Epitaxy (MBE), offering an interpretation of the observed growth window.

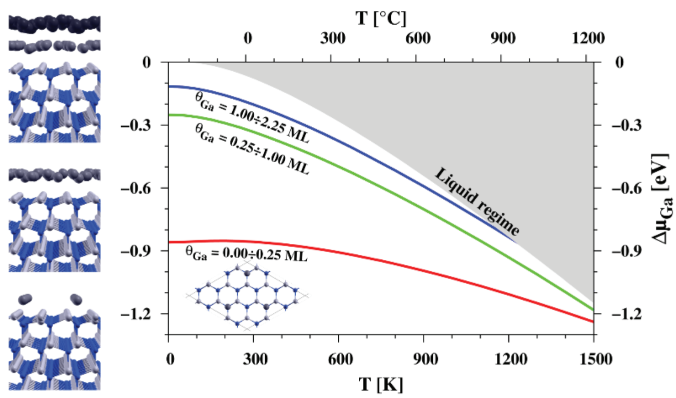

Figure 1. Temperature dependencies of the chemical potential of Ga adsorbate on the GaN(0001) surface.

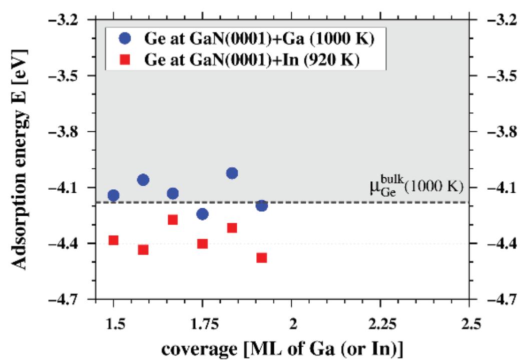

Figure 2. Adsorption free energy of the Ge atom on the GaN(0001) surface with different surface metal layers at high temperature.

Furthermore, we explored the role of gallium and indium adlayers in the context of InGaN crystal growth. The indium surfactant layer exhibits better regularity and a closer lattice match to GaN, while the gallium layer appears denser and more amorphous in nature. Additionally, we investigated the adsorption free energy difference of germanium (Ge) and silicon (Si) atoms on Ga and In layers as a function of temperature. Our findings indicate that the free energy of Ge adatoms on a Ga-covered GaN(0001) surface can exceed the chemical potential of bulk Ge (see Fig. 2), potentially leading to segregation of Ge crystallites on the surface. These results agree well with observations made during the growth of InGaN and GaN by MBE.

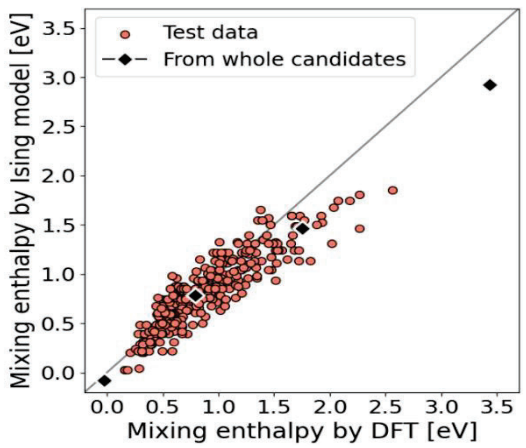

Figure 3. Comparison of mixing enthalpies of gallium and hydrogen coverage estimated by Ising model and calculated by DFT.

The next stage of the research involved considering mixed surface reconstructions with the presence of gallium and hydrogen. The analysis was performed on a slab model with a size of 6×6 surface cells. Calculating the energy of all node occupancy combinations explicitly through ab initio methods was not feasible. Therefore, we have identified surface structures by the DFT calculations combined with machine learning technique Bayesian optimization. We successfully identified the most stable structure among 4,686,825 candidate structures with various adsorbate configurations by incorporating a data-driven Ising model and augmenting the well-known electron counting rule. Our interpretable trained model revealed a stabilization mechanism, enabling the evaluation of the entire set of candidates.

Conclusion

The project demonstrated the effectiveness of integrating density functional theory (DFT) calculations with machine learning, resulting in a powerful tool for predicting material properties. We investigated the thermodynamic properties of GaN surfaces under gallium-rich conditions and mixed gallium-hydrogen coverages. The proposed approach utilized Bayesian optimization to explore the parameter space and identify surface site occupations. Additionally, the Ising model was employed to predict the most promising cases, streamlining the research process for subsequent DFT calculations.

Measurable effects of participation in the programme

As part of the project, Dr. Kempisty undertook a short research visit at RIAM Kyushu University from November 12 to December 2, 2023. During this period, he actively participated in the14th International Conference on Nitride Semiconductors (ICNS-14) held in Fukuoka from November 12 to 17, 2023. A poster presentation entitled "*Ab initio thermodynamic study of the metallic surface wetting layer during MBE (In)GaN growth and its consequences for dopants incorporation*" was presented by P. Kempisty, K. Kawka, A. Kusaba, and Y. Kangawa. A significant portion of the project's results has been published in an article entitled "*Polar GaN Surfaces under Gallium Rich Conditions: Revised Thermodynamic Insights from Ab Initio Calculations*" by P. Kempisty, K. Kawka, A. Kusaba, Y. Kangawa in Materials, 16(17), 5982, 2023 (doi: https://doi.org/10.3390/ma16175982). Additionally, another manuscript entitled "*Augmentation of the Electron Counting Rule with Ising Model*" by K. Kawka, P. Kempisty, K. Sakowski, S. Krukowski, M. Bockowski, D. Bowler, and A. Kusaba has been submitted to the Journal of Applied Physics. It is based on the results previously presented by Dr. Kusaba in an oral presentation entitled "*Ising model-based analysis of the GaN(0001) surface reconstructed structures sampled from Bayesian optimization*" at the 20th International Conference on Crystal Growth and Epitaxy (ICCGE-20) held in Naples from July 30 to August 4, 2023.

国際化推進共同研究概要

No. 22

23RE-2

タイトル： Modelling of carrier injection efficiency in polarization-doping AlGaN heterostructures

研究代表者： SAKOWSKI Konrad

所内世話人： 寒川　義裕

研究概要：

　コロナウィルスやバクテリアの不活化、殺菌に資する AlGaN 深紫外 LED（Light Emitting Diode）、LD（Laser Diode）の開発が行われている。最近の研究では、導波路/EBL（Electron Blocking Layer）界面での電子捕獲の減少が注入効率の大幅な増加につながることが示されており、実験的および数値的に確認されている。本研究の目的は、この現象をさらに研究し、注入効率の改善目標を定量的に示すことである。この研究の最初のステップは、すでに確立された半導体構造をシミュレーションし、シミュレーションと実験との整合を得るためにパラメータ・フィッティングを行うことである。この共同研究で使用するモデルはドリフト拡散法に基づく。次のステップは、高い注入効率を得るために構造を最適化することである。このステップでは、AlGaN ヘテロ構造におけるキャリア輸送を支配する関連現象を考慮に入れるために、モデルを拡張する必要がある。現在、モデルの修正案を提案し、その結果を実験グループと議論している段階にある。

Modelling of carrier injection efficiency in polarization-doping AlGaN heterostructures

SAKOWSKI Konrad, Institute of High Pressure Physics, Polish Academy of Sciences

This project focus on study of the polarization doping aluminum-gallium nitride heterostructures, i.e. light-emitting diodes and laser diodes, by numerical simulations. We performed simulations of heterostructures based on experimentally-made devices, published earlier by Meijo University and Mie University experimental groups. Our simulations were supplemented by results of the ab initio calculations, which enabled us to confirm the polarization doping effect and to verify the material parameters. Moreover, a theoretical model for Shockley-Read-Hall recombination was proposed, which accounts for Coulomb attraction between charged defects and charge carriers. The drift-diffusion model is used for efficient simulations of semiconductor heterostructures and it requires material parameters as an input. On the other hand, density functional theory (DFT) ab initio model is used to simulate properties of semiconductors at nanometer scale.

The carrier injection efficiency is an important parameter for operation of the luminescent semiconductor devices. In such devices, light is emitted due to recombination of of charge carriers, electrons and holes, which have to be transported to the active region, in particular to quantum wells. In the AlGaN structures, hole transport is considered to be most problematic, due to several factors, in particular to poor p-type acceptor efficiency, high electron escape, and nonradiative recombination. While polarization doping can be used instead of an efficient acceptor, there is still the problem of electron escape. Electrons which escape the active region either recombine, mostly nonradiatively, with holes in the p-type, preventing them from reaching quantum wells, or they reach the p-type contact, where they thermalize. Both processes result in device heating and decreases its efficiency.

We performed the initial calculations to fit the simulation parameters and then we simulated the structures developed by Japanese experimental groups. Simulations confirmed that introduction of the EBL, which is separated from the graded p-cladding by an additional interface, increase the hole injection efficiency within the specified operation parameters. The results indicate that it may still be improved by slight modifications of the structure. Moreover, the additional interface is only necessary if the effective electron mass in the semiconductor material is low, as otherwise the p-cladding interface alone is sufficient to provide an effective barrier for electrons. The ab initio simulation results were used for calculations of material parameters (for interfacial/bulk polarization charge estimation). It was shown that the linear material gradient introduces an uniform polarization charge within the graded region. Results included AlGaN and also InGaN alloys, the latter being used in devices emitting blue or green light.

Electron escape from the active region is not the only source of low hole injection efficiency to the quantum wells. Another problem is related to nonradiative recombination, especially in the active region, where both electron and hole concentrations are high. To dwell into this problem, a theoretical analysis of the Shockley-Read-Hall(SRH) recombination was performed. New model was developed, which accounts not only for thermal velocity of the carriers, which is standard, but additionally for Coulomb attraction between charged deep defects and approaching charge carriers. Depending on the doping, the latter effect may have different impact on the nonlinear recombination rate. What is more, it does not vanish at low temperatures. The mathematical estimates of the SRH recombination rate with the new model were derived.

List of publications:

- Conference poster: K. Sakowski, A. Ahmad, P. Strak, P. Kempisty, Y. Kangawa, J. Piechota, S. Krukowski, *A numerical study of UV AlGaN heterostructures with polarization doping*, 14th International Conference on Nitride Semiconductors ICNS-14, 12–17.11.2023, Fukuoka
- Preprint, submitted: K. Sakowski, P. Strak, P. Kempisty, J. Piechota, I. Grzegory, P. Perlin, E. Monroy, A. Kaminska, S. Krukowski, *Coulomb contribution to Shockley-Read-Hall recombination*, arXiv, https://doi.org/10.48550/arXiv.2310.11823

国際化推進共同研究概要

No.23

22RE-3

タ イ ト ル: AI-based Interactive Integrated Design, a novel method for Floating Offshore Wind Turbines Design and Optimisation

研究代表者: HU Zhiqiang

所内世話人: 胡　長洪

研 究 概 要:
浮体式洋上風力発電システム用のセミサブ型浮体の運動特性解析に Software-in-the-Loop 法と AI 技術を応用する国際化推進共同研究について今年度はは 2 年目で、予定通り実施した。特に、Digital Twins の応用について研究を行い、有望な成果が得られた。2024 年１月に応力研で開催されたオンライン国際研究集会「The 2nd International Symposium on Marine Renewable Energy System Dynamics」に参加し、「Offshore Wind and Artificial Intelligence: Steps to Real-time Monitoring and Digital Twins for Offshore Wind Turbines」のタイトルで共同利用成果の発表を行い、参加者との研究交流を行った。

Report for 2023 RIAM International Joint Research Project

[23RE-3]

AI-based Interactive Integrated Design, a novel method for Floating Offshore Wind Turbines Design and Optimization

Zhiqiang Hu
Marine, Offshore and Subsea Technology, School of Engineering, Newcastle University, UK

This collaborative research between RIAM Kyushu University and Marine Offshore and Subsea Technology group, Newcastle University was planned in the year 2022, aiming to propose an AI-based interactive Integrated Design and Optimization method for the development of floating offshore wind turbines. This project continued in year 2023 by the same research groups.

This method was initially proposed based on the novel concept SADA, which was brought out by Zhiqiang Hu and Peng Chen on a journal Ocean Engineering publication in year 2020. The fundamentals of SADA were introduced on RIAM symposium in year 2021 and an engineering practice case-of-study was also presented on RIAM symposium in year 2022.

From year 2023, Zhiqiang Hu led his research team at Newcastle University, devoting into the research developing SADA and integrating the AI technology in a further step with monitoring and maintenance of FOWT, to solve the challenges for lowing O&M cost and achieve digital twins for offshore wind industry. During the year of 2023, the collaborative research outcomes are listed as below.

1) The 2nd International Symposium on Marine Renewable Energy System Dynamics was held at RIAM Kyushu University in Jan 2024. Zhiqiang Hu made a presentation on the topic of ‘Offshore Wind and Artificial Intelligence: Steps to real-time monitoring and Digital Twins for offshore wind turbines’. In this presentation, Zhiqiang firstly presented a strategy to realize digital twin system for monitoring and prediction of offshore wind turbines, via the AI technology, SADA method and Inverse SADA method. This presentation attracted many attentions from the audience and a fruitful discussion with other attendants was made during the symposium.

2) During year 2023, the collaborative research has been carried out to extend the AI-based Interactive Integrated Design method into the digital twins’ application field. During this investigation, the proposed method was updated to digital twin level. With the SADA concept which is an AI-based method, the Inverse SADA method is currently under investigation. When the updated Inverse SADA method is completed, it can work together with SADA to realize the digital twin for offshore wind turbines. The first engineering practice case will be put on the monitoring of scour development of fixed-bottom offshore foundation.

3) Based on the research in year 2023, a collaborative conference paper entitled ‘Time-domain

Integrated Analysis of Multi-segment Mooring System for Floating Offshore Wind Turbines' was written, and the abstract was submitted to EAWE Conference 2024. Unfortunately, due to the first author's personal healthy circumstance, the full paper was not submitted successfully. But the research team has a plan to resubmit the paper to some other conference in year 2024.

4) Another collaboration outcome is PhD exchanging between Kyushu University and Newcastle University. Mr Chaozhi Qiu, a PhD in RIAM, started an academic visit at Newcastle University on Nov 2023 and would stay at NU for four months. During his visit at Newcastle University, he followed lectures, attended academic events, and discussed with Zhiqiang Hu, all of which benefiting his PhD research on multi-rotor FOWT.

In year 2024, the collaborative research between Newcastle University and Kyushu University will be conducted to a further step. The focus will be put on the digital twins system application on O&M for offshore wind. The development of Inverse SADA method is the key challenge, but it is promising to benefit offshore wind industry. In addition, the symposium at RIAM will also be upgraded to a conference. It is expected to make further improvement of the collaborative project within year 2024 and present the research outcomes in the new conference.

国際化推進共同研究概要

No. 24

23RE-4

タイトル： Mooring design and coupled dynamic analysis of wave energy converter and its mooring system under typical sea states

研究代表者： XIANG Gong

所内世話人： 劉　盈溢

研究概要：　従来の懸垂型または半張力型係留綱と比較し、張力型係留システムは浮体式波力発電装置の発電中において係留綱の負荷、侵食、疲労損傷の削減など、多くの面で優れる。本論文では、点状吸収型波力発電装置向けの大きな伸縮を経験できる合成繊維係留綱から成る張力型係留システムを提案する。点状吸収装置の係留動態を調査するために、有限要素法（FEM）に基づく引張係留綱モデルが提案された。開発された係留綱モデルを用いた時間領域モデリング手法を採用し、三本の張力型係留綱によって係留される点状吸収装置基礎の動態を規則的な波下で調査した。本論文で提案された新しい引張係留綱モデルと従来の硬直係留綱を用いた計算結果を、基礎の動的応答と係留綱の張力について比較した。提案された引張係留綱モデルは、浮体式波力発電装置の上下運動および前後運動、三本の張力型係留綱のフェアリードにかかる張力の予測精度を向上させることが分かった。

国際化推進共同研究報告書

No.
23RE-4

タ イ ト ル: Mooring design and coupled dynamic analysis of wave energy converter and its mooring system under typical sea states

研究代表者: XIANG, Gong

所内世話人: 劉 盈溢

Introduction

In the past decades, an increasing number of floating marine systems have been designed, produced and operated in the sea to adhere to the demand of exploring the ocean energy resources deeper and further away from the land [1-5]. The typical floating systems for harvesting ocean resources include traditional oil and gas platforms [2,6,7], as well as renewable energy devices, such as wind turbines, tidal/current turbines, wave energy converters and their associated operational systems [4,8,9,10].

There are three main types of mooring design for floating wave energy converters: the catenary mooring system, semi-taut mooring system, and taut mooring system. Most of the mooring systems under operations are catenary or semi-taut. Several catenary mooring configurations were proposed that could be accomplished with single or multi-connections [1]. Astariz and Iglesias [11] found the most appropriate mooring was CALM (catenary anchor leg mooring), which has the advantages of easy installation, lower cost, and fewer effects of corrosion. However, the use of catenaries may suffer from wear and fatigue damage and affect the structure safety due to vortex-induced vibration. Gao and Moan [12] also pointed out that a catenary line system usually consisting of chain links relies on the weight of links or clump weights to provide horizontal restoring force. If no clump weight is used, a long mooring line of chain links must be considered to obtain adequate flexibility. Furthermore, catenary line systems will bring large, vertically downward loads to the floating structures. This could limit the allowable deck loads for floating wave energy converters. Therefore, this concept might not be suitable in shallow waters.

As shown in Fig.1, with synthetic fibers becoming very promising mooring materials, the taut mooring system can also be treated as a good alternative to a mooring system for floating wave energy converters. New materials, such as AI foam, might also be used for the composition of the mooring lines after enhancement of the structural strength. The diameter sizes of those synthetic fiber ropes used for commercial purposes vary within the range of 16 mm to 240 mm [13] and are typically made of nylon (polyamide), polyester (polyethylene terephthalate), aramid (para-aramid), or HMPE (high-modulus polyethylene). Synthetic fiber ropes are significantly lighter than other materials and, therefore, can be used in the water column of a taut mooring system. Casaubieilh [14] found that the new generation of mooring system, taut configuration using tether mooring lines, can significantly reduce the loads on mooring lines, floating structure, and anchors, and it can also reduce the device excursions when compared to the conventional catenary moorings. The elastic properties of fiber ropes are also of interest to damp mooring loads, and they avoid snap loads [13].

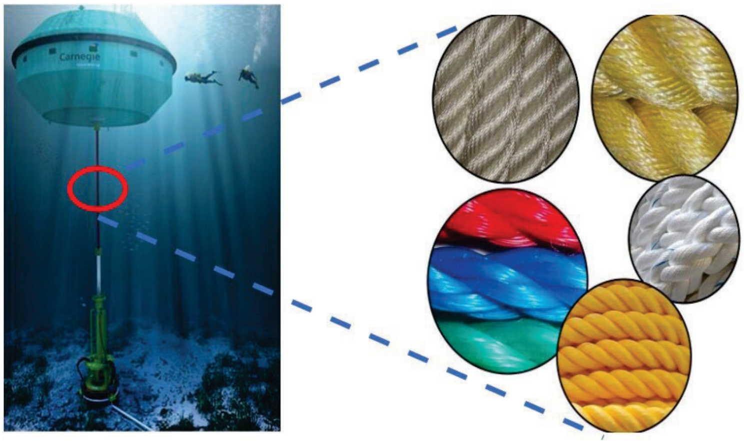

Fig. 1 Synthetic fibers applied into the taut mooring system of floating device

In this study, a time domain modelling method is proposed to study the dynamics of a point absorber-type wave energy converter moored by the synthetic fiber mooring lines under regular waves. The simulations of motion response and the tension force on the mooring lines at the fairlead of the foundation with a three-point (T3) taut mooring system under regular waves are studied using traditional stiff and proposed tensile mooring line model. The dynamics of a spar-type floating wave energy converter foundation moored by synthetic fiber mooring lines of different lengths and pretensions have been simulated. Comparative performance analysis of two-point (T2) and three-point (T3) taut mooring systems are also conducted.

Methodology

Dynamics of a tensile mooring line

The mooring line is generally treated as a slender rod when studying its dynamics. In a 3-D Cartesian coordinate system, the rod is expressed as a function of time t and the arc length s along the rod, namely a position vector, r(s, t) as shown in Fig.2. In Fig.2, the unit vectors in tangential, normal and binormal directions are expressed by t, n and b, respectively. The rod tensile is usually assumed to allow for large axial elongation, that is, the original arc length is s while the deformed arc length is $\bar{S}$ as shown in Fig.2.

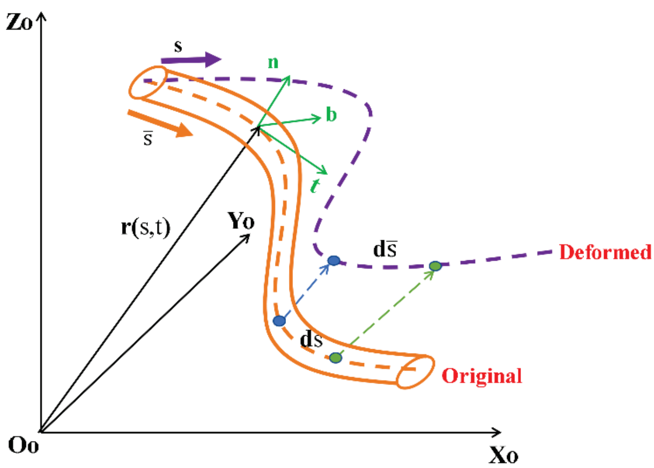

Fig.2.The rod in original and deformed state

For a slender rod, the equations of motion are developed based on general conservation of linear momentum and moment of momentum and can be expressed as,

$$\tilde{\mathbf{M}}' + \mathbf{r}' \times \mathbf{F} + \mathbf{m} = 0 \tag{1}$$

$$\mathbf{F}' + \mathbf{q} = \rho \ddot{\mathbf{r}}(s,t) \tag{2}$$

Where, q is the external load acting on the rod per unit length, ρ and m is the mass and the external moment per unit length, respectively. The symbol of prime indicates the space derivative with respect to s, while the symbol of superposed dot represents time derivative. Correspondingly, F is the total force acting at a point while $\tilde{\mathbf{M}}$ is the total moment acting at the centerline of the rod.

Based on the Bernoulli-Euler theory, the related total moment $\tilde{\mathbf{M}}$ can be expressed by

$$\tilde{\mathbf{M}} = \mathbf{r}' \times (B\mathbf{r}'') + H\mathbf{r}' \tag{3}$$

By merging Eqs.2~3, the equations of motion of slender rod are represented by

$$\mathbf{r}' \times (B\mathbf{r}'')' + H'\mathbf{r}' + H\mathbf{r}'' + \mathbf{r}' \times \mathbf{F} + \mathbf{m} = 0 \tag{4}$$

For a tensile mooring line such as the studied synthetic fiber rope here, it is regarded as a long slender tensile rod with negligible moments and shear forces which can also experience large elongations. As a result, the bending stiffness B, the torsional stiffness H, and the shear deformations can be all neglected in the above equations. Therefore, the only remaining internal force is caused by the cable tension tangential to the local direction. Finally, the governing equation is simplified as

$$(\lambda \mathbf{r}')' + \mathbf{q} = \rho \ddot{\mathbf{r}} \tag{5}$$

where λ is the Lagrange multiplier. The total external forces applied on a submerged slender rod per unit length are

$$\mathbf{q} = \mathbf{q}_{F-K} + \mathbf{q}_I + \mathbf{q}_D + \mathbf{q}_B + \mathbf{q}_G \tag{6}$$

where the first three terms represent the hydrodynamic forces including Froude-Krylov force, $\mathbf{q}_{F-K}$, added mass force, $\mathbf{q}_I$, and drag force, $\mathbf{q}_D$; Here $\mathbf{q}_D$ stands for the damp forces which is dependent on the velocities of the mooring line. It is noted that the fourth term, $\mathbf{q}_B$ is hydrostatic force; the last term, $\mathbf{q}_G$ is the Gravity force. The total force **q** can be also expressed in detail as

$$\mathbf{q} = \rho A\left(\mathbf{I} + C_{\mathrm{Mn}}\mathbf{N} + C_{\mathrm{Mt}}\mathbf{T}\right)\mathbf{a} + \frac{1}{2}\rho D C_{\mathrm{Dn}}\mathbf{N}\left(\mathbf{v} - \dot{\mathbf{r}}\right)\left|\mathbf{N}\left(\mathbf{v} - \dot{\mathbf{r}}\right)\right|$$

$$+\frac{1}{2}\rho D C_{\mathrm{Dt}}\mathbf{T}\left(\mathbf{v} - \dot{\mathbf{r}}\right)\left|\mathbf{T}\left(\mathbf{v} - \dot{\mathbf{r}}\right)\right| + \frac{\left(\rho A - \rho_t A_t\right) g\mathbf{e}_{\mathrm{y}}}{\left(1 + \cdot\right)} \tag{7}$$

where T=r'Tr' and N=I-T, C_{Mn}, C_{Mt}, C_{Dn}, and C_{Dt} are added mass coefficients in normal and tangential direction, drag coefficients in normal and tangential direction, respectively while A_t, A and D denote the area of geometric cross section of the rod, the area of outer cross section of the rod and the diameter of the outer cross section of the rod. In the fluid domain, **v** and **a** represent velocity and acceleration of the ambient fluid. where the subscripts f, i and t denote the sea water, the fluid inside the tube and the tube itself.

At the same time, the dynamics of n tensile mooring line can be calculated in rectangular Cartesian coordinates. The governing equation and constraint equation for a tensile mooring line can be also expressed as.

$$\frac{\partial(T\mathbf{t})}{\partial s} + \mathbf{q} = \rho\ddot{\mathbf{r}} \tag{8}$$

where T is the local tension, s is original length between one end to a waypoint along the rod, $\bar{S}$ is deformed length, t is the unit vector tangential to the deformed length expressed by $\mathbf{t} = \frac{\partial \mathbf{r}}{\partial s}$. The relation between deformed length and original length can be described as:

$$d\bar{s} = (1 + \varepsilon)ds \tag{9}$$

$$\varepsilon = \frac{T}{EA} \tag{10}$$

where EA is the axial stiffness of the slender rod.

Therefore,

$$\mathbf{r}' = \frac{\partial \mathbf{r}}{\partial s} = \frac{\partial \mathbf{r}}{\partial \bar{s}}(1 + \varepsilon) = \mathbf{t}(1 + \varepsilon) \tag{11}$$

$$\mathbf{t} = \frac{\mathbf{r}'}{1 + \varepsilon} \tag{12}$$

Substitute Eq. (12) into Eq.(8),

$$(\frac{T}{1 + \varepsilon}\mathbf{r}')' + \mathbf{q} = \rho\ddot{\mathbf{r}} \tag{13}$$

By comparing Eq.(13) and Eq.(5), the Lagrange multiplier λ is defined as

$$\lambda = \frac{T}{1+\varepsilon} \tag{14}$$

Substitute Eq.(14) into Eq.(10),

$$\varepsilon = \frac{T}{EA} = \frac{\lambda}{EA\text{-}\lambda} = \frac{\frac{\lambda}{EA}}{1\text{-}\frac{\lambda}{EA}} = \frac{\bar{\varepsilon}}{1\text{-}\bar{\varepsilon}} \tag{15}$$

$$\bar{\varepsilon} = \frac{\lambda}{EA} \tag{16}$$

Additionally, r must satisfy a stretching constrain equation:

$$\mathbf{r}' \cdot \mathbf{r}' = (1+\varepsilon)^2 \tag{17}$$

By substituting Eq.(15) into Eq.(17),

$$\mathbf{r}' \cdot \mathbf{r}'(1-\bar{\varepsilon})^2 = 1 \tag{18}$$

Finite Element Simulation Approach

A global-coordinate-based nonlinear finite element method is used for the simplicity of numerical computation. The Galerkin's method was used to discretize the dynamic equations in space, resulting into a set of nonlinear 2nd-order ordinary differential equations in the time domain. Finally, a Newmark-β method was employed for time-domain integration of the discretized equations. For each element, the mooring line dynamic equation at the *K*th time step becomes:

$$\gamma_{ikm} M_{njm} \ddot{u}_{kj} + \beta_{ikm} \lambda_m u_{kn} = \mu_{im} q_{mn} + f_{in} \tag{19}$$

The coefficients in Eq.(19) are obtained through integration over the length of the element :

$$\begin{aligned} \beta_{ikm} &= \frac{1}{L} \int_0^1 a_i'(\xi) a_k'(\xi) p_m(\xi) d\xi \\ \gamma_{ikm} &= L \int_0^1 a_i(\xi) a_k(\xi) p_m(\xi) d\xi \\ \mu_{im} &= L \int_0^1 a_i(\xi) p_m(\xi) d\xi \end{aligned} \tag{20}$$

Similarly, the constrain equation is discretized as

$$\beta_{ikm}u_{in}u_{kn}+\eta_{iklm}(-2\overline{\varepsilon}_l+\overline{\varepsilon}_l^2)u_{in}u_{kn}-\tau_m=0 \tag{21}$$

The coefficients in Eq.(21) are obtained through integration over the length of the element :

$$\tau_m=L\int_0^1 p_m(\xi)d\xi$$
$$\eta_{iklm}=\frac{1}{L}\int_0^1 a_i'(\xi)a_k'(\xi)p_l(m)p_m(\xi)d\xi \tag{22}$$

where, a(s) is the Hermite cubic shape function, and p(s) is the quadratic shape function, ξ is a nondimensional position expressed as ξ=s/L, L is the original length of the element.

During simulations, the tensile mooring line is discretized into 100 line elements each of which should be solved as per the relation expressions in Eq.(19) and (21) using Newmark-β method. The boundary conditions for the finite element simulations of the mooring lines include that the first element is attached to the fairlead of the floating point absorber while the 100th element gets connected to the seabed. Therefore, the first element will transfer the pretension force to the point absorber and in turn will move following the motion of the point absorber. For the last element, it is treated to be fixed at the seabed. To begin with the dynamic analysis of the mooring lines, static analysis is conducted to achieve the static equilibrium position, namely, the initial condition for mooring dynamic analysis. The time step is set as 0.05s to achieve the independence while the whole simulation time lasts 30 wave excitation time cycles. After the simulation is finished, totally 15 unknowns relating to u and λ can be obtained.

Coupling dynamics of floating point absorber with taut mooring system

To accomplish the coupling dynamic analysis of a floating point absorber foundation with taut mooring system as shown in Fig.1, the equations of motion for the foundation shown in Eqs.(23)-(24) and mooring lines shown in Eq.(5) and Eq.(18) are solved simultaneously using Newmark-β method. The six degree-of-freedom (6-DOF) nonlinear motion equations of a rigid body were derived as follows:

$$m\ddot{\xi}+m\mathbf{T}^t\left(\dot{\boldsymbol{\omega}}\times\mathbf{r}_g\right)+m\mathbf{T}^t\left(\boldsymbol{\omega}\times\left(\boldsymbol{\omega}\times\mathbf{r}_g\right)\right)=\tilde{\mathbf{F}} \tag{23}$$

$$\mathbf{I}\dot{\boldsymbol{\omega}}+\boldsymbol{\omega}\times\mathbf{I}\boldsymbol{\omega}+m\mathbf{r}_g\times\left(\mathbf{T}\ddot{\xi}\right)=\mathbf{M} \tag{24}$$

The translational motion and the rotational motion of a rigid body are expressed in the spaced-fixed coordinate system OXYZ with origin at O and the body-fixed coordinate system oxyz with origin at o, respectively. Where, ξ is the translational displacement of the body at point o in OXYZ, $\boldsymbol{\omega}$ is the rotational velocity in OXYZ, $r_g=(x_g, y_g, z_g)t$, is the point vector of mass center of the body in OXYZ, **I** is the moment of inertia of the body with respect to point o in OXYZ, T is a transfer matrix between the oxyz and OXYZ ; The total external forces $\tilde{\mathbf{F}}$

acting on the body in OXYZ and the total external moments with respect to ***o***, M can be unified by F as shown in

$$\mathbf{F} = \begin{bmatrix} \tilde{\mathbf{F}} \\ \mathbf{M} \end{bmatrix} \tag{25}$$

Correspondingly, the 6 DOF motion equations for the floating foundation can be derived as

$$\left[\mathbf{M}_b + \mathbf{M}_a\right]\ddot{\mathbf{X}}(t) + \mathbf{CX}(t) = \mathbf{F}_H + \mathbf{F}_{Morison} + \mathbf{F}_M + \mathbf{F}_\varepsilon \tag{26}$$

$$\mathbf{F}_e = \begin{Bmatrix} -m\mathbf{T}^t(\boldsymbol{\omega}\times(\boldsymbol{\omega}\times\mathbf{r}_g)) - m\mathbf{T}^t(\boldsymbol{\alpha}_q\times\mathbf{r}_g) \\ -\boldsymbol{\omega}\times\mathbf{I}_o\boldsymbol{\omega} - \mathbf{I}_o\boldsymbol{\alpha}_q \end{Bmatrix} \tag{27}$$

Where $\mathbf{M}_b$ and $\mathbf{M}_a$ are the mass and added mass of the foundation respectively, C is the hydrostatic stiffness matrix, $\mathbf{F}_H$ represent nonlinear hydrostatic restoring forces, $\mathbf{F}_{Morison}$ denotes Morison forces, and $\mathbf{F}_M$ refers to mooring line forces. The generalized form of Eq.(26) can be expressed as

$$\mathbf{A}\ddot{\mathbf{X}}(t) + \mathbf{CX}(t) = \mathbf{F}(t) + \mathbf{F}_M(t) \tag{28}$$

where, $\mathbf{F}_M(t)$ denote mooring line forces and $\mathbf{F}(t)$ denote the rest of forces. At the Kth time step, the motion equation can be re-written in the following form

$$\mathbf{A}^{(K)}\ddot{\mathbf{X}}(t)^{(K)} + \mathbf{C}^{(K)}\mathbf{X}^{(K)} = \mathbf{F}^{(K)} + \mathbf{F}_M{}^{(K)} \tag{29}$$

Correspondingly, a numerical modelling code, which is composed of a main program and a subroutine program is developed. The subroutine program namely a mooring dynamics program developed accordingly is called by the main program at each time step to calculate the motions of the foundation. It should be noted that the values of f_{in} in Eq.(19) are transmitted to $\mathbf{F}_M{}^{(K)}$ in Eq.(29) through the hinged boundary conditions.

Results

The floating point absorber foundation coupled with a T3 mooring system is simulated according to the proposed methodology. Fig.4 shows the comparison of surge and heave motions using the traditional stiff mooring line model and tensile mooring line model proposed in this paper respectively. Through the comparisons, it is found that the surge and heave motions of the foundation using the traditional stiff mooring line model will underestimate the range of the motion responses of the foundation. In a real situation, the elongation of the mooring line cannot be ignored since the elongation of the mooring line will make the whole floating point absorber system less stiff and more elastic. Fig.3 shows the comparison of corresponding tension forces at the fairlead of three mooring lines. It can be found that tensions at Line 1 and Line 2 calculated by stiff mooring line model are much larger than stiff mooring line model. This is because the surge motion of the foundation is larger in the tensile mooring line model than in stiff mooring line mode; much larger tension forces at the fairlead of mooring lines 1 and 2, whose configurations are more aligned with surge direction are required to limit the surge responses of the foundation. Also, it is noted that the mooring line is made of Polyester, which, in reality, can hardly be compressed. But in Fig.3, it is observed that if using the traditional mooring line model, the calculated minimum mooring tension force of line 3 is much smaller than zero, which means the mooring line can be compressed a lot during wave-induced dynamic motions. By ignoring the bending stiffness of the mooring line, the proposed tensile mooring line model can overcome the inaccuracy of predicting the compressions of the elastic mooring line, such as polyester, using the traditional stiff mooring line model.

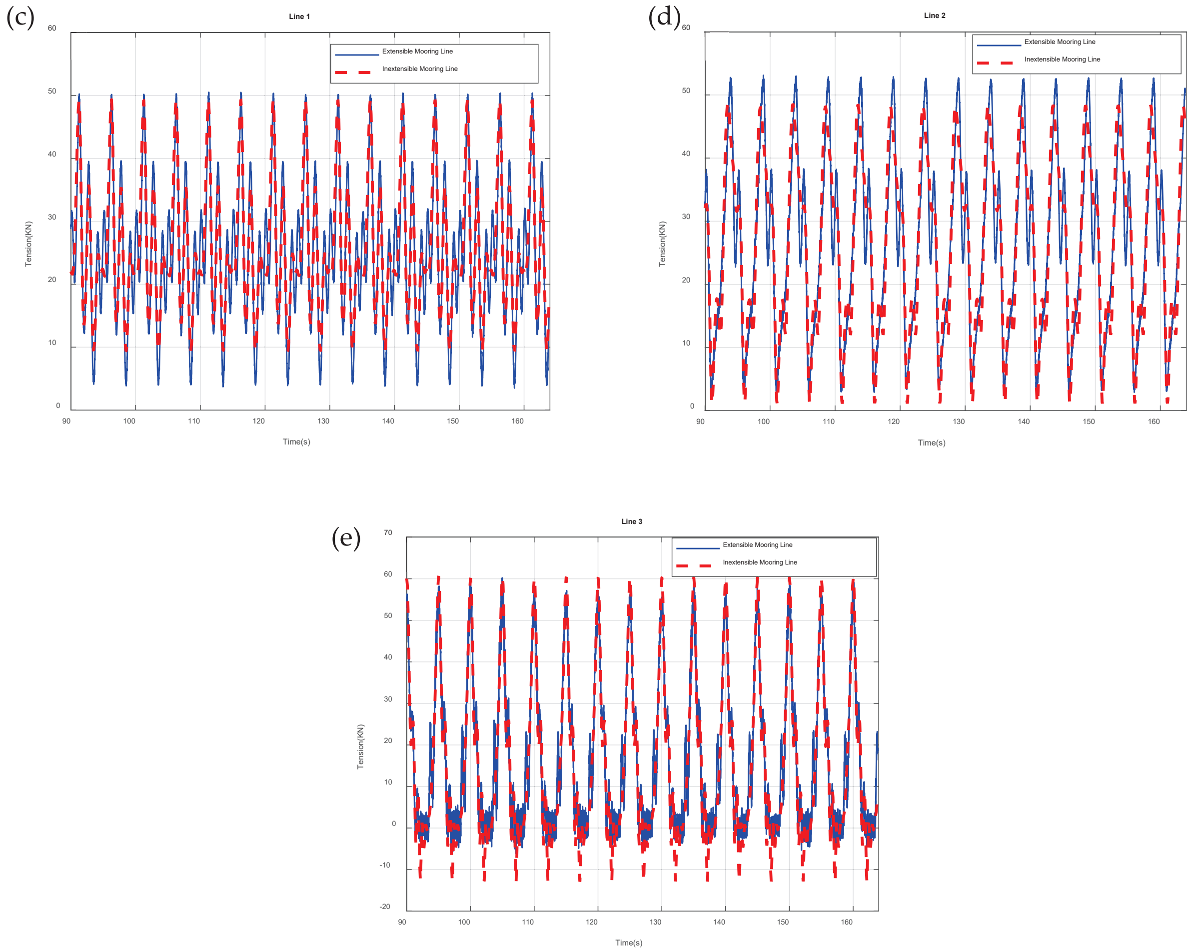

Fig.3. Comparison of time series of surge and heave motion time series, mooring tension at the fairlead using traditional stiff line model and proposed tensile mooring line model,(a) Surge (b) Heave (c) Line 1 (d)Line 2 (e) Line 3

References

1. Fitzgerald, J., and Lars, B., 2008. Including Moorings in the Assessment of a Generic Offshore Wave Energy Converter: A Frequency Domain Approach. Marine Structures 21 (1): 23–46. doi:10.1016/j.marstruc.2007.09.004.

2. Kim, J.D., Jiang, B.S., 2016. Application of multi-objective optimization for TLP considering hull-form and tendon system. Ocean Engineering, 116: 142-156.
3. Xiang, X.B., Yu, C.Y., Zhang, Q., 2017. On intelligent risk analysis and critical decision of underwater robotic vehicles. Ocean Engineering, 140: 453-465.
4. Sergiienko, N.Y., Rafiee, A., Cazzolato, B.S., Ding, B., and Arjomandi, M. 2018. A feasibility study of the three-tether axisymmetric wave energy converter. Ocean Engineering, 150:221-233
5. Wang, Z., Yang, S.L., Xiang, X.B., Vasilijevic´, A., Miškovic´, N, Nad, Đula., 2021. Cloud-based mission control of USV fleet: architecture, implementation and experiments. Control Engineering Practice, 106: 104657
6. Kang, H.S., Kim, M.H., Aramanadka, S.B., 2020. Numerical Analysis on Mathieu Instability of a Top-Tensioned Riser in a Dry-Tree Semisubmersible. Journal of Offshore Mechanics and Arctic Engineering 142 (2).
7. Subbulakshmiab, A., Sundaravadivelub, R. 2021. Effects of damping plate position on heave and pitch responses of spar platform with single and double damping plates under regular waves. Ocean Engineering, 224:108719.
8. Liu, Y., Yoshida, S., Hu, C., Sueyoshi, M., Sun, L., Gao, J., Cong, P., He, G., 2018. A reliable open-source package for performance evaluation of floating renewable energy systems in coastal and offshore regions. Energy Conversion and Management 174:516-536
9. Zhang, Q., Zhang, J.L., Chemori, A., Xiang, X.B., 2018. Virtual Submerged Floating Operational System for Robotic Manipulation. Complexity, 1–18. DOI: 10.1155/2018/9528313.
10. Bachynskia E., Thysb M., Delhayec. V., 2019. Dynamic response of a monopile wind turbine in waves: Experimental uncertainty analysis for validation of numerical tools. Applied Ocean Research, 89:96-114
11. Astariz, S., and G. Iglesias., 2015. The Economics of Wave Energy: A Review. Renewable and Sustainable Energy Reviews 45: 397–408.
12. Gao, Z., and Moan, T., 2009. Mooring system analysis of multiple wave energy converters in a farm configuration. Proceedings of the 8th European Wave and Tidal Energy Conference, Uppsala, Sweden.
13. Harnois, V. Analysis of Highly Dynamic Mooring Systems: Peak Mooring Loads in Realistic Sea Conditions. Ph.D. Thesis, University of Exeter, Exeter, UK, 2014.
14. Casaubieilh, P., Thiebaut, F., Sheng, W., Retzler, C., Shaw, M., and Letertre, Y., 2015. "Performance Improvements of Mooring Systems for Wave Energy Converters." Renewable Energies Offshore – Guedes Soares (Ed.) ©, no. Wang 2013: 897–903.

国際化推進共同研究概要

No.25

23RE-5

タイトル：Numerical prediction of annual power production of wave farms at an Australia or Japan localised site under multi-directional irregular sea wave conditions

研究代表者： DING Boyin

所内世話人： 劉　盈溢

研究概要： 波力発電施設の設置前に性能の事前評価が必要である。本研究では南東オーストラリアの 3 つの潜在的な場所で波力発電施設の最適な設置場所を分析した。生成電力の期待値は多重散乱理論及び多方向不規則波理論に基づいて数値的に予測され、最良の場所は他の 2 つの場所よりも約 2.6 倍から 6.0 倍ほど高い性能を示した。

Introduction

Ocean waves can supply a significant source of clean and renewable energy due to the vast ocean area on the earth [1]. These converters work collectively to generate electricity from the kinetic energy of ocean waves. Wave farms are situated either near the coast or offshore and typically comprise various devices, including floating buoys, oscillating water columns, or other wave energy converters, all interconnected to the electrical grid.

In this study, we aim to analyse the best location for wave farm deployment in a set of candidate sites. Figure 1 shows several potential sea sites in south-east Australia [2] to deploy wave energy devices, in which "CB" stands for Cape Bridgewater, "WP" stands for Wilson's Promontory, and "LE" stands for Lakes Entrance. We are going to predict the power expectation generated by a 2×3 small-scale wave farm to be deployed at these three sites, based on the multiple-scattering wave interaction theory.

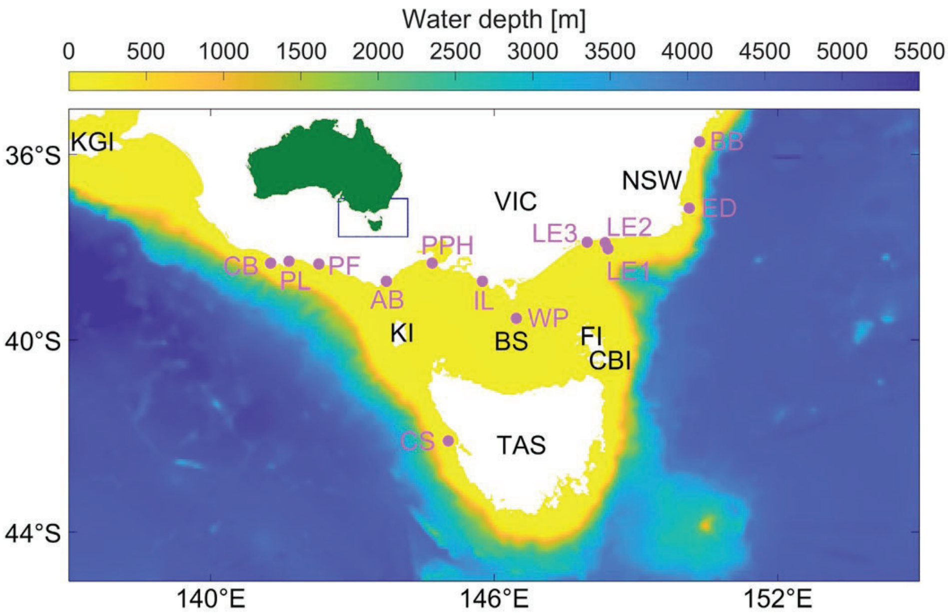

Figure 1. Potential sea sites in south-east Australia [2].

Multiple-scattering theory for wave energy arrays

Let us consider a train of regular incident waves that propagates to the positive x-direction with a small amplitude A, a heading angle β measured from the positive x-axis, and a wave number k, in water of a finite depth h. The ambient wave potential incident to body j can be written as

$$\phi_j^A(x_j, y_j, z_j) = -\frac{\mathrm{i}gA}{\omega}\frac{\cosh k(z_j+h)}{\cosh kh} e^{\mathrm{i}k[(x_j+\bar{x}_j)\cos\beta+(y_j+\bar{y}_j)\sin\beta]}, \tag{1}$$

where $(\bar{x}_j, \bar{y}_j, 0)$ refers to the origin of the local coordinate system of body j in terms of the global Cartesian coordinates and (x_j, y_j, z_j) refers to an arbitrary spatial point in terms of the local Cartesian coordinates. By converting the local Cartesian coordinates to the polar coordinates (r_j, θ_j, z_j), Eq. (1) can be expanded as a summation of partial cylindrical waves incident to the body *j* in the form of matrices

$$\phi_j^A(x_j, y_j, z_j) = \{a_j^I\}^T \{\psi_j^I\}, \tag{2}$$

where $\{a_j^I\}$ is a scalar vector of expansion coefficients, and $\{\psi_j^I\}$ is a scalar vector of the basis function that is also named as the incident partial wave component.

In arrays of floating bodies, each individual body experiences not only the ambient incident plane wave but also the outgoing waves that are scattered from all the other neighboring bodies in the arrays. Based on Graf's addition theorem, the scattered waves from body *i* can be expressed as incident waves to body *j* as the following equation

$$\phi_i^S(r_i, \theta_i, z_i) = \{A_i^S\}^T [T_{ij}]\{\psi_j^I\}, \tag{3}$$

where $\{A_i^S\}$ is a scalar vector of the scattering coefficients, and the *T*-transfer matrix yields

$$[T_{ij}]_{nn}^{mq} = \begin{cases} H_{m-q}(kL_{ij})e^{\mathrm{i}\alpha_{ij}(m-q)}, & n = 0, \\ K_{m-q}(k_n L_{ij})e^{\mathrm{i}\alpha_{ij}(m-q)}(-1)^q, & n \geq 1. \end{cases} \tag{4}$$

Using a so-called diffraction transfer matrix $[D_j]$ as the form that is defined in Liu et al. [3] based on the hybrid dipole-source formulation, the scattered wave from body *j* and all the incident waves to the same body can be connected based on the following relation

$$\{A_j^S\} = [D_j]\left(\{a_j^I\} + \textstyle\sum_{i=1,i\neq j}^{N_B}[T_{ij}]^T\{A_i^S\}\right), \quad (j = 1,2, \dots N_B), \tag{5}$$

where N_B is the number of wave energy converters. From Eq. (5), scattering coefficients and the wave potentials can be solved numerically. Wave excitation forces, etc., can be calculated via pressure integration over each body using matrix operations.

Wave farm performance in multi-directional irregular waves

According to Evans [4] and Falnes [5], in regular waves, the maximum absorbed power of a wave farm can be evaluated in terms of the wave excitation force and the radiation damping matrices:

$$\left(\textstyle\sum_{i=1}^{N_B} P_j(\omega, \beta)\right)_{max} = \frac{1}{8}\{F^E\}^*[B_{rad}]^{-1}\{F^E\}, \tag{6}$$

where $P_j(\omega, \beta)$ is the maximum absorbed power of each device, and the superscript * denotes complex conjugate transpose. In real seas, the overall generation power of the wave farm can be evaluated as

$$P = \int_{-\pi}^{\pi}\int_0^{\infty}\left(\textstyle\sum_{i=1}^{N_B} P_j(\omega, \beta)\right)_{max} S(\omega)G(\omega, \beta)\mathrm{d}\omega\mathrm{d}\beta, \tag{7}$$

where $S(\omega)$ is the localised wave frequency spectrum and $G(\omega, \beta)$ is the directional spectrum (also named as directional spreading function). In case of JONSWAP spectra, the frequency spectrum reads [6]

$$S(\omega) = \beta_J H_s^2 T_p^{-4} f^{-5} \exp[-\frac{5}{4}(T_p f)^{-4}] \gamma^{\exp[-(f/f_p - 1)^2/2\sigma^2]}, \quad (8)$$

where H_s is the significant wave height, T_p is the peak spectral period, f_p is the peak spectral period, γ is the peak shape parameter of a given irregular sea state and σ is a scaling factor. The directional spectrum yields

$$G(\omega, \beta) = C(n) \cos^{2n}\left(\frac{\beta - \beta_m}{2}\right), \quad (9)$$

where $n = H_s/2$ and β_m is the mean wave direction. The factorial function in Eq. (9) reads

$$C(n) = \frac{1}{\sqrt{\pi}} \frac{\Gamma(n+1)}{\Gamma(n+1/2)}. \quad (10)$$

Results

We consider designing a wave farm composed of 2×3 point absorbers (see Figure 2) at three sites in South-East Australia (see Figure 1). The wave energy device has a CorPower-like geometry (see Figure 3). The localised sea site information is listed in Table 1, sourced from Liu et al. [2]. By using the aforementioned methodology and considering the localised sea conditions (such as peak wave height, peak wave period mean wave direction, etc.), we numerically predicted the expected power generated by the potential wave farm. It is found that the Cape Bridgewater is best suitable to deploy the wave farm, which generates an overall wave power of 2.63 times that of Wilson's Promontory, and 6.04 times that of Lakes Entrance.

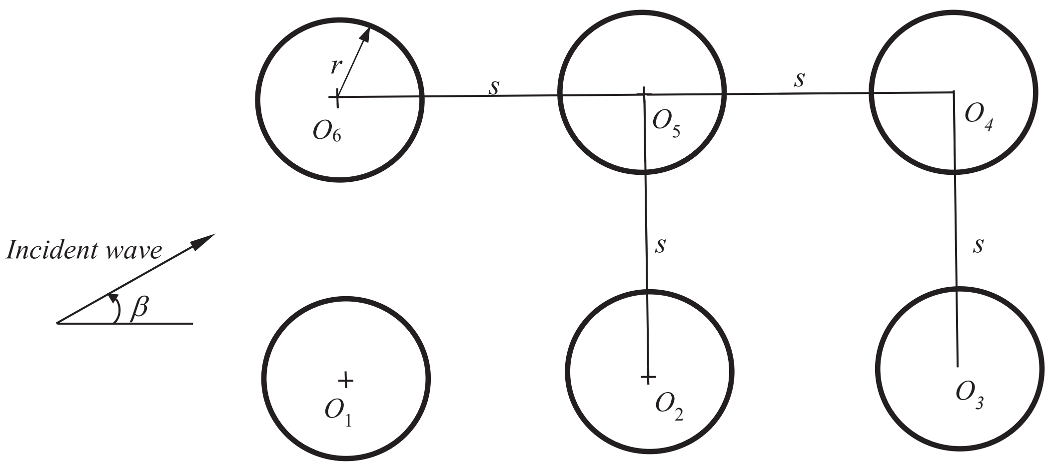

Figure 2. Array layout of the wave farm.

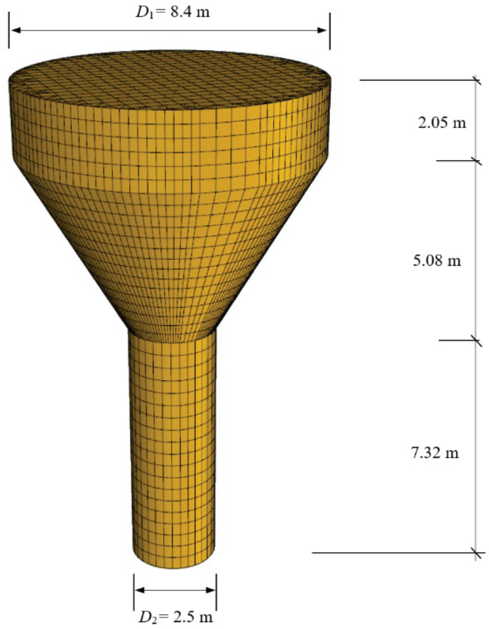

Figure 3. Surface mesh and geometrical dimensions of the point absorber device.

Table 1. Sea site information and the predicted wave power expectation.

Location	Longitude (°E)	Latitude (°S)	Depth (m)	Peak wave height (m)	Peak wave period (s)	Mean wave direction (°)	Expected power (kw)
Cape Bridgewater	141.27	38.36	66.88	2.52	12.5	225	15.144
Wilson's Promontory	146.47	39.54	75.98	1.74	7.65	240	5.756
Lakes Entrance	148.41	38.05	53.08	1.05	6.25	200	2.506

References

[1] Isaacs, J. D., and Schmitt, W. R. (1980). Ocean energy: Forms and prospects. Science 207, 265–273.

[2] Liu, J., Meucci, A., Liu, Q., Babanin, A. V., Ierodiaconou, D., & Young, I. R. (2022). The wave climate of Bass Strait and south-east Australia. Ocean Modelling, 172, 101980.

[3] Liu, Y., Liang, H., Kashiwagi, M., & Cong, P. (2021). Alternative approaches of evaluating diffraction transfer matrix and radiation characteristics using the hybrid source-dipole formulation. Applied Ocean Research, 114, 102769.

[4] Evans, D. (1979). Some theoretical aspects of three-dimensional wave-energy absorbers. Proceedings of the 1st Symposium on Wave Energy Utilization, Gothenburg, Sweden, pp.78–112.

[5] Falnes, J. (1980). Radiation impedance matrix and optimum power absorption for interacting oscillators in surface waves. Applied ocean research, 2(2), 75-80.

[6] Goda, Y. (1999). A comparative review on the functional forms of directional wave spectrum. Coastal Engineering Journal, 41(1), 1-20.

国際化推進共同研究概要

No. 26

23RE-6

タ イ ト ル： Fully nonlinear coupled motion and energy conversion characteristics study of an integrated system consisting of a floating offshore wind turbine and oscillating body wave energy converters

研究代表者： ZHOU, Binzhen

所内世話人： 劉　盈溢

研究概要： 浮体式洋上風力発電機と波力発電装置（WECs）から成るハイブリッドシステムは、複数の海洋再生可能エネルギーを抽出する有望な手段ですが、広範な運用海域における連成動的特性は、設計において重要な参考情報であるにもかかわらず、まだ十分に理解されていない。この研究では、AeroDyn（NREL）と独自開発の計算コードを組み合わせ、風力-波力-制御-係留の連成数値ツールを開発した。DeepCWind-Wave Stars および Hywind-annular WEC の動的特性、係留張力、エネルギー変換性能を分析した。その結果、WECs の存在が運用サイトのピーク波周期周辺で浮体の安定性を向上させることが示した。係留張力変動を減少させつつ、平均値をわずかに増加させる。生成された波力は、特に風速が小さい場合には風力に適した補完となる。

雑誌論文：

[1] Zhou, B., Zheng, Z., Hu, J., Lin, C., Jin, P., Wang, L., Liu, Y. (2023) Annual performance and dynamic characteristics of a hybrid wind-wave floating energy system at a localized site in the North Sea. Ocean Engineering, 280: 114872.

[2] Jin, P., Zheng, Z., Zhou, Z., Zhou, B., Wang, L., Yang, Y., Liu, Y. (2023) Optimization and evaluation of a semi-submersible wind turbine and oscillating body wave energy converters hybrid system. Energy, 282: 128889.

[3] Zhou, B., Wang, J., Ding, K., Wang, L., Liu, Y. (2023). Prediction of the Occurrence Probability of Freak Waves in Unidirectional Sea State Using Deep Learning. Journal of Marine Science and Engineering, 2023, 11(12): 2296.

Introduction

To fully use the abundant renewable energy resources in the ocean, co-located energy extraction by combining different kinds of ocean renewable energy equipment becomes a research frontier. Hybrid systems consisting of offshore wind turbines and wave energy converters (WECs) provide a promising scenario of sufficient use of the strong sea wind and high waves, offering an excellent synergetic application since the high winds and waves often coexist[1]. Such combinations also show several merits of mutual benefits in addition to more sufficient use of the local energy resource[2]. For example, wave energy is less developed than offshore wind energy and is still an industry in its early age, facing the problem of high cost[3]. By integrating WECs on an offshore wind turbine, the turbine can share infrastructure such as moorings, supporting structures, power grids, and maintenance with the WECs, helping reduce the cost of the WECs[4]-[6]. In turn, the power generated by the WECs can compensate for the shortage of power output of the wind turbine during its downtime, improving the stability of power generation[7]-[8]. Till now, many concepts of wind-wave hybrid systems have been proposed inspired by government or industrial support through innovative projects such as the EU EP7 MA-RINA[9]. Although many concepts of wind-wave hybrid systems have been proposed and extensively studied, none have been constructed and applied in the real world. Few of them are in the sea trail stage. The development speed of hybrid systems depends on the technological maturity of wind and wave energy equipment and their compatibility.

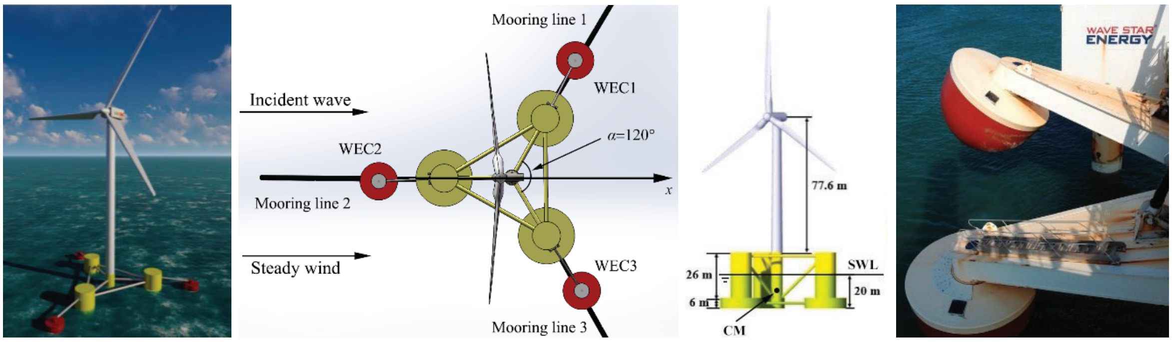

(a) Hybrid system (b) Configuration of hybrid system (c) DeepCWind (d) Wave Star

Fig. 1 Sketch and configuration of the DeepCWind-Wave Stars hybrid system and its components

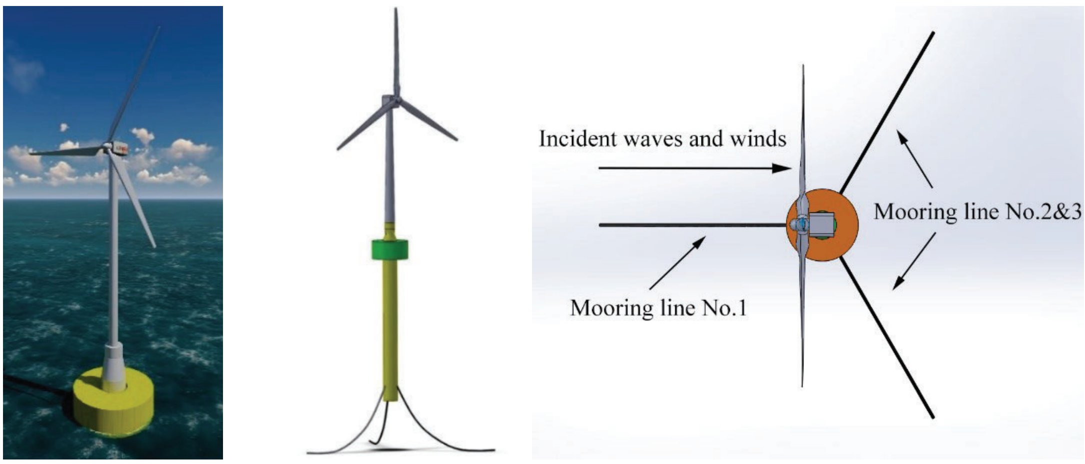

(a) 3D effect (b) Sketch of the hybrid system

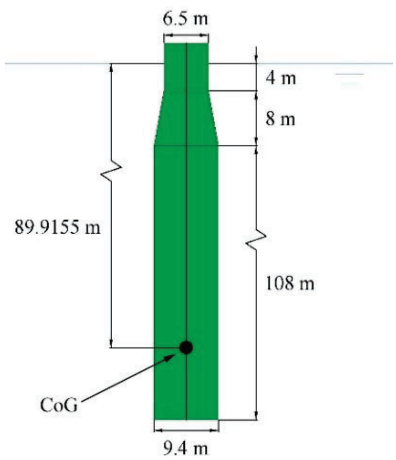

(c) Underwater part of the spar

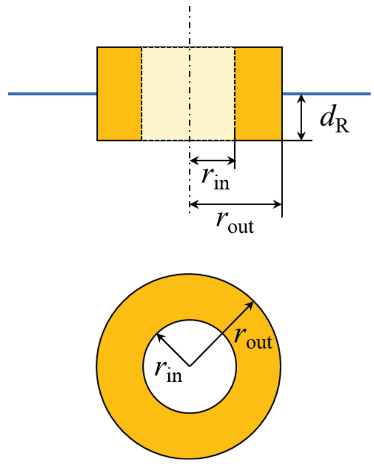

(d) Sketch of the annular WEC

Fig. 2 Layout of the Hywind-annular WEC hybrid system

In this study, two kinds of hybrid system are proposed as shown in Fig. 1 and Fig. 2. The dynamic response of the platform and both the wind and wave power performance of the hybrid system is investigated through the full aero-hydro-servo couplings numerical model, emphasizing on the influence of the addition of the WECs.

Methodology

Motion equations

Based on Cummins' equation, the matrix form multi-body motion equation of the DeepCWind-Wave Stars hybrid system is

$$[\mathbf{M}+\mathbf{A}_{\infty}]\ddot{\mathbf{X}}(t)+\mathbf{K}\mathbf{X}(t)+\int_0^t \mathbf{R}(t-\tau)\dot{\mathbf{X}}(\tau)d\tau=\mathbf{F}_{ex}(t)+\mathbf{F}_{c}(t) \tag{1}$$

where $\mathbf{X}(t)$, $\dot{\mathbf{X}}(t)$, and $\ddot{\mathbf{X}}(t)$ are the vectors of displacement, velocity, and acceleration, respectively. $\mathbf{M}$ is the matrix of mass. $\mathbf{A}_{\infty}$ is the matrix of added mass at infinite wave frequency. The inertia and hydrodynamic coefficients (added mass, radiation damping, and wave excitation force) of the floats are calculated using the WAFDUT code based on the potential flow theory of linear waves. $\mathbf{K}$ is the matrix of the hydrostatic restoration coefficient. $\mathbf{R}$ is the matrix of radiation impulse response function (RIRF). t and τ are time terms. $\mathbf{F}_c(t)$ is the constraint force, which can be dealt with using the augment method based on the Lagrange multiplier. $\mathbf{F}_{ex}(t)$ is the sum of external forces:

$$\mathbf{F}_{ex}(t)=\mathbf{F}_{wave}(t)+\mathbf{F}_{PTO}(t)+\mathbf{F}_{wind}(\mathbf{X},t)+\mathbf{F}_{moor}(\mathbf{X},t)+\mathbf{F}_{vis}(t) \tag{2}$$

where $\mathbf{F}_{wave}(t)$, $\mathbf{F}_{PTO}(t)$, $\mathbf{F}_{wind}(t)$, $\mathbf{F}_{moor}(t)$, and $\mathbf{F}_{vis}(t)$ are the wave excitation force, power take-off force, aerodynamic force, mooring force, and fluid viscous force, respectively.

Power take-off model

Linear power take-off damping b_{PTO} is assumed and it is also assumed that the amount of stiffness k_{PTO} is zero. As for the flap-type WEC, the power take-off force on the hinge and the wave power generated by a Wave Star are:

$$F_{\mathrm{PTO}} = b_{\mathrm{PTO}}\dot{\theta}(t) \tag{3}$$

$$P = F_{\mathrm{PTO}}\dot{\theta}(t) = b_{\mathrm{PTO}}\dot{\theta}^2(t) \tag{4}$$

where θ and $\dot{\theta}$ are the angular displacement and velocity relative to the hinge, respectively, with

$$\theta = \arccos\sqrt{\frac{(L^2_{\mathrm{JW}} + L^2_{\mathrm{JP}} - L^2_{\mathrm{WP}})}{2\times L_{\mathrm{JW}}\times L_{\mathrm{JP}}}} \tag{5}$$

where L_{JW}, L_{JP} and L_{WP} are the characteristic lengths illustrated in Fig. 3.

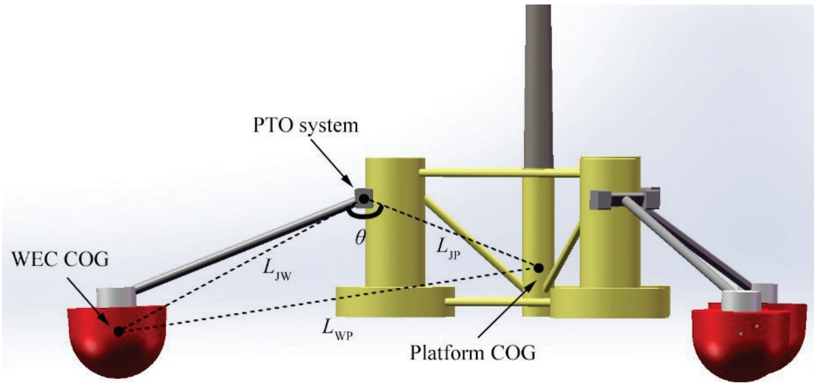

Fig. 3 Profile of the Wave Stars in the hybrid system

As for heave-type WEC, the instant wave power generated through the relative heave motion of the platform and the WEC is:

$$P_{\mathrm{wave}}(t) = \frac{1}{2}b_{\mathrm{PTO}}\left|\dot{z}_{\mathrm{Platform}}(t) - \dot{z}_{\mathrm{WEC}}(t)\right|^2 \tag{6}$$

The aero-hydro-servo couplings framework

The full aero-hydro-servo couplings in the hybrid system are included in the present model, and its framework is shown in Fig. 4. The wind turbine is simulated by the aero-servo module of OpenFAST. The coupled frequency-domain hydrodynamic coefficients of the floats, including added mass, radiation damping, and wave excitation force, are calculated by the WAFDUT code developed by the Dalian University of Technology based on a Higher Order Boundary Element Method (HOBEM). The mooring loads are calculated based on the catenary theory. All three tools are compiled by Fortran language. An in-house code also compiled by Fortran is developed to create interfaces to bridge the three. The in-house code also simulates the multi-body constraint dynamics, performs the frequency-to-time domain transformation of the multi-body motion equation, and calculates the wave power. The wind power is calculated by OpenFAST. The aerodynamic loads on the blades, nacelle, and tower are calculated by OpenFAST according to the wind speed and position of the turbine and are delivered by the in-house code to calculate the motion of the platform. The displacement and velocity of the platform are in turn delivered by the in-house code to the turbine. The mooring loads are calculated according to the motion of the platform and delivered by the in-house code to the platform.

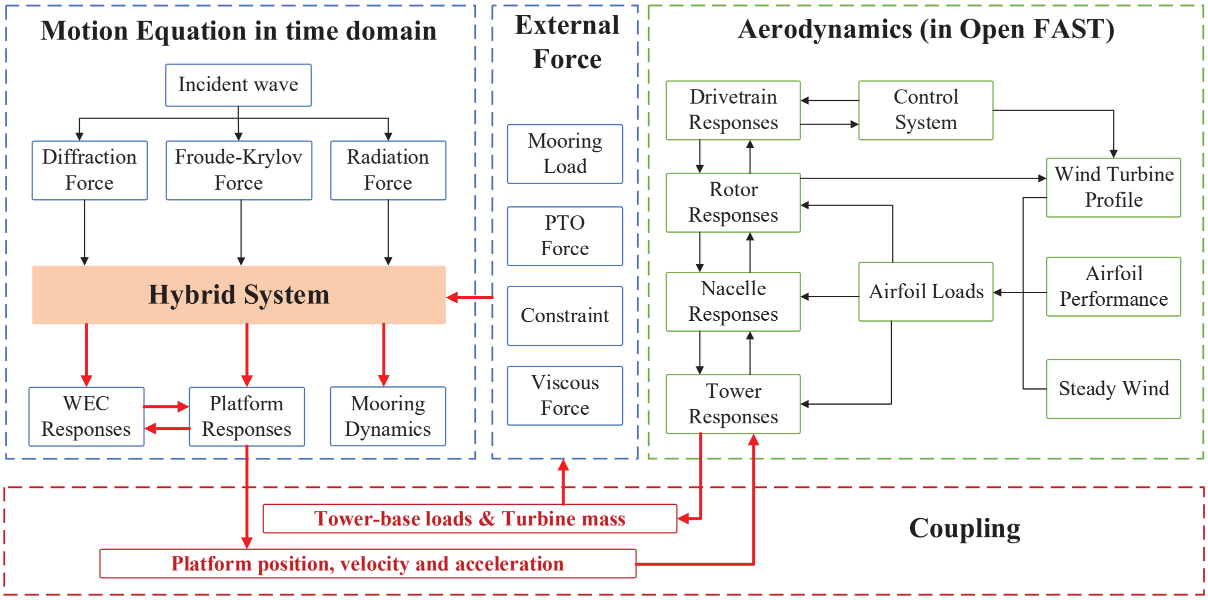

Fig. 4 Coupling framework of the present numerical model

Results

DeepCWind-Wave Stars hybrid system

The influence of the arm projection L_h on wave power generation is investigated. The tendency of wave power and wave amplitude along the direction of the arm are also compared. The contained angle is set as φ=0. Fig. 5 shows the wave power P and wave amplitude of the Wave Stars layout location A for a range of arm projection lengths under the incident wave of T_p=5.3 s. Fig. 5a shows that the tendency of the wave power of WEC #2 is similar to that of the wave amplitude but with a slight drift to larger L_h. This deviation caused by the addition of the WEC has a small disturbance on the local wave amplitude by diffraction and radiation. Fig. 5b shows that while the distance between WEC #1 or WEC #3 and the corresponding side column is far, the tendency of wave power is coherent with that of the wave amplitude. The radiation and diffraction of the WEC also cause a little deviation. Both Fig. 5a and Fig. 5b show that while a WEC is close to the side column, its power generation dramatically increases. This is due to the complex radiation and diffraction as the device is placed close to the column. In this mode, water resonates in the narrow gap between the Wave Star and the side column, inducing a very high wave force that promotes the motion of the Wave Star to obtain a large power output. Fig. 5c shows the tendency of the total power generation, which is similar to that of WEC #2. The maximum wave power can be obtained at L_h=25.13 m, while the maximum wave amplitude occurs at L_h=22.87 m. Although the maximum power cannot be obtained when the Wave Stars are precisely placed where the highest wave amplitude exists due to the disturbance of the platform, the difference (2.26 m) is not significant compared with the radius of the Wave Star, and the power output only decreases by 7.06%.

Therefore, for rapid design of the layout of the Wave Stars, the location of the highest wave amplitude can be used as a criterion. L_h=22.87 m is thereafter used as the optimal arm projection.

The optimal contained angle φ is then determined. Fig. 6 shows the total wave power under contained angles φ = 0, 15°, 22°, 30°, 37°, and 45° while the arm projection remains L_h=22.87 m. The total power first increases and then decreases as the contained angle grows, peaking at φ=30°. From the perspective of power output maximization, the arm projection L_h=22.87 m and included angles φ=30° are regarded as the preliminary optimized layout of the Wave Stars, which will be used in the rest of the analysis.

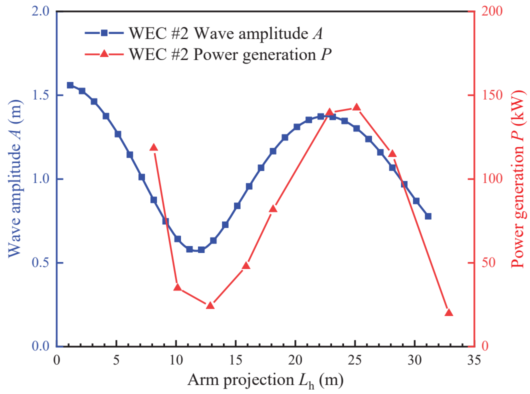

(a) WEC #2

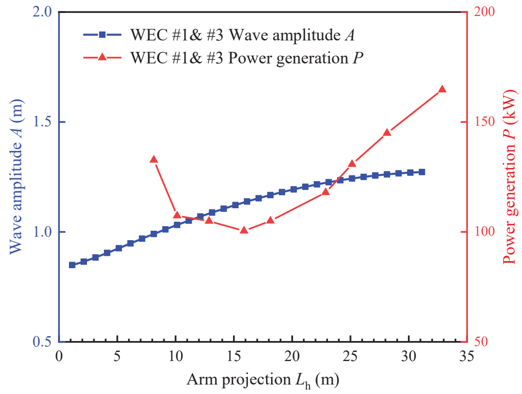

(b) WEC #1 or #3

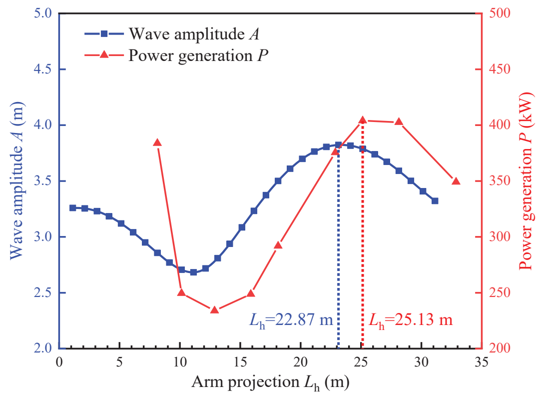

(c) Total power

Fig. 5 The power generation and amplitude for different arm projections (T=5.3 s, φ=0°)

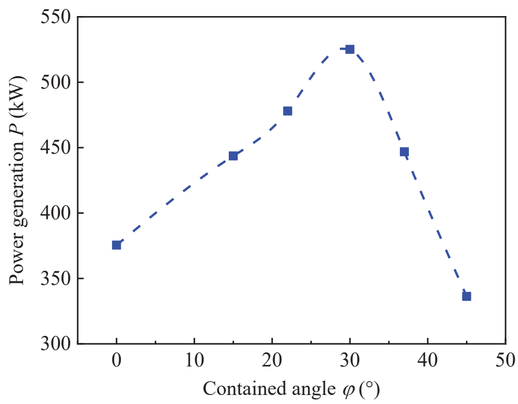

Fig. 6 The power generation for different included angles (T=5.3 s, L_h=22.87 m)

Fig. 7 shows the total power generation (sum of wind and wave power) of the hybrid system and the proportions of wind power and wave power. The regular incident wave is T_p=5.3 s. The wind speed is U=0, 8 m/s, 11.4 m/s, and 14 m/s. The integration of the Wave Stars will not reduce the power generated by wind turbine. Also, under each wind condition, the Wave Stars can provide power over 500 kW, which can be valuable to the whole while the wind turbine is experiencing downtime. As wind speed increases, the proportion of wave power becomes smaller. As the wind speed reaches the critical speed of U=11.4 m/s, the proportion of the wave power keeps about 10%. Considering that in most situations, the average wind speed in the South China Sea is smaller than 10.7 m/s and the average wave height is larger than 2 m, the percentage of wave power in the total power generation can be larger than that in the U= 8 m/s (23.8%), which could be an effective supplement.

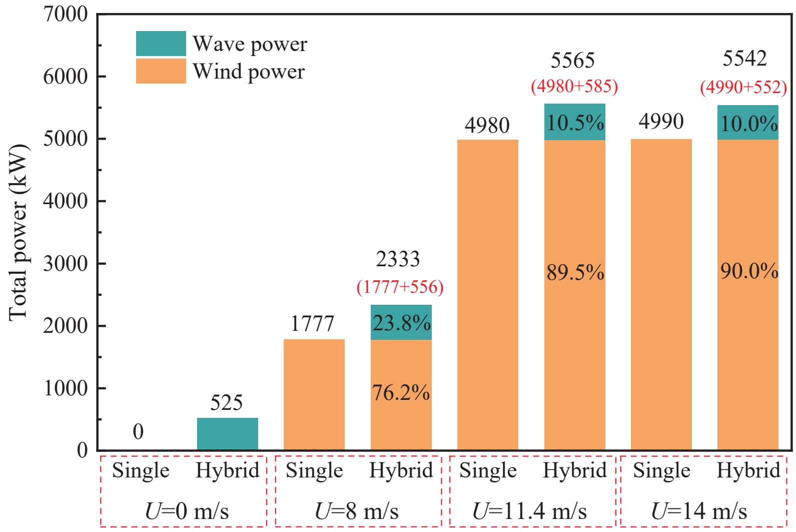

Fig. 7 Power generation of the hybrid system at different wind speeds (T_p=5.3 s, A=1 m)

Hywind-annular WEC hybrid system

The motion response of the Hywind platforms in the hybrid system, in isolation, and the difference between the two in the surge, heave, and pitch directions are shown in Fig. 8-Fig. 10, respectively. In each DoF, the changing trends of motion response of the Hywind in the hybrid system and isolation are nearly the same, but those in the surge and pitch directions are slightly different from that in the heave direction. The heave motion response almost changes little for different wind speeds, increasing as the wave period increases. The fundamental pattern can be divided into two parts in the surge and pitch directions, separated by the rated wind speed. In either part with wind speed smaller or larger than the rated wind speed, the motion response changes quite slightly against wind speed, which increases as the wave period increases. A sudden drop in motion response occurs around the rated wind speed, and this phenomenon is more evident in long waves.

As shown in Fig. 8c~Fig. 10c, the difference in the motion response is quite evenly distributed against the wind speed but changes largely against the wave period, indicating that the sudden drop is not caused by the annular WEC. The sudden declines in the surge and pitch motion response are caused by the servo system. As wind speed grows beyond the rated value, a switch of mode in the servo system changes the dynamic feature of Hywind, which triggers the sudden drop. The working principle of the servo system is to adjust the position of the wind turbine to make the rotor directly face the input wind. The servo system is sensitive to the surge and pitch motions of the platform as they affect the relative speed between the rotor and the input wind but is not sensitive to the heave motion. As the waves become longer, the wave forces increase and excite a larger motion, which exerts a greater influence on the servo system and intensifies the sudden drop.

The difference between the Hywinds in the hybrid system and isolation shows that the motion in any of the three DoFs will be increased by installing an annular WEC. The mechanism is quite simple in the surge and pitch directions. The annular WEC brings additional wave force, damping, and hydrostatic restoration stiffness in any of the three DoFs. A rigid connection passes the wave forces on the annular WEC to the wind platform. The increase in wave force will increase the motion response of the Hywind, whereas the increases in damping and hydrostatic restoration stiffness will reduce the motion response. The results indicate that the increase in wave force exceeds the increases in damping and hydrostatic restoration stiffness, and the motion response is consistently increased. As the surge motion of the hybrid system has a limited effect on the wave power generation using the relative heave motion, an extended active tuned mass damper or tuned mass damper-nonlinear energy sink can be employed to mitigate the WEC-induced increase in the surge motion response. In the heave direction, the mechanism is a bit more complex as the presence of the PTO force constitutes an additional source of the force that intensifies the motion response of Hywind. The difference in the motion response between the Hywind in the hybrid system and isolation is also dominated by wave conditions. Above all, the dynamic stability of the Hywind depends on wave conditions and is reduced by the annular WEC. The reduction in the heave direction is greater than in the surge and pitch directions.

Fig. 11 shows differences between the Hywinds in the hybrid system and isolation in the maximum displacements in the surge, heave, and pitch directions. Generally, the annular WEC reduces the maximum displacements of the Hywind in the surge and pitch direction and increases that in the heave direction. It improves the stability of the Hywind in the pitch direction, particularly around the rated wind speed. On the other hand, a compromise between the generation of wave power and the increase in the heave motion has to be made according to specific situations.

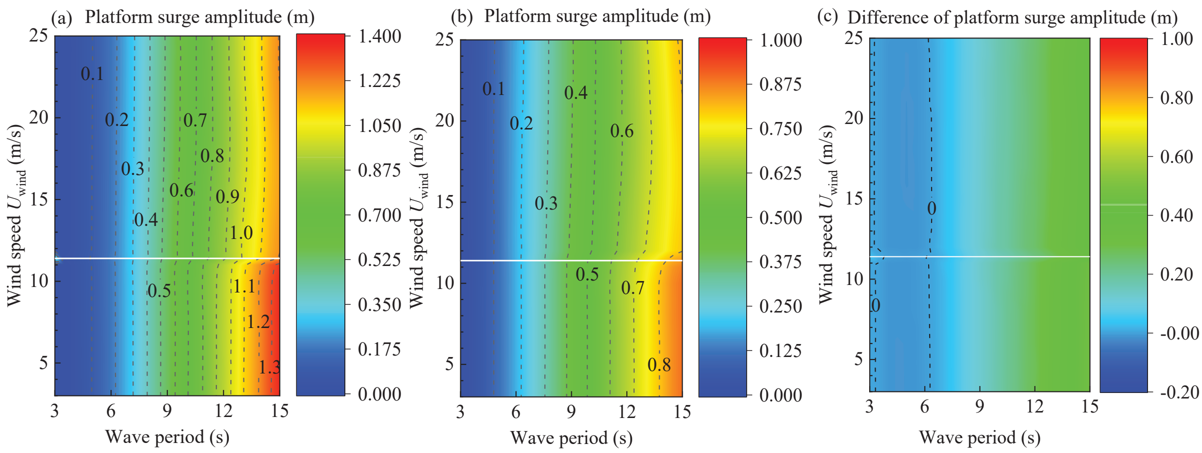

(a) Hybrid (b) Hywind (c) Difference (Hybrid−Hywind)

Fig. 8 Motion amplitudes of Hywind in surge direction

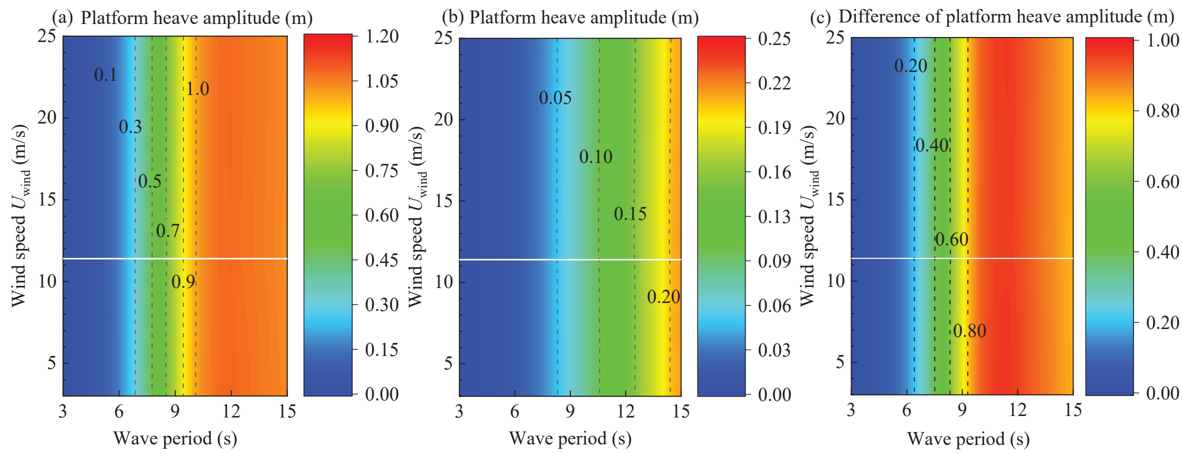

(a) Hybrid (b) Hywind (c) Difference (Hybrid−Hywind)

Fig. 9 Motion amplitudes of Hywind in heave direction

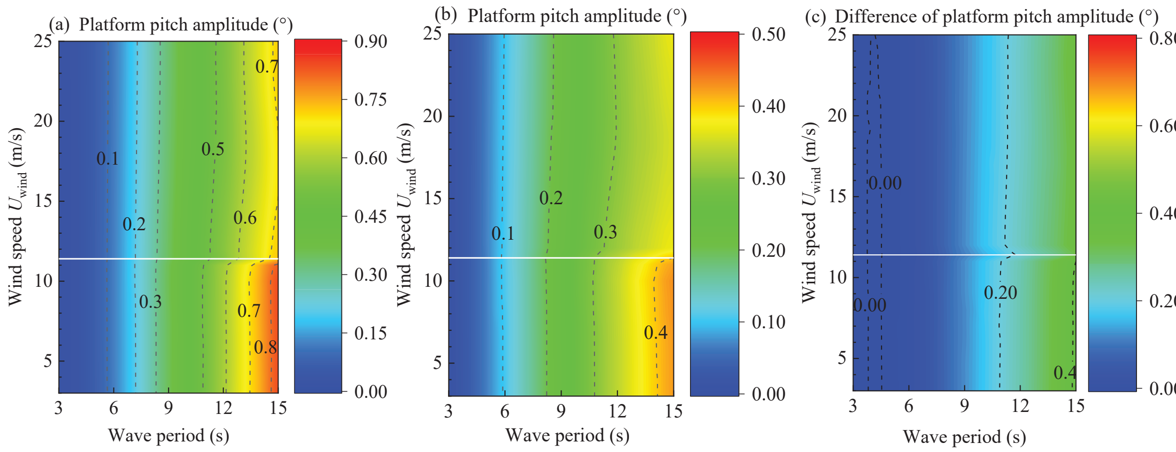

(a) Hybrid (b) Hywind (c) Difference (Hybrid−Hywind)

Fig. 10 Motion amplitudes of Hywind in the pitch direction

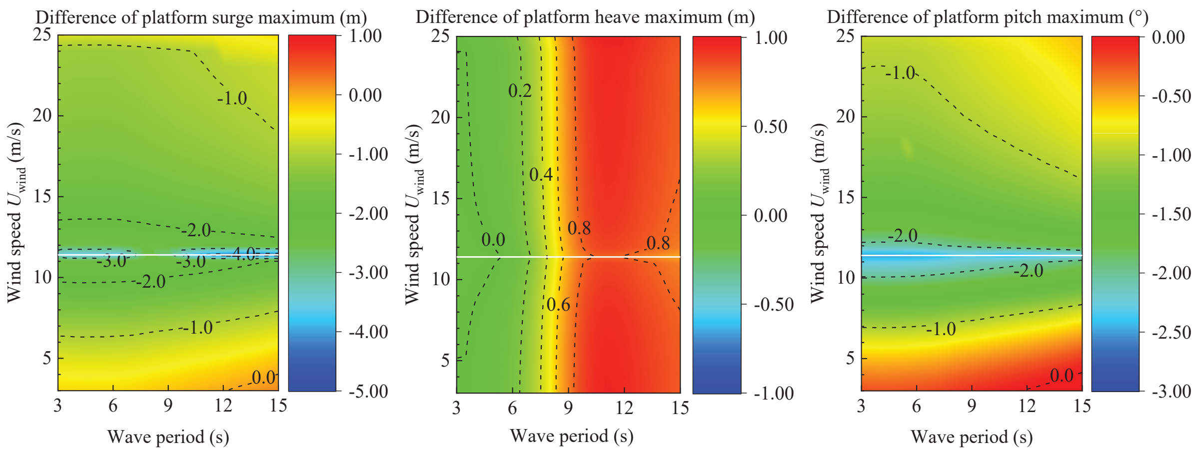

(a) Surge (b) Heave (c) Pitch

Fig. 11 Difference of platform maximum displacements between hybrid system and Hywind

This section investigates the mutual influence between the wind turbine and the annular wave energy converter on their transient wind and wave energy conversion performance. Fig. 12 shows the wind power of the hybrid system, the isolated Hywind, and the difference between the two. The general trend of wind power in different sea states is not affected by the annular WEC. The wind power increases to its rate power 5 MW as wind speed increases to U=11.4 m/s and keeps approximately constant as wind speed further increases, which is the same as that shown in Fig. 12b. The wind power distributes quite evenly against the wave period, indicating it is nearly unaffected by the wave condition.

Fig. 12c shows that the annular WEC slightly improves the wind power while the wind is below the rated speed, particularly in shorter waves. This is because the annular WEC reduces the equilibrium tilted angle of the Hywind in the pitch direction, making the rotor face the input wind more directly. In the shorter waves, the motion amplitude in the pitch direction is smaller, which leads to a more stable increase in wind power. While wind is beyond the rated speed, the wind power reaches its upper limit and cannot be further improved by the annular WEC. Evidence can be found in the comparison between Fig. 11c and Fig. 12c, where the increase in wind power shows similar trends to that of the decrease of the platform displacement in the pitch direction.

Fig. 13 shows the wave power of the hybrid system in different sea states. The mean peak period T_{ave}=8.54 s is marked by a white line. The wave power increases and then decreases, reaching a peak at 8.54 s, whereas it is nearly not affected by wind speed.

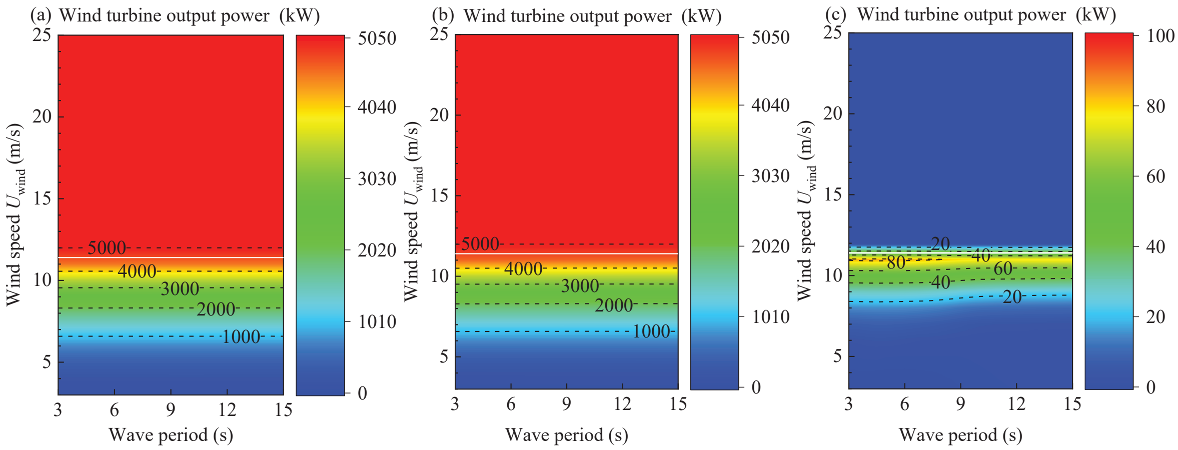

(a) Hybrid (b) Hywind (c) Difference (Hybrid−Hywind)

Fig. 12 Wind turbine output power under different wind speeds and wave periods

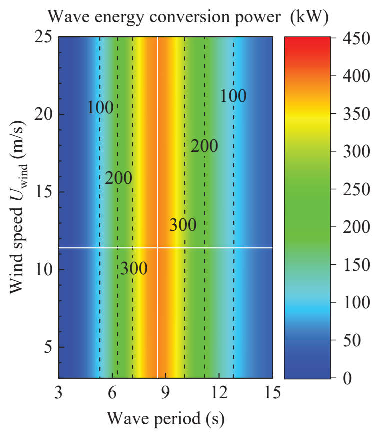

Fig. 13 Wave power production of the hybrid system under different wave periods and wind speeds

References

[1] Chen, X., Wang, K., Zhang, Z., Zeng, Y., Zhang, Y., & O'Driscoll, K. (2017). An assessment of wind and wave climate as potential sources of renewable energy in the nearshore Shenzhen coastal zone of the South China Sea. Energy, 134, 789-801.

[2] Clemente, D., Rosa-Santos, P., & Taveira-Pinto, F. (2021). On the potential synergies and appli-cations of wave energy converters: A review. Renewable and Sustainable Energy Reviews, 135, 110162.

[3] Astariz, S., & Iglesias, G. (2015). The economics of wave energy: A review. Renewable and Sustainable Energy Reviews, 45, 397-408.

[4] Hu, J., Zhou, B., Vogel, C., Liu, P., Willden, R., Sun, K., & Collu, M. (2020). Optimal design and performance analysis of a hybrid system combing a floating wind platform and wave energy converters. Applied Energy, 269, 114998.

[5] Zhang, H., Zhou, B., Zang, J., Vogel, C., Fan, T., & Chen, C. (2021). Effects of narrow gap wave resonance on a dual-floater WEC-breakwater hybrid system. Ocean Engineering, 225, 108762.

[6] Zhang, H., Zhou, B., Zang, J., Vogel, C., Jin, P., & Ning, D. (2021). Optimization of a three-dimensional hybrid system combining a floating breakwater and a wave energy converter array. Energy Conversion and Management, 247, 114717.

[7] Chozas, J. F., Sørensen, H. C., & Jensen, N. H. (2012). Economic benefit of combining wave and wind power productions in day-ahead electricity markets. In 4th International Conference on Ocean Energy.

[8] Chozas, J. F., Kofoed, J. P., & Sørensen, H. C. (2013). Predictability and Variability of Wave and Wind: wave and wind forecasting and diversified energy systems in the Danish North Sea. Department of Civil Engineering, Aalborg University. DCE Technical reports No. 156.

[9] Platform, M. A. R. I. N. A. European Union Seventh Framework Programme (EU FP7) Marine Renewable Integrated Application Platform (MARINA Platform).

国際化推進共同研究概要

No.27

23RE-7

タイトル： CFD Simulation of Offshore Wind Turbine in Realistic Ocean Environment

研究代表者： LI Ye

所内世話人： 胡　長洪

研究概要：

本国際化推進共同研究について、共同研究・研究集会とも予定通り実施した。共同研究について、浮体式洋上風車に関する高性能 CFD 手法の開発や、風車・浮体一体化した解析手法の開発に関する研究などが行われ、関連の研究成果は７編の学術論文に纏められ投稿された。2024 年 1 月 15 日～16 日に国際研究集会「The 2nd International Symposium on Marine Renewable Energy System Dynamics」が応力研で開催され、中国、韓国、英国、台湾から 10 件、日本から 7 件の講演があり、洋上風力ファームに関する数値シミュレーション、各種の海洋再生可能エネルギー技術の研究開発などに関して有意義な国際研究集会となった。

Report for 2023 RIAM International Joint Research Project

[23RE-7]

CFD Simulation of Offshore Wind Turbine in Realistic Ocean Environment

Ye Li
School of Naval Architecture, Ocean and Civil Engineering, Shanghai Jiao Tong University, China

1. Purpose

Offshore wind turbines (OffWT) and onshore wind turbines (OnWT) have different working conditions, design loads, and wake characteristics. An in-depth analysis of the influence of the incoming atmospheric characteristics and wake evolution characteristics of OffWT and OnWT on the design value of wind turbines is important to reduce the cost and improve the power coefficient. This joint research project will focus on the analysis of atmospheric conditions, wakes, and their interactions with wind turbine loads, and explore the role of the real atmosphere on wind turbine power fluctuations, and wake evolution. In addition, the project also provides an opportunity for researchers, including but not limited to SJTU and RIAM, to exchange knowledge on the renewable energy research.

2. Research Plan

This research project is planned for two years. FY 2023 is the second year of the project. The major research topic is the development of wind turbine simulation methods, advanced atmospheric turbulence generation methods and wave models for the ocean waves, especially on the wake and load analysis of wind turbines under typical offshore and onshore atmospheric conditions. At the end of FY2023, as the main event of this international joint research project, the 2nd International Symposium on Marine Renewable Energy System Dynamics will be carried out. Researchers involved in this joint research project will present and discuss their research progresses.

The members involved in this collaborative research are shown in the following table.

Researcher's Name	Name of University or Institute	Present Status or Grade (graduate students)	Researcher role
Ye Li	SJTU	Professor	Representative person (CFD)
Changhong Hu	RIAM	Professor	RIAM Attendant
Zhiteng Gao	SJTU	Assistant Professor	Co-researcher (CFD)
Xiaobo Zheng	SJTU	Associate Professor	Co-researcher (CFD)
Jun Leng	SJTU	Assistant Professor	Co-researcher (CFD)
Lijun Zhang	SJTU	Assistant professor	Co-researcher (CFD)
Seiya Watanabe	RIAM	Assistant professor	Co-researcher (CFD)

3. Summary of Collaboration Research

In 2023, research discussions have been made between the two research groups through the Internet. Main topics that have been studied include (1) next-generation CFD development; (2) wind turbine and wake modeling; (3) advanced atmospheric turbulence generation methods; (4) machine learning application to hydro- and aerodynamic analysis and (5) related ocean renewable energy technologies. Most of the research results will be presented at the 2nd International Symposium on Marine Renewable Energy System Dynamics, which was held on 15-16 January 2024.

Research papers related to this joint research project in 2023~2024 are listed as follows.

[1] Zhou Y, Bhowmick P, Zhang L, Chen L, Nagamune R, Ye Li Y*. A model reference adaptive control framework for floating offshore wind turbines with collective and individual blade pitch strategy[J]. Ocean Engineering, 2024, 291: 116054.

[2] Xu W, Li G, Li Y*. Feasibility analysis of aerodynamic characteristics for vertical-axis turbines in offshore: A comprehensive analysis on scale and design of wind system[J]. Ocean Engineering, 2023, 285: 115406.

[3] Leng J, Gao Z, Wu M C H, T Guo, Li Y*. A fluid–structure interaction model for large wind turbines based on flexible multibody dynamics and actuator line method[J]. Journal of Fluids and Structures, 2023, 118: 103857.

[4] Wang H, Zheng X, Pröbsting S, Hu C, Wang Q, Li Y*. An unsteady RANS simulation of the performance of an oscillating hydrofoil at a high Reynolds number[J]. Ocean Engineering, 2023, 274: 114097.

[5] Xu Q, Wang S, Li Y*. A semi-analytical solution for water wave scattering by partially immersed perforated and solid barriers with a quadratic pressure discharge condition[J]. Ocean Engineering, 2023, 270: 113460.

[6] Zheng X, Wang H, Xu W, Gao Z, Leng J, Li Y*. Aerodynamic responses of vertical-axis wind turbine foil to different vortex shedding patterns[J]. ACTA AERODYNAMICA SINICA, 2023, 41(6): 26-34.

[7] Gyatso N, Li Y*, Gao Z, et al. Wind power performance assessment at high plateau region: A case study of the wind farm field test on the Qinghai-Tibet plateau[J]. Applied Energy, 2023, 336: 120789.

As a main event of this year's international joint research project, 'The 2nd International Symposium on Marine Renewable Energy System Dynamics' was carried out on January 15-16, 2024. At the symposium, overseas and domestic scholars were invited to present their recent research results on the research and development of marine renewable energy system dynamics. The program of the symposium is as follows.

The 2nd International Symposium on Marine Renewable Energy System Dynamics

Organized by Research Institute for Applied Mechanics (RIAM), Kyushu University

Date: January 15-16, 2024

Venue: Meeting Room at 2nd Floor of RIAM

Kyushu University, 6-1 Kasuga-koen, Kasuga, Fukuoka 816-8580, Japan

TIME TABLE

12:50 -13:00	Opening Address by **Ye Li**

Session 1 ***Advanced Theoretical, Numerical, and Experimental Research***

13:00 - 13:40	**Cheng Liu** (Shanghai Jiao Tong University, China) *Invited Lecture* Numerical Method in the Simulation of Two-Phase Flow with Adaptive Mesh
13:40 - 14:05	**Seiya Watanabe** (RIAM, Kyushu University) Lattice Boltzmann Simulation of a Multi-Rotor Diffuser Augmented Wind Turbine
14:05 - 14:30	**Jun Leng** (Shanghai Jiao Tong University, China) A Fluid-Structure Interaction Model for Large Wind Turbines based on Flexible Multibody Dynamics and Actuator Line Method
14:30 – 14:55	**Yingyi Liu** (RIAM, Kyushu University) 3p Effect of a Downstream Horizontal Axis Turbine in Partially Waked Flows
14:55 – 15:20	**Hiroki Yamazaki,** Hidetsugu Iwashita, Keigo Okazaki, Takahiro Tsuchimoto (Hiroshima University) Unsteady Ship-Side Wave Measurement of a Ship Advancing in Waves by Image Analysis

15:20 - 15:30	Break

Session 2 Ocean Renewable Energy Technology

15:30 - 16:10	**Ning Ma** (Shanghai Jiao Tong University, China) Invited Lecture Direct Stability Assessment of an Offshore Supply Vessel
16:10 - 16:35	**Zhiqiang Hu** (Newcastle University, UK) Offshore Wind and Artificial Intelligence: Steps to Real-time Monitoring and Digital Twins for Offshore Wind Turbines
16:35 - 17:00	**Hongzhong Zhu** (RIAM, Kyushu University) Control of Floating Type Hybrid Wind-Wave Energy System for Floater Motion Reduction
17:00 - 17:25	**Binzhen Zhou** (South China University of Technology, China) Development of Oscillating Body Wave Energy Converter Related Hybrid Systems
17:25 - 17:50	**Yusaku Kyozuka** (Nagasaki University) Impact of Tidal Array Interactions on Power Production: a Case Study in Naru Strait, Goto, Nagasaki

Session 3 Floating Offshore Wind Turbine

9:20 - 10:00	**Motohiko Murai** (Yokohama National University) Invited Lecture A Problem of Long Period Yaw Motion of 15MW Class Floating Offshore Wind Turbine
10:00 - 10:25	**Hoseong Yang**, Young-Ho LEE (KMOU, Korea) A Study on the Uncertainty Analysis of FOWT Response Using Engineering Tools Based on the Potential Method and CFD
10:25 - 10:50	**Sangwon Lee** (Jeju National University, Korea) Ultimate Load Analysis for Large Floating Offshore Wind Turbines under Wind-Wave Misalignment Condition
10:50-11:15	**Yarong Zhou** (Shanghai Jiao Tong University, China) A Model Reference Adaptive Control Framework for Floating Offshore Wind Turbines with Collective and Individual Blade Pitch Strategy
11:15 - 11:40	**Lijun Zhang** (Shanghai Jiao Tong University, China) Study on the Interaction of Floating Offshore Wind Turbines Under Wind and Wave Coupling Conditions
11:40 - 12:05	**Ryoya Hisamatsu** (Kyushu University) Experimental and Numerical Study of the Dynamics of Water Intake Riser for OTEC Application
12:05 - 12:30	**Shiu-Wu Chau** (National Taiwan University, Taiwan, R.O.C.) Hydrodynamic Property Prediction of Floating Bodies via a Viscous Approach

12:30 - 12:35	Closing Address by **Changhong Hu**